

# Synthesis, Properties, and Applications of Multifunctional Magnetic Nanostructures 2018

Lead Guest Editor: Vidyadhar Singh

Guest Editors: Anil Annadi, Biswanath Bhoi, Rajasekhar Madugundo, Manikandan Muthu, and Murtaza Bohra





---

**Synthesis, Properties, and Applications of  
Multifunctional Magnetic Nanostructures 2018**

Journal of Nanomaterials

---

# **Synthesis, Properties, and Applications of Multifunctional Magnetic Nanostructures 2018**

Lead Guest Editor: Vidyadhar Singh

Guest Editors: Anil Annadi, Biswanath Bhoi,

Rajasekhar Madugundo, Manikandan Muthu, and Murtaza Bohra



---

Copyright © 2019 Hindawi. All rights reserved.

This is a special issue published in "Journal of Nanomaterials." All articles are open access articles distributed under the Creative Commons Attribution License, which permits unrestricted use, distribution, and reproduction in any medium, provided the original work is properly cited.

## Editorial Board

- Domenico Acierno, Italy  
Katerina Aifantis, USA  
Nageh K. Allam, USA  
Margarida Amaral, Portugal  
Martin Andersson, Sweden  
Raul Arenal, Spain  
Ilaria Armentano, Italy  
Vincenzo Baglio, Italy  
Lavinia Balan, France  
Thierry Baron, France  
Andrew R. Barron, USA  
Stefano Bellucci, Italy  
Enrico Bergamaschi, Italy  
D. Bhattacharyya, New Zealand  
Sergio Bietti, Italy  
Giovanni Bongiovanni, Italy  
Mohamed Bououdina, Bahrain  
Victor M. Castaño, Mexico  
Albano Cavaleiro, Portugal  
Bhanu P. S. Chauhan, USA  
Shafiq Chowdhury, USA  
Yu-Lun Chueh, Taiwan  
Elisabetta Comini, Italy  
Giuseppe Compagnini, Italy  
David Cornu, France  
Miguel A. Correa-Duarte, Spain  
P. Davide Cozzoli, Italy  
Anuja Datta, USA  
Loretta L. Del Mercato, Italy  
Yong Ding, USA  
Yu Dong, Australia  
Zehra Durmus, Turkey  
Joydeep Dutta, Oman  
Ovidiu Ersen, France  
Ana Espinosa, France  
Claude Estournès, France  
Giuliana Faggio, Italy  
Andrea Falqui, Saudi Arabia  
Matteo Ferroni, Italy  
Ilaria Fratoddi, Italy  
Siddhartha Ghosh, Singapore  
Filippo Giubileo, Italy  
Fabien Gasset, Japan  
Jean M. Greneche, France
- Kimberly Hamad-Schifferli, USA  
Simo-Pekka Hannula, Finland  
Michael Harris, USA  
Yasuhiko Hayashi, Japan  
Michael Z. Hu, USA  
Nay Ming Huang, Malaysia  
Zafar Iqbal, USA  
Balachandran Jeyadevan, Japan  
Jeong-won Kang, Republic of Korea  
Hassan Karimi-Maleh, Iran  
Antonios Kelarakis, UK  
Alireza Khataee, Iran  
Ali Khorsand Zak, Iran  
Philippe Knauth, France  
Prashant Kumar, UK  
Eric Le Bourhis, France  
Jun Li, Singapore  
Meiyong Liao, Japan  
Shijun Liao, China  
Silvia Licocchia, Italy  
Nathan C. Lindquist, USA  
Zainovia Lockman, Malaysia  
Jim Low, Australia  
Gaurav Mago, USA  
Muhamamd A. Malik, UK  
Francesco Marotti de Sciarra, Italy  
Ivan Marri, Italy  
Laura Martinez Maestro, UK  
Sanjay R. Mathur, Germany  
Tony McNally, UK  
Yogendra Mishra, Germany  
Paulo Cesar Morais, Brazil  
Paul Munroe, Australia  
J.-M. Myoung, Republic of Korea  
Rajesh R. Naik, USA  
Albert Nasibulin, Russia  
Toshiaki Natsuki, Japan  
Hiromasa Nishikiori, Japan  
Natalia Noginova, USA  
Sherine Obare, USA  
Won-Chun Oh, Republic of Korea  
Abdelwahab Omri, Canada  
Ungyu Paik, Republic of Korea  
Edward A. Payzant, USA
- Alessandro Pegoretti, Italy  
Oscar Perales-Pérez, Puerto Rico  
Jorge Pérez-Juste, Spain  
Alexey P. Popov, Finland  
Thathan Premkumar, Republic of Korea  
Helena Prima-García, Spain  
Alexander Pyatenko, Japan  
Haisheng Qian, China  
You Qiang, USA  
Philip D. Rack, USA  
Mohammad Rahimi-Gorji, Belgium  
Peter Reiss, France  
Ilker S. Bayer, Italy  
Lucien Saviot, France  
Sudipta Seal, USA  
Shu Seki, Japan  
Donglu Shi, USA  
Bhanu P. Singh, India  
Surinder Singh, USA  
Vladimir Sivakov, Germany  
Adolfo Speghini, Italy  
Marinella Striccoli, Italy  
Fengqiang Sun, China  
Ashok K. Sundramoorthy, India  
Angelo Taglietti, Italy  
Bo Tan, Canada  
Leander Tapfer, Italy  
Valeri P. Tolstoy, Russia  
Muhammet S. Toprak, Sweden  
R. Torrecillas, Spain  
Achim Trampert, Germany  
Takuya Tsuzuki, Australia  
Tamer Uyar, Turkey  
Luca Valentini, Italy  
Antonio Vassallo, Italy  
Ester Vazquez, Spain  
Ajayan Vinu, Australia  
Ruibing Wang, Macau  
Shiren Wang, USA  
Yong Wang, USA  
Magnus Willander, Sweden  
Ping Xiao, UK  
Zhi Li Xiao, USA  
Yingchao Yang, USA



---

Yoke K. Yap, USA  
Dong Kee Yi, Republic of Korea

Jianbo Yin, China  
William Yu, USA

Michele Zappalorto, Italy  
Renyun Zhang, Sweden

# Contents

## **Synthesis, Properties, and Applications of Multifunctional Magnetic Nanostructures 2018**

Vidyadhar Singh , Anil Annadi , Biswanath Bhoi, Rajasekhar Madugundo , Manikandan Muthu, and Murtaza Bohra 

Editorial (3 pages), Article ID 1847262, Volume 2019 (2019)

## **A Short Review on Verwey Transition in Nanostructured Fe<sub>3</sub>O<sub>4</sub> Materials**

Murtaza Bohra , Nishit Agarwal, and Vidyadhar Singh 

Review Article (18 pages), Article ID 8457383, Volume 2019 (2019)

## **In Vitro Safety Evaluation and In Vivo Imaging Studies of Superparamagnetic Iron Oxide Nanoparticles through Biomimetic Modification**

Xinfeng Song, Yancong Zhang , Hanwen Sun , Pingxuan Dong, Zhongyu Zhang, and Jing Liu

Research Article (9 pages), Article ID 9827625, Volume 2019 (2019)

## **Investigation of the Magnetic Properties of Ferrites in the CoO-NiO-ZnO Using Simplex-Lattice Design**

Liliya Frolova  and Oleg Khmelenko

Research Article (8 pages), Article ID 5686741, Volume 2018 (2019)

## **Directional Control of the Structural Adsorption Properties of Clays by Magnetite Modification**

Tetiana A. Dontsova , Elena I. Yanushevskaya, Svitlana V. Nahirniak, Oksana V. Makarchuk , Andrei I. Ivanets, Marina Yu Roshchina, Anastasiya S. Kutuzova, and Leonid M. Kulikov

Research Article (9 pages), Article ID 6573016, Volume 2018 (2019)

## **Magnetic Fe<sub>3</sub>O<sub>4</sub>@Chitosan Carbon Microbeads: Removal of Doxycycline from Aqueous Solutions through a Fixed Bed via Sequential Adsorption and Heterogeneous Fenton-Like Regeneration**

Bo Bai , Xiaohui Xu, Changchuan Li, Jianyu Xing, Honglun Wang , and Yourui Suo

Research Article (14 pages), Article ID 5296410, Volume 2018 (2019)

## **Appearance of Ferromagnetic Property for Si Nanopolycrystalline Body and Vanishing of Electrical Resistances at Local High Frequencies**

Taku Saiki , Yukio Iida, and Mitsuru Inada

Research Article (12 pages), Article ID 9260280, Volume 2018 (2019)

## **Surface Profile Measurement and Error Compensation of Triangular Microstructures Employing a Stylus Scanning System**

Qin Yin, Bin Xu , Guofu Yin, Peng Gui, Wei Xu, and Bin Tang

Research Article (7 pages), Article ID 6396871, Volume 2018 (2019)

## **Preparation and Evaluation of Smart Nanocarrier Systems for Drug Delivery Using Magnetic Nanoparticle and Avidin-Iminobiotin System**

Shuguo Sun , Beiping Li, Tao Yang , Meihu Ma , Qinlu Lin , Juanhong Zhao, and Feijun Luo

Research Article (11 pages), Article ID 1627879, Volume 2018 (2019)

## **Structural, Morphological, Optical, and Room Temperature Magnetic Characterization on Pure and Sm-Doped ZnO Nanoparticles**

Khalil Badreddine , I. Kazah , M. Rekaby , and R. Awad

Research Article (11 pages), Article ID 7096195, Volume 2018 (2019)

## Editorial

# Synthesis, Properties, and Applications of Multifunctional Magnetic Nanostructures 2018

Vidyadhar Singh <sup>1</sup>, Anil Annadi <sup>2</sup>, Biswanath Bhoi,<sup>3</sup> Rajasekhar Madugundo <sup>4</sup>,  
Manikandan Muthu,<sup>5</sup> and Murtaza Bohra <sup>6</sup>

<sup>1</sup>Department of Physics, Jai Prakash University, Chapra, 841301 Bihar, India

<sup>2</sup>Department of Materials Science and Engineering, National University of Singapore, Singapore, Singapore 117576

<sup>3</sup>Seoul National University, Seoul, Republic of Korea

<sup>4</sup>BC Materials, UPV/EHU Science Park, 48940 Leioa, Spain

<sup>5</sup>School of Environmental Sciences, Konkuk University, Seoul, Republic of Korea

<sup>6</sup>Mahindra École Centrale College of Engineering, Hyderabad 500043, India

Correspondence should be addressed to Vidyadhar Singh; [vsraj47@gmail.com](mailto:vsraj47@gmail.com)

Received 17 January 2019; Accepted 17 January 2019; Published 4 April 2019

Copyright © 2019 Vidyadhar Singh et al. This is an open access article distributed under the Creative Commons Attribution License, which permits unrestricted use, distribution, and reproduction in any medium, provided the original work is properly cited.

Magnetic nanostructures have emerged as the novel class of materials being used in a variety of applications such as ultra-high-density magnetic recording media, drug delivery, magnetic resonance imaging (MRI), sensing, hyperthermia, water treatments, and catalysts. Recent advances in multifunctional nanostructured design, synthesis, and characterization techniques have led to the realization of various magnetic nanostructures exhibiting several physical and chemical properties that are unique and interesting. Magnetic nanostructures with varied geometries are complex and manifest diverse properties differing from their parent bulk compound because the energies associated with the various physical parameters are comparable to the nanostructure dimensions. Controlling these properties, thus, enables researchers to understand and develop new concepts that would potentially result in novel applications. This annual special issue is comprised of a wide range of original research articles as well as review papers on the topic of synthesis, properties, and applications of new designed multifunctional magnetic nanostructures.

In this special issue, a total of nine manuscripts were accepted for publication out of fourteen manuscripts. These articles covered a broad variety of topics related to magnetic nanomaterials. We hope that these articles will give the

readers useful information and pathway for futuristic scientific applications. In the following, we will summarize the results from accepted manuscripts.

B. Bai et al. investigated magnetic  $\text{Fe}_3\text{O}_4$ @chitosan carbon microbeads (MCM), which were synthesized by a simple thermal cracking process under a nitrogen atmosphere at 350°C. Based on the XRD, SEM, and FT-IR characterization results, a possible mechanism for the formation of MCM was proposed. The application of MCM composites for the adsorptive removal of doxycycline (DC) was evaluated using a fixed-bed column. The results showed that pH, initial concentration, flow rate, and bed depth are found to be important factors to control the adsorption capacity of DC. The Thomas and Yoon-Nelson models showed a good agreement with the experimental data and could be applied for the prediction of the fixed-bed column properties and breakthrough curves. More importantly, the saturated fixed bed can be easily recycled by  $\text{H}_2\text{O}_2$  which shows excellent reusability for the removal of doxycycline. Thus, the combination of the adsorption advantage of chitosan carbon with catalytic properties of magnetic  $\text{Fe}_3\text{O}_4$  nanoparticles might provide a new tool for addressing water treatment challenges.

S. Sun et al. studied avidin-immobilized magnetic nanoparticles (AMNPs) as a novel targeted drug delivery system

to deliver iminobiotinylated daunomycin (IDAU). In their study, an IDAU was connected to AMNPs based on the avidiniminobiotin binding system. The drug loading capacity and release behavior were then determined through adsorption dissociation kinetics experiments, and the inhibitory effects of IDAU on liver tumour cell DLKP growth were also evaluated. Therapeutic efficacy and the regulation of drug release can be improved by using selective targeting drug delivery systems. TEM, XRD, VSM, and FTIR were employed for the physicochemical characterization of the drug-loaded MNPs. The binding of IDAU had little effect on sizes of AMNPs (~35 nm), but the stability and dispersibility of the nanoparticles were improved. The study also found that the loading capacity and efficiency of nanoparticles were mainly dependent on affinity interaction between IDAU and AMNPs. The optimal loading capacity and efficiency of MNPs for IDAU were measured according to the reversed-phase high-performance liquid chromatography (RP-HPLC) data. Under the conditions of pH 6.8 and 1 mmol/L of biotin, the drug-loaded MNPs released rapidly at the beginning and then maintained at a certain controllable release level. The effect of IDAU on DLKP proliferation was also tested. These findings indicated that AMNPs hold tremendous potential as an effective drug delivery system.

The article "Investigation of the Magnetic Properties of Ferrites in the CoO-NiO-ZnO Using Simplex-Lattice Design" by L. Frolova and O. Khmelenko is devoted to the analysis of changes in the magnetic characteristics of spinel ferrite in the CoO-NiO-ZnO system by the simplex method. In this study, ferrites of Ni-Zn, Co-Zn, and Co-Ni were synthesized in the form of nanoparticles (20-40 nm) using a new method for processing contact nonequilibrium low-temperature plasma (CNP). The effect of the mutual influence of the content of different bivalent cations on the saturation magnetization and the coercive field was investigated. The Ni-Zn ferrites show low magnetization values compared to the entire Co-Zn, Co-Ni ferrite series. The EPR spectra of ferrites are analyzed by superexchange interaction, which shows that the value of the resonant field and line width corresponds to the value of magnetic saturation and is due to the arrangement of cations on sublattices, i.e., the distribution between the tetrahedral and octahedral sites.

Q. Yin et al. reported a study introducing a measurement system specifically designed and constructed for surface profile measurement of triangular microstructures generated on the surface of flat workpieces. Microstructures with the shape of an equilateral right triangle were employed as the measurement specimen. The surface profile measurement of triangular microstructures was carried out by employing two methods to correct errors caused by the specimen inclination and the radius of the stylus tip. The shape, depth, and period of the measured microstructures were also detected based on the results of surface profile measurement. Also, the proposed measurement system was experimentally tested. Experimental results demonstrate the feasibility of the proposed surface profile measurement for microstructures with complex surface topographies.

T. A. Dontsova et al. investigated the effect of the nanomagnetite modification on textural characteristics of clay

matrices, adsorption properties, and parameters of the spent sorbent separation. The nitrogen adsorption-desorption method has shown that the obtained magnetic nanocomposite sorbents have large specific surface areas (in 1.2–2 times more) than the initial clays due to the formation of the secondary porous structure on the surface and in macropores of clay matrices. The best adsorption properties concerning dyes belong to magnetic sorbents with nanomagnetite content of 7 wt.%. The additional modification of the third phase of graphene-like molybdenum disulphide into magnetic sorbents leads to the significant increase in the sorption capacity of both cationic (up to 1100 mg/g) and anionic (up to 1830 mg/g) dyes. The conducted investigations of the total acidity and acid-base sites on the surface of clay, magnetite-modified clay, and molybdenum disulfide-modified magnetic sorbent indicate the significant influence of the Lewis base sites on the adsorption properties of these materials. In their research, data are presented on the change in the adsorption and textural characteristics of clay matrices depending on the magnetite content, the amount of the modifier on the magnetic separation process and the moisture content of waste sorbents, and the influence of the third-phase presence (nanomolybdenum disulphide) in the magnetic mineral sorbent on its adsorption and textural properties. Thus, authors attempted to analyze the possibility of directed modification of the adsorption and textural properties of various clay matrices modified with nanomagnetite by a simple impregnation method.

K. Badreddine et al. studied the effect of Sm doping with different concentrations up to 10% on the structural, morphological, optical, and magnetic properties of the ZnO nanoparticles. The  $Zn_{1-x}Sm_xO$  ( $0.00 \leq x \leq 0.10$ ) nanoparticles were prepared by coprecipitation technique that provides nanopowders with good quality despite the low cost and simplicity of this method. XRD analysis showed the hexagonal wurtzite structure of ZnO and absence of any residual  $Sm_2O_3$  phase, indicating that Sm dissolved completely into ZnO lattice. The fluctuating lattice parameters ( $a$  and  $c$ ) with an increase of Sm doping indicated that the structure of ZnO was perturbed by the doping of Sm. TEM micrographs revealed that the size and the shape of the ZnO nanocomposites were changed by modifying the doping level of Sm. The band gap energy and Urbach energy were calculated for  $Zn_{1-x}Sm_xO$ . The band energy gaps of pure and Sm-doped ZnO samples are in the range 2.6–2.98 eV. Pure ZnO exhibited a room temperature ferromagnetic behavior along with diamagnetic and paramagnetic contributions. Ferromagnetic behavior was reduced for the doped samples with  $x = 0.01$  and  $x = 0.04$ . The samples with  $x = 0.02$  and  $0.06 \leq x \leq 0.10$  tend to be superparamagnetic.

T. Saiki et al. estimated the density of the unpaired electrons by ESR technique in sintered nanopolycrystalline Si. Reduction in the skin effect for the sintered Si nanopolycrystalline body as an electricity conductor at a high frequency due to its nanostructure was studied. Singular disappearance of electrical resistances near a local high magnetic harmonic frequency of a few MHz was observed. This phenomenon has not been observed for conventional ferromagnetic metals. The measured electrical resistances changed to

almost 0 m $\Omega$  at room temperature. At the same time, negative resistance of the sintered Si nanopolycrystalline body was observed. It will apply to electronic transmittance lines or semiconductors. The numerical calculation was also performed on the electrical resistance with frequency dependency while considering the electric field and magnetic field in the sintered Si nanopolycrystalline body. The experimental and calculated results were compared. The calculation could explain the variation of the relative permittivity of the Si nanopolycrystalline body and the phenomenon for the theoretical disappearance of the resistivity at the MHz frequency. Reduced Si nanoparticles from SiO<sub>2</sub> powder were synthesized by laser ablation in liquid. A Si nanopolycrystalline body made of the reduced Si nanoparticles was fabricated. It was found by measuring the magnetization property of the sintered Si nanopolycrystalline body which is ferromagnetic. Dangling bonds (unpaired electrons) have long been known to occur due to defects in Si crystals. Perfect Si without defective crystals has no dangling bonds. However, Si nanoparticles have many dangling bonds. High-density dangling bonds cause the sintered Si nanopolycrystalline body to have ferromagnetism.

X. Song et al. report *in vitro* safety evaluation and *in vivo* imaging studies of superparamagnetic iron oxide nanoparticles (SPION) through biomimetic modification. Magnetic resonance imaging (MRI) is an advanced medical imaging diagnostic technique that utilizes different resonance signals generated by the signal strength of water content and the relaxation time of protons in water molecules under the influence of an external magnetic field. This technique requires contrast agents, such as Gd-DTPA and Gd-DOTA, which could increase the risk of renal fibrosis in patients with severe renal insufficiency. The magnetic moment or susceptibility of SPION is higher than that of other paramagnetic substances and could significantly reduce the dosage of the contrast agent required. Animal acute toxicity test also had proved its high safety *in vivo*. In this work, c(RGDyK)-PDA-SPION was further studied for the cell toxicity and effect on HepG2 cells *in vitro*, and the MRI imaging of this contrast agent in HepG2 tumour-bearing mice was also studied. The results showed that it possessed high safety and enrichment phenomenon on HepG2 cells *in vitro*. Animal experimental data preliminarily prove that the contrast agent could enhance the MRI *T2*-weighted imaging capability of HepG2 carcinoma in tumour-bearing mice and could be a potential *T2* contrast agent.

Finally, the review conducted by M. Bohra et al. features on “well-known” Verwey transition of Fe<sub>3</sub>O<sub>4</sub>, particularly in nanoscale dimensions. Considering sharp changes occur in the physical properties of Fe<sub>3</sub>O<sub>4</sub> near Verwey transition, numerous potential applications based on spin/charge transport, multiferroicity, exchange bias, and spin Seebeck effect have been reviewed. They briefly reviewed recent research work on the origin of Verwey transition though it is still debatable. The size and shape effect on the Verwey transition of various geometries and their synthesis methods have been discussed in length. The Verwey transition is a low-temperature transition around 120 K; various artificial ways are summarized on how to shift this transition at higher

temperature end. Authors also discussed the best growth and characterization methods which are being currently employed to investigate Verwey transition of nanostructured Fe<sub>3</sub>O<sub>4</sub> material because conventional methods have their limitations. Authors also highlighted a pathway for futuristic spintronics and nanotechnology applications wherein Verwey transition-based applications can be potentially employed.

We hope that this special issue will contribute to the nanomagnetic society of their current understanding.

## Conflicts of Interest

The authors declare that there is no conflict of interest regarding the publication of this article.

## Acknowledgments

We would like to express our gratitude to all the authors for their contribution and all reviewers for their critical inputs.

Vidyadhar Singh  
Anil Annadi  
Biswanath Bhoi  
Rajasekhar Madugundo  
Manikandan Muthu  
Murtaza Bohra

## Review Article

# A Short Review on Verwey Transition in Nanostructured $\text{Fe}_3\text{O}_4$ Materials

Murtaza Bohra <sup>1</sup>, Nishit Agarwal,<sup>1</sup> and Vidyadhar Singh <sup>2</sup>

<sup>1</sup>Mahindra École Centrale, College of Engineering, Hyderabad, 500043 Telangana, India

<sup>2</sup>Department of Physics, Jai Prakash University, Chapra, 841301 Bihar, India

Correspondence should be addressed to Murtaza Bohra; [murtazaphy@gmail.com](mailto:murtazaphy@gmail.com) and Vidyadhar Singh; [vsraj47@gmail.com](mailto:vsraj47@gmail.com)

Received 5 August 2018; Revised 22 November 2018; Accepted 17 December 2018; Published 25 March 2019

Academic Editor: P. Davide Cozzoli

Copyright © 2019 Murtaza Bohra et al. This is an open access article distributed under the Creative Commons Attribution License, which permits unrestricted use, distribution, and reproduction in any medium, provided the original work is properly cited.

Verwey transition (VT) of  $\text{Fe}_3\text{O}_4$  has been extensively investigated as this results in sharp changes in its physical properties. Exploitation of VT for potential applications in spin/charge transport, multiferroicity, exchange bias, and spin Seebeck effect-based devices has attracted researchers recently. Although hundreds of reports have been published, the origin of VT is still debatable. Besides, not only the size effects have a significant impact on VT in  $\text{Fe}_3\text{O}_4$ , even the conditions of synthesis of  $\text{Fe}_3\text{O}_4$  nanostructures mostly affect the changes in VT. Here, we review not only the effects of scaling but also the growth conditions of the  $\text{Fe}_3\text{O}_4$  nanostructures on the VT and their novel applications in spintronics and nanotechnology.

## 1. Introduction

The metal-insulator transition also known as Verwey transition (VT) in strongly correlated magnetite ( $\text{Fe}_3\text{O}_4$ ) system is vital for its potential applications in nanoelectronics, spintronics, and mottoronix [1]. From a scientific point of view, the VT provides information to understand the extraordinary crystal lattice (regarding the freezing-in fluctuating lattice) and electronic structure (charge, spin, and orbital) order of  $\text{Fe}_3\text{O}_4$  [2, 3]. However, owing to the many competing degrees of freedom, the close energetic proximity of the different phases (presence of twinning) often obscures the exact nature of the VT as they are probed in thermal equilibrium. Technologically, the resistive switching behaviour in  $\text{Fe}_3\text{O}_4$  thin films at VT shows high potential for alternative memory applications, such as gate voltage-driven resistive switching in field-effect transistors [4]. On the other hand, the large change observed in magnetoresistance and spin Seebeck coefficient around VT makes it useful for sensors and solid-state energy conversion devices [5–7]. Thus, ever since then  $\text{Fe}_3\text{O}_4$  and in particular the VT has been an object of extensive research and great debate. Although experimental and theoretical progress has recently been made on  $\text{Fe}_3\text{O}_4$ , the origin of the VT is still under discussion.

$\text{Fe}_3\text{O}_4$  is a cubic ferrimagnetic oxide with the highest magnetization  $M = 4.2 \mu_B$  below Curie temperature,  $T_C = 858$  K. Band structure calculations predict half-metallic (-100% spin polarization) character of  $\text{Fe}_3\text{O}_4$  with room temperature conductivity,  $\sigma = 200 (\Omega \cdot \text{cm})^{-1}$  [8, 9]. Stoichiometric  $\text{Fe}_3\text{O}_4$  shows VT wherein first-order structural phase transformation occurs around 124 K ( $T_V$ ) [10]. In the low-temperature phase,  $\text{Fe}_3\text{O}_4$  is an insulator, has a monoclinic structure connected to the charge ordering, and exhibits an orbital order on the  $\text{Fe}^{2+}$  sites [11]. Also, it was found that localized electrons are shared between three Fe ions on octahedral *B*-lattice sites which can be termed as trimerons [8]. This transition also has manifestations in resistivity, heat capacity, magnetization, and many other properties [3]. Therefore, VT, which has a potential in cutting-edge technologies, provides an external tuning competency of the properties by changing the temperature. Despite the tremendous progress in nanostructured  $\text{Fe}_3\text{O}_4$ , it is still an open question how the VT changes in the nanoregime. The most critical difficulty in the size-dependent characterization of VT is the synthesis of uniform and stoichiometric nanostructured  $\text{Fe}_3\text{O}_4$  because VT is reported to be extremely sensitive to the oxygen stoichiometry [12]. The size of nanostructure having the VT varies in different reports, as stoichiometry

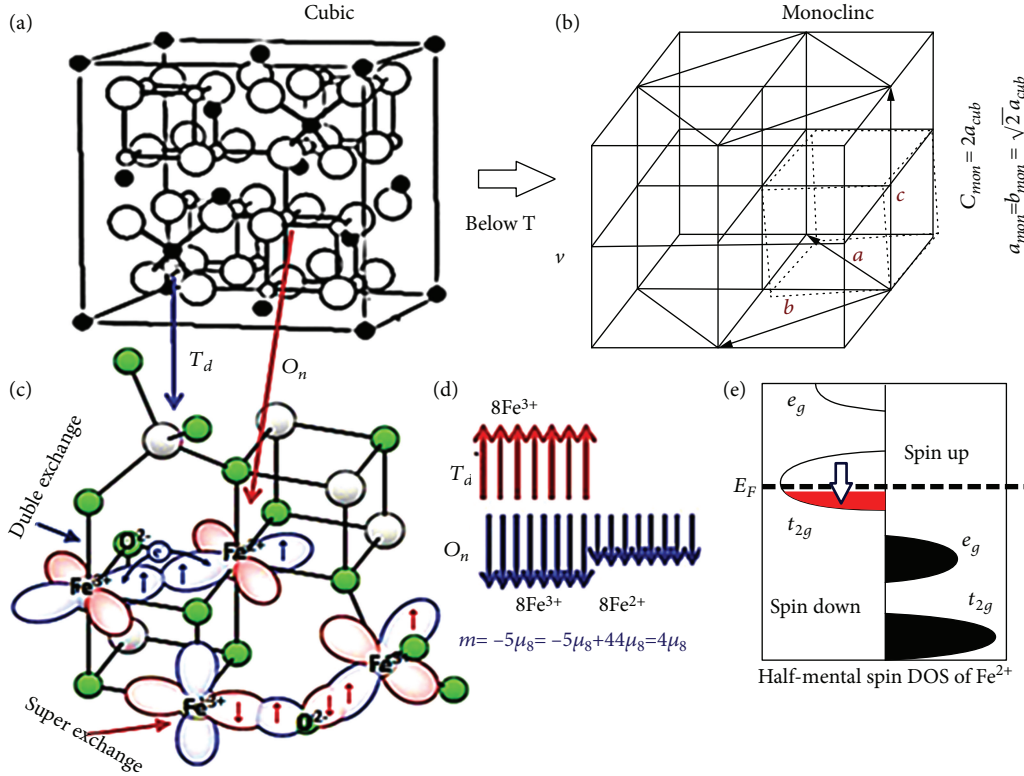


FIGURE 1: Cubic inverse spinel structure of Fe<sub>3</sub>O<sub>4</sub> with tetrahedral and octahedral sites above T<sub>V</sub> (a) and distorted monoclinic crystal structure below the T<sub>V</sub> (b). The double and superexchange interaction mechanisms (c) [13]. Sketch of the localized structure of the spins at tetrahedral and octahedral sites (d). The density of states occupied by electrons of Fe<sup>2+</sup> ions at octahedral sites (e).

commonly depends on growth conditions. Furthermore, at the nanoscale, the VT is difficult to technically observe because diffraction methods suffer from severe peak broadening due to the small crystallite size [9]. The occurrence of superparamagnetism hampers the observation in magnetometry, and measurements of the conductivity are difficult to interpret in the case of ensembles of nanoparticles, since the path of the electric current may simply change [9].

Thus, the understanding of VT in nanostructured Fe<sub>3</sub>O<sub>4</sub> is the main focus of this review. Here, we shall discuss the best growth methods and characterization techniques which are being currently employed to investigate nanostructured Fe<sub>3</sub>O<sub>4</sub> material and their potential applications. Before presenting the results on nanostructured Fe<sub>3</sub>O<sub>4</sub>, some basic properties of Fe<sub>3</sub>O<sub>4</sub> shall be summarized.

## 2. Material Properties of Fe<sub>3</sub>O<sub>4</sub>

**2.1. Crystalline Properties.** Fe<sub>3</sub>O<sub>4</sub> possesses an inverse spinel structure AB<sub>2</sub>O<sub>4</sub> (space group *Fd3m*; *a* = 8.39 Å) (Figure 1(a)), wherein oxygen anions form a cubic face-centred (fcc) lattice, and the large interstices between O<sup>2-</sup> are partially occupied by iron cations. Tetrahedral *A* positions are occupied by Fe<sup>3+</sup> cations, while octahedral *B* positions are equally occupied by Fe<sup>3+</sup> and Fe<sup>2+</sup> cations ([Fe<sub>T<sub>d</sub></sub><sup>3+</sup>]<sub>A</sub>[Fe<sub>Oh</sub><sup>3+</sup>Fe<sub>Oh</sub><sup>2+</sup>]<sub>B</sub>O<sub>4</sub>) [8, 9]. In Fe<sub>3</sub>O<sub>4</sub>, ferrimagnetism exists through two main mechanisms, as shown in

Figure 1(c). The first is the antiferromagnetic superexchange interactions between the Fe<sub>Oh</sub><sup>3+</sup> and Fe<sub>T<sub>d</sub></sub><sup>3+</sup> cations through the O<sup>2-</sup> anions [13, 14]. The spin-up 5*d* electrons in the Fe<sub>Oh</sub><sup>3+</sup> couple with the overlapping 2*p* orbitals in the O<sup>2-</sup> making them spin down. The other 2*p* electron is thus spin-up which makes the Fe<sub>Oh</sub><sup>3+</sup> 5*d* electrons spin down. Thus, Fe<sub>Oh</sub><sup>3+</sup> and Fe<sub>Oh</sub><sup>3+</sup> are antiparallel and cancel out each other's unpaired spin magnetic moments. The second factor is related to the double-exchange interaction [15] in which the spin-down electron can only hop from Fe<sub>Oh</sub><sup>2+</sup> to Fe<sub>Oh</sub><sup>3+</sup> if the majority spins are the same. Hence, they are coupled and aligned parallel. Therefore, all the Fe<sup>2+</sup> cations contribute to the magnetic moment while all Fe<sup>3+</sup> cations cancel each other out, resulting net magnetic moment (9 - 5 = 4) μ<sub>B</sub> (see Figure 1(d)). Because of the strong antiferromagnetic A-B superexchange interaction, A-A and B-B superexchange interactions become ferromagnetic resulting in the ferrimagnetic structure of Fe<sub>3</sub>O<sub>4</sub>. The extra electron of Fe<sub>Oh</sub><sup>2+</sup> ions is transferred to the empty orbitals of Fe<sub>Oh</sub><sup>3+</sup> by displacing electrons from the intervening O<sup>2-</sup> ions in a double-exchange process: Fe<sub>Oh</sub><sup>2+</sup> to O<sup>2-</sup> and O<sup>2-</sup> to Fe<sub>Oh</sub><sup>3+</sup>. The room temperature conductivity of Fe<sub>3</sub>O<sub>4</sub> is, thus, attributed to this hopping of electrons (Fe<sup>2+</sup> ⇌ Fe<sup>3+</sup> + e<sup>-</sup>) at octahedral *B*-sites. The extra electron of the Fe<sup>2+</sup> ion occupies the minority *t*<sub>2*g*</sub> band, which is the only band located at Fermi level E<sub>f</sub>, giving rise to half-metallicity as predicted by band structure calculation, shown in a simplistic form in Figure 1(e) [8, 9].

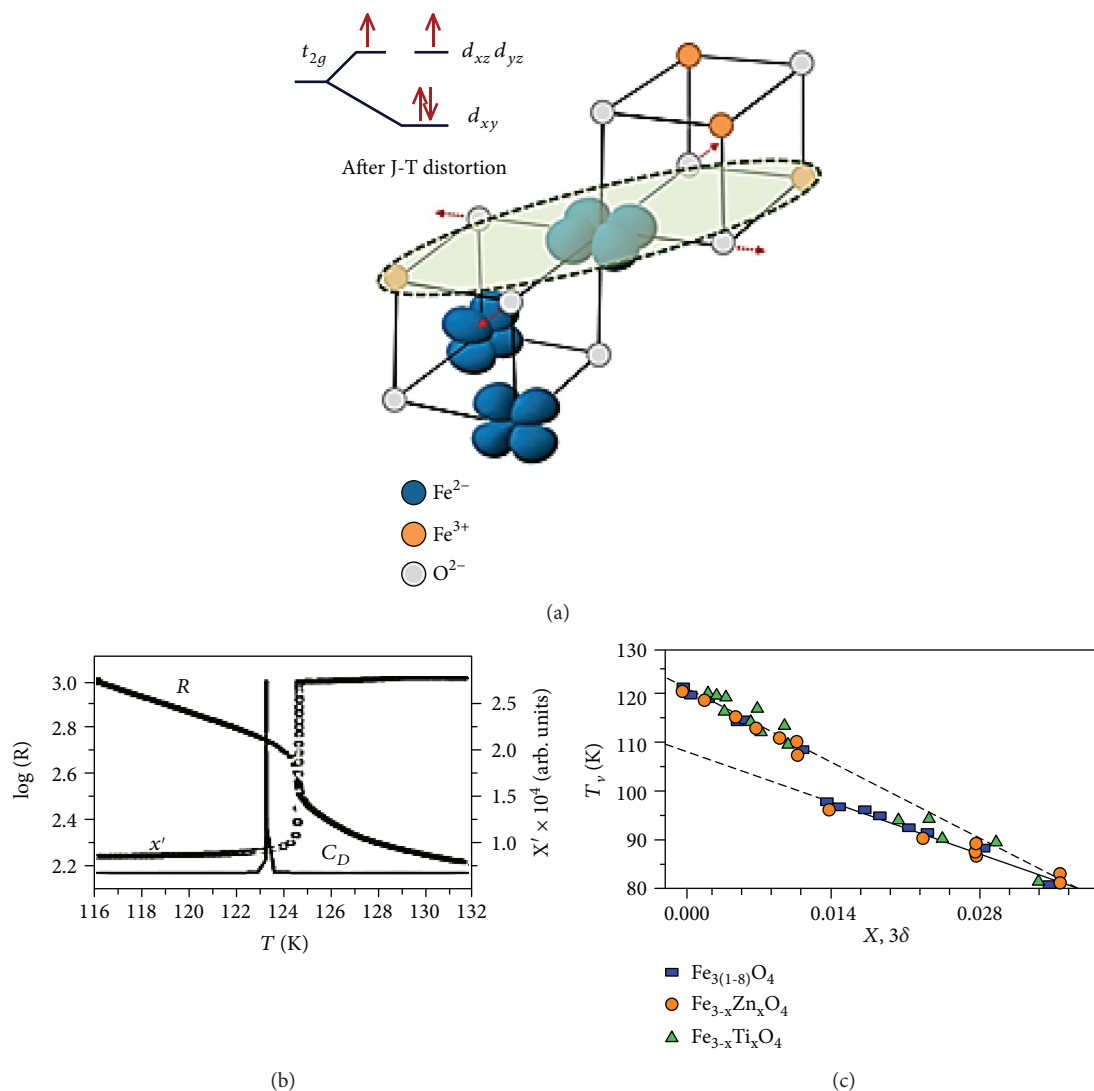


FIGURE 2: Energy separation due to Jahn-Teller distortion (up) and depiction of trimeron concept in single  $\text{Fe}^{2+}\text{O}_6$  octahedra (down) (a) [8]. Changes in magnetic susceptibility, resistance, and specific heat at  $T_V$  (b) [10, 17]. For clarity, the temperature scale for  $R$  and  $\chi'$  was shifted concerning the true temperature scale. With an increasing number of vacancies or doped atoms, the VT shifts to low temperatures (c) [18].

**2.2. Verwey Transition.** Upon cooling of  $\text{Fe}_3\text{O}_4$  below the  $T_V$ , the electron hopping between  $\text{Fe}^{2+}$  and  $\text{Fe}^{3+}$  ions freezes, and the combination of 2+ and 3+ species then arranges themselves in a regular pattern without moving (charge ordering). In this nonconducting state, the stagnant  $\text{Fe}^{2+}$  ions are Jahn-Teller (J-T) active [8]; this means that the extra electron in  $\text{Fe}^{2+}$  has a choice between occupying any one of the three available half-filled orbitals  $d_{xy}$  or the two  $d_{xz}/d_{yz}$ , as they all have the same energy (see the top of Figure 2(a)). Electrons prefer to occupy the orbit with the least energy. To break this choice, an effective energy separation between  $d_{xy}$  and  $d_{yz}/d_{zx}$  is created in the four Fe-O bonds (depicted by red arrows in the bottom of Figure 2(a)) in the  $xy$  plane that are elongated or contracted. The negative value of  $\Delta t_{2g}$  signifies that the energy of  $d_{xy}$  is lower than that of  $d_{yz}/d_{zx}$ , that is, tetragonal distorted  $\text{Fe}^{2+}\text{O}_6$  octahedra with elongated Fe-O bonds in the  $xy$  plane. On top of this, an additional

structural distortion in which B-site Fe-Fe distances within linear  $\text{Fe}^{3+}\text{-Fe}^{2+}\text{-Fe}^{3+}$  units (depicted by the grey ellipsoid in the bottom of Figure 2(a)) is anomalously shortened showing that electrons are not fully localized as  $\text{Fe}^{2+}$  states but are instead spread over the three sites resulting in highly structured three-site polarons defined as a single *trimeron* [8]. The J-T distortion in  $\text{Fe}^{2+}\text{O}_6$  octahedra mentioned earlier directly couples to the neighbouring  $\text{Fe}^{3+}\text{O}_6$  octahedra constituting the trimerons, although they are J-T inactive in the first approximation. Due to trimeron formation, distances from  $\text{Fe}^{2+}$  states to their two B-site neighbours in the local orbital ordering plane are anomalously shortened. The cumulative effect of this trimeron shortening penetrates throughout the crystal in the various trimeron locations to significantly perturb the cubic  $\text{Fe}_3\text{O}_4$  structure to the complex overall distortion. The cubic spinel- ( $a = b = c$ ) type structure of  $\text{Fe}_3\text{O}_4$  distorts to a monoclinic superstructure with Cc space group symmetry ( $a = b \neq c$ ) ( $\sqrt{2}, \sqrt{2}, 2$ ), as

shown in Figure 1(b). This structural transformation was first found by Verwey in 1939 and was named after him [16, 17]. The charge, orbital, and trimeron orders of  $\text{Fe}_3\text{O}_4$  stand out perhaps as the most complex electron-ordered ground state known.

Because of this structural transformation in  $\text{Fe}_3\text{O}_4$ , many physical properties (specific heat, magnetic susceptibility, and resistance) show abrupt change around  $T_V$  [3] (see Figure 2(b)). It has been reported that several factors can affect VT of bulk  $\text{Fe}_3\text{O}_4$  negatively, such as oxygen off-stoichiometry and cation substitution. The  $T_V$  gradually decreases from 124 to 80 K and finally vanishes completely with increasing oxygen off-stoichiometry or cation substitution ( $\text{Ti}^{2+}$ ,  $\text{Zn}^{2+}$ , etc.) (see Figure 2(c)) [18].

Even after an intense research, there still exist two major schools of interpretation: the first one interprets the VT as a transition driven by charge/orbital ordering and the second one exploits the mechanism of a lattice distortion-driven charge ordering leading to metal-insulator behaviour.

### 3. Observation of Verwey Transition in Various $\text{Fe}_3\text{O}_4$ Nanostructures

Recently, a lot of work has been carried out to study the effect of various nanostructured  $\text{Fe}_3\text{O}_4$  morphologies on VT, which include single crystals, epitaxial and polycrystalline thin films, particles, arrays of colloidal nanocrystals, heterostructures, and also in the form of nanocontacts. The eventual utilization of these morphologies is to develop novel VT-based devices, and this is a critical issue for further investigations.

**3.1. Nanoparticles** (1 nm < Particle Size < 100 nm). The recent advancement in the synthesis of uniform and size-controllable  $\text{Fe}_3\text{O}_4$  nanocrystals has enabled the size-dependent physical property characterization and their applications [21]. Recently, Lee et al. [20] have successfully synthesized stoichiometric and uniform-sized  $\text{Fe}_3\text{O}_4$  nanocrystals with sizes ranging from 5 to 100 nm. These nanocrystals show the VT in the conductance, magnetization, and heat capacity measurements (see Figures 3(a)–3(c)). The VT is generally masked in magnetization data of superparamagnetic nanocrystals below the blocking temperature; therefore, it was reassured that the heat capacity of nanocrystals shows a lambda-like anomaly similar to the single crystal  $\text{Fe}_3\text{O}_4$ , confirming a truly thermodynamic transition.  $^{57}\text{Fe}$  nuclear magnetic resonance (NMR) of  $\text{Fe}_3\text{O}_4$  nanocrystals (7 nm–7  $\mu\text{m}$ ) was also measured [19]. The line width of NMR spectra changes drastically around 120 K (see Figure 3(d)), showing microscopic evidence of the Verwey transition. The inset shows the NMR spectral intensity for one of the representative samples (25 nm) obtained at temperatures around the  $T_V$ . In the region above the transition temperature, the line width of the spectrum increases and the spin-spin relaxation time decreases as the nanocrystal size decreases. The line width broadening indicates the significant deformation of magnetic structure and reduction of charge order compared to bulk crystals, even when the structural distortion is unobservable. The VT is weakly size-dependent (see Figure 3(e)) and gets suppressed in

nanocrystals smaller than 20 nm before completely disappearing for a size less than 6 nm, which is a clear yet highly interesting indication of a size effect of this well-known phenomenon.

**3.2. Nanocrystalline Thin Films** (1 nm < Grain Size < 100 nm). Considering the spintronic applications concerning magnetoresistance (MR) that depends on the spin polarization of the materials being used, an in-depth study of the growth of nanocrystalline  $\text{Fe}_3\text{O}_4$  thin films is of interest. A relatively large low-field MR (-6% at 300 K to -10.0% at 200 K at the field of 5 kOe) was indeed found in nanocrystalline films [22]; however, in most cases, large MR could only be obtained at a high field and especially at low temperatures. The MR response in  $\text{Fe}_3\text{O}_4$  seems to be very sensitive to the preparation conditions, and the reason for low or inconsistent MR response could be because of the nonstoichiometry grain boundaries and surface spin arrangement. In literature, nanocrystalline  $\text{Fe}_3\text{O}_4$  thin films have been grown by a range of deposition techniques, such as evaporation, sputtering, molecular beam epitaxy, and pulsed laser deposition (PLD) [23–25].

Previously, the author has worked extensively on oxide films, and we consider that the PLD [26–28] is the most suitable technique for stoichiometric growth of complex oxides. The deposition of  $\text{Fe}_3\text{O}_4$  has been performed in a reducing atmosphere (under the vacuum of  $1 \times 10^{-5}$  mbar and substrate temperature,  $T_S$ : RT–850°C) from the  $\alpha\text{-Fe}_2\text{O}_3$  target on an amorphous quartz substrate [26]. This regime can produce  $\text{Fe}_3\text{O}_4$  in a limited  $T_S$  window of 350–500°C (see Figure 4(a): Fe/O phase diagram). These films were followed by two different annealing processes, namely, (1) vacuum annealing and (2) wet  $\text{H}_2$  annealing, in that the wet  $\text{H}_2$  annealing only produces single-phase  $\text{Fe}_3\text{O}_4$  films with grain sizes ranging 30–60 nm. The normalized  $M$  vs.  $T$  curve shows noticeable VT (see Figure 4(b)) which is a useful indicator for the stoichiometry of the samples, except for a higher  $T_S$  film showing a broad transition due to slight Fe/O off-stoichiometry.

The electric transport properties of the nanocrystalline  $\text{Fe}_3\text{O}_4$  thin films are not well defined as compared to the magnetic properties, particularly the absence of VT (see Figure 4(b)). To understand this contradictory behaviour, we plotted  $M/M(300\text{ K})$  vs.  $T$  curves at different fields for one of the representative samples ( $T_S = 500^\circ\text{C}$ ), as shown in Figure 5(a). We see that the magnitude of the drop in magnetizations at VT has severely reduced from 40% to 0.4% with the increasing field from 0.5 to 20 kOe [27]. This raises a question if this drop in magnetization is due to a change of the magnetic moment of  $\text{Fe}_3\text{O}_4$  or is it just a manifestation of the increased anisotropy. The  $M$ - $H$  loops (inset) support our arguments that the nonsaturation of magnetization at high fields and coercivity have increased significantly below VT. We fitted the high-field part of  $M$ - $H$  loops to the approach to saturation formula,  $4\pi M = Q[1 - (H^*/H)^{1/2}]$ , where  $Q$  is the magnetization at the infinite field and  $H^*$  is related to the magnetocrystalline anisotropy [27]. The  $Q$  vs.  $T$  curve (Figure 5(b)) does not show any drop in magnetizations around VT as was seen in Figure 5(a) for low fields. We

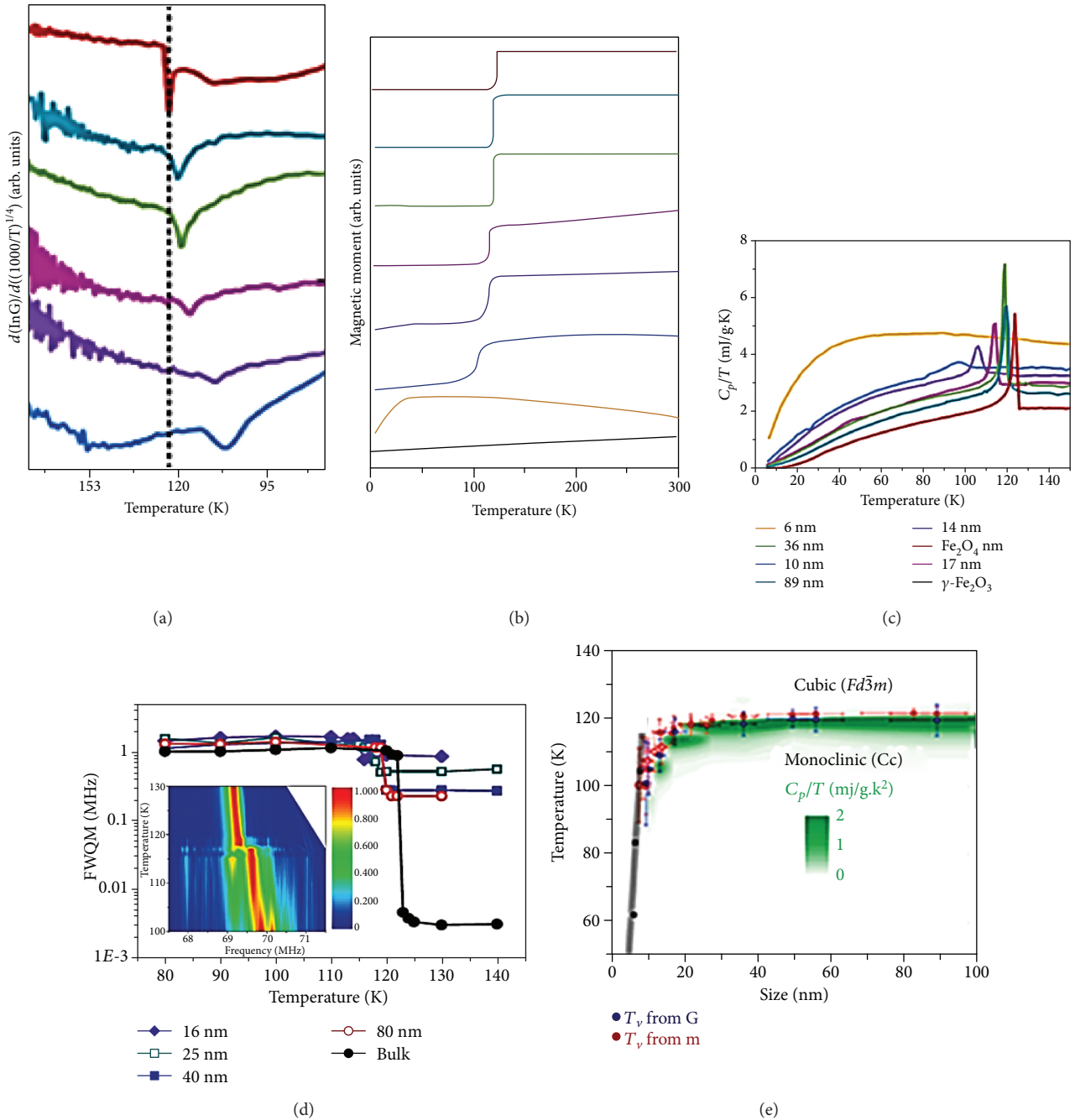


FIGURE 3: Size-dependent characterization of the VT: temperature dependence of the first derivative of conductance (a), magnetization data measured at 100 Oe (b), and total heat capacity divided by temperature (c). The full width at quarter maximum (FWQM) of the Fe NMR spectra versus temperature [19]. The inset shows the Fe NMR spectral intensity of the 25 nm sample obtained at temperatures around  $T_v$  (d). Size dependence of VT from combined data (e) [20].

can conclude that the intrinsic saturation magnetic moment does not show any drop while cooling across VT, and whatever drop in magnetization we observed in Figure 5(a), it is just because of inadequate saturation field and there is nothing to do with any magnetic interaction change. This transition can also happen even if there is no structural transition but if there is a change in anisotropy. We now argue that charge order is triggered by the structural transition and it has nothing to do with magnetic ordering, as discussed by

us elsewhere [28]. So the absence of VT in electronic transport may have a different origin like grain boundary volume, and defects/vacancies induced intergranular strain in nanocrystalline  $\text{Fe}_3\text{O}_4$  films that suppress the resistivity change caused during VT [28].

Another interesting feature comes from large magnetocaloric effect observed in these nanocrystalline  $\text{Fe}_3\text{O}_4$  films around VT, as shown in Figure 5(c). The fitting of  $M$ - $H$  loops in Maxwell equations [29],  $\delta S_M = \int_{H_i}^{H_f} (\partial M / \partial T) dH$ ,

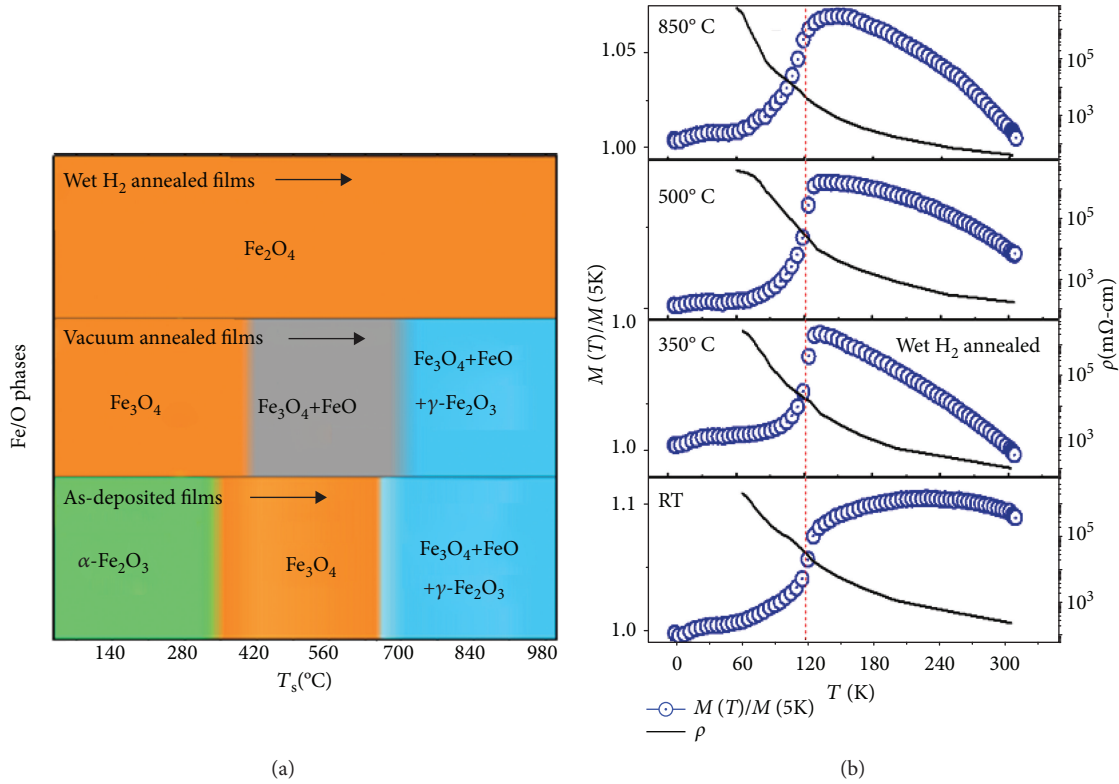


FIGURE 4: Various Fe/O phases at different  $T_s$  before and after reduction treatments (a),  $M(T)/M(5\text{K})$  (at the fixed field of 5 kOe) and  $\rho$  vs.  $T$  curves for wet H<sub>2</sub> annealed films at different  $T_s$  (b) [26].

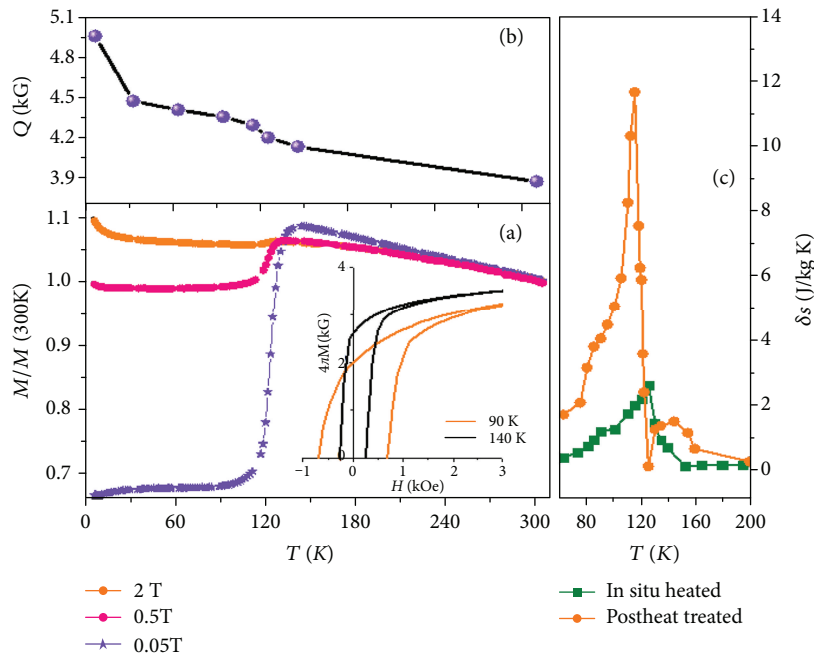


FIGURE 5:  $M$  vs.  $T$  curves under various fixed fields (a). The inset shows  $M-H$  loops below and above VT. The  $Q$  vs.  $T$  curves deduced from Chikazumi's formula (b) [27] and  $\delta S$  vs.  $T$  curves for in situ and ex situ annealed  $\text{Fe}_3\text{O}_4$  films (c) [29].

yield large positive entropy change  $\delta S = 2\text{-}12\text{ J/kg K}$  at VT under the field of 10 kOe. The magnitude of  $\delta S$  depends upon the detail microstructures of nanocrystalline films

produced by different thermal treatments. This result is significant for cooler on-chip devices for next-generation nano-/microelectromechanical systems (NEMS/MEMS).

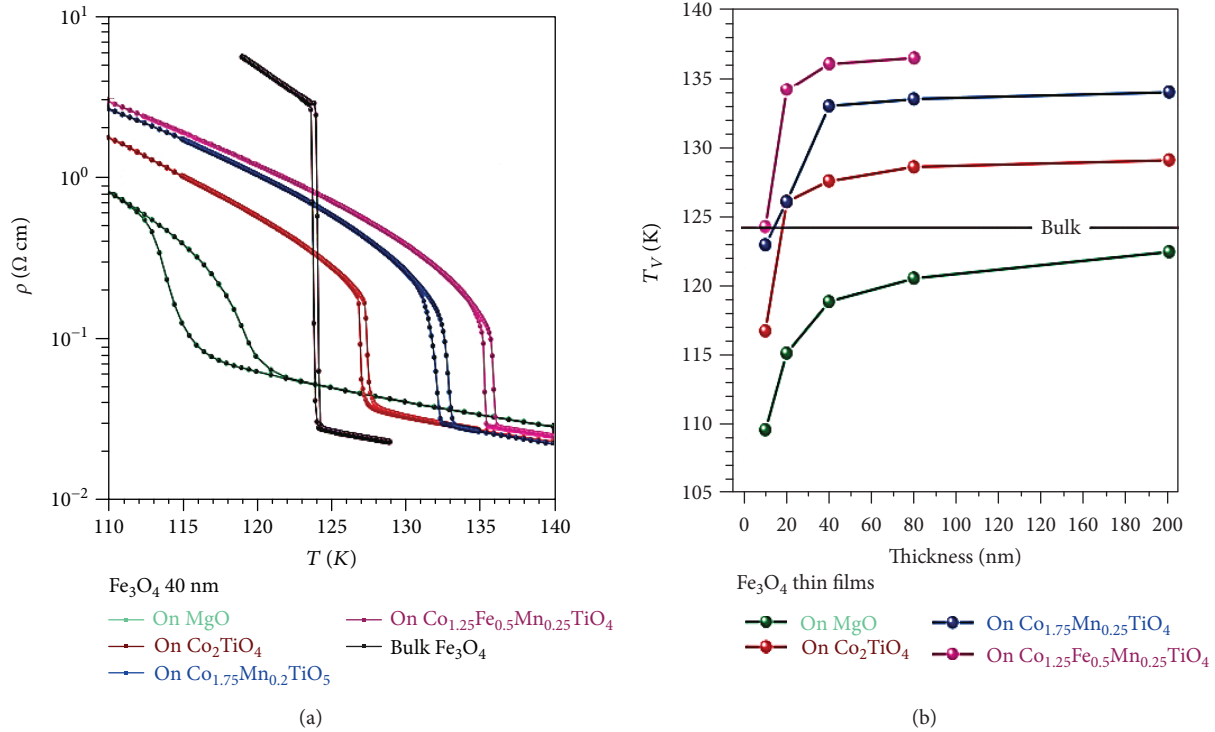


FIGURE 6:  $\rho$  vs.  $T$  curves for 40 nm epitaxial  $\text{Fe}_3\text{O}_4$  films grown on  $\text{MgO}$  (001),  $\text{Co}_2\text{TiO}_4$  (001),  $\text{Co}_{1.75}\text{Mn}_{0.25}\text{TiO}_4$  (001), and  $\text{Co}_{1.25}\text{Fe}_{0.5}\text{Mn}_{0.25}\text{TiO}_4$  (001) substrates along with single-crystal  $\text{Fe}_3\text{O}_4$  (a). Corresponding  $T_V$  vs. thickness curves (b) [30].

**3.3. Epitaxial Films** ( $1 \text{ nm} < \text{Nanothickness} < 200 \text{ nm}$ ). Despite the remarkable amount of work devoted in preparing  $\text{Fe}_3\text{O}_4$  thin films in the last two decades, the VT even in epitaxial thin films is extremely broad and occurs at substantially lower temperatures as compared to the high-quality bulk single crystals. A systematic study on the influence of oxygen stoichiometry on epitaxial  $\text{Fe}_3\text{O}_4$  films found that even for the optimal oxygen composition, the transition remains broad [22]. The study also discovered that the microstructure of the films has an important role; particularly, a larger domain size distribution results in a broader transition and a small domain size gives lower transition temperatures. The transition itself is still first order as it shows hysteresis, and there are indications that each domain has its transition temperature. Various substrates have been used in the literature to grow epitaxial  $\text{Fe}_3\text{O}_4$  thin films, e.g.,  $\text{MgO}$ ,  $\text{MgAl}_2\text{O}_4$ ,  $\text{Al}_2\text{O}_3$ ,  $\text{SrTiO}_3$ , and  $\text{BaTiO}_3$  [30]. These studies suggest that the larger the lattice mismatch, the broader the transition and the lower the average transition temperature.

Recently, Liu et al. [30] succeeded in making a particular class of spinel substrates that allows the growth of  $\text{Fe}_3\text{O}_4$  thin films with the VT as sharp as in bulk. The key principle was to obtain sufficiently large domain sizes of  $\text{Fe}_3\text{O}_4$  thin films with small domain size distribution. Figure 6(a) shows  $\rho$  vs.  $T$  curves of 40 nm thick  $\text{Fe}_3\text{O}_4$  (001) films grown on  $\text{MgO}$  and spinel substrates ( $\text{Co}_2\text{TiO}_4$ ,  $\text{Co}_{1.75}\text{Mn}_{0.25}\text{TiO}_4$ , and  $\text{Co}_{1.25}\text{Fe}_{0.5}\text{Mn}_{0.25}\text{TiO}_4$ ), along with bulk  $\text{Fe}_3\text{O}_4$  single crystal. We can see that the bulk sample has a sharp VT at 124 K, whereas the film on  $\text{MgO}$  shows the typical broad transition at lower temperatures. In contrast, the thin films grown on the spinel substrates all show a very sharp transition, almost

as sharp as the bulk with a hysteresis value of 0.7 K. The most exciting feature is that now the transition temperatures of thin films grown on spinel substrates (127 K on  $\text{Co}_2\text{TiO}_4$  (lattice mismatch +0.66%), 133 K on  $\text{Co}_{1.75}\text{Mn}_{0.25}\text{TiO}_4$  (+0.98%), and 136 K on  $\text{Co}_{1.25}\text{Fe}_{0.5}\text{Mn}_{0.25}\text{TiO}_4$  (+1.11%)) are even higher than those of the bulk [31–35]. Figure 6(b) shows that  $T_V$  gradually increases with the film thickness and, again, that it is larger for the spinel substrates with the larger lattice constant mismatch between the film and the substrate. Although films with the thicknesses of 5 nm and less do not show a VT, we can see a well-defined transition for films when they are 10 nm or thicker. Thus, using tensile strain, one can increase the transition temperature into considerably higher values than bulk. The occurrence of the VT in the highly anisotropic strained films raises a new question on the intricacies of the interplay between the charge and orbital degrees of freedom of the Fe ions in  $\text{Fe}_3\text{O}_4$ , adding another aspect to the elusiveness of this quantum material.

The anisotropic magnetoresistance (AMR) of high-quality epitaxial  $\text{Fe}_3\text{O}_4$  films on  $\text{MgO}$  (100) and  $\text{Al}_2\text{O}_3$  (0001) substrates [36] was investigated in charge-ordering state, as shown in Figure 7(a). It was found that the Verwey transition contains two processes, a fast charge-ordering process and a continuous formation of trimeron process. In the  $\text{Fe}_3\text{O}_4$  (100) film, the twofold AMR at  $104 \text{ K} < 116 \text{ K}$  comes from the uniaxial magnetic anisotropy, whereas the fourfold AMR at  $T = 104 \text{ K}$  can be ascribed to the in-plane trimerons (Figure 7(b)). However, AMR in the  $\text{Fe}_3\text{O}_4$  (111) film maintains twofold symmetry (Figure 7(c)). By comparing the AMR below  $T_V$  between two oriented films, it shows the maxima when the trimerons are parallel to the magnetic

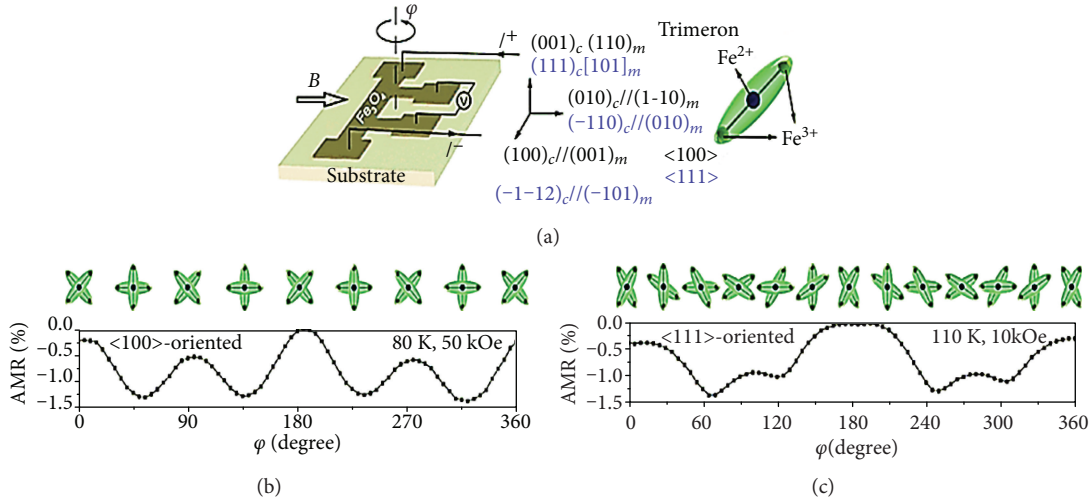


FIGURE 7: Sketch map of the sample, magnetic field, and current arrangement in the left corner (a). The structure of trimeron is shown in the right corner (a). AMR at 80 K and 50 kOe of Fe<sub>3</sub>O<sub>4</sub> (100) film and the in-plane trimeron distribution at the corresponding angle (b). AMR at 110 K and 10 kOe of Fe<sub>3</sub>O<sub>4</sub> (111) film and the in-plane trimeron distribution at the corresponding angle (c) [36].

field. A uniaxial magnetic anisotropy might appear in the trimeron, and the easy axis is along the trimeron. Thus, in-plane trimerons play an important role in the complex AMR behaviour below the  $T_V$ .

**3.4. Other Nanostructured Fe<sub>3</sub>O<sub>4</sub> Geometries.** While a lot of work has been done in thin film form, little is known about the potential use of Fe<sub>3</sub>O<sub>4</sub> for device applications in nanoparticle morphology. Also, the VT is very sensitive to stoichiometry, and it is hardly observed in superparamagnetic length scale; an alternate approach to optimize the stoichiometry is to tailor the shape of the particles, since anisotropy plays a crucial role in deciding the magnetic characteristics of the magnetic nanocrystals. Recently, Mitra et al. [1] investigated the VT in shape-controlled small amine-coated Fe<sub>3</sub>O<sub>4</sub> nanoparticles (6–14 nm). The VT of Fe<sub>3</sub>O<sub>4</sub> near 120 K is seen in octahedral particles (Figure 8(a)), but it is not observed in their spherical particles (Figure 8(b)) in the FC- (field cooled-) ZFC (zero field cooled) measurements. The facets of octahedral particles consist of energetically most stable {111} planes which are protected against surface oxidation. The surface anisotropy is substantially reduced since the flat surface of octahedron has fewer broken bonds and oxygen vacancies. A lower concentration of defects and almost no oxidized layer at the surface provide a better stoichiometry to octahedral particles, which is the cause of the VT in octahedral nanoparticles.

Unfortunately, the crystal quality of spherical nanoparticles suffers from surface spin disorder and uncompensated bonds; epitaxial Fe<sub>3</sub>O<sub>4</sub> nanorods with well-defined magnetic anisotropy are very promising as building blocks in spintronic devices. Chandra et al. [37] demonstrated the epitaxial growth of highly oriented Fe<sub>3</sub>O<sub>4</sub> nanorods on SrTiO<sub>3</sub> substrates by hydrothermal synthesis, as depicted in Figure 8(c). The epitaxial nanorods show biaxial magnetic anisotropy with an order of magnitude difference between the anisotropy field values of the easy and hard axes along

with sharp VT. The interplay of epitaxy and enhanced magnetic anisotropy at room temperature, concerning randomly oriented Fe<sub>3</sub>O<sub>4</sub> powder, and the nanorods are useful materials for magnetic data storage. Differently, Fe<sub>3</sub>O<sub>4</sub> nanocubes [38] synthesized by the oxidation of Fe<sub>1-x</sub>O/Fe<sub>3-δ</sub>O<sub>4</sub> core-shell nanocubes (see in Figure 8(d)) show a kink at 110 K in the ZFC curve which can be attributed to the VT; however, it is not that much sharp as observed in nanorods and octahedral particles of Fe<sub>3</sub>O<sub>4</sub>.

## 4. Applications

**4.1. Multiferroic Properties.** In addition to all its acclaimed fame, Fe<sub>3</sub>O<sub>4</sub> is also probably one of the first multiferroics, which shows the ferroelectric effect (FE) in its insulating state below VT [39–48]. However, the microscopic nature of the FE in Fe<sub>3</sub>O<sub>4</sub> is still a matter of debate. Probably, it is related to the coexistence of bond-centred and charge-centred charge ordering. In the proposed structural and charge pattern, besides the site-centred charge ordering, one also notices the alternation of the formal Fe<sup>2+</sup> and Fe<sup>3+</sup> valence states and strong modulation of the Fe-Fe distances (the bond lengths). In the structure shown in Figure 9(a) [49], one sees that, e.g., along the Fe chains running in the (110) direction (in cubic setting), i.e., in the *xy* chains, there is an alternation of Fe<sup>2+</sup> and Fe<sup>3+</sup> (open and filled circles), but simultaneously there is an alternation of short and long Fe-Fe bonds. This direction corresponds to the monoclinic *b*-direction, in which the polarization is observed. In this framework, each of such (110) mixed bond- and site-centred charge-ordering chains gives a nonzero contribution to the electrical polarization.

Firmly, the proof for the existence of FE order (as shown in Figure 9(b)) in 150 nm thick Fe<sub>3</sub>O<sub>4</sub> films synthesized by pulsed laser deposition and magnetron sputtering on Nb-doped SrTiO<sub>3</sub> substrates has been investigated recently [50]. The appearance of ferroelectric order below 38 K was

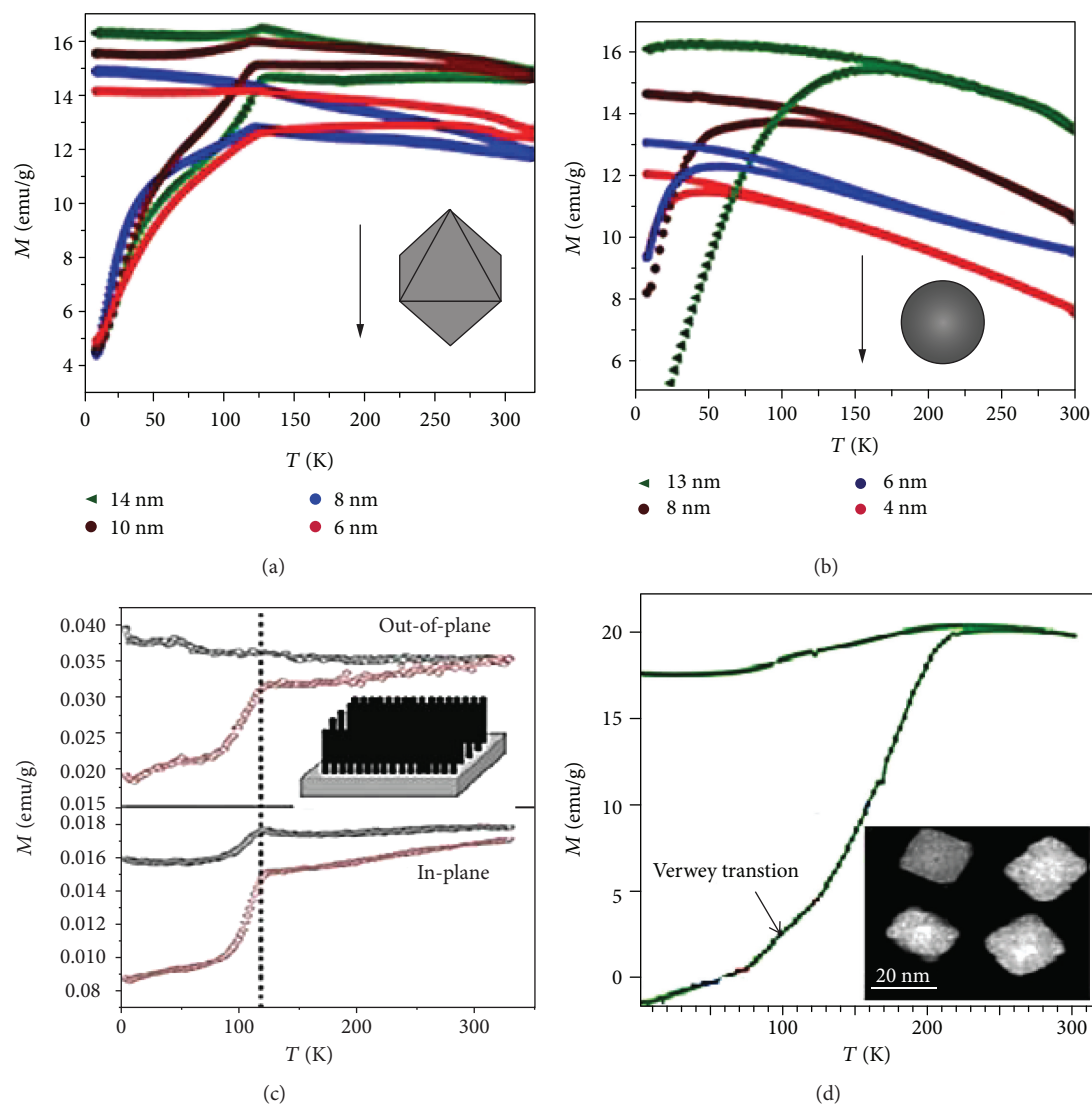


FIGURE 8: FC and ZFC magnetizations for different sizes of spherical and octahedral  $\text{Fe}_3\text{O}_4$  nanoparticles (a, b) [1]. FC and ZFC magnetization of epitaxial  $\text{Fe}_3\text{O}_4$  nanorods (along in- and out-of-plane directions) (c) and nanocubes (d) [37]. Insets (a–d) show the surface morphology of nanostructured  $\text{Fe}_3\text{O}_4$  materials [38].

explained by the existence of spontaneous electric polarization in the noncentrosymmetric monoclinic  $Cc$  structure, which arises from an alternation of charge states and bond lengths [51, 52]. However, it is surprising that the electric polarization does not already develop at the VT. This is because in between 40 K and  $T_V$ , the electric polarization is suppressed by relaxation processes due to electron tunnelling and electron hopping processes [53], glassy polar degrees of freedom [54], or thermally activated structural processes [55]. Since the easy-axis direction is generally stabilized by the film-substrate strain, it would be easier to observe a ferroelectric polarization in thin films than in bulk. Indeed, the polarization values measured in  $\text{Fe}_3\text{O}_4$  films tend to be larger than in single crystals. This scenario explains the close relation between magnetoelectric effects and relaxation processes observed both in the electric and magnetic susceptibilities. In contrast to conventional relaxor

ferroelectrics [56], the relaxor behaviour in  $\text{Fe}_3\text{O}_4$  is not driven by chemical heterogeneity but by the dynamical structural disorder.

Conventionally, the multiferroics are single-phase materials with the coexistence of ferromagnetism, ferroelectricity, or ferroelasticity, which can result in novel functionalities. Because of advancement of the thin-film growth techniques and computational capabilities, the coupling in multiferroics that was predicted in 1894 has developed rapidly [57, 58]. In the class of single-phase multiferroic materials, magnetism occurs independently from ferroelectricity. Some multiferroic heterostructures have been produced by compound ferromagnetics ( $\text{Fe}_3\text{O}_4$ ) with ferroelectrics  $\text{BaTiO}_3$  [59],  $\text{Pb}(\text{Mg}_{1/3}\text{Nb}_{2/3})\text{O}_3$ - $\text{PbTiO}_3$  (PMN-PT) [60],  $\text{PdZr}_x\text{Ti}_{1-x}\text{O}_3$  (PZT) [61],  $\text{BiFeO}_3$  [62],  $\text{HoMnO}_3$ , and  $\text{YMnO}_3$  [63]. These multiferroic heterostructures show the strong interfacial magnetoelectric effects [64–69], which can be used in

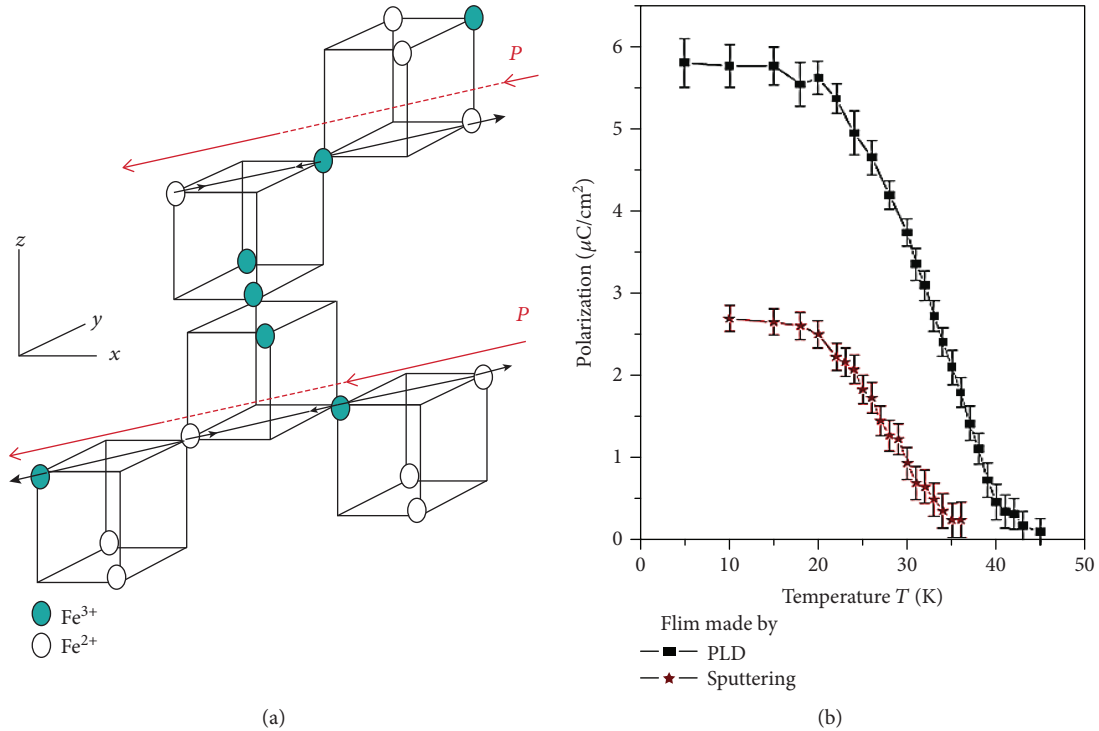


FIGURE 9: Sketch of the possible origin of ferroelectricity in  $\text{Fe}_3\text{O}_4$  and emphasis on the Fe chains running in the (110) direction of  $\text{Fe}_3\text{O}_4$  [49]. In the  $xy$  chains, there is an alternation of  $\text{Fe}^{2+}$  and  $\text{Fe}^{3+}$  ions (open and filled circles). Concurrently, there is an alternation of short and long Fe-Fe bonds; shifts of Fe ions are shown by black arrows. The resulting polarization is indicated by the red arrows (a) [49]. Electric saturation polarization of the  $\text{Fe}_3\text{O}_4$  films made by pulsed laser deposition and sputtering (b) [50].

multifunctional spintronic, nanoelectronic, and optoelectronic devices.

Electric-field-controlled magnetism and VT in highly correlated  $\text{Fe}_3\text{O}_4$  materials have generated great interest recently both scientifically and technologically [51]. Ferroelastic strain control of VT was observed in epitaxial  $\text{Fe}_3\text{O}_4$  thin films grown on PMN-PT (011) substrate [4], as shown in four-point geometry (Figure 10(a)). Through ferroelastic control of lattice strain, the  $T_V$  shot up by 8 K, evidenced by large changes in resistivity once the sample is poled with a DC field of 10 kV/cm (inset Figure 10(a)). Thus, electrical modulation of in-plane epitaxial strain is a far more effective way to manipulate VT than a pure volume change argument. On the other hand, epitaxial  $\text{Fe}_3\text{O}_4$  films incorporated into a gated device structure [51] (Figure 10(b)) demonstrate the ability to control the VT with static electric fields. The  $T_V$  increases for both polarities of the electric field, indicating that the effect is not driven by changes in carrier concentration. The energetics of induced electric polarization and strain within the  $\text{Fe}_3\text{O}_4$  film provides a possible explanation for this behaviour.

Another example of magnetoelectric coupling is the magnetic properties of  $\text{Fe}_3\text{O}_4/\text{BaTiO}_3$  heterostructures which observe remarkable changes (as shown in Figure 11) at various structural phase transitions of  $\text{BaTiO}_3$  substrate [70]. Upon tetragonal to orthorhombic transition (T to O), the lattice parameter of  $\text{BaTiO}_3$  dramatically decreases, which induces compressive strain in the  $\text{Fe}_3\text{O}_4$  thin film. This increased strain anisotropy leads to an abrupt increase of

in-plane magnetization, coercivity, and remanent magnetization of  $\text{Fe}_3\text{O}_4$  (Figures 11(b) and 11(c)) [70]. While in transition from orthorhombic to rhombohedral (O to R), the lattice parameter of  $\text{BaTiO}_3$  now dramatically increases, resulting in a decrease of the compressive strain, which leads to an opposite effect on magnetic properties of  $\text{Fe}_3\text{O}_4$  (Figures 11(b) and 11(c)). The  $\text{Fe}_3\text{O}_4$  (001) film, which has a negative magnetostriction coefficient, is under compressive stress when it is in contact with  $\text{BaTiO}_3$ . With the decrease of temperature, the lattice mismatch between  $\text{Fe}_3\text{O}_4$  and  $\text{BaTiO}_3$  increases. These temperature-driven structural transformations of  $\text{BaTiO}_3$  induce various anisotropies that cause magnetic properties to change, in a way similar to the VT, however at elevated temperatures.

The quantitative understanding of converse magneto-electric effects, i.e., the variation of the magnetization as a function of an applied electric field in extrinsic multiferroic hybrids, is a key prerequisite for the development of future spintronic devices. The strain-mediated converse magneto-electric effect in  $\text{Fe}_3\text{O}_4/\text{BaTiO}_3$  heterostructures was also realized at room temperature [34]. This demonstrates that the electric-field-induced changes of the magnetic state in the  $\text{Fe}_3\text{O}_4$  thin film can be well described by the presence of two different ferroelastic domains in the  $\text{BaTiO}_3$  substrate, resulting in two differently strained regions in the  $\text{Fe}_3\text{O}_4$  film with different magnetic properties. The two-region model allows predicting the converse magneto-electric effects in multiferroic hybrid structures consisting of ferromagnetic thin films on ferroelastic substrates.

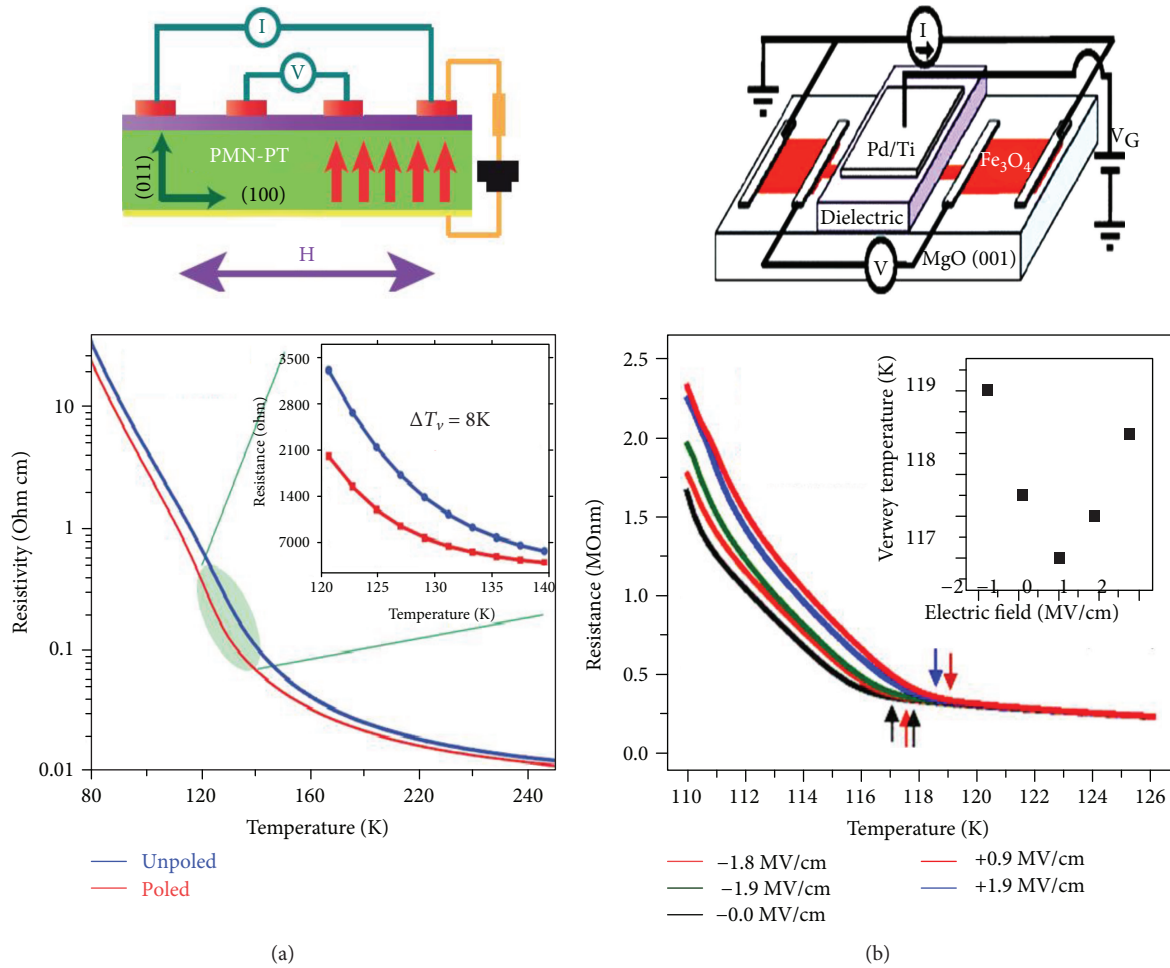


FIGURE 10: Schematics of four-point resistance measurement for  $\text{Fe}_3\text{O}_4/\text{PMN-PT}$  structure and ferroelastic strain state dependence of resistivity as a function of temperature (a) [4]. Electrical gating of  $\text{Fe}_3\text{O}_4$  where the dielectric layer consists of PMMA (900 nm)/ $\text{Al}_2\text{O}_3$  (50 nm)/MgO (10 nm). Temperature dependence of resistance for applied electric fields of +1.8 MV/cm (blue), +0.9 MV/cm (orange), 0 MV/cm (black), -0.9 MV/cm (green), and -1.8 MV/cm (red). The arrows show  $T_V$  for each electric field, which is summarized in the inset (b) [51].

Digital memory comes with the ability to switch between distinct electronic and magnetic phases with a control voltage. Small changes in structure and charge density near a transition between competing phases can tip the balance among them, leading to large changes in electronic and magnetic properties. Devices based on this principle can be both fast and energy efficient [71], overcome some of the intrinsic limitations in conventional field-effect transistors [72], and also provide new functionalities [73–75]. While these properties point to a pathway for creating novel functionalities, reversible and nonvolatile switching between different phases using strain has been unexplored. In nonvolatile switching, the electronic/magnetic states that are realized remain in a stable remnant state after the control voltage has been switched off.

**4.2. Spin Seebeck Effect.** The spin Seebeck effect (SSE) refers to the generation of a spin voltage caused by a temperature gradient in a ferromagnet, which enables the thermal injection of spin currents from the ferromagnet into an attached

nonmagnetic metal over a macroscopic scale of several millimetres. Despite decades of research into thermoelectric materials and properties, the efficiency of thermoelectric devices has remained low due to the interdependence of the Seebeck voltage,  $S$ ; the resistivity,  $\rho$ ; and the thermal conductivity [76, 77]. One promising approach to overcome this problem and increase the versatility of thermoelectric devices involves exploiting the spin of the electron in addition to its charge and heat transport properties. In contrast to conventional thermoelectrics, this effect offers the possibility for another approach in all-solid-state energy conversion devices, since it involves properties of at least two different materials that can be optimized independently. The SSE for the laser-ablated  $\text{Fe}_3\text{O}_4$  (thickness = 50 nm)// $\text{SrTiO}_3(001)$  (thickness = 0.5 mm) samples was measured using the so-called longitudinal configuration. In such geometry (as shown in Figure 12(a)), a temperature gradient ( $\delta T$ ) is applied in the  $\pm z$ -direction, generating a temperature difference ( $\pm \delta T$ ) between the bottom and the top of the sample, with temperatures  $T \pm \delta T$  and  $T$ , respectively [5].

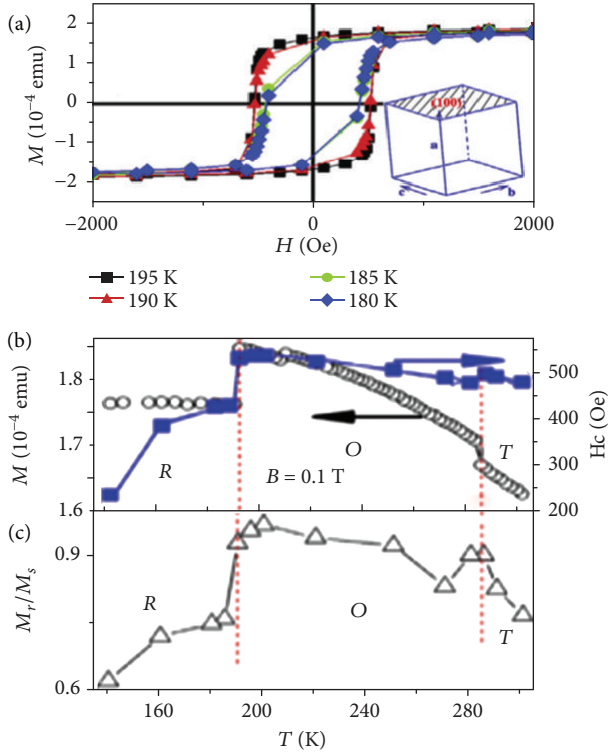


FIGURE 11: In-plane  $M$ - $H$  loops of  $\text{Fe}_3\text{O}_4/\text{BaTiO}_3$  (100) heterostructures [70] measured at different temperatures (a); a variation of the in-plane magnetization vs.  $T$  under a magnetic field of 0.1 T (b). The in-plane  $M_r/M_s$  vs.  $T$  obtained from the magnetization hysteresis loops (c).

The voltage ( $V_y$ ) is measured along the  $y$ -direction, while a sweeping magnetic field is applied at an angle  $h$  concerning the  $x$ -direction.

The focus is to observe the SSE below the Verwey transition ( $T < T_V$ ) (Figure 12(b)), and an SSE coefficient ( $S_{zy}$ ) at 105 K was estimated to be 52 nV/K. There is a clear reduction in SSE compared to the value observed at 300 K that could be related to the changes induced by the VT on the thermal and magnetic properties of the film, which can affect the thermal spin pumping at the  $\text{Fe}_3\text{O}_4/\text{Pt}$  interface and therefore the observed SSE signal. Such thermoelectric effects result from the combination between charge and heat current in suitable materials having applications as electric cooling systems or thermal power generators.

**4.3. Exchange Bias.** An exchange bias (EB) phenomenon is a property of coupled antiferromagnetic- (AFM-) ferromagnetic (FM) systems that occur due to magnetic interface effects [78]. It manifests itself in a shifting ( $H_{EB}$ ) of  $M$ - $H$  loop along the field axis and enhancement of coercivity ( $H_C$ ) when the system is cooled down in an external magnetic field through the magnetic ordering temperatures of the AFM ( $T_N$ ) and FM ( $T_C$ ) phases. It has been reported that the EB can be influenced by many factors in the FM/AFM system, such as the FM magnetization  $M_{FM}$ , the thickness of FM layer  $t_{FM}$  or AFM layer  $t_{AFM}$ , and the anisotropy of AFM ( $K_{AFM}$ ) or FM ( $K_{FM}$ ) [79]. A rapid change in  $K_{FM}$  is observed

in the vicinity of  $T_V = 120$  K due to the structural transformation from cubic to a more anisotropic monoclinic phase. Therefore, this change in  $K_{FM}$  will result in variation in  $H_E$ . Liu et al. [6] verify this transition tunability by preparing an interface with thicknesses of  $\text{Fe}_3\text{O}_4$  and CoO as 40 nm and 5 nm, respectively, in the FM/AFM bilayer system.

The FC-ZFC magnetization curves of CoO (5 nm)/ $\text{Fe}_3\text{O}_4$  (40 nm)/MgO (001) AF/FM system in Figure 13(a) show a rapid change in magnetization at the VT. At the same temperature,  $H_C$  observes a sharp enhancement in the AF/FM system compared to the bare  $\text{Fe}_3\text{O}_4$  (40 nm)/MgO (001) layer (inset a), indicating exchange anisotropy that is coupled with magnetocrystalline anisotropy change due to structural transformation. Figure 13(b) shows notable  $H_E$  change below VT. For  $\text{Fe}_3\text{O}_4$ , the low-temperature monoclinic magnetocrystalline anisotropy constants are considerably greater (about 10 times) than those of the high-temperature cubic structure. The correlation between  $H_E^2$  and  $H_C$  (inset b) indicates further that  $K_{FM}$  has a sole responsibility for such enhancement at VT.

**4.4. Spin Accumulation.** Spin-dependent transports (particularly spin injection, manipulation, and detection) are the integral parts of semiconductor spintronic devices and have attracted tremendous attention. Recent studies have demonstrated that spin-polarized carriers injected from a ferromagnetic material to a semiconductor lead to nonequilibrium spin accumulation and spin current over spin diffusion length [80, 81]. The magnitude of spin accumulation in any system depends on factors like type of the injector, the spin polarization of the ferromagnet/insulator combination, junction resistance, and the uniformity of film at the interface. Half-metallic  $\text{Fe}_3\text{O}_4$  can be a potential choice for spin injector material compared to the ferromagnetic metals.

Recently, Bhat and Kumar [7] investigated spin injection from  $\text{Fe}_3\text{O}_4$  as a spin source into GaAs and Si (both  $n$  and  $p$ -type) semiconductors using with and without a tunnel barrier (MgO) via three-terminal electrical Hanle (3TH) measurement, as shown in Figure 14(a). Application of a constant current  $I$  through the  $\text{Fe}_3\text{O}_4$  layer makes sure that sufficient spin-polarized carriers are pumped into the semiconductor where the decay of spin-polarized carriers will be measured. Once, the spins are injected into the semiconductor, these accumulated spin-polarized carriers at the junction of semiconductor get scattered or processed depending on the type of semiconductor. Thus, there is a gradient in the measured voltage  $\Delta V$  between the device and the far end of semiconductor due to the spin-scattering process within these semiconductors which can be further controlled by applying a perpendicular magnetic field  $B$ . The  $\Delta V$  can be expressed as  $\Delta V = \text{TSP} \times \Delta\mu/2$ , where TSP is the tunnel spin polarization of the ferromagnet/insulator combination and  $\Delta\mu = \mu_\uparrow - \mu_\downarrow$  the difference in chemical potential for up-spins and down-spins, which is nothing but the spin accumulation at the injected material. Strikingly, the normalized spin accumulation voltage ( $\Delta V/\Delta V_{\max}$ ) (see Figure 14(b)) in the semiconductor is found to be associated with a drastic increment in  $\text{Fe}_3\text{O}_4$ -based devices below  $T_V$ . Such an enhancement of  $\Delta V$  is absent in the devices with Fe as a spin

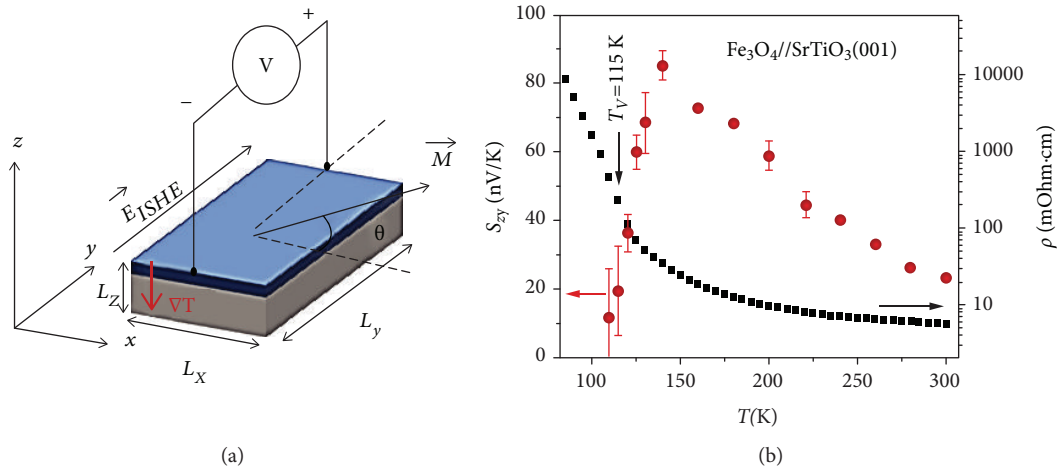


FIGURE 12: Schematic of the measurement setup (a) and estimated SSE coefficient ( $S_{xy}$ ) vs.  $T$  (b) for the  $\text{Fe}_3\text{O}_4/\text{SrTiO}_3$  (001) sample [5].

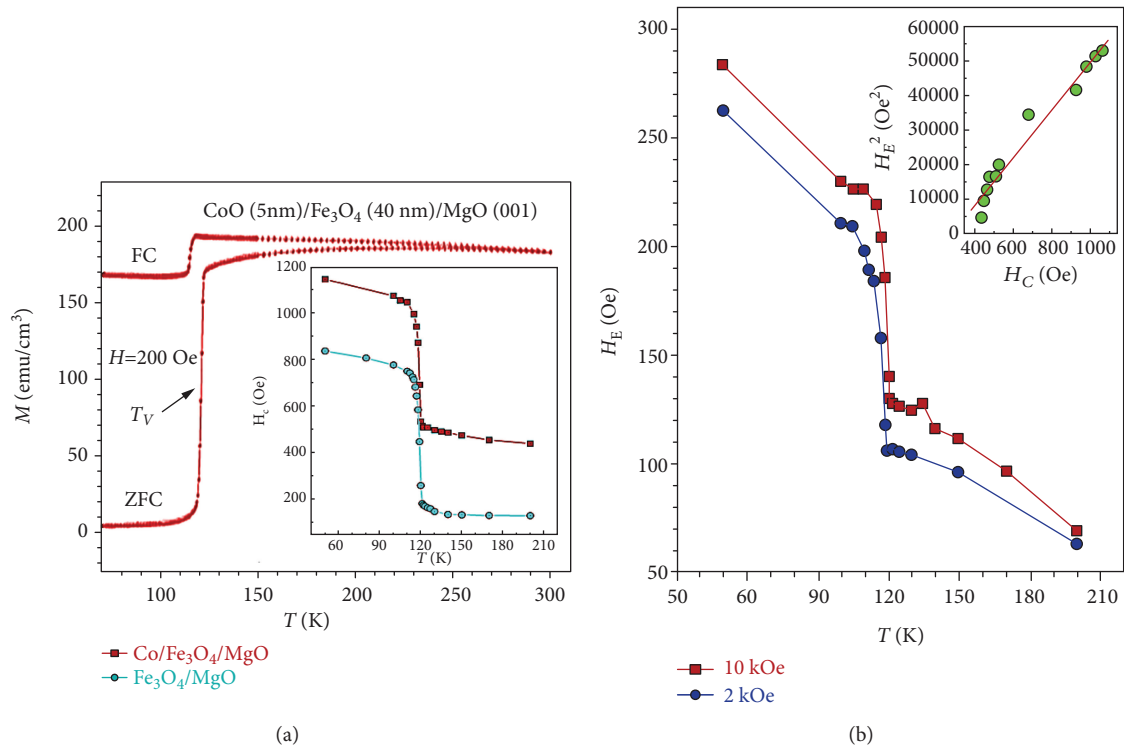


FIGURE 13: FC-ZFC magnetization curves of  $\text{CoO}$  (5 nm)/ $\text{Fe}_3\text{O}_4$  (40 nm)/ $\text{MgO}$  (001) AF/FM system (a). Inset of (a): temperature dependence of coercivity field ( $H_c$ ) for  $\text{CoO}$  (5 nm)/ $\text{Fe}_3\text{O}_4$  (40 nm)/ $\text{MgO}$  (001) and  $\text{Fe}_3\text{O}_4$ (40 nm)/ $\text{MgO}$  (001) systems. The exchange bias field ( $H_E$ ) as a function of temperature at the cooling field of 10 kOe and 2 kOe (b). Inset of (b):  $H_c$  vs.  $H_E^2$  (right) [6].

source. Further, the overall device resistance measured by 2 probes has no drastic difference at the  $T_V$  (see Figure 14(c)). From this, it can be concluded that the  $T_V$  of the  $\text{Fe}_3\text{O}_4$  film has a direct influence on the magnitude of spin accumulation, and the resistance enhancement of  $\text{Fe}_3\text{O}_4$  film itself has no vital role in the observed enhancement of spin accumulation. This result is consistent with the investigation of Wang et al. [82] and Ziese et al. [83] showing the maximum spin polarization of  $\text{Fe}_3\text{O}_4$  observed at  $T_V$  using MR measurements.

Thus, an anomalous increase in  $\Delta V$  can be attributed purely to the spin subband modification across  $T_V$  but not to the increase in resistance. Since the VT is associated with a structural modification, the configuration of subbands of  $\text{Fe}_3\text{O}_4$  along with the tunnel barrier might influence the total spin accumulation, as  $\Delta V$  depends directly on the tunnel spin polarization of  $\text{Fe}_3\text{O}_4/\text{MgO}$ . But the similar magnitude of enhancement in spin accumulation is even present in the Schottky junction of  $\text{Fe}_3\text{O}_4$  on GaAs, ruling out the role of MgO electronic band structure. Hence, the spin

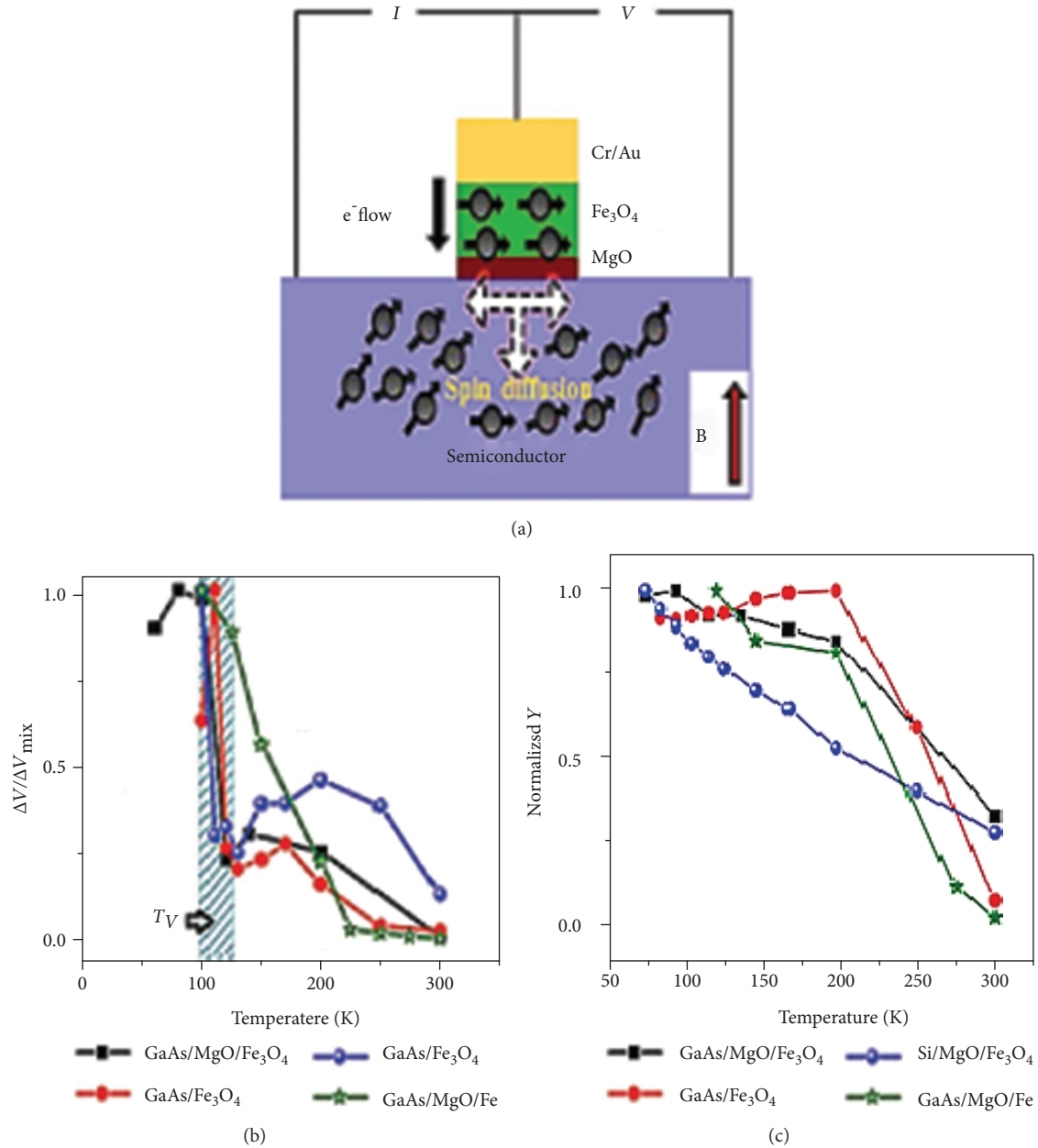


FIGURE 14: Schematics of the electrical 3TH measurement and the spin relaxation in a semiconductor (a). The plot of normalized spin accumulation voltage  $\Delta V$  vs.  $T$  of  $\text{Fe}_3\text{O}_4/\text{MgO}/\text{GaAs}$ ,  $\text{Fe}_3\text{O}_4/\text{GaAs}$ ,  $\text{Fe}_3\text{O}_4/\text{MgO}/\text{Si}$ , and  $\text{Fe}/\text{MgO}/\text{GaAs}$  devices showing the Verwey transition (shaded region) coinciding exactly the region of enhancement in  $\Delta V$  (b) while the normalized value of local 2-probe voltages as a function of  $T$  for this sample is plotted for comparison (c) [7].

injection and detection into conventional semiconductors like GaAs and Si can be improved with the help of materials like  $\text{Fe}_3\text{O}_4$  with higher spin polarization. This result also suggests that the theoretical prediction of room temperature half-metallicity of  $\text{Fe}_3\text{O}_4$  above and below  $T_V$  has to be reinvestigated.

**4.5. Organic Spintronics.**  $\Pi$ -conjugated organic semiconductors (OS) are extremely attractive materials for the transport of spin-polarized electrons to long distances [84, 85]. The major difference between inorganic and organic solids is that electrical transport is via band conduction in the former and

carrier hopping in the latter. The conduction (carrier/spin injection and extraction) takes place through an abstract spin valve (SV) (shown in the inset of Figure 15(c)) that filters spin-polarized electrons by alignment of the energetic position of the highest occupied molecular orbital (HOMO) or the lowest unoccupied molecular orbital (LUMO) of the OS relative to the Fermi level ( $E_F$ ) of the ferromagnetic (FM) electrode (Figure 15(a)). This concept is applied to make memory and sensor devices working on giant magnetoresistance (GMR) and tunnel magnetoresistance (TMR). As discussed previously,  $\text{Fe}_3\text{O}_4$  provides excellent spin injection at RT and supplementary spin accumulation at and below

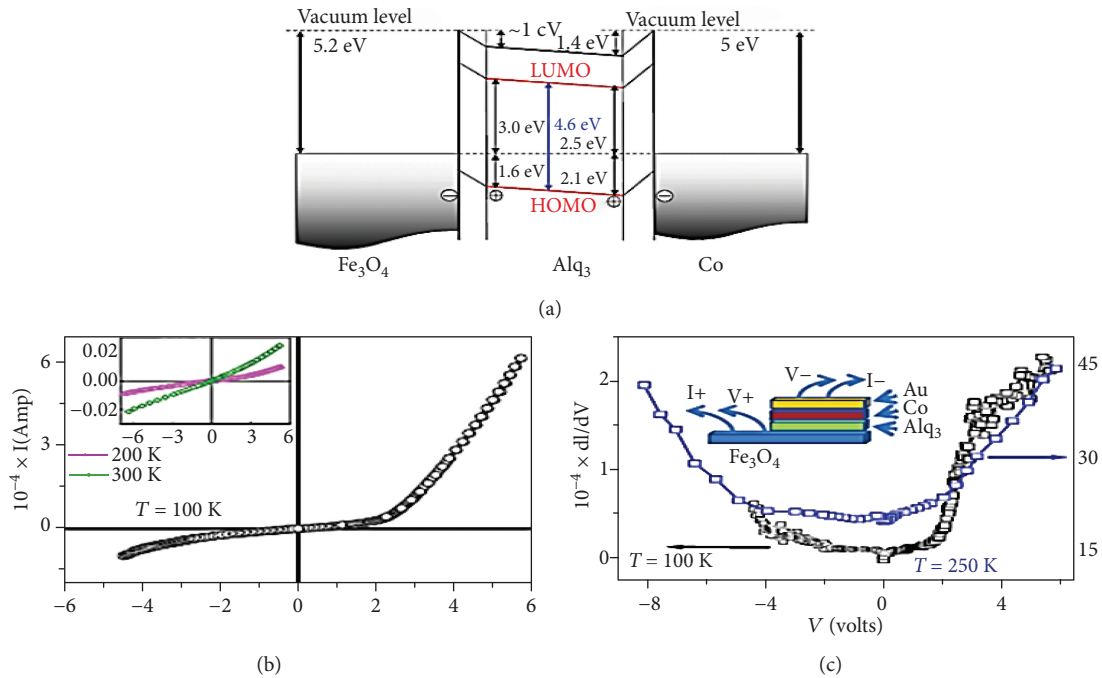


FIGURE 15: Energy level diagram at the interfaces of Alq3 and Fe<sub>3</sub>O<sub>4</sub>/Co electrodes (a). Current-voltage (*I-V*) characteristics of Fe<sub>3</sub>O<sub>4</sub>/Alq<sub>3</sub>/Co/Au SV at  $T = 100$  K (b). Inset in (b) shows *I-V* curves at  $T = 200$  and  $300$  K. Differential conductance vs. bias voltage at  $T = 100$  K and  $250$  K (c). Inset in (c) shows a schematic view of transport measurement geometry [84].

$T_V$  [6]. Convincingly, tuning of charge gap (0.15 eV) at  $E_F$  across VT due to charge ordering on the octahedral iron sites of Fe<sub>3</sub>O<sub>4</sub> is believed to result in a corresponding tuning of conduction mode and a unique crossover from GMR to TMR in Fe<sub>3</sub>O<sub>4</sub>/Alq<sub>3</sub>(C<sub>27</sub>H<sub>18</sub>N<sub>3</sub>O<sub>3</sub>Al)/Co interface as proposed by Dey et al. [86] with the energy band diagram given in Figure 15(a).

Interestingly, the *I-V* curves (Figure 15(b)) at higher temperatures  $T > T_V$  exhibit clear signs of tunnelling which further confirms from parabolic differential  $dI/dV$  curves (Figure 15(c)). But, at  $T < T_V$ , the curve is different and exhibits the beginning of the injection mode at a bias of 2 V (Figure 15(b)). The conduction observed at  $T < T_V$  is described by “activated” carrier injection into the molecular orbitals of OSC at the electrode-OSC interface, followed by “activated” carrier hopping through the molecular orbitals towards the opposite electrode, where the extraction of carriers from OSC takes place. While the  $T > T_V$  conduction is achieved through carrier tunnelling process, there is a drastic change in conductivity mode in SV from injection to tunnel mode as a function of “temperature,” signifies VT, as the origin of this effect. For  $T < T_V$ , there is a formation of charge gap at  $E_F$ ; consequently, activated carrier transport with the device current governed by carrier injection and transport through molecular levels of Alq<sub>3</sub> could be assigned as GMR. For  $T > T_V$ , with the decrease or even closure of this energy gap, all the charge carriers take part in the conduction process. Activated carrier transport no more remains relevant in this scenario, and the device current should be governed by tunnelling conduction in this temperature regime. Both GMR and TMR have been observed in a single

SV below/above the  $T_V$ , and a drastic tuning in SV properties is triggered by VT of Fe<sub>3</sub>O<sub>4</sub> electrode.

## 5. Conclusions

The aim of current day research is to innovate electromagnetic devices with advanced materials that can operate at lower power with higher speed, yet without compromising the aim of shrinking their size. For this goal, a comprehensive review of the growth of various nanostructured Fe<sub>3</sub>O<sub>4</sub> geometries and its hallmark Verwey transition is in a time of need. It is very exciting to observe the ensemble of anomalies VT brought forth at the nanoscale. It is not full-size dependent, but shape morphology also plays a crucial role in determining the energetically stable surface of stoichiometric Fe<sub>3</sub>O<sub>4</sub>. In nanocrystalline thin films, the electronic transport properties behave differently compared to the magnetic properties, particularly the absence of VT and the presence of antiphase boundaries caused by defects, off-stoichiometric Fe<sup>2+</sup>/Fe<sup>3+</sup> ratio, and micro-/nanostrains emanating from different growth conditions. Interestingly, the Verwey transition temperature  $T_V$  can be tailored in epitaxial Fe<sub>3</sub>O<sub>4</sub> thin films either by compressive strain using underneath special spinel substrates or integrated with a gated circuit using the electric field.

The following are the possible applications of nanostructured Fe<sub>3</sub>O<sub>4</sub> wherein VT can be exploited in the future:

- (1) Different Fe<sub>3</sub>O<sub>4</sub>-based multiferroic heterostructures can be developed by interfacial engineering (epitaxial strain, charge, oxygen vacancy, exchange, and spin-

orbital coupling) for various novel applications like resistive switching, spin filters for data storage, and spatial light modulators for optical switching

- (2) In contrast to conventional thermoelectrics, the spin Seebeck effect in  $\text{Fe}_3\text{O}_4$  thin films offers new possibility in all-solid-state energy conversion devices such as electric cooling systems and thermal power generators while the observation of large magnetocaloric effect paves the way for cooler on-chip devices for nano-/microelectromechanical systems
- (3) The concept of integration of  $\pi$ -conjugated organic semiconductors into spintronic devices owing to its robust spin coherence can be realized by using band alignment at the electrode  $\text{Fe}_3\text{O}_4/\text{Alq}_3$  interface, which gives GMR to TMR crossover in a single spin valve
- (4) Currently, basic research is mainly focused on spin dynamics and transport in semiconductor environment (spin transistors, spin diodes, optospintronic devices, memories, etc.) for all-electrical spin control via spin-orbit interactions and fixed or mobile spin qubits for quantum computing
- (5) Lastly,  $\text{Fe}_3\text{O}_4$  can be convincingly used for manufacturing cheap and efficient spintronic devices because of properties like excellent spin accumulation that can be successfully controlled using the Verwey transition. It can be used in various biomedical sensors like molecular detection, e.g., protein detection, and as a potential biomarker due to its positive integration with an organic semiconductor. Microarrays of sensing devices can make use of these properties of Verwey transition in cryogenic units for electrical fault sensing

Convincingly, VT proves to be an efficient needle to tailor the fabric of  $\text{Fe}_3\text{O}_4$  into useful nanoscale devices, yet shifting VT towards the room temperature range still remains a major challenge and can be manipulated by having in-depth knowledge of complicated electron-electron and electron-phonon interactions that involve the interplay of interaction, exchange orbital, and spin degrees of freedom.

## Conflicts of Interest

The authors declare that there is no conflict of interests.

## References

- [1] A. Mitra, J. Mohapatra, S. S. Meena, C. V. Tomy, and M. Aslam, "Verwey transition in ultrasmall-sized octahedral  $\text{Fe}_3\text{O}_4$  nanoparticles," *The Journal of Physical Chemistry C*, vol. 118, no. 33, pp. 19356–19362, 2014.
- [2] S. de Jong, R. Kukreja, C. Trabant et al., "Speed limit of the insulator–metal transition in magnetite," *Nature Materials*, vol. 12, no. 10, pp. 882–886, 2013.
- [3] L. R. Bickford Jr., "The low temperature transformation in ferrites," *Reviews of Modern Physics*, vol. 25, no. 1, pp. 75–79, 1953.
- [4] M. Liu, J. Hoffman, J. Wang, J. Zhang, B. Nelson-Cheeseman, and A. Bhattacharya, "Non-volatile ferroelastic switching of the Verwey transition and resistivity of epitaxial  $\text{Fe}_3\text{O}_4/\text{PMN-PT}$  (011)," *Scientific Reports*, vol. 3, no. 1, p. 1876, 2013.
- [5] R. Ramos, T. Kikkawa, K. Uchida et al., "Observation of the spin Seebeck effect in epitaxial  $\text{Fe}_3\text{O}_4$  thin films," *Applied Physics Letters*, vol. 102, no. 7, article 072413, 2013.
- [6] X. H. Liu, W. Liu, Z. D. Zhang, and C. F. Chang, "Mediating exchange bias by Verwey transition in  $\text{CoO}/\text{Fe}_3\text{O}_4$  thin film," *Journal of Applied Physics*, vol. 123, no. 8, article 083903, 2018.
- [7] S. G. Bhat and P. S. A. Kumar, "Enhanced spin accumulation in  $\text{Fe}_3\text{O}_4$  based spin injection devices below the Verwey transition," *Materials Research Express*, vol. 3, no. 12, article 125905, 2016.
- [8] H. Y. Huang, Z. Y. Chen, R. . P. Wang et al., "Jahn-Teller distortion driven magnetic polarons in magnetite," *Nature Communications*, vol. 8, article 15929, 2017.
- [9] C. Schmitz-Antoniak, D. Schmitz, A. Warland et al., "Reversed ageing of  $\text{Fe}_3\text{O}_4$  nanoparticles by hydrogen plasma," *Scientific Reports*, vol. 6, no. 1, 2016.
- [10] E. Gmelin, N. Lenge, and H. Kronüller, "Specific heat of magnetite near the Verwey transition is there more than one phase transition?," *Philosophical Magazine B*, vol. 50, no. 3, pp. L41–L44, 1984.
- [11] D. J. Huang, H. J. Lin, J. Okamoto et al., "Charge-orbital ordering and Verwey transition in magnetite measured by resonant soft X-ray scattering," *Physical Review Letters*, vol. 96, no. 9, 2006.
- [12] T. Kim, S. Lim, and J. Hong, "Giant thermal hysteresis in Verwey transition of single domain  $\text{Fe}_3\text{O}_4$  nanoparticles," *Scientific Reports*, vol. 8, no. 5092, 2018.
- [13] J. A. Cuenca, K. Bugler, S. Taylor et al., "Study of the magnetite to maghemite transition using microwave permittivity and permeability measurements," *Journal of Physics: Condensed Matter*, vol. 28, no. 10, article 106002, 2016.
- [14] M. A. Gilleo, "Superexchange interaction energy for  $\text{Fe}^{3+}\text{O}^{2-}\text{Fe}^{3+}$  linkages," *Physical Review*, vol. 109, no. 3, pp. 777–781, 1958.
- [15] C. Zener, "Interaction between the  $d$ -shells in the transition metals. II. Ferromagnetic compounds of manganese with perovskite structure," *Physical Review*, vol. 82, no. 3, pp. 403–405, 1951.
- [16] E. J. W. Verwey and P. W. Haayman, "Electronic conductivity and transition point of magnetite (" $\text{Fe}_3\text{O}_4$ ")," *Physica*, vol. 8, no. 9, pp. 979–987, 1941.
- [17] Z. Tarnawski, A. Wiecheć, M. Madej et al., "Studies of the Verwey transition in magnetite," *Acta Physica Polonica A*, vol. 106, no. 5, pp. 771–775, 2004.
- [18] A. Kozłowski, Z. Kąkol, and Z. Tarnawski, "Magnetite  $\text{Fe}_3\text{O}_4$ : the correlated electron-phonon system," *Acta Physica Polonica A*, vol. 111, no. 4, pp. 537–547, 2007.
- [19] S. Lim, B. Choi, S. Y. Lee et al., "Microscopic states and the Verwey transition of magnetite nanocrystals investigated by nuclear magnetic resonance," *Nano Letters*, vol. 18, no. 3, pp. 1745–1750, 2018.
- [20] J. Lee, S. G. Kwon, J.-G. Park, and T. Hyeon, "Size dependence of metal–insulator transition in stoichiometric

- Fe<sub>3</sub>O<sub>4</sub> nanocrystals,” *Nano Letters*, vol. 15, no. 7, pp. 4337–4342, 2015.
- [21] A. Akbarzadeh, M. Samiei, and S. Davaran, “Magnetic nanoparticles: preparation, physical properties, and applications in biomedicine,” *Nanoscale Research Letters*, vol. 7, no. 1, p. 144, 2012.
- [22] Z. L. Lu, M. X. Xu, W. Q. Zou et al., “Large low field magneto-resistance in ultrathin nanocrystalline magnetite Fe<sub>3</sub>O<sub>4</sub> films at room temperature,” *Applied Physics Letters*, vol. 91, no. 10, article 102508, 2007.
- [23] R. Aragon, P. M. Gehring, and S. M. Shapiro, “Stoichiometry, percolation, and Verwey ordering in magnetite,” *Physical Review Letters*, vol. 70, no. 11, pp. 1635–1638, 1993.
- [24] V. A. M. Brabers, F. Walz, and H. Kronmüller, “Impurity effects upon the Verwey transition in magnetite,” *Physical Review B*, vol. 58, no. 21, pp. 14163–14166, 1998.
- [25] X. H. Liu, A. D. Rata, C. F. Chang, A. C. Komarek, and L. H. Tjeng, “Verwey transition in Fe<sub>3</sub>O<sub>4</sub> thin films: influence of oxygen stoichiometry and substrate-induced microstructure,” *Physical Review B*, vol. 90, no. 12, article 125142, 2014.
- [26] M. Bohra, K. E. Prasad, R. Bollina, S. C. Sahoo, and N. Kumar, “Characterizing the phase purity of nanocrystalline Fe<sub>3</sub>O<sub>4</sub> thin films using Verwey transition,” *Journal of Magnetism and Magnetic Materials*, vol. 418, pp. 137–142, 2016.
- [27] M. Bohra, S. Prasad, N. Venketaramani, N. Kumar, S. C. Sahoo, and R. Krishnan, “Magnetic properties of magnetite thin films close to the Verwey transition,” *Journal of Magnetism and Magnetic Materials*, vol. 321, no. 22, pp. 3738–3741, 2009.
- [28] M. Bohra, D. Roy Chowdhury, J.-F. Bobo, and V. Singh, “Anomalous electric transport across Verwey transition in nanocrystalline Fe<sub>3</sub>O<sub>4</sub> thin films,” *Journal of Applied Physics*, vol. 125, no. 1, article 013901, 2017.
- [29] M. Bohra and S. C. Sahoo, “Large magnetocaloric effect at Verwey point in nanocrystalline Fe<sub>3</sub>O<sub>4</sub> thin films,” *Journal of Alloys and Compounds*, vol. 699, pp. 1118–1121, 2017.
- [30] X. Liu, C.-F. Chang, A. D. Rata, A. C. Komarek, and L. H. Tjeng, “Fe<sub>3</sub>O<sub>4</sub> thin films: controlling and manipulating an elusive quantum material,” *npj Quantum Materials*, vol. 1, no. 1, article 16027, 2016.
- [31] M. Ziese, “Extrinsic magnetotransport phenomena in ferromagnetic oxides,” *Reports on Progress in Physics*, vol. 65, no. 2, pp. 143–249, 2002.
- [32] J. B. Moussy, “From epitaxial growth of ferrite thin films to spin-polarized tunnelling,” *Journal of Physics D: Applied Physics*, vol. 46, no. 14, article 143001, 2013.
- [33] G. Q. Gong, A. Gupta, G. Xiao, W. Qian, and V. P. Dravid, “Magnetoresistance and magnetic properties of epitaxial magnetite thin films,” *Physical Review B*, vol. 56, no. 9, pp. 5096–5099, 1997.
- [34] S. Geprägs, D. Mannix, M. Opel, S. T. B. Goennenwein, and R. Gross, “Converse magnetoelectric effects in Fe<sub>3</sub>O<sub>4</sub>/BaTiO<sub>3</sub> multiferroic hybrids,” *Physical Review B*, vol. 88, no. 5, article 054412, 2013.
- [35] W. Eerenstein, T. T. M. Palstra, T. Hibma, and S. Celotto, “Origin of the increased resistivity in epitaxial Fe<sub>3</sub>O<sub>4</sub> films,” *Physical Review B*, vol. 66, no. 20, article 201101, 2002.
- [36] X. Liu, W. Mi, Q. Zhang, and X. Zhang, “Anisotropic magnetoresistance across Verwey transition in charge ordered Fe<sub>3</sub>O<sub>4</sub> epitaxial films,” *Physical Review B*, vol. 96, no. 21, article 214434, 2017.
- [37] S. Chandra, R. Das, V. Kalappattil et al., “Epitaxial magnetite nanorods with enhanced room temperature magnetic anisotropy,” *Nanoscale*, vol. 9, no. 23, pp. 7858–7867, 2017.
- [38] A. Lak, D. Niculaes, G. C. Anyfantis et al., “Facile transformation of FeO/Fe<sub>3</sub>O<sub>4</sub> core-shell nanocubes to Fe<sub>3</sub>O<sub>4</sub> via magnetic stimulation,” *Scientific Reports*, vol. 6, no. 1, article 33295, 2016.
- [39] G. T. Rado and J. M. Ferrari, “Electric field dependence of the magnetic anisotropy energy in magnetite (Fe<sub>3</sub>O<sub>4</sub>),” *Physical Review B*, vol. 12, no. 11, pp. 5166–5174, 1975.
- [40] S. Iida, M. Mizoguchi, S. Umemura, J. Yoshida, K. Kato, and K. Yanai, “Typical spontaneous symmetry breakdown in solid state as revealed by Fe<sub>3</sub>O<sub>4</sub>,” *Journal of Applied Physics*, vol. 50, no. B11, p. 7584, 1979.
- [41] G. T. Rado and J. M. Ferrari, “Linear and bilinear magnetoelectric effects in magnetically biased magnetite (Fe<sub>3</sub>O<sub>4</sub>),” *Physical Review B*, vol. 15, no. 1, pp. 290–297, 1977.
- [42] Y. Miyamoto and S. Chikazumi, “Crystal symmetry of magnetite in low temperature phase deduced from magnetoelectric measurements,” *Journal of the Physical Society of Japan*, vol. 57, no. 6, pp. 2040–2050, 1988.
- [43] Y. Miyamoto and M. Shindo, “Magnetoelectric measurement of magnetite (Fe<sub>3</sub>O<sub>4</sub>) at low temperatures and direct evidence for nonexistence of *ac* mirror plane,” *Journal of the Physical Society of Japan*, vol. 62, no. 5, pp. 1423–1426, 1993.
- [44] Y. Miyamoto, S. Ishihara, T. Hirano, M. Takada, and N. Suzuki, “Ferroelectricity of magnetite (Fe<sub>3</sub>O<sub>4</sub>) observed by means of magnetoelectric effect,” *Solid State Communications*, vol. 89, no. 1, pp. 51–54, 1994.
- [45] L. Pauling, “The structure and entropy of ice and of other crystals with some randomness of atomic arrangement,” *Journal of the American Chemical Society*, vol. 57, no. 12, pp. 2680–2684, 1935.
- [46] L. Pauling, *The Nature of the Chemical Bond*, Cornell University Press, Ithaca, NY, USA, 1938.
- [47] J. P. Wright, J. P. Attfield, and P. G. Radaelli, “Long range charge ordering in magnetite below the Verwey transition,” *Physical Review Letters*, vol. 87, no. 26, article 266401, 2001.
- [48] J. P. Wright, J. P. Attfield, and P. G. Radaelli, “Charge ordered structure of magnetite Fe<sub>3</sub>O<sub>4</sub> below the Verwey transition,” *Physical Review B*, vol. 66, no. 21, article 214422, 2002.
- [49] J. van den Brink and D. I. Khomskii, “Multiferroicity due to charge ordering,” *Journal of Physics: Condensed Matter*, vol. 20, no. 43, article 434217, 2008.
- [50] M. Ziese, P. D. Esquinazi, D. Pantel, M. Alexe, N. M. Nemes, and M. Garcia-Hernández, “Magnetite (Fe<sub>3</sub>O<sub>4</sub>): a new variant of relaxor multiferroic?,” *Journal of Physics: Condensed Matter*, vol. 24, no. 8, article 086007, 2012.
- [51] J. J. I. Wong, A. G. Swartz, R. Zheng, W. Han, and R. K. Kawakami, “Electric field control of the Verwey transition and induced magnetoelectric effect in magnetite,” *Physical Review B*, vol. 86, no. 6, article 060409, 2012.
- [52] K. Yamauchi, T. Fukushima, and S. Picozzi, “Ferroelectricity in multiferroic magnetite Fe<sub>3</sub>O<sub>4</sub> driven by noncentrosymmetric Fe<sup>2+</sup>/Fe<sup>3+</sup> charge-ordering: first-principles study,” *Physical Review B*, vol. 79, no. 21, article 212404, 2009.
- [53] F. Walz and H. Kronmüller, “Analysis of magnetic point-defect relaxations in electron-irradiated magnetite,” *Physica Status Solidi B*, vol. 181, no. 2, pp. 485–498, 1994.

- [54] F. Schrettle, S. Krohns, P. Lunkenheimer, V. A. M. Brabers, and A. Loidl, "Relaxor ferroelectricity and the freezing of short-range polar order in magnetite," *Physical Review B*, vol. 83, no. 19, article 195109, 2011.
- [55] V. Chlan, K. Kouřil, H. Štěpánková et al., "Magnetically induced structural reorientation in magnetite studied by nuclear magnetic resonance," *Journal of Applied Physics*, vol. 108, no. 8, article 083914, 2010.
- [56] L. E. Cross, "Relaxor ferroelectrics," *Ferroelectrics*, vol. 76, no. 1, pp. 241–267, 1987.
- [57] Y. Tokura, "Multiferroics—toward strong coupling between magnetization and polarization in a solid," *Journal of Magnetism and Magnetic Materials*, vol. 310, no. 2, pp. 1145–1150, 2007.
- [58] I. E. Dzyaloshinskii, "On the magneto-electrical effects in anti-ferromagnets," *Soviet Physics JETP*, vol. 10, pp. 628–629, 1960.
- [59] M. K. Niranjana, J. P. Velev, C.-G. Duan, S. S. Jaswal, and E. Y. Tsymlal, "Magnetolectric effect at the  $\text{Fe}_3\text{O}_4/\text{BaTiO}_3$  (001) interface: a first-principles study," *Physical Review B*, vol. 78, no. 10, article 104405, 2008.
- [60] Y. Zhang, M. Liu, L. Zhang et al., "Multiferroic heterostructures of  $\text{Fe}_3\text{O}_4/\text{PMN-PT}$  prepared by atomic layer deposition for enhanced interfacial magnetoelectric couplings," *Applied Physics Letters*, vol. 110, no. 8, article 082902, 2017.
- [61] I. Vrejoiu, D. Preziosi, A. Morelli, and E. Pippel, "Multiferroic  $\text{PbZr}_x\text{Ti}_{1-x}\text{O}_3/\text{Fe}_3\text{O}_4$  epitaxial sub-micron sized structures," *Applied Physics Letters*, vol. 100, no. 10, article 102903, 2012.
- [62] J. Wang, J. B. Neaton, H. Zheng et al., "Epitaxial  $\text{BiFeO}_3$  multiferroic thin film heterostructures," *Science*, vol. 299, no. 5613, pp. 1719–1722, 2003.
- [63] H. W. Brinks, H. Fjellvag, and A. Kjekshus, "Synthesis of metastable perovskite-type  $\text{YMnO}_3$  and  $\text{HoMnO}_3$ ," *Journal of Solid State Chemistry*, vol. 129, no. 2, pp. 334–340, 1997.
- [64] Y.-M. Kim, A. Morozovska, E. Eliseev et al., "Direct observation of ferroelectric field effect and vacancy-controlled screening at the  $\text{BiFeO}_3/\text{La}_x\text{Sr}_{1-x}\text{MnO}_3$  interface," *Nature Materials*, vol. 13, no. 11, pp. 1019–1025, 2014.
- [65] C. Becher, M. Trassin, M. Lilienblum et al., "Functional ferroic heterostructures with tunable integral symmetry," *Nature Communications*, vol. 5, no. 1, p. 4295, 2014.
- [66] W. Saenrang, B. A. Davidson, F. Maccherozzi et al., "Deterministic and robust room-temperature exchange coupling in monodomain multiferroic  $\text{BiFeO}_3$  heterostructures," *Nature Communications*, vol. 8, no. 1, p. 1583, 2017.
- [67] G. De Luca, N. Strkalj, S. Manz, C. Bouillet, M. Fiebig, and M. Trassin, "Nanoscale design of polarization in ultrathin ferroelectric heterostructures," *Nature Communications*, vol. 8, no. 1, p. 1419, 2017.
- [68] Y. Zhang, L. Xie, J. Kim et al., "Discovery of a magnetic conductive interface in  $\text{PbZr}_{0.2}\text{Ti}_{0.8}\text{O}_3/\text{SrTiO}_3$  heterostructures," *Nature Communications*, vol. 9, no. 1, p. 685, 2018.
- [69] C. Ju, J.-C. Yang, C. Luo et al., "Anomalous electronic anisotropy triggered by ferroelastic coupling in multiferroic heterostructures," *Advanced Materials*, vol. 28, no. 5, pp. 876–883, 2016.
- [70] H. F. Tian, T. L. Qu, L. B. Luo et al., "Strain induced magneto-electric coupling between magnetite and  $\text{BaTiO}_3$ ," *Applied Physics Letters*, vol. 92, no. 6, article 063507, 2008.
- [71] Z. Yang, C. Ko, and S. Ramanathan, "Oxide electronics utilizing ultrafast metal-insulator transitions," *Annual Review of Materials Research*, vol. 41, no. 1, pp. 337–367, 2011.
- [72] T. N. Theis and P. M. Solomon, "It's time to reinvent the transistor!," *Science*, vol. 327, no. 5973, pp. 1600–1601, 2010.
- [73] C. H. Ahn, J. M. Triscone, and J. Mannhart, "Electric field effect in correlated oxide systems," *Nature*, vol. 424, no. 6952, pp. 1015–1018, 2003.
- [74] T. Kopp and J. Mannhart, "Calculation of the capacitances of conductors: perspectives for the optimization of electronic devices," *Journal of Applied Physics*, vol. 106, no. 6, article 064504, 2009.
- [75] R. Scherwitzl, P. Zubko, I. G. Lezama et al., "Electric-field control of the metal-insulator transition in ultrathin  $\text{NdNiO}_3$  films," *Advanced Materials*, vol. 22, no. 48, pp. 5517–5520, 2010.
- [76] J. P. Heremans, V. Jovovic, E. S. Toberer et al., "Enhancement of thermoelectric efficiency in  $\text{PbTe}$  by distortion of the electronic density of states," *Science*, vol. 321, no. 5888, pp. 554–557, 2008.
- [77] H. Jin, C. M. Jaworski, and J. P. Heremans, "Enhancement in the figure of merit of p-type  $\text{Bi}_{100-x}\text{Sb}_x$  alloys through multiple valence-band doping," *Applied Physics Letters*, vol. 101, no. 5, article 053904, 2012.
- [78] W. H. Meiklejohn and C. P. Bean, "New magnetic anisotropy," *Physical Review*, vol. 102, no. 5, pp. 1413–1414, 1956.
- [79] X. H. Liu, W. Liu, S. Guo, W. J. Gong, J. N. Feng, and Z. D. Zhang, "Strong effects of magnetic anisotropy on exchange coupling and magnetotransport properties of ferromagnetic/ $\text{NiO}$ /ferromagnetic trilayers," *Applied Physics Letters*, vol. 97, no. 7, article 072502, 2010.
- [80] C. H. Li, O. M. J. van 't Erve, and B. T. Jonker, "Electrical injection and detection of spin accumulation in silicon at 500 K with magnetic metal/silicon dioxide contacts," *Nature Communications*, vol. 2, no. 1, p. 245, 2011.
- [81] H. Saito, S. Watanabe, Y. Mineno et al., "Electrical creation of spin accumulation p-type germanium," *Solid State Communications*, vol. 151, no. 17, pp. 1159–1161, 2011.
- [82] W. Wang, M. Yu, M. Batzill, J. He, U. Diebold, and J. Tang, "Enhanced tunneling magnetoresistance and high-spin polarization at room temperature in a polystyrene-coated  $\text{Fe}_3\text{O}_4$  granular system," *Physical Review B*, vol. 73, no. 13, article 134412, 2006.
- [83] M. Ziese, U. Köhler, A. Bollero, R. Höhne, and P. Esquinazi, "Schottky barrier and spin polarization at the  $\text{Fe}_3\text{O}_4\text{-Nb:SrTiO}_3$  interface," *Physical Review B*, vol. 71, no. 18, article 180406, 2005.
- [84] G. Schmidt, D. Ferrand, L. W. Molenkamp, A. T. Filip, and B. J. van Wees, "Fundamental obstacle for electrical spin injection from a ferromagnetic metal into a diffusive semiconductor," *Physical Review B*, vol. 62, no. 8, pp. R4790–R4793, 2000.
- [85] J. S. Moodera, L. R. Kinder, T. M. Wong, and R. Meservey, "Large magnetoresistance at room temperature in ferromagnetic thin film tunnel junctions," *Physical Review Letters*, vol. 74, no. 16, pp. 3273–3276, 1995.
- [86] P. Dey, R. Rawat, S. R. Potdar, R. J. Choudhary, and A. Banerjee, "Temperature driven transition from giant to tunneling magneto-resistance in  $\text{Fe}_3\text{O}_4/\text{Alq}_3/\text{Co}$  spin valve: role of Verwey transition of  $\text{Fe}_3\text{O}_4$ ," *Journal of Applied Physics*, vol. 115, no. 17, article 17C110, 2014.

## Research Article

# In Vitro Safety Evaluation and In Vivo Imaging Studies of Superparamagnetic Iron Oxide Nanoparticles through Biomimetic Modification

Xinfeng Song,<sup>1</sup> Yancong Zhang ,<sup>2,3</sup> Hanwen Sun ,<sup>1</sup> Pingxuan Dong,<sup>1</sup> Zhongyu Zhang,<sup>1</sup> and Jing Liu<sup>1</sup>

<sup>1</sup>Shandong Provincial Engineering Laboratory of Novel Pharmaceutical Excipients, Sustained and Controlled Release Preparations, College of Medicine and Nursing, Dezhou University, Decheng District, Dezhou 253023, China

<sup>2</sup>Dezhou People's Hospital, Decheng District, Dezhou 253014, China

<sup>3</sup>School of Stomatology, Shandong University, China

Correspondence should be addressed to Hanwen Sun; hanwen916@163.com

Received 26 July 2018; Revised 20 September 2018; Accepted 8 November 2018; Published 6 February 2019

Guest Editor: Manikandan Muthu

Copyright © 2019 Xinfeng Song et al. This is an open access article distributed under the Creative Commons Attribution License, which permits unrestricted use, distribution, and reproduction in any medium, provided the original work is properly cited.

Magnetic resonance imaging (MRI) is an advanced medical imaging diagnostic technique that utilizes different resonance signals generated by the signal strength of water content and the relaxation time of protons in water molecules under the influence of an external magnetic field. This technique requires contrast agents, such as Gd-DTPA and Gd-DOTA, which could increase the risk of renal fibrosis in patients with severe renal insufficiency. The magnetic moment or susceptibility of superparamagnetic iron oxide nanoparticle (SPION) is higher than that of other paramagnetic substances and could significantly reduce the dosage of the contrast agent required. In our previous work, the novel magnetic composite nanoparticles (abbreviated as c(RGDyK)-PDA-SPION) had been successfully synthesized by a facile and simple approach. Further evaluation had demonstrated that it had an average particle size of about 50 nm and uniform distribution, superparamagnetic properties, and good dispersion stability in water solution. Animal acute toxicity test also had proved that it had high safety in vivo. In this work, c(RGDyK)-PDA-SPION was further studied for the cell toxicity and effect on HepG2 cells in vitro, and the MRI imaging of this contrast agent in HepG2 tumor-bearing mice was also studied. It is an extension of the published work. The results showed that it possessed high safety and enrichment phenomenon on HepG2 cells in vitro. Animal experimental data preliminarily prove that the contrast agent could enhance the MRI  $T_2$ -weighted imaging capability of HepG2 carcinoma in tumor-bearing mice and could be a potential  $T_2$  contrast agent.

## 1. Introduction

Magnetic resonance imaging (MRI), which was first proposed by Lauterbur in 1973 [1], is an advanced medical imaging diagnostic technique that utilizes different resonance signals generated by the signal strength of water content and the relaxation time of protons in the water molecules under the influence of an external magnetic field [2]. In clinical practice, the relaxation time of different healthy or tumor tissues overlaps with one another, leading to difficult diagnosis. Thus, researchers investigated the use of contrast agents to enhance the signal contrast and improve the resolution

of soft tissue images. At present, more than 30% of MRI examinations require the use of an MRI contrast agent [3]. By shortening the proton relaxation times  $T_1$  and  $T_2$ , an MRI contrast agent can improve the signal differences of different organizations or pathological changes and thus facilitate the diagnosis of lesions.

The paramagnetic metal ion  $Gd^{3+}$  contains seven unpaired electrons; as such, the ion possesses large electron spin magnetic moment, relaxation efficiency, and symmetric electric field and can easily coordinate with seven to eight water molecules.  $Gd^{3+}$  has become the best choice for  $T_1$  MRI contrast agent [4, 5]. However,  $Gd^{3+}$  easily accumulates

in the human liver, spleen, bone, and brain and is highly toxic because of its ionic form [6, 7]. Therefore, scholars must explore suitable ligands that can form complexes with  $Gd^{3+}$  to reduce its toxicity.

In 1983, Yim et al. [8] applied Gd-DTPA to diagnose brain tumors for the first time; this contrast agent has been widely used after securing FDA certification in 1987. However, Gd-DTPA can produce high osmotic pressure in the form of sodium or glucosamine ions. In this regard, many nonionic Gd-DTPA derivatives have been synthesized. To date, Gd-DOTA is the most stable gadolinium coordination contrast agent [9]. However, at the end of 2006, the FDA issued a warning stating that gadolinium contrast agents could increase the risk of renal fibrosis in patients with severe renal insufficiency [10, 11].

As a  $T_2$  MRI contrast agent, superparamagnetic contrast agents are usually composed of a nanometer-sized iron oxide crystal nucleus and a stable coating material. The core of the iron oxide crystal is typically  $Fe_3O_4$ ,  $\gamma-Fe_2O_3$ , or  $FeOOH$  [12]. Among these substances, SPION has attracted increasing attention because of its higher magnetic moment and susceptibility ratio than other paramagnetic materials; moreover, the relaxation efficiency of the hydrogen nucleus after entering the tissue could significantly reduce the dosage of the contrast agent required [13]. However, naked SPION easily coagulates, exhibits large particle sizes, and is poorly dispersed because of its surface hydrophobicity, high surface energy, and magnetic field influence, which prevent the particles to pass through capillaries and into tissues; as such, naked SPION has limited biomedical applications [14]. These issues are circumvented by using physical or chemical methods to modify the particle surface. The most common coating materials are dextran, glucan derivatives, starch, silicone oil, arabic galactose, and albumin.

A literature review on SPION surface modification revealed that most preparation methods are relatively complicated and require strict procedures. Therefore, the preparation and surface functionalization of SPION is a key step for solving the limited application of magnetic nanomaterials. Dopamine (DA) is the main component of the adhesion protein of mussel, and its homopolymer is extremely adhesive and can modify the surface coating of various materials [15, 16]. Researchers have used the self-polymerization and super adhesion properties of DA to create various hydrophilic composite materials [17, 18]. However, few studies have investigated the surface modification of SPION by using DA and MRI imaging. In a previous work [19] (*J Nanosci Nanotechnol.* 2016. <http://www.aspbs.com/jnn/>), c(RGDyK)-PDA-SPION was successfully synthesized. Preliminary results demonstrated that the particles of c(RGDyK)-PDA-SPION are about 50 nm in size and are distributed evenly; the particles possess significant magnetic properties, good water dispersibility, and high internal security. Given its superior performance, c(RGDyK)-PDA-SPION was further studied for its in vitro cell toxicity and in vitro enrichment effect on HepG2. The in vivo MRI imaging law of this contrast agent in HepG2 tumor-bearing mice was discussed in this paper.

## 2. Methods and Materials

**2.1. Reagents and Instruments.** SPION, PDA-SPION, c(RGDyK)-PDA-SPION (prepared by our laboratory), trypsin, EDTA, DMSO, MTT, RPMI 1640 medium, fetal bovine serum (Shanghai Yuanye Bio-Technology Co. Ltd.), hepatocellular carcinoma cell line HepG2 (Institute of Basic Medicine, Chinese Academy of Medical Sciences), Prussian blue stain kit (Beijing Solarbio Science & Technology Co. Ltd.), and HepG2 tumor-bearing mice (Shanghai Ruantuo Biotechnology Co. Ltd.) were used in this study.

A  $CO_2$  incubator (Thermo HERAcell 240i), a full-wavelength multifunctional enzyme marker (Thermo Varioskan Flash), an inverted fluorescence microscope (Leica, DMI3000B), and a small nuclear magnetic resonance apparatus (Suzhou Niumag Analytical Instrument Corporation, MesoMR23-060H-I) were also adopted.

**2.2. Cytotoxicity of Magnetic Nanoparticles.** HepG2 cells were cultured and used to investigate the cytotoxicity of three kinds of particles to human liver cells. The effects of the three types of nanoparticles on the activity of HepG2 cells were studied by MTT experiment. The inoculation density of HepG2 cells in the logarithmic growth phase was  $4.7 \times 10^5$ /mL. After the cells became adherent, the supernatants of the intervention groups were mixed with different concentrations of serum-free mixture containing different surface-modified magnetic nanoparticles (SPION, PDA-SPION, and c(RGDyK)-PDA-SPION). Three particle concentration gradients, namely, 5, 10, and 20  $\mu\text{g}/\text{mL}$ , were applied. A blank control group was used and added only with serum-containing RPMI 1640 medium. The cell suspensions were then cultured at 37°C and 5%  $CO_2$  in an incubator for 24 h. Each hole was added with 15  $\mu\text{L}$  of MTT and 85  $\mu\text{L}$  of PBS. After 4 h, the culture plate was removed from the incubator, and the supernatant was discarded. Each hole was added with DMSO (100  $\mu\text{L}$ ), and 490 nm wavelength was used to determine the absorbance value (optical density (OD)) of each aperture.

**2.3. In Vitro Cell Targeting Enrichment Effect of Magnetic Nanoparticles.** We then determined the concentrations of the SPION, PDA-SPION, and c(RGDyK)-PDA-SPION magnetic nanoparticles in hepatoma cells. The concentrations of the RPMI 1640 culture medium without serum were 2, 5, and 10  $\mu\text{g}/\text{mL}$  for the three magnetic nanoparticle-exposed liquids of SPION, PDA-SPION, and c(RGDyK)-PDA-SPION. HepG2 cells in the logarithmic growth stage were inoculated at a cell density of  $4.7 \times 10^5$ /mL and in a six-hole cell culture plate with a cover glass. The cells were cultured at 37°C in a 5%  $CO_2$  incubator. After the cells were adherent for 24 h, different concentrations of the three magnetic nanoparticle-exposed liquids and a blank control group composed of only serum-containing RPMI 1640 medium were added separately and incubated for 24 h. The magnetic nanoparticles were then observed in the liver cancer cells.

Based on the enrichment effect, 10  $\mu\text{g}/\text{mL}$  was selected for SPION-, PDA-SPION-, and c(RGDyK)-PDA-SPION-exposed liquids. In the logarithmic phase,  $4.7 \times 10^5$ /mL HepG2

cells were inoculated in a six-hole cell culture plate with a cover and incubated at 37°C in a 5% CO<sub>2</sub> incubator. After the cells adhered to the wall and the exposed liquids were added, exposure was performed for 6, 12, 24, and 48 h. The cells were fixed with 4% paraformaldehyde for 20 min, dried, cleaned with PBS, and subjected to 10% Prussian blue staining (K<sub>4</sub>Fe(CN)<sub>6</sub>·3H<sub>2</sub>O) and nuclear solid red staining. The samples were sealed with neutral resin, observed under an inverted microscope and photographed.

**2.4. T<sub>2</sub> Relaxation Time Test of Magnetic Nanoparticles.** The resonant frequency of the small nuclear magnetic resonance instrument (MesoMR23-060H-I) was 23 MHz, the magnetic strength was 0.5 T, the coil diameter was 60 mm, and the magnetic temperature was 32.0°C. The three magnetic nanoparticles of SPION, PDA-SPION, and c(RGDyK)-PDA-SPION were, respectively, assigned to concentrations of 10.449, 20.898, 41.797, 83.594, and 167.188 μg/mL. Five concentration gradient solutions were placed in the small nuclear magnetic resonance instrument coil for testing and analyzing T<sub>2</sub> relaxation time of the contrast agent with nuclear magnetic resonance analysis software.

**2.5. In Vitro T<sub>2</sub>-Weighted Imaging Test of Magnetic Nanoparticles.** Debugging small nuclear magnetic resonance instrument (MesoMR23-060H-I) used resonant frequency of 23 MHz, magnet strength of 0.5 T, coil diameter of 60 mm, and magnet temperature of 32.0°C. Six concentration gradients (0, 10.449, 20.898, 41.797, 83.594, and 167.188 μg/mL) of the solutions of the three magnetic nanoparticles (SPION, PDA-SPION, and c(RGDyK)-PDA-SPION) were placed in the coil for detection. Imaging software and MSE sequence were used to collect images.

**2.6. In Vivo MRI Imaging Test of Magnetic Nanoparticles in Normal Mice.** In this experiment, the resonant frequency of the small nuclear magnetic resonance instrument (MesoMR23-060H-I) was 23 MHz, the magnetic strength was 0.5 T, the coil diameter was 60 mm, and the magnetic temperature was 32.0°C. The abdominal cavity of Kunming mice weighing 18–25 g was injected with 0.08 mL/10 g weight of 8% chloral hydrate. After anesthesia, 0.2 mL of 167.188 μg/mL each of the SPION, PDA-SPION, and c(RGDyK)-PDA-SPION magnetic nanoparticle solutions was injected through the tail vein. MRI signals were collected at 0, 0.5, 1, 2, and 24 h, and the coronal plane images of mice were recorded using MRI software and MSE sequence.

**2.7. MRI Imaging Test of c(RGDyK)-PDA-SPION Contrast Agent in Tumor-Bearing Mice.** A suspension of 1 × 10<sup>7</sup>/mL HepG2 cells in the logarithmic phase was prepared in serum-free medium. Subsequently, 0.2 mL of the cell suspension was inoculated subcutaneously in the side hip of BALB/c nude mice. After 15 days, the tumors were about 0.8–1 cm in size.

The resonant frequency of the debug small nuclear magnetic resonance (MesoMR23-060H-I) was 23 MHz, the magnetic strength was 0.5 T, the coil diameter was 60 mm, and the magnetic temperature was 32.0°C. The abdominal cavity of tumor-bearing mice weighing 20 g was injected with

0.08 mL/10 g weight of 8% chloral hydrate. After anesthesia, 0.2 mL of 167.188 μg/mL of the c(RGDyK)-PDA-SPION nanoparticle solution was injected through the tail vein. The T<sub>2</sub>-weighted enrichment of MRI imaging of the c(RGDyK)-PDA-SPION magnetic nanoparticle contrast agent was tested after 0, 0.5, 1, 2, 6, and 24 h in the cancer, liver, spleen, heart, and kidney tissues through nuclear magnetic resonance imaging software. The imaging effect of the tumor and the tissues and organs of the tumor-bearing mice was determined by unifying mapping and pseudo-color image processing. The optimum imaging times of the induced tumor and the tissues and organs were determined.

### 3. Results and Discussion

**3.1. Cytotoxicity of the Magnetic Nanoparticles.** The MTT experimental results showed that the three types of magnetic nanoparticles within the concentration range of 0–20 μg/mL showed no significant influence on the activity of HepG2 cells (Figure 1). Hence, the three kinds of nanoparticles were biocompatible and safe for liver cells within a controlled concentration range.

**3.2. Enrichment Effect of Magnetic Nanoparticles In Vitro in HepG2 Cells.** Studies shown that integrin α<sub>v</sub>β<sub>3</sub> is highly expressed on the surface of various malignant tumor cells [20], which plays a significant role in tumor growth, local infiltration, and metastasis, especially in tumor-induced angiogenesis. The c(RGDyK), an arginine-glycine-aspartic tripeptide sequence, could target specifically to integrin α<sub>v</sub>β<sub>3</sub>-rich tumor cells such as primary hepatocellular carcinoma [21, 22]. As shown in Figure 2, HepG2 cells were exposed to different concentrations of SPION solution. The amount of SPION in the hepatoma cells did not increase with increasing SPION concentration. Similarly, the content of PDA-SPION magnetic nanoparticles in HepG2 cells did not increase with increasing concentration of PDA-SPION magnetic nanoparticles. In contrast to SPION and PDA-SPION, the content of c(RGDyK)-PDA-SPION magnetic nanoparticles in HepG2 cells augmented upon exposure to different concentrations of c(RGDyK)-PDA-SPION magnetic nanoparticle-containing liquid for 24 h (Figure 2).

As shown in Figure 3, HepG2 cells were exposed to 10 μg/mL SPION magnetic particle solution. As the exposure time was prolonged, the content of SPION magnetic nanoparticle did not change significantly in HepG2 cells. Similarly, the content of PDA-SPION magnetic nanoparticles in HepG2 cells exposed to 10 μg/mL PDA-SPION magnetic nanoparticle solution showed no significant changes. The content of c(RGDyK)-PDA-SPION magnetic particles in HepG2 cells did not significantly increase with prolonged exposure to c(RGDyK)-PDA-SPION magnetic particle-containing liquid. Given the surface bonding of SPION magnetic nanoparticles to the specific molecular target c(RGDyK), the targeting effect of c(RGDyK)-PDA-SPION magnetic nanoparticles on liver cancer cells enhanced the enrichment effect of the agent on the cells. This effect may be enhanced by increasing the concentration and extending the exposure time.

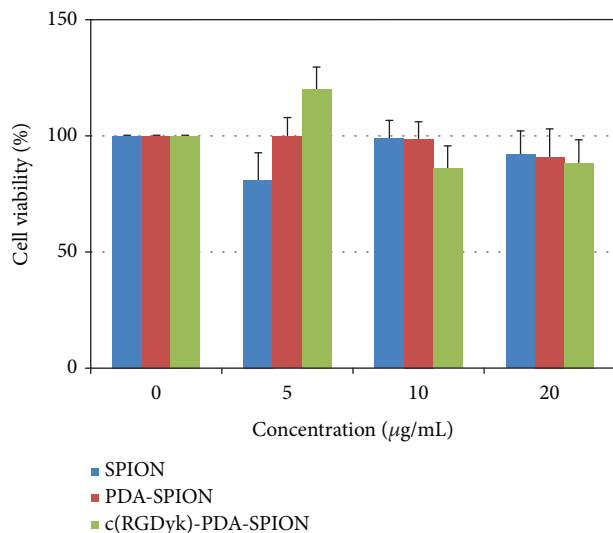


FIGURE 1: The MTT assay on the effects of three magnetic nanoparticles on HepG2 cells. HepG2 cells were exposed to 0, 5, 10, and 20 µg/mL SPION, PDA-SPION, and c(RGDyK)-PDA-SPION magnetic nanoparticles for 24 hours. Three magnetic nanoparticles all showed no significant effects on HepG2 cells.

**3.3.  $T_2$  Relaxation Time of Magnetic Nanoparticles.** The process of nuclei returning from an excited state to an equilibrium state is called relaxation. The time which it takes is called relaxation time. There are two types of relaxation time, namely,  $T_1$  and  $T_2$ .  $T_1$  is spin-lattice or longitudinal relaxation time, and  $T_2$  is spin-spin or transverse relaxation time, which depends on the proton density in the tissues [23]. The magnetic moment and the magnetic susceptibility of SPION are greater than the human body structure. When water molecules diffusing through them and interacting with the proton, the proton transverse magnetization phase changes and accelerates the process of phase, which makes  $T_2$  of the proton shortened [24]. As shown in Table 1, increasing concentrations of the three magnetic nanoparticle contrast agents resulted in decreased  $T_2$  relaxation time. The variation trend in the c(RGDyK)-PDA-SPION contrast group was more pronounced than those of the SPION and PDA-SPION contrast groups. Hence, c(RGDyK)-PDA-SPION exhibited better imaging capability than the two other magnetic nanoparticles and can be used as a good MRI  $T_2$  contrast agent.

**3.4. In Vitro  $T_2$ -Weighted Imaging of Magnetic Nanoparticles.** A  $T_2$ -weighted image highlights the relaxation time  $T_2$  and can be divided into grayscale and pseudo-color images. The grayscale is darker, and the relaxation time  $T_2$  is shorter. The pseudo-color images are bluer, and the relaxation time  $T_2$  is shorter. As shown in Figure 4, the grayscale color progressively darkened, and the color in the pseudo-color image slanted blue with increasing concentration of the three kinds of magnetic nanoparticles. Hence, the shortened  $T_2$  relaxation time corresponded with increasing concentration of the three kinds of magnetic nanoparticles. The imaging pattern of the c(RGDyK)-PDA-SPION

contrast agent group was more prominent than those of the SPION and PDA-SPION contrast agent groups. After SPION coupled with c(RGDyK), aggregation was prevented to a certain extent. The color gradient of the c(RGDyK)-PDA-SPION contrast group consequently became evident, which revealed that it was more suitable than the other particles as  $T_2$  contrast agent.

**3.5. In Vivo MRI Imaging of Magnetic Nanoparticles in Normal Mice.** In the coronal plane  $T_2$ -weighted images (Figure 5), the liver tissue of the normal mice given with the SPION contrast agent began to darken in 30 min (pseudo-color became blue), and the color change was the most obvious after 1 h. The color of the liver tissue faded (pseudo-color blue faded) at 2 h. In the PDA-SPION contrast agent group, changes were observed in the coronal plane  $T_2$ -weighted images of liver tissues compared with those in normal mice 24 h after PDA-SPION was injected via the tail vein. From the gray image, a slight dimming appeared in the liver tissue at 30 min (pseudo-color became blue). The imaging effect was the most obvious at 60 min, and the color of the liver began to fade (pseudo-color blue faded) at 120 min. Finally, the color of the liver tissue was basically restored after 24 h to that before the contrast agent was injected. For the c(RGDyK)-PDA-SPION contrast agent group, changes were noted in the coronal plane  $T_2$ -weighted image of the liver tissues of the normal mice after c(RGDyK)-PDA-SPION was injected through the tail vein. In the gray image, the liver tissue began to darken (pseudo-color became blue) at 30 min, and the color change was the most obvious at 60 min. After 24 h, the color of the liver tissue was basically restored to that before the c(RGDyK)-PDA-SPION contrast agent was injected.

Experimental results showed that the enrichment effects of the three contrast agents on the liver were stronger than that on any other organ. Within 1 h, the maximum concentration of the three types of particles was achieved in the liver; the most obvious color change was also observed in the liver relative to the surrounding tissue. The color change abated and basically recovered after 24 h to the color before the injection. Thus, in the c(RGDyK)-PDA-SPION contrast agent group, the best liver imaging acquisition time was about 1 h. The basic metabolism of the particle in the liver was completed within 24 h. The results provide experimental basis for in vivo study of the c(RGDyK)-PDA-SPION contrast agent in tumor-bearing mice.

**3.6. MRI Imaging of c(RGDyK)-PDA-SPION Contrast Agent in Tumor-Bearing Mice.** As shown in the grayscale and pseudo-color images of Figure 6, after the tail vein injection of c(RGDyK)-PDA-SPION contrast agent,  $T_2$ -weighted imaging of a tumor-burdened mouse liver and tumor showed variation law with prolonged time after injection of the contrast agent into the tumor-burdened mouse liver. The tumor tissues were gray in the grayscale image and bright blue in the pseudo-color image. The gray color of the liver tissue in the grayscale image and the blue color in the pseudo-color images became deepest at 60 min. After 2 h, the gray color of the grayscale image lightened, and the blue color of the

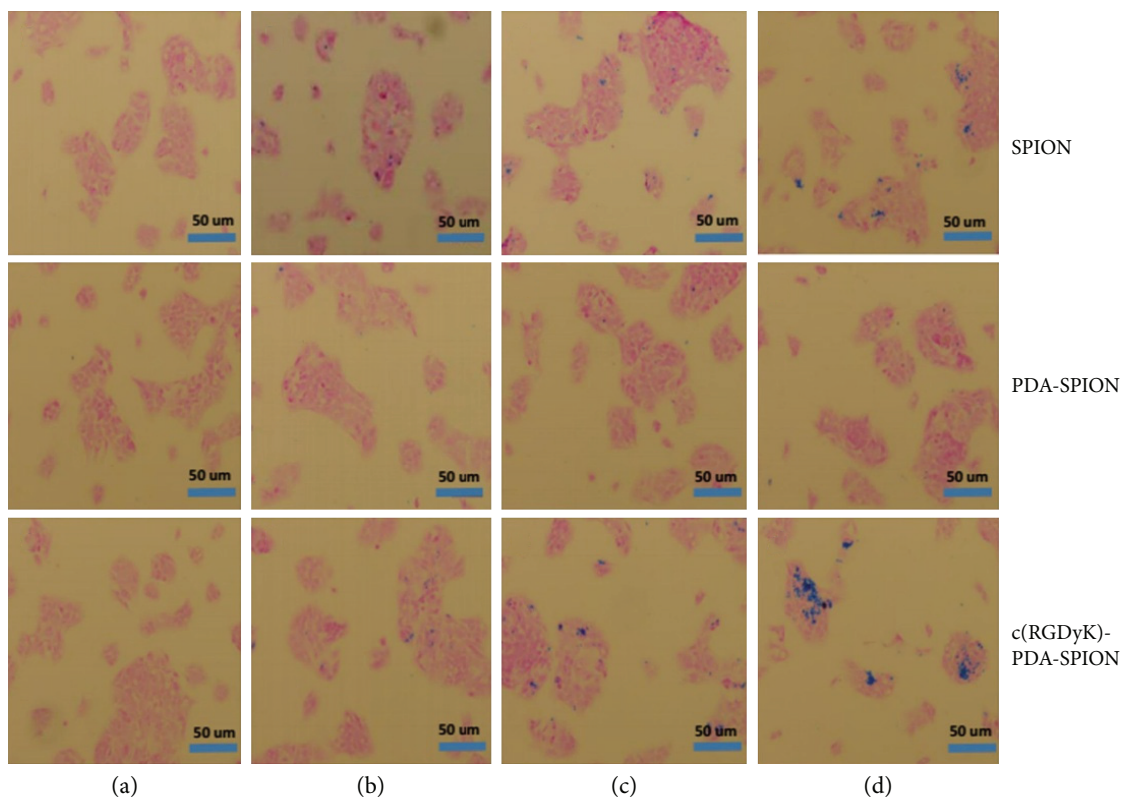


FIGURE 2: HepG2 cells were exposed to 0 (a), 2 (b), 5 (c), and 10 µg/mL (d) SPION, PDA-SPION, and c(RGDyK)-PDA-SPION magnetic nanoparticles for 24 hours. Enrichment results of magnetic nanoparticles in HepG2 cells were detected.

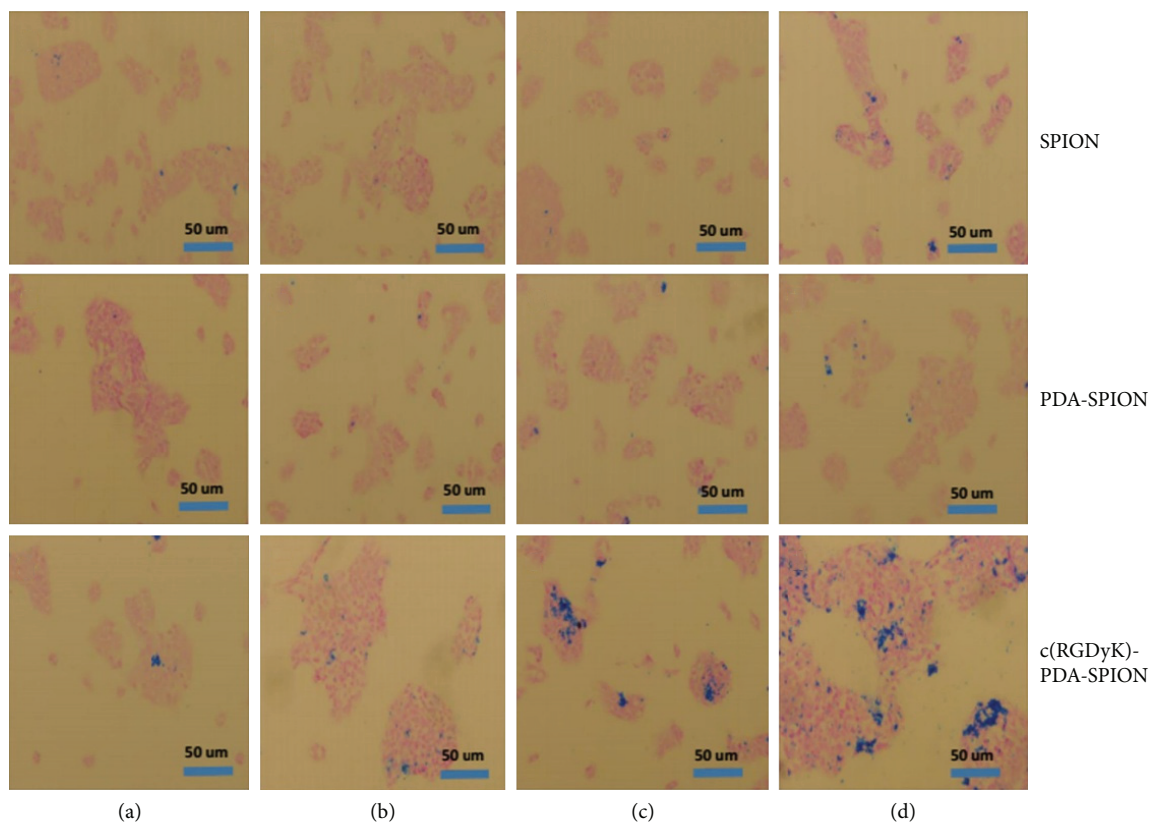
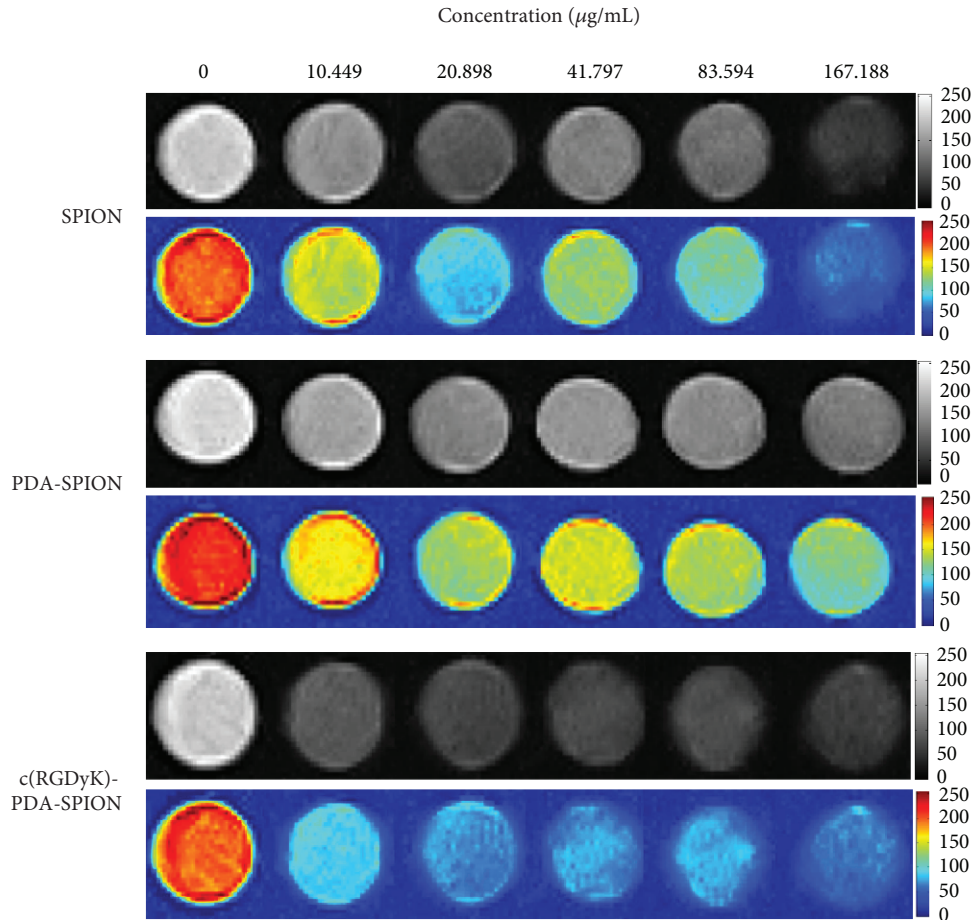


FIGURE 3: HepG2 cells were exposed to 10 µg/mL SPION, PDA-SPION, and c(RGDyK)-PDA-SPION magnetic nanoparticles for 6 (a), 12 (b), 24 (c), and 48 hours (d). Enrichment results of magnetic nanoparticles in HepG2 cells were detected.

TABLE 1:  $T_2$  relaxation time shorten of SPION, PDA-SPION, and c(RGDyK)-PDA-SPION, with the concentrations increasing.

$T_2$ (ms)	Concentration ( $\mu\text{g}/\text{mL}$ )				
	10.449	20.898	41.797	83.594	167.188
SPION group	159.873	116.743	81.228	50.084	29.506
PDA-SPION group	241.383	208.930	120.440	72.596	37.770
c(RGDyK)-PDA-SPION group	94.364	63.525	42.030	22.070	11.692

FIGURE 4: In vitro  $T_2$ -weighted image of three magnetic nanoparticles, namely, SPION, PDA-SPION, and c(RGDyK)-PDA-SPION. In the  $T_2$ -weighted MR image, the c(RGDyK)-PDA-SPION displayed a significant signal reduction with increasing nanoparticle concentration.

pseudo-color images became pale blue; these changes revealed that the c(RGDyK)-PDA-SPION contrast agent in the liver has an optimal imaging time of 60 min. The results and preliminary experimental results were unified.

For tumor tissues in the tumor-bearing mice (Figure 6), the gray color of the grayscale image reached its deepest and the blue color of the pseudo-color images reached the darkest 2 h after tail vein injection. The gray color of the grayscale image lightened, and the blue color of the pseudo-color image became red after 6 h. These results suggest that 2 h may be the best imaging time, which is about 1 h later than that of the liver. Given the growth of tumor inside the skin rather than in in situ liver cancer, the penetration of the c(RGDyK)-PDA-SPION contrast agents into the tumor tissue was difficult through the tumor blood vessels.

This difference delayed the optimal imaging time. The above experimental results need to be further studied in an in situ liver cancer model.

#### 4. Conclusion

In summary, a nanoparticle named c(RGDyK)-PDA-SPION with a particle size of about 50 nm had been successfully prepared in our previous work. In this work, c(RGDyK)-PDA-SPION was further investigated. We found that the c(RGDyK)-PDA-SPION displayed a significant signal reduction with increasing nanoparticle concentration, and they were nontoxic at lower concentrations from 5 to 20  $\mu\text{g}/\text{mL}$ , and they had significant targeting effect of c(RGDyK)-PDA-SPION on liver cancer cells. The animal experiment

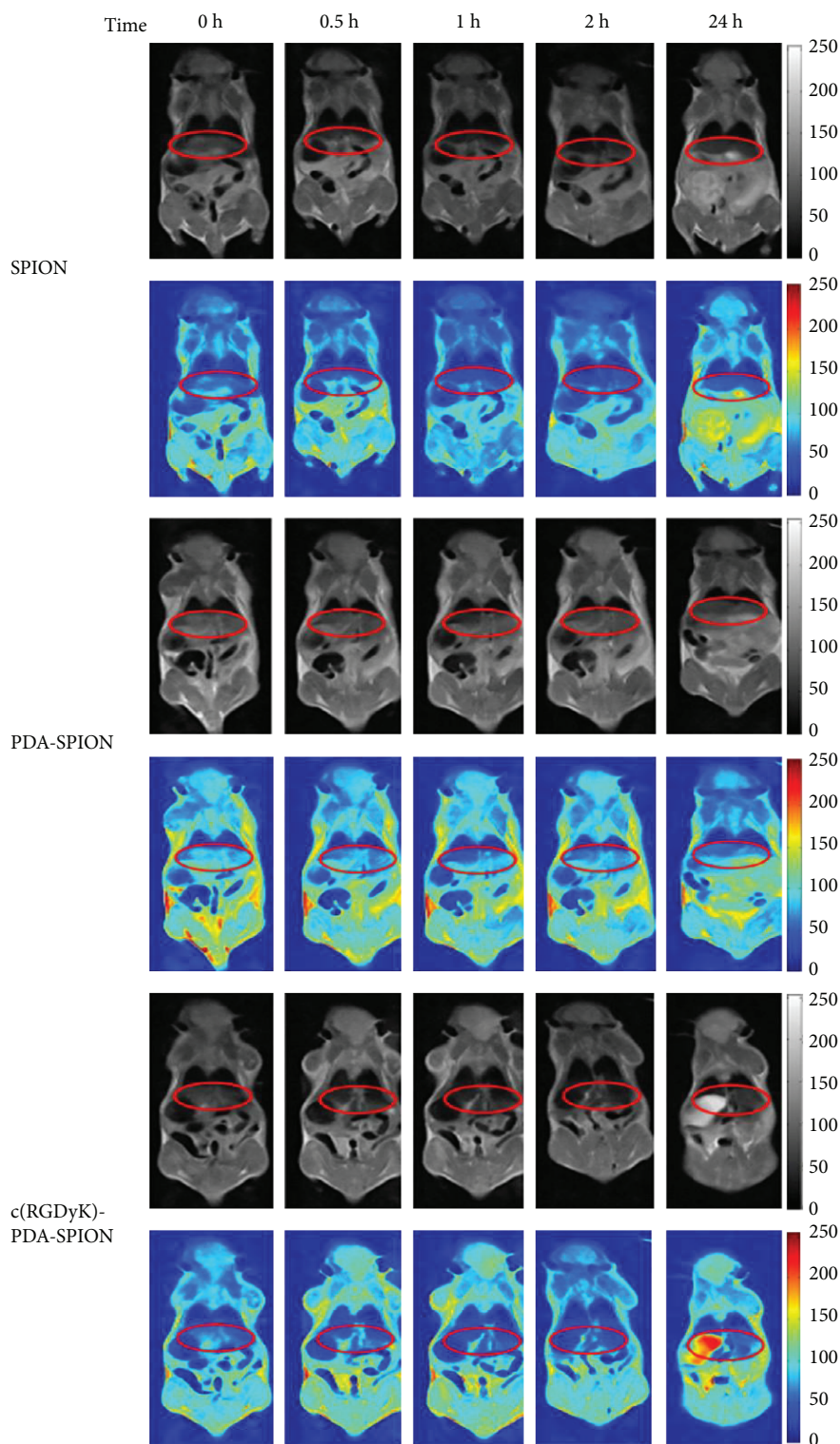


FIGURE 5:  $T_2$ -weighted image of three magnetic nanoparticles, namely, SPION, PDA-SPION, and c(RGDyK)-PDA-SPION. The  $T_2$ -weighted image change of SPION, PDA-SPION, and c(RGDyK)-PDA-SPION on the liver tissue of the normal mice (ellipse labeled as liver). The enrichment effects of the three magnetic nanoparticles on the liver were significant compared to the other organs. At about one hour, the maximum concentration of the three particles accumulated in the liver and was almost completely cleared about 24 hours.

results showed that the maximum concentration of the particles accumulated in the liver was at about one hour, and they were almost completely cleared about 24 hours. Further

animal experiments have shown that they could enhance the MRI  $T_2$ -weighted imaging capability of tumor-burdened, and two hours was probably the best imaging time. Animal

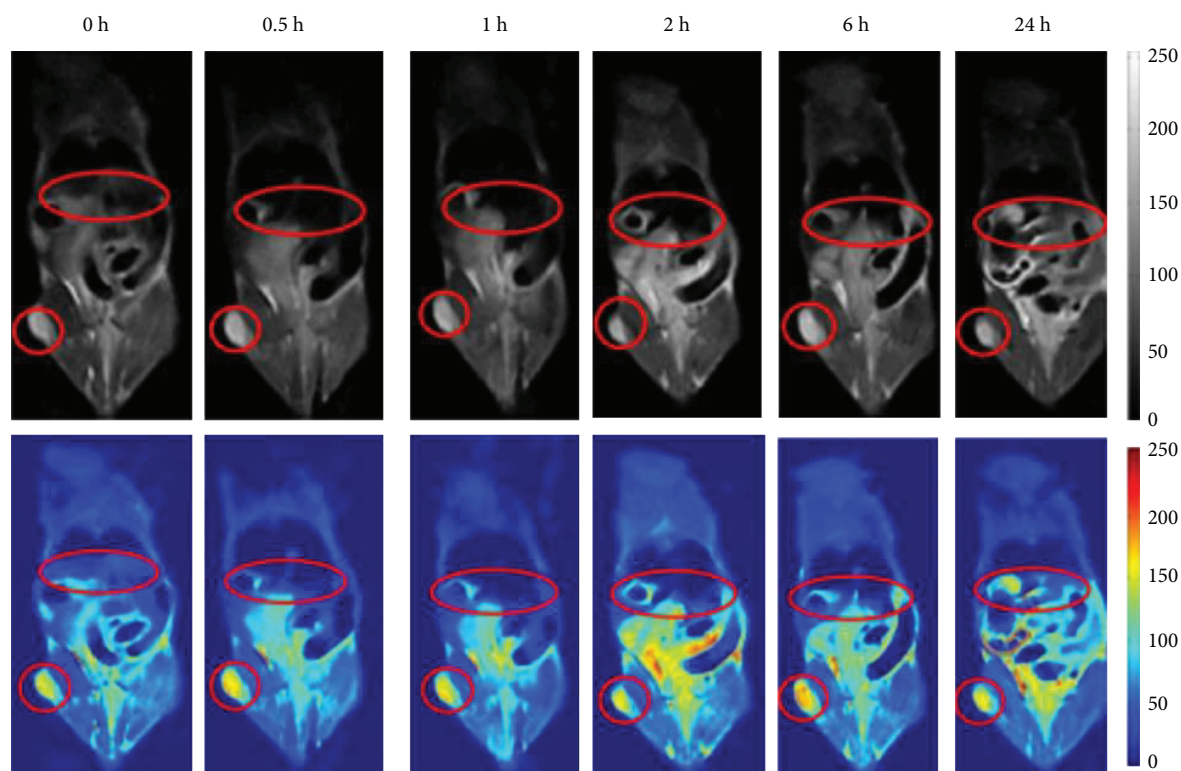


FIGURE 6: C(RGDyK)-PDA-SPION contrast agent tumor-bearing mice with  $T_2$ -weighted image. The  $T_2$ -weighted image changes of C(RGDyK)-PDA-SPION on the liver tissue and the tumor tissue of the tumor-bearing mice (ellipse labeled as liver, circle labeled as tumor). Two hours is probably the best imaging time of C(RGDyK)-PDA-SPION in the tumor, which was about one hour later than the optimal liver imaging time.

experimental data preliminarily proved that this contrast agent can enhance the MRI  $T_2$ -weighted imaging of HepG2 human hepatocellular carcinoma in mice and is a potentially good  $T_2$  contrast agent.

### Data Availability

The figure and table data used to support the findings of this study are included within the article.

### Disclosure

Xinfeng Song and Yancong Zhang are the co-first authors.

### Conflicts of Interest

The authors declare that there is no conflict of interests regarding the publication of this paper.

### Acknowledgments

We are grateful to the National Natural Science Foundation of China (no. 51273033).

### References

- [1] P. C. Lauterbur, "Image formation by induced local interactions: examples employing nuclear magnetic resonance," *Nature*, vol. 242, no. 5394, pp. 190–191, 1973.
- [2] D. Rugar, C. S. Yannoni, and J. A. Sidles, "Mechanical detection of magnetic resonance," *Nature*, vol. 360, no. 6404, pp. 563–566, 1992.
- [3] P. Caravan, J. J. Ellison, T. J. McMurry, and R. B. Lauffer, "Gadolinium(III) chelates as MRI contrast agents: structure, dynamics, and applications," *Chemical Reviews*, vol. 99, no. 9, pp. 2293–2352, 1999.
- [4] T. Kanda, K. Ishii, H. Kawaguchi, K. Kitajima, and D. Takenaka, "High signal intensity in the dentate nucleus and globus pallidus on unenhanced T1-weighted MR images: relationship with increasing cumulative dose of a gadolinium-based contrast material," *Radiology*, vol. 270, no. 3, pp. 834–841, 2014.
- [5] D. A. Stojanov, A. Aracki-Trenkic, S. Vojinovic, D. Benedeto-Stojanov, and S. Ljubisavljevic, "Increasing signal intensity within the dentate nucleus and globus pallidus on unenhanced T1W magnetic resonance images in patients with relapsing-remitting multiple sclerosis: correlation with cumulative dose of a macrocyclic gadolinium-based contrast agent, gadobutrol," *European Radiology*, vol. 26, no. 3, pp. 807–815, 2016.
- [6] T. Kanda, T. Fukusato, M. Matsuda et al., "Gadolinium-based contrast agent accumulates in the brain even in subjects without severe renal dysfunction: evaluation of autopsy brain specimens with inductively coupled plasma mass spectroscopy," *Radiology*, vol. 276, no. 1, pp. 228–232, 2015.
- [7] H. Wei, O. T. Bruns, M. G. Kaul et al., "Exceedingly small iron oxide nanoparticles as positive MRI contrast agents," *Proceedings of the National Academy of Sciences of the United States of America*, vol. 114, no. 9, pp. 2325–2330, 2017.

- [8] H. Yim, S. G. Yang, Y. S. Jeon et al., "The performance of gadolinium diethylene triamine pentaacetate-pullulan hepatocyte-specific T1 contrast agent for MRI," *Biomaterials*, vol. 32, no. 22, pp. 5187–5194, 2011.
- [9] C. U. Herborn, E. Honold, M. Wolf et al., "Clinical safety and diagnostic value of the gadolinium chelate gadoterate meglumine (Gd-DOTA)," *Investigative Radiology*, vol. 42, no. 1, pp. 58–62, 2007.
- [10] T. Grobner, "Gadolinium—a specific trigger for the development of nephrogenic fibrosing dermopathy and nephrogenic systemic fibrosis?," *Nephrology, Dialysis, Transplantation*, vol. 21, no. 4, pp. 1104–1108, 2006.
- [11] W. A. High, R. A. Ayers, J. Chandler, G. Zito, and S. E. Cowper, "Gadolinium is detectable within the tissue of patients with nephrogenic systemic fibrosis," *Journal of the American Academy of Dermatology*, vol. 56, no. 1, pp. 21–26, 2007.
- [12] Y. X. J. Wang, S. M. Hussain, and G. P. Krestin, "Superparamagnetic iron oxide contrast agents: physicochemical characteristics and applications in MR imaging," *European Radiology*, vol. 11, no. 11, pp. 2319–2331, 2001.
- [13] R. Qiao, C. Yang, and M. Gao, "Superparamagnetic iron oxide nanoparticles: from preparations to in vivo MRI applications," *Journal of Materials Chemistry*, vol. 19, no. 35, pp. 6274–6293, 2009.
- [14] A. Zhu, L. Yuan, and T. Liao, "Suspension of Fe<sub>3</sub>O<sub>4</sub> nanoparticles stabilized by chitosan and o-carboxymethylchitosan," *International Journal of Pharmaceutics*, vol. 350, no. 1-2, pp. 361–368, 2008.
- [15] H. G. Silverman and F. F. Roberto, "Understanding marine mussel adhesion," *Marine Biotechnology*, vol. 9, no. 6, pp. 661–681, 2007.
- [16] H. Lee, S. M. Dellatore, W. M. Miller, and P. B. Messersmith, "Mussel-inspired surface chemistry for multifunctional coatings," *Science*, vol. 318, no. 5849, pp. 426–430, 2007.
- [17] H. Lee, Y. Lee, A. R. Statz, J. Rho, T. G. Park, and P. B. Messersmith, "Substrate-independent layer-by-layer assembly by using mussel-adhesive-inspired polymers," *Advanced Materials*, vol. 20, no. 9, pp. 1619–1623, 2008.
- [18] Y. Liao, Y. Wang, X. Feng, W. Wang, F. Xu, and L. Zhang, "Antibacterial surfaces through dopamine functionalization and silver nanoparticle immobilization," *Materials Chemistry and Physics*, vol. 121, no. 3, pp. 534–540, 2010.
- [19] X. Song, X. Gu, H. Sun, C. Fu, Y. Zhang, and P. Dong, "Biomimetic modification and *in vivo* safety assessment of superparamagnetic iron oxide nanoparticles," *Journal of Nanoscience and Nanotechnology*, vol. 16, no. 4, pp. 4100–4107, 2016.
- [20] H. Zhao, J. C. Wang, Q. S. Sun, C. L. Luo, and Q. Zhang, "RGD-based strategies for improving antitumor activity of paclitaxel loaded liposomes in nude mice xenografted with human ovarian cancer," *Journal of Drug Targeting*, vol. 17, no. 1, pp. 10–18, 2009.
- [21] J. Xie, K. Chen, H.-Y. Lee et al., "Ultrasmall c(RGDyK)-coated Fe<sub>3</sub>O<sub>4</sub> nanoparticles and their specific targeting to integrin  $\alpha_v\beta_3$ -rich tumor cells," *Journal of the American Chemical Society*, vol. 130, no. 24, pp. 7542–7543, 2008.
- [22] J.-P. Xiong, T. Stehle, R. Zhang et al., "Crystal structure of the extracellular segment of integrin  $\alpha V\beta 3$  in complex with an Arg-Gly-Asp ligand," *Science*, vol. 296, no. 5565, pp. 151–155, 2002.
- [23] H. A. Resing, "Apparent phase-transition effect in the NMR spin-spin relaxation time caused by a distribution of correlation times," *The Journal of Chemical Physics*, vol. 43, no. 2, pp. 669–678, 1965.
- [24] Y. Gossuin, P. Gillis, A. Hocq, Q. L. Vuong, and A. Roch, "Magnetic resonance relaxation properties of superparamagnetic particles," *Wiley Interdisciplinary Reviews: Nanomedicine and Nanobiotechnology*, vol. 1, no. 3, pp. 299–310, 2009.

## Research Article

# Investigation of the Magnetic Properties of Ferrites in the CoO-NiO-ZnO Using Simplex-Lattice Design

Liliya Frolova <sup>1</sup> and Oleg Khmelenko<sup>2</sup>

<sup>1</sup>Department of Inorganic Materials Technology and Ecology, Ukrainian State University of Chemical Technology, Dnepr/49005, Ukraine

<sup>2</sup>Department Radiophysics, Oles Honchar Dnipro National University, Dnepr/49000, Ukraine

Correspondence should be addressed to Liliya Frolova; 19kozak83@gmail.com

Received 29 August 2018; Accepted 26 October 2018; Published 19 December 2018

Guest Editor: Anil Annadi

Copyright © 2018 Liliya Frolova and Oleg Khmelenko. This is an open access article distributed under the Creative Commons Attribution License, which permits unrestricted use, distribution, and reproduction in any medium, provided the original work is properly cited.

The article is devoted to the analysis of changes in the magnetic characteristics of ferrites in the CoO-NiO-ZnO system by the simplex method. Ferrites of Ni-Zn, Co-Zn, and Co-Ni were synthesized in the form of nanoparticles (20-40 nm) using a new method for processing contact nonequilibrium low-temperature plasma (CNP). The effect of the mutual influence of the contents of different cations on the saturation magnetization and the coercive field was investigated using the simplex-lattice method. A magnetic investigation using a vibrational magnetometer shows that low magnetization values are observed for Ni-Zn ferrites and high for the entire Co-Zn and Co-Ni ferrite series. EPR spectra show that the value of the resonant field and line width corresponds to the value of magnetic saturation and is due to the arrangement of cations on sublattices.

## 1. Introduction

Oxides of composition  $\text{MeFe}_2\text{O}_4$  ( $\text{Me}=\text{Ni}^{2+}, \text{Co}^{2+}, \text{Zn}^{2+}$ ) have important technological properties. For example, ferrites of transition metals with a spinel structure are used as magnetic electrical materials [1, 2] catalysts of a number of reactions [3, 4]. Technological operations for the synthesis of such compounds require, as a rule, the use of high-temperature heat treatment and complex hardware. In this case, both traditional ceramic (from metal oxides) methods and novel technologies are used. For example, in the synthesis of nickel (II) ferrite, cobalt (II) and zinc (II), and hydrothermal methods [5], microwave treatment [6] is used. The attention of chemists is concentrated on the development of new methods for obtaining ferrites of transition materials with a given set of properties. A characteristic trend of recent times is the development of technologies for obtaining nanodispersed ferrites.

It is known that nanosized spinel ferrites exhibit properties and phenomena that cannot be explained on the basis of the structure and properties of the consolidated substance [1, 2]. Thus, the transition of ferrites of transition metals to a nanoscale state is accompanied by a significant change in their magnetic properties (coercive field, magnetization magnitudes, crystallographic anisotropy, and Curie temperature). And their properties essentially depend on the technology of obtaining samples. The authors of [7] point out that the effect of size effects in the synthesis of nanoscale ferrosinels by coprecipitation of salt solutions with the use of additional high-energy short-term exposures is much stronger than in the case of using traditional technologies. The creation of adequate models of the magnetic state of such materials is one of the urgent problems of materials science. This is due both to the wide possibilities of their practical use and to the need to develop theoretical ideas about the effect of dimensional and surface effects on magnetic

properties [8, 9]. There is no unified theory that explains the variation of magnetic properties over a wide range. At present, there are basic theories. The “shell” model gives a qualitative explanation of the effect of decreasing magnetization with decreasing particle sizes. Neel’s theory establishes the dependence of the magnetization on the distribution of cations over the sublattices. A theory is known [10] about the formation of the magnetic properties of nanosized ferrimagnets due to the anisotropy induced by internal elastic microstrains.

The aim of this work is to establish the relationship between the magnetic characteristics of ferrites of the composition  $\text{MeFe}_2\text{O}_4$  (Me-Ni, Co, Zn) and structural characteristics obtained by processing a contact nonequilibrium low-temperature plasma.

## 2. Materials and Methods

In order to reduce energy consumption, temperature, and time of synthesis in the production of ferrites of different composition, in this work, a method of precipitation of hydroxides was used, followed by treatment of the suspension with CNP, washing, and drying.

Reagent grade  $\text{FeSO}_4 \cdot 7\text{H}_2\text{O}$ ,  $\text{NiSO}_4 \cdot 7\text{H}_2\text{O}$ ,  $\text{CoSO}_4 \cdot 7\text{H}_2\text{O}$ , and  $\text{ZnSO}_4 \cdot 7\text{H}_2\text{O}$  were used as the starting materials.

The hydroxide sol which was obtained by alkali precipitation was treated with contact low-temperature nonequilibrium plasma in a laboratory plasma chemical plant, which consists of a single-stage plasma reactor of a discrete type, a step-up transformer, an ignition transformer, and a vacuum pump. After treatment, the resulting precipitate was washed and dried for further investigation. Plasma-chemical treatment of suspensions was carried out in a gas-liquid plasma-chemical reactor of periodic action. The reactor is made of glass and is equipped with an external jacket for thermostating the medium to be treated. Electrodes of stainless steel are placed in the lower and upper part of the reactor.  $40\text{ cm}^3$  of slurry was poured into the reactor; the anode position was adjusted so that the distance between its lower base and the surface of the liquid was 10.0 mm. The plasma column formed as a result of breakdown was a tool for processing. To obtain a plasma discharge, the pressure in the reactor was maintained at 0.08 MPa. Electrodes were supplied with a direct current with a voltage in the range of 500-600 V, the value of which was varied so that the current strength in the circuit was 100-150 mA.

X-ray diffraction patterns of the pigments were obtained on a DRON-2.0 instrument in monochromatized  $\text{Co}_\alpha$  radiation. The lattice parameter was calculated from the Selyakov-Scherrer equation.

The determination of the magnetic characteristics was carried out using a vibration magnetometer. A change in the solution medium was observed at regular intervals using a pH meter-pH-150 MI. EPR spectra were obtained using a Radiopan SE/X-2543 radio spectrometer. The signal strength, the resonant magnetic field, and the signal width were used to characterize the ESR signals.

TABLE 1: Matrix planning of the simplex-lattice design {3,3}.

$N_0$	Co	Ni	Zn	$y_i$
1	1.0	0.0	0.0	$y_1$
2	0.0	1.0	0.0	$y_2$
3	0.0	0.0	1.0	$y_3$
4	0.333	0.667	0.0	$y_{112}$
5	0.667	0.333	0.0	$y_{122}$
6	0.0	0.667	0.333	$y_{223}$
7	0.0	0.333	0.667	$y_{233}$
8	0.333	0.0	0.667	$y_{133}$
9	0.667	0.0	0.333	$y_{113}$
10	0.333	0.333	0.333	$y_{123}$

Simplex-lattice design was used to study the effect of the composition on the properties of ferrites, requiring a minimum number of experiments to study the influence of factors on the selected response functions [11]. The molar concentrations of cobalt, nickel, and zinc cations, respectively, were chosen as factors  $x_1$ ,  $x_2$ , and  $x_3$ . The design of the experiment is shown in Table 1.

The upper and lower limits of each component were distributed as follows:

$$0 \leq x_1 \leq 0.33(\%), \quad (1)$$

$$0 \leq x_2 \leq 0.33(\%), \quad (2)$$

$$0 \leq x_3 \leq 0.33(\%), \quad (3)$$

$$x_1 + x_2 + x_3 = 0.33(\%). \quad (4)$$

Iron cation content is 0.67 (%). Three components of the model recipes changed simultaneously.

When studying the properties of a mixture, depending on the content of the components in it, the factor space can be represented as a regular simplex. An example of a simplex in two-dimensional space is a regular triangle.

For mixtures, the following relation holds:  $\sum_{i=1}^N x_i = 1$ , where  $x_i \geq 0$  is the content of components;  $N$  is the number of components.

If at each vertex of the simplex we take the content of one of the components of the mixture as 1, then in the above-mentioned normalization condition, all the points located inside the two-dimensional regular simplex whose number of vertices equals the number of components of the mixture will satisfy. For example, in our case, this simplex is an equilateral triangle.

To each point of such a simplex, there corresponds a mixture of the corresponding composition, and any combination of the relative content of the components corresponds to a specific point on the simplex.

When planning the experiment in the form of “composition-property” diagrams, it is assumed that the property under investigation is a continuous function of the argument and is described with sufficient accuracy by the

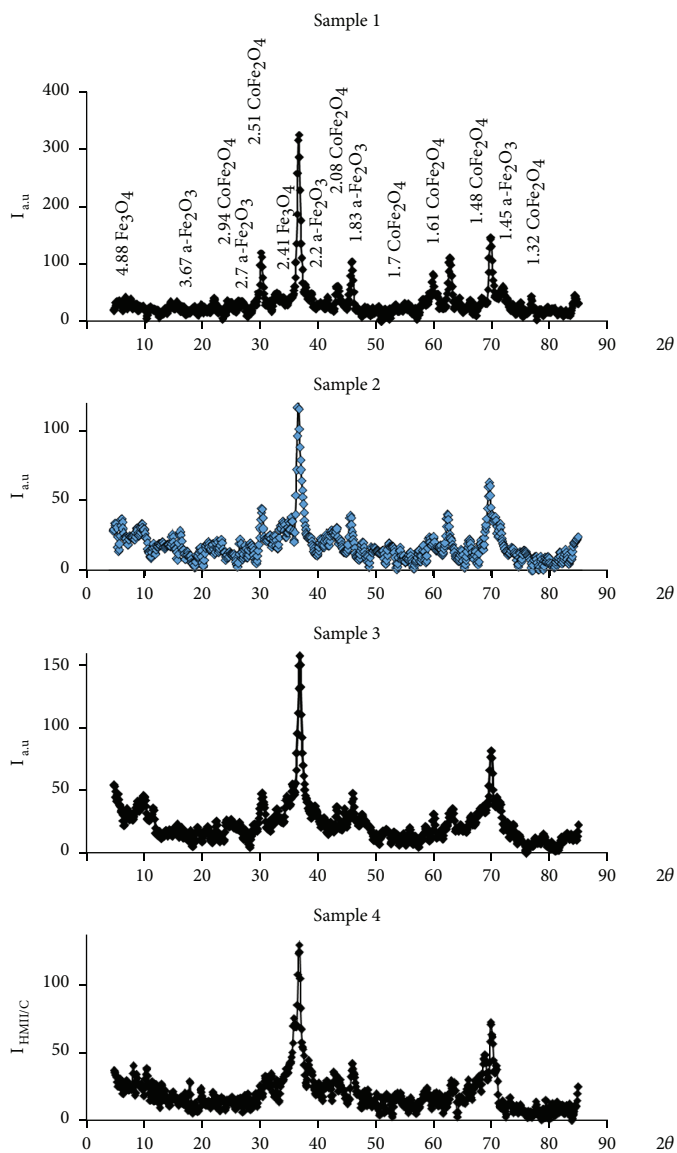


FIGURE 1: X-ray patterns of samples 1-4 (Table 1).

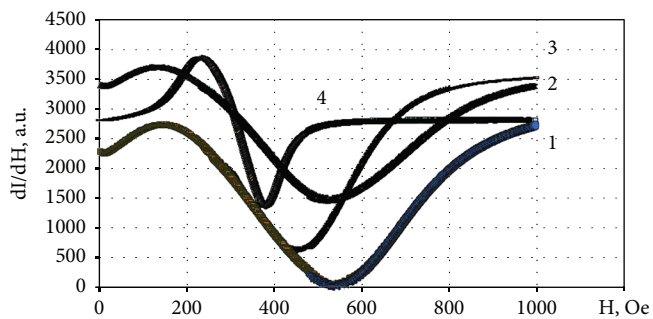


FIGURE 2: EPR spectra for samples 1-4 (Table 1).

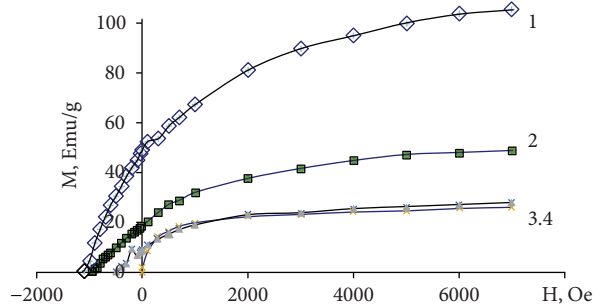


FIGURE 3: Magnetization curves of samples 1-4 (Table 1).

TABLE 2: Characteristics of Co-Zn-Ni ferrites.

N <sup>o</sup>	Composition	H <sub>c</sub>	M <sub>s</sub>	H <sub>R</sub> (mT)	I (a.u)	ΔH <sub>pp</sub> (mT)	a (Å)
1.	CoFe <sub>2</sub> O <sub>4</sub>	1124	105.41	547	2700	398.7	8.35160
2.	Co <sub>0.667</sub> Ni <sub>0.333</sub> Fe <sub>2</sub> O <sub>4</sub>	955	48.76	530	2242	383.65	8.34111
3.	Co <sub>0.333</sub> 7Ni <sub>0.667</sub> Fe <sub>2</sub> O <sub>4</sub>	503	27.80	445	3325	384	8.34016
4.	NiFe <sub>2</sub> O <sub>4</sub>	2	26.05	364	2429	141.5	8.32012
5.	Ni <sub>0.667</sub> Zn <sub>0.333</sub> Fe <sub>2</sub> O <sub>4</sub>	7	19.00	359	3824	63	8.37950
6.	Ni <sub>0.333</sub> Zn <sub>0.667</sub> Fe <sub>2</sub> O <sub>4</sub>	9	7.70	345	3693	29.71	8.42310
7.	ZnFe <sub>2</sub> O <sub>4</sub>	19	3.93	342	3008	21.83	8.36890
8.	Co <sub>0.333</sub> Zn <sub>0.667</sub> Fe <sub>2</sub> O <sub>4</sub>	1	37.26	382	2538	156	8.37950
9.	Co <sub>0.667</sub> Zn <sub>0.333</sub> Fe <sub>2</sub> O <sub>4</sub>	70	74.94	501	1121	366	8.34870
10.	Co <sub>0.333</sub> Zn <sub>0.333</sub> Ni <sub>0.333</sub> Fe <sub>2</sub> O <sub>4</sub>	37	5.37	358	3189	122	8.38530

H<sub>c</sub> is the coercive field; M<sub>s</sub> is the saturation magnetization; H<sub>R</sub> is the resonance field of the EPR spectrum, mT; ΔH<sub>p</sub> is the line width between the points of maximum slope on the EPR spectrum, mT; I is the intensity of the EPR line of the spectrum, a.u.; a is the lattice parameter, Å.

polynomial. The response surfaces in multicomponent systems have a complicated form and, for an adequate description of them, the necessary polynomials of a high degree.

For three-component mixtures, we write down a possible polynomial ( $n = 3$ )

$$y = \beta_1 x_1 + \beta_2 x_2 + \beta_3 x_3 + \beta_{12} x_1 x_2 + \beta_{13} x_1 x_3 + \beta_{23} x_2 x_3 + \gamma_{12} x_1 x_2 (x_1 - x_2) + \gamma_{13} x_1 x_3 (x_1 - x_3) + \gamma_{23} x_2 x_3 (x_2 - x_3) + \beta_{123} x_1 x_2 x_3. \quad (5)$$

Calculation of the coefficients in the regression equation and checking its adequacy were carried out using the program STATISTICA 12.

The response surface in the composition-property diagrams was represented using isolines. The response functions were coercive field (H<sub>c</sub>), saturation magnetization (M<sub>s</sub>), resonant field (H<sub>R</sub>), width of the EPR peak (ΔH<sub>pp</sub>), and intensity of the EPR peak of the spectrum (I, a.u.).

### 3. Results and Discussion

The magnetic properties of ferrites obtained under the action of CNP on the suspension of iron(II) and Me(II) polyhydroxides complexes are dependent on the pH of the solution of the iron(II) salt or the Fe(OH)<sub>2</sub> suspension, the temperature of the reaction medium, the rate of oxidation, its activity and efficiency distribution in the reaction medium, and the concentration of iron(II) ions in the solution or iron(II) hydroxide in suspension [12–15]. But one of the most important factors is the cationic composition of ferrites [16–22]. In accordance with the simplex method, ten samples were synthesized and their properties were investigated.

Better samples are shown in Figures 1, 2, and 3. All results are shown in Table 2.

Mathematical processing of the experimental data using the program STATISTICA 12 allowed obtaining regression

equations adequately describing the relationship between the magnetic indices and the composition of prototypes.

$$I_{\bar{n}} = 1124.0x_1 + 749.81x_1x_2 - 2409.19x_1x_3 + 523.69x_1x_2(x_1 - x_2) - 2023.50x_1x_3(x_1 - x_3) - 4305.38x_1x_2x_3, \quad (6)$$

$$M_s = 106x_1 + 26x_2 - 125x_1x_2 + 57911x_2x_3 - 174445x_1x_2x_3 - 173732x_2x_3(x_2 - x_3). \quad (7)$$

The resulting regression equations were used to construct isolines of the magnetic characteristics of ferrites in the factorial space under study (Figures 3 and 4).

The highest value of the coercive field corresponds to the composition containing the maximum number of cobalt cations. An increase in the content of cobalt cations leads to an increase in the coercive field in all compositions. A positive effect of nickel cations on the saturation magnetization of ferrites along the side of the triangle Ni-Zn and opposite on the Ni-Co side was also observed (Figure 4).

Moreover, the value of the saturation magnetization depends more on the content of cobalt cations. The highest magnetic indices correspond to the maximum content of cobalt. Thus, magnetic ferrites with an increased coercive field correspond to compositions 1,2,3, and magnetic ferrites with low coercive field 4,5,6,7. In the diagrams, an equilateral triangle with coordinates of the vertices of Co (1,0,0) -Ni (0.75,0,0) -Zn (0.25,0,0) can be identified, which corresponds to a region of higher values of the saturation magnetization.

Comparison of the main characteristics on the EPR spectra with magnetic properties makes it possible to explain the mechanism of action and to establish the contribution of the presence of ferrimagnetic cations and the degree of inversion of spinel. X-ray phase analysis showed that the samples contain the ferromagnetic phase probably MeFe<sub>2</sub>O<sub>4</sub> and antiferromagnetic α-Fe<sub>2</sub>O<sub>3</sub>.

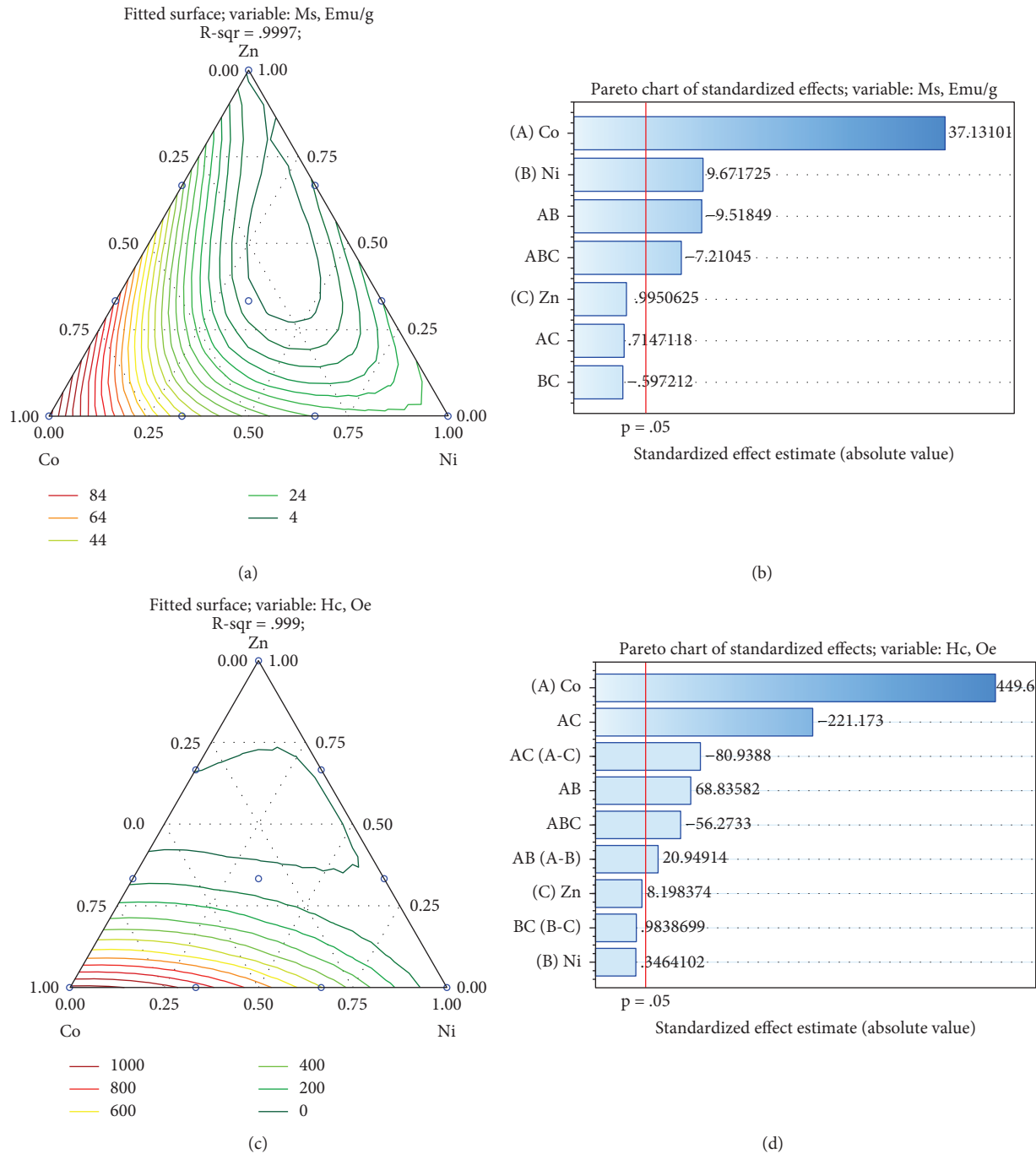


FIGURE 4: Dependence of the saturation magnetization (a) and the coercive field (c) on the composition and the corresponding Pareto diagrams (b), (d).

The magnetic characteristics correspond to the data of X-ray phase analysis and EPR data (Figures 4 and 5).

All EPR spectra have a symmetric broad resonance signal, but their line width ( $\Delta H_{pp}$ ) and resonant magnetic field ( $H_R$ ) are very different (Table 2). It can be seen from Figures 5(a) and 5(b) that there is an increase in the resonance field and a change in the line width with an increase in the molar concentration of cobalt and nickel cations. It is seen that  $\Delta H_{pp}$  is narrow; the intensity of the peaks is larger

for a higher concentration of Zn. The spectrum of the cobalt ferrite sample shows a rather wide signal ( $\Delta H_{pp} = 398.7$  mT). It is interesting that the effect of cobalt cations on the main characteristics of the EPR spectrum is much more significant than that of nickel. Consider the equation [21]

$$\Delta H_{pp} = \frac{K_1}{2M_s} + 4\pi M_s \frac{p}{1-p} + H_c + H_{id}, \quad (8)$$

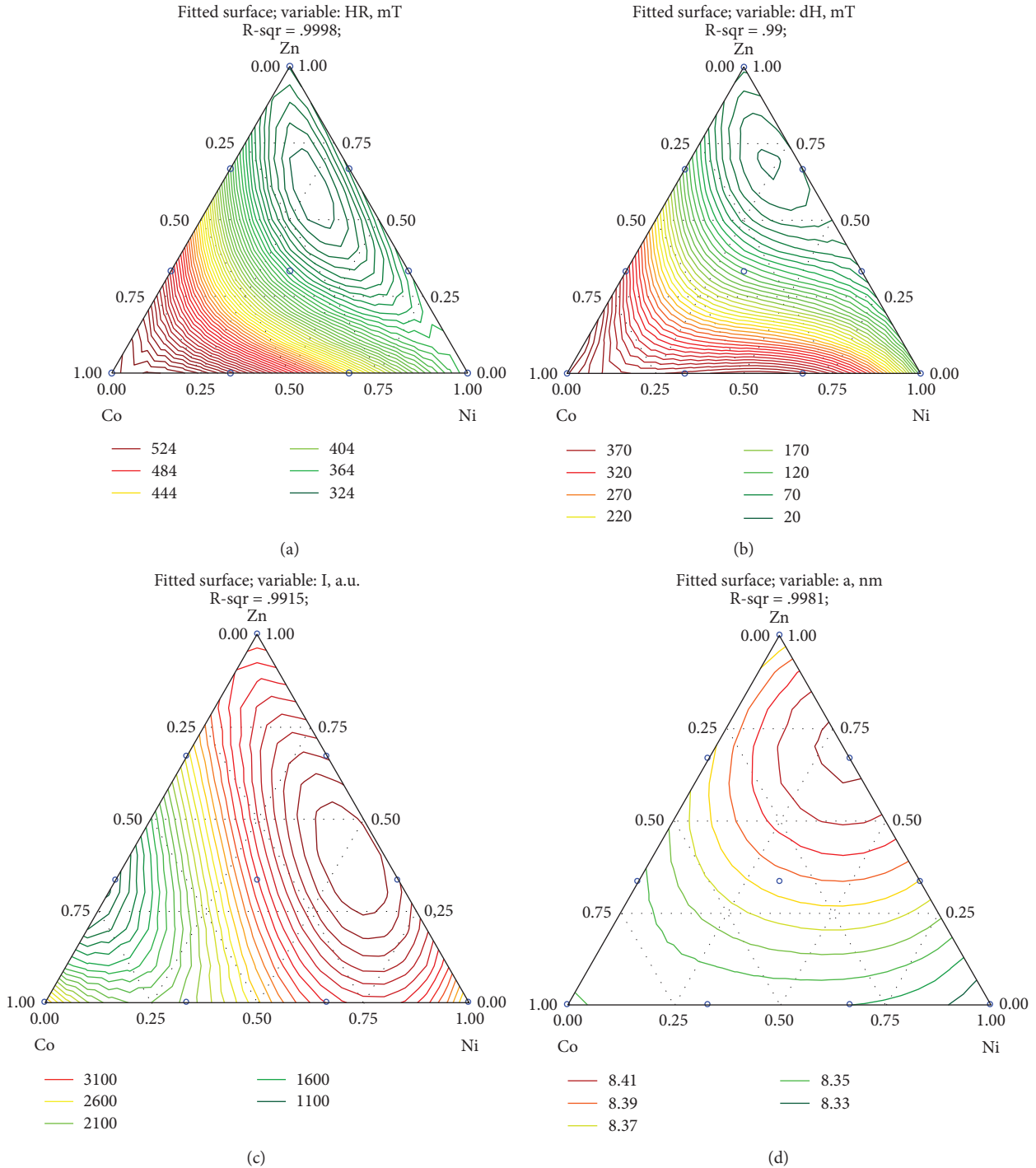


FIGURE 5: Dependence of the resonant field  $H_R$  (a), the width of the ESR peak  $\Delta H_{\max}$  (b), the intensity of the ESR peak of the spectrum  $I$  (c), and the lattice parameter of the composition (d).

where  $\Delta H_{pp}$  is the width of the EPR line of the spectrum,  $K_1$  is the anisotropy,  $p$  is the porosity,  $H_e$  is the noneddy currents, and  $H_{id}$  is the inhomogeneous demagnetization.

Earlier studies have shown that the magnetic parameters of ferrites, in the system CoO-NiO, -ZnO, depend on the composition. An increase in the cobalt content in the system leads to an increase in the coercive field and

the saturation magnetization. The increase in the content of cobalt cations in ferrites from 0 to 1.0 mol. shares causes a significant increase in the coercive field from 2-3 to 1140 Oe. This fact is confirmed by a shift in the values of the lattice parameter  $d$  (8.35 Å) to a region of lower values (8.32 Å) as well as an increase in the bandwidth on the EPR spectrum.

From the values of coercivity ( $H_c$ ) and saturation magnetization ( $M_s$ ), the value of the anisotropy constant  $K_1$  can be calculated using the following relation:

$$K_1 = \frac{H_c M_s}{0.96}. \quad (9)$$

Then

$$\Delta H_{pp} = \frac{H_c}{1.82} + 4\pi M_s \frac{p}{1-p} + H_e + H_{id}. \quad (10)$$

Taking into account that the largest value of the anisotropy constant corresponds to cobalt-containing ferrites, the contribution of the first term to equation (6) is the greatest. This determines a fairly broad peak of the EPR spectrum for samples 1-3.

The composition-property diagrams for the value of the resonance field and the line width correlate with the diagram for magnetic saturation. The resonant magnetic field increases with increasing content in cobalt and nickel samples. Reducing the width of the line, i.e., the narrowing of the derivative of the resonance signal with increasing content of  $Zn^{2+}$  and  $Ni^{2+}$  is associated with various causes. For zinc cations, first of all, these are their diamagnetic properties. For  $Ni^{2+}$  ions, this can be caused by their redistribution along sublattices and a decrease in the magnetic moment of the sublattice B, taking into account the vacancies formed. This causes a general decrease in the magnetic moment. In accordance with this, a decrease in the resonant field for nickel ferrite occurs in accordance with formula

$$H_r = 2\omega \frac{(M_\Sigma)_A - (M_\Sigma)_B}{(M_{sp})_A - (M_{sp})_B}. \quad (7)$$

With an increase in the content of zinc cations, an increase in the intensity of the peaks and their narrowing are observed. Since the anisotropy constant for zinc ferrite is the smallest, it can be assumed that this is primarily due to the decrease of the first term in equation (6); the second term is also small, so the total value is also small. In these systems, the concentration of diamagnetic  $Zn^{2+}$  ions plays a decisive role. The existing dependence of  $H_{pp}$  on the concentration of Zn is due to the superexchange interaction between  $Ni^{2+}$  and  $Fe^{2+}$  through nonmagnetic  $O^{2-}$  ions.

Almost complete coincidence of the isolines for the graphs  $M_s = f(Ni, Co, Zn)$  and  $H_r = f(Ni, Co, Zn)$  makes it possible to assume that the main factor determining the ferrite magnet is the cation distribution over the sublattices with allowance for the concentration of diamagnetic ions.

#### 4. Conclusions

The article is devoted to the analysis of changes in the magnetic characteristics of ferrites in the  $Fe_2O_3$ -CoO-ZnO system by the simplex method. Ferrites of Ni-Zn, Co-Zn, and Co-Ni were synthesized in the form of nanoparticles using a new method for processing contact nonequilibrium low-temperature plasma. The crystalline, magnetic, and

microstructure of the finished crystallites were elucidated using several methods. The macroscopic characteristics of magnetic materials are inherently rooted in their atomic structure. Understanding the crystal structure is necessary for the synthesis of magnetic nanomaterials with optimal properties. For spinel ferrites, in particular, the choice of a bivalent cation and its distribution between the tetrahedral and octahedral sites directly determine their magnetic behavior. The effect of the mutual influence of the content of different cations on the saturation magnetization and the coercive field was investigated using the simplex-lattice method. A magnetic investigation using a vibrational magnetometer shows that under these synthesis conditions, low magnetization values for Ni-Zn ferrites and high magnetization values for the whole Co-Zn and Co-Ni ferrite series are observed. The EPR spectra show that the value of the resonant field and line width corresponds to the value of the magnetic saturation. In this work, a new method of synthesis of combustion is the nanoferrite used to produce Ni-Zn. The EPR spectra of ferrites are explained on the basis of superexchange interaction.

#### Data Availability

Previously described method simplex-lattice design was used to support this study and is available at <https://books.google.com.ua/>. This prior study is cited at the relevant place within the text as reference [11].

#### Conflicts of Interest

The authors declare that they have no competing interests.

#### References

- [1] A. B. Gadkari, T. J. Shinde, and P. N. Vasambekar, "Ferrite gas sensors," *IEEE Sensors Journal*, vol. 11, no. 4, pp. 849–861, 2011.
- [2] W. Hu, N. Qin, G. Wu, Y. Lin, S. Li, and D. Bao, "Opportunity of spinel ferrite materials in nonvolatile memory device applications based on their resistive switching performances," *Journal of the American Chemical Society*, vol. 134, no. 36, pp. 14658–14661, 2012.
- [3] L. Živanov, M. Damjanović, N. Blaž, A. Marić, M. Kisić, and G. Radosavljević, "Soft ferrite applications," in *Magnetic, Ferroelectric, and Multiferroic Metal Oxides*, pp. 387–409, Elsevier, 2018.
- [4] V. M. Chernyshev and N. P. Shabelskaya, "Comparative analysis of catalytic activity in complex NiO-CuO- $Fe_2O_3$ - $Cr_2O_3$  Oxide system of different production technologies," *Materials Science Forum*, vol. 870, pp. 118–122, 2016.
- [5] R. S. Melo, P. Banerjee, and A. Franco, "Hydrothermal synthesis of nickel doped cobalt ferrite nanoparticles: optical and magnetic properties," *Journal of Materials Science: Materials in Electronics*, vol. 29, no. 17, pp. 14657–14667, 2018.
- [6] L. A. Frolova and A. A. Pivovarov, "Investigation of conditions for ultrasound-assisted preparation of nickel ferrite," *High Energy Chemistry*, vol. 49, no. 1, pp. 10–15, 2015.
- [7] L. A. Frolov, A. A. Pivovarov, A. S. Baskevich, and A. I. Kushnerev, "Structure and properties of nickel ferrites

- produced by glow discharge in the  $\text{Fe}^{2+}$ - $\text{Ni}^{2+}$ - $\text{SO}_4^{2-}$ - $\text{OH}^-$  system,” *Russian Journal of Applied Chemistry*, vol. 87, no. 8, pp. 1054–1059, 2014.
- [8] R. N. Bhowmik and K. S. Aneeshkumar, “Low temperature ferromagnetic properties, magnetic field induced spin order and random spin freezing effect in  $\text{Ni}_{1.5}\text{Fe}_{1.5}\text{O}_4$  ferrite; prepared at different pH values and annealing temperatures,” *Journal of Magnetism and Magnetic Materials*, vol. 460, pp. 177–187, 2018.
- [9] G. Avramovic-Cingara, J. Zweck, J. D. Giallonardo, G. Palumbo, and U. Erb, “Magnetic domain structure in nanocrystalline nickel electrodeposits,” *Journal of Applied Physics*, vol. 123, no. 23, pp. 234301–234301, 2018.
- [10] R. N. Bhowmik, R. Ranganathan, R. Nagarajan, B. Ghosh, and S. Kumar, “Role of strain-induced anisotropy on magnetic enhancement in mechanically alloyed  $\text{Co}_{0.2}\text{Zn}_{0.8}\text{Fe}_2\text{O}_4$  nanoparticle,” *Physical Review B*, vol. 72, no. 9, 2005.
- [11] J. A. Cornell, *Experiments with Mixtures: Designs, Models, and the Analysis of Mixture Data*, vol. 403, John Wiley & Sons, 2011.
- [12] C. Singh, S. Bansal, and S. Singhal, “Synthesis of  $\text{Zn}_{1-x}\text{Co}_x\text{Fe}_2\text{O}_4$ /MWCNTs nanocomposites using reverse micelle method: investigation of their structural, magnetic, electrical, optical and photocatalytic properties,” *Physica B: Condensed Matter*, vol. 444, pp. 70–76, 2014.
- [13] M. Sundararajan, L. John Kennedy, and J. Judith Vijaya, “Synthesis and characterization of cobalt substituted zinc ferrite nanoparticles by microwave combustion method,” *Journal of Nanoscience and Nanotechnology*, vol. 15, no. 9, pp. 6719–6728, 2015.
- [14] A. Manikandan, L. J. Kennedy, M. Bououdina, and J. J. Vijaya, “Synthesis, optical and magnetic properties of pure and Co-doped  $\text{ZnFe}_2\text{O}_4$  nanoparticles by microwave combustion method,” *Journal of Magnetism and Magnetic Materials*, vol. 349, pp. 249–258, 2014.
- [15] I. Zālīte, G. Heidemane, A. Krūmiņa, D. Rašmane, and M. Maiorov, “ $\text{ZnFe}_2\text{O}_4$  containing nanoparticles: synthesis and magnetic properties,” *Materials Science and Applied Chemistry*, vol. 34, no. 1, pp. 38–44, 2017.
- [16] K. Sun, Z. Pu, Y. Yang et al., “Rietveld refinement, microstructure and ferromagnetic resonance linewidth of iron-deficiency NiCuZn ferrites,” *Journal of Alloys and Compounds*, vol. 681, pp. 139–145, 2016.
- [17] M. Su, C. Liao, T. Chan et al., “Incorporation of cadmium and nickel into ferrite spinel solid solution: X-ray diffraction and X-ray absorption fine structure analyses,” *Environmental Science & Technology*, vol. 52, no. 2, pp. 775–782, 2018.
- [18] T. R. Tatarchuk, N. D. Paliychuk, M. Bououdina et al., “Effect of cobalt substitution on structural, elastic, magnetic and optical properties of zinc ferrite nanoparticles,” *Journal of Alloys and Compounds*, vol. 731, pp. 1256–1266, 2018.
- [19] B. Thangjam and I. Soibam, “Structural, electrical and magnetic properties of Mg doped Ni-Cu-Zn nanoferrites synthesized by citrate precursor method,” *International Journal of Applied Engineering Research*, vol. 12, no. 23, pp. 13201–13206, 2017.
- [20] M. T. Jamil, J. Ahmad, S. H. Bukhari et al., “Effect on structural and optical properties of Zn-substituted cobalt ferrite  $\text{CoFe}_2\text{O}_4$ ,” *Journal of Ovonic Research*, vol. 3, no. 1, pp. 45–53, 2017.
- [21] C. M. Srivastava and M. J. Patni, “Ferromagnetic relaxation processes in polycrystalline magnetic insulators,” *Journal of Magnetic Resonance*, (1969), vol. 15, no. 2, pp. 359–366, 1974.
- [22] R. N. Bhowmik, S. Kazhugasalamoorthy, R. Ranganathan, and A. K. Sinha, “Tuning of composite cubic spinel structure in  $\text{Co}_{1.75}\text{Fe}_{1.25}\text{O}_4$  spinel oxide by thermal treatment and its effects on modifying the ferromagnetic properties,” *Journal of Alloys and Compounds*, vol. 680, pp. 315–327, 2016.

## Research Article

# Directional Control of the Structural Adsorption Properties of Clays by Magnetite Modification

**Tetiana A. Dontsova** <sup>1</sup>, **Elena I. Yanushevskaya**,<sup>1</sup> **Svitlana V. Nahirniak**,<sup>1</sup>  
**Oksana V. Makarchuk** <sup>1</sup>, **Andrei I. Ivanets**,<sup>1</sup> **Marina Yu Roshchina**,<sup>1</sup>  
**Anastasiya S. Kutuzova**,<sup>1</sup> and **Leonid M. Kulikov**<sup>2</sup>

<sup>1</sup>*Department of Inorganic Substances, Water Purification and General Chemical Technology, National Technical University of Ukraine "Igor Sikorsky Kyiv Polytechnic Institute", Kyiv 03056, Ukraine*

<sup>2</sup>*Department of Fine Inorganic Synthesis, Thermodynamics and Kinetics of Heterophase Processes, Institute for Problems of Materials Science, National Academy of Sciences of Ukraine, Kyiv 03142, Ukraine*

Correspondence should be addressed to Tetiana A. Dontsova; dontsova@xtf.kpi.ua

Received 7 August 2018; Accepted 27 September 2018; Published 16 December 2018

Guest Editor: Vidyadhar Singh

Copyright © 2018 Tetiana A. Dontsova et al. This is an open access article distributed under the Creative Commons Attribution License, which permits unrestricted use, distribution, and reproduction in any medium, provided the original work is properly cited.

This article presents the results of the study on the effect of nanomagnetite modification on textural characteristics of clay matrices, adsorption properties, and parameters of the spent sorbents separation. The nitrogen adsorption-desorption method has shown that the obtained magnetic nanocomposite sorbents have large specific surface areas (in 1.2–2 times more) than the initial clays due to the formation of the secondary porous structure on the surface and in macropores of clay matrices. The best adsorption properties with respect to dyes belong to magnetic sorbents with nanomagnetite content of 7 wt.%. The additional modification of the third phase of graphene-like molybdenum disulphide into magnetic sorbents leads to the significant increase in the sorption capacity of both cationic (up to 1100 mg/g) and anionic (up to 1830 mg/g) dyes. The conducted investigations of the total acidity and acid-base sites on the surface of clay, magnetite-modified clay, and molybdenum disulfide-modified magnetic sorbent indicate the significant influence of the Lewis base sites on the adsorption properties of these materials.

## 1. Introduction

The nanotechnology and nanochemistry of magnetic materials are one of the most actively developing areas of modern nanoscience, which in recent years has been attracting increasing attention from researchers from various fields in chemistry, physics, biology, and medicine [1]. Magnetic nanoparticles of the size from 5 to 100 nm have a significant application potential in biomedicine, magnetic resonance imaging, data storage systems, various detectors and immunoassay systems, magnetically controllable fluids, environmental chemical engineering, etc. In the latter case, magnetic nanoparticles are used as sorbents or catalysts in their pure form or as a component of composite material to

extract toxic pollutant (organic, heavy metal ions, etc.) substances from the aqueous medium [2–4].

In recent years, there has been an active search for methods and approaches aimed at creating new, efficient, and magnetically controllable composite sorption materials of broad functional purpose. The most promising method for creating magnetic sorbents today is the impregnation of various sorption matrices by magnetic nanoparticles [5, 6], which is simple in implementation and not expensive. This method is usually used for the creating sorption materials of water purification. Another popular method is layer-by-layer functionalization of magnetic nanoparticles [7, 8]. The functionalization is used mainly for the synthesis of magnetic sorbents for analytical purposes. At the same time,

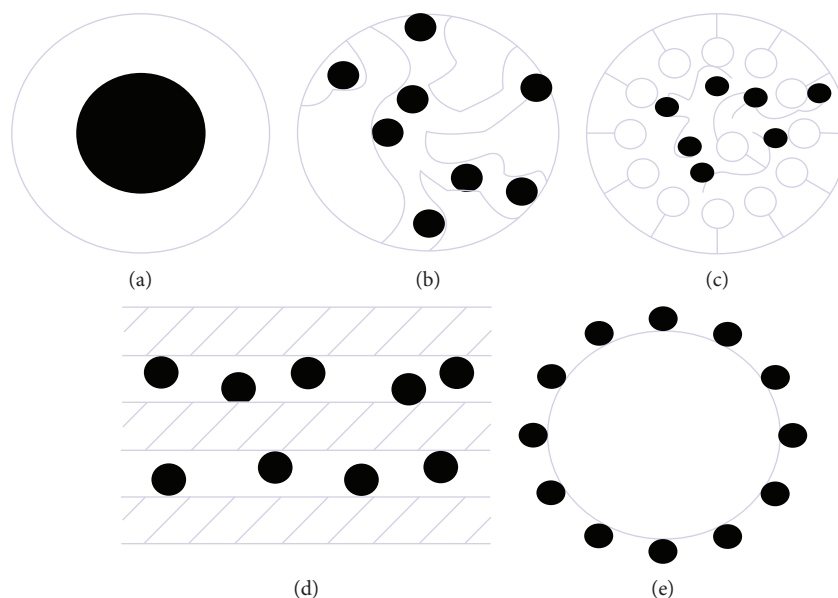


FIGURE 1: Methods of magnetic composite sorbents forming: (a) core-shell structure, (b) based on carbon materials, (c) based on polymers, (d) surface modification of clay minerals, and (e) nonporous particles, for example, metal oxides.

publications in this field, the number of which increases every year, indicate that the search continues and is still far from its completion.

An overwhelming number of publications is devoted to the synthesis and use of magnet-containing sorbents with a core-shell structure (see Figure 1(a)), which are obtained by noncovalent or covalent immobilization of various inorganic or organic compounds on the surface of previously synthesized iron oxide nanoparticles [9]. There is also a lot of research, e.g., [10–12], on the synthesis and application of magnetic composite carbon or polymer-based sorption materials with incorporated iron oxide nanoparticles (see Figures 1(b) and 1(c)). One of the most promising methods of obtaining magnetic nanocomposite sorbents include surface modification of various sorption materials by nanoscale magnetic iron oxide particles, predominantly  $\text{Fe}_3\text{O}_4$  (see Figures 1(d) and 1(e)). This is associated with the almost unlimited opportunity to modify sorption properties of the obtained magnetic nanocomposites due to the variation of their structure whilst maintaining the relative simplicity and cheapness of their synthesis [13, 14].

From this point of view, the magnetic sorbents based on clay minerals are of great scientific and practical interest, since they combine unique sorption properties and low cost of clays with the possibility of their rapid separation from the suspension after the sorption process is completed by means of the magnetic field. A lot of publications are devoted to magnetic sorbents with the matrix made of bentonite, montmorillonite, kaolin, zeolite, and other clays which are usually synthesized using the method of coprecipitation [15–21].

However, in the literature, there are no comparative investigations of various approaches to obtaining such magnetic sorption nanomaterials. In [22], we carried out comparative research on the influence of the synthesis method (mechanical mixing, coprecipitation, and impregnation) on

the sorption properties of magnetic nanocomposites using saponite clay as a clay mineral. We have shown that simple impregnation method is more efficient than the other mentioned methods as the obtained materials had better sorption characteristics towards dye contains at low concentrations in aqueous solutions. Also, effective and inexpensive nanocomposite sorbents based on palygorskite and spondyl clay were obtained using impregnation. These synthesized materials were characterized by high sorption capacity towards dyes, surfactants, and polyphosphates of various natures [23, 24].

Thus, further research is needed in the field of directed modification of clay materials with nanomagnetite in order to identify structural and sorption parameters that will lead to the creation of new, efficient, and magnetically controllable composite sorbents.

In this research, data are presented on the change in the adsorption and textural characteristics of clay matrices depending on the magnetite content; the amount of the modifier on the magnetic separation process and the moisture content of waste sorbents; and the influence of the third-phase presence (nanomolybdenum disulphide) in the magnetic mineral sorbent on its adsorption and textural properties. Thus, we attempted to analyze the possibility of directed modification of the adsorption and textural properties of various clay matrices modified with nanomagnetite by a simple impregnation method.

## 2. Materials and Methods

**2.1. Magnetic Composite Clay Sorbents.** Magnetic composite clay sorbents were synthesized by the method of impregnation of the corresponding clay minerals (saponite, palygorskite, and spondyl clay of Ukrainian deposits) with freshly prepared  $\text{Fe}_3\text{O}_4$ -based magnetic fluid. The method of magnetic fluid and clay-based magnetic nanocomposite synthesis is presented in detail in [23, 24]. It has been shown that

TABLE 1: Synthesized clay-based magnetic nanocomposites.

Sample	Clay mineral	Magnetite content in the composite (wt.%)
Sap7	Saponite	7
Sap10		10
Pal7	Palygorskite	7
Pal10		10
Spo7	Spondyl clay	7
Spo10		10

regardless of the composition (see Table 1), the obtained magnetic composite mineral sorbents contain magnetite with a particle size of up to 10 nm [25].

The nanocomposite with better sorption properties was additionally modified with graphene-like MoS<sub>2</sub>, nanoparticles of which had the following characteristics: average dimensions  $d[013] = 2.9(2)$  nm,  $d[110] = 10.4(6)$  nm; unit cell parameters  $a = 0.3135(1)$  nm,  $c = 1.258(1)$  nm; and the estimated average number of S-Mo-S nanolayers  $n \sim 4$  [26]. The modification of Sap7 was carried out in an aqueous suspension using an ultrasonic bath (44 kHz) for 30 minutes. The suspension was then filtered, and after that, the obtained precipitate was dried. The synthesized Sap7-MoS<sub>2</sub> sample contained 1 wt.% of molybdenum disulphide and 99 wt.% of Sap7.

**2.2. Adsorption of Dyes on Magnetic Nanocomposite Sorbents.** The adsorption properties of magnetic sorbents based on different clay minerals were investigated by the static adsorption of dyes of various natures. The concentration of dyes was determined using a UV/Vis spectrophotometer. The characteristics of dyes are presented in Table 2.

Sorption properties were investigated as described in [23, 24]. The equilibrium adsorption capacities ( $Q_e$ ) were calculated according to the following equation:

$$Q_e = \frac{(C_e - C_0) \cdot V}{m}, \quad (1)$$

where  $C_0$  and  $C_e$  are the initial and equilibrium concentrations of the dyes in the solution, respectively, in  $\text{mg} \cdot \text{l}^{-1}$ ;  $V$  is model solution volume, in l; and  $m$  is the mass of sorbent sample, in g.

**2.3. Magnetic Separation.** Magnetic separation of spent sorbents was carried out in a pyramidal magnetic module with magnetic field intensity over the height of the settling tank from 20 mT to 220 mT [25]. The residual concentration of the suspended particles of the spent magnetic sorbent was determined by turbidimetric method using a UV/Vis spectrophotometer. The moisture content of the obtained precipitate of the spent sorbent was investigated by gravimetric analysis.

**2.4. Structural Adsorption Characteristics of Magnetic Nanocomposite Sorbents.** The adsorption and textural characteristics of the obtained materials were carried out by low-temperature nitrogen adsorption-desorption method

( $T = 77$  K) on Quantachrome Autosorb (Nova 2200e). The specific surface area was calculated using Brunauer–Emmett–Teller (BET) equation. Adsorption pore volumes ( $V_{sp}$  ads) were calculated using a single point method. The pore size distribution of the mesopores was determinate by Barrett–Joyner–Halenda (BJH) method.

**2.5. Acid-Base Properties of Magnetic Sorbent Surface.** The total acidity of the surface was evaluated from the pH value of the isoionic point ( $\text{pH}_{\text{iip}}$ ) by potentiometric method. 25 cm<sup>3</sup> of double-distilled water was introduced into the potentiometric cell, and after the stabilization of the glass-combined electrode potential, 0.25 g of the sample was added. After certain periods of time, the pH of the suspension was measured under constant stirring. Thus, the curves of pH change over time were obtained, which reflect the acid-base state of the surface.

Investigation of the surface active sites distribution with respect to the acid-base properties was carried out with the help of Hammett method using 9 indicators with pKa values in the range of  $-0.29$  to  $12.8$ . For this purpose, the optical density of the indicators' initial solutions with a concentration of 2.5 mg/l ( $D_0$ ) was measured on a UV/Vis spectrophotometer. After that, the sorbent suspensions were prepared in these solutions ( $\sim 0.02$  g of sorbent sample, 2 ml the indicators' initial solutions, and 3 ml of distilled water), and after reaching the adsorption equilibrium and subsequent decantation, the optical density ( $D_1$ ) was measured. In order to take into account the influence of medium pH change on optical density caused by the contact between the solution and the sorbent, similar suspensions were prepared in distilled water ( $\sim 0.02$  g of sample and 3 ml of water), and after 120 minutes, an indicator initial solution was added to the decantate and the optical density ( $D_2$ ) was measured. Optical density of the solutions was determined in glass cuvettes (10 mm) at the wavelength corresponding to the maximum adsorption of the indicator solution. The content of active sites with a specific acidic strength ( $q$ ,  $\text{mkg/g}$ ) was calculated according to the following equation:

$$q = \frac{C_i \cdot V_i}{D_0} \cdot \left[ \frac{|D_0 - D_1|}{m_1} \pm \frac{|D_0 - D_2|}{m_2} \right], \quad (2)$$

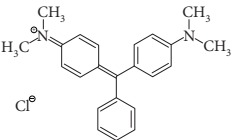
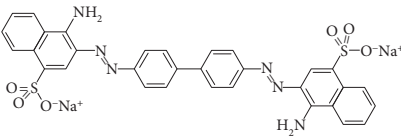
where  $C_i$  and  $V_i$  are the concentration and volume of the indicator,  $\text{mkg} \cdot \text{l}^{-1}$  and l, respectively, and  $m_1$  and  $m_2$  are the masses of sorbent sample during measurements of  $D_1$  and  $D_2$ , g.

### 3. Results and Discussion

**3.1. Structural Sorption Properties and Sorption Capacities in Relation to Dyes of Magnetic Nanocomposites.** The synthesized magnetic nanocomposites based on saponite, palygorskite, and spondyl clays initially were investigated for the determination the structural sorption properties by nitrogen adsorption-desorption method and the adsorption properties with respect to dyes of various natures.

Figures 2, 3, and 4 show the isotherms of adsorption-desorption in nitrogen for initial clays and clay-based

TABLE 2: Characteristics of dyes.

Dye	Structural formula	Nature dye	D (nm)
Malachite green		Cationic	1.33
Congo red		Anionic	2.52

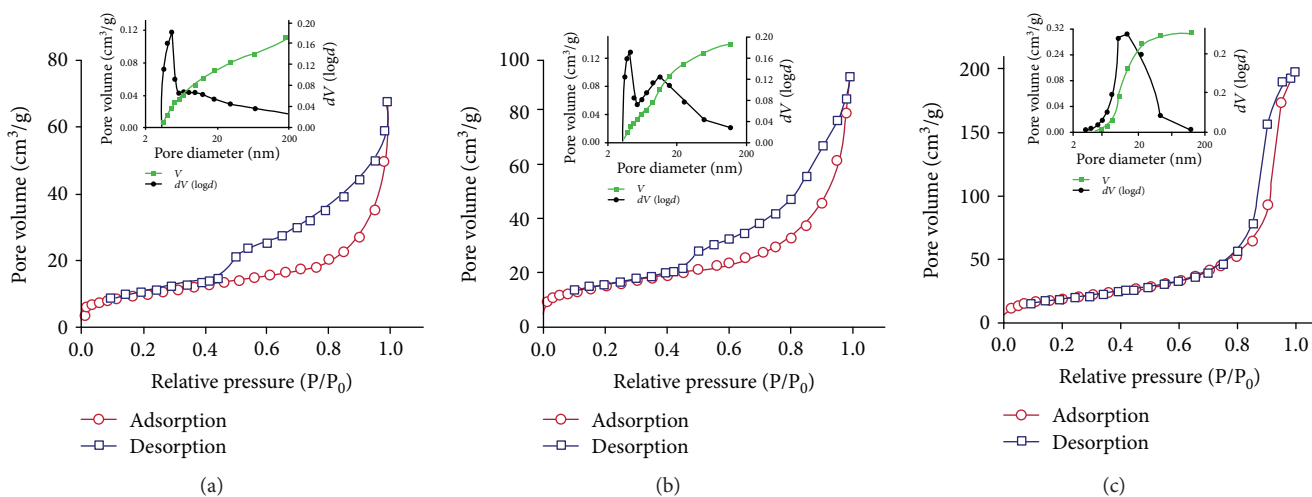


FIGURE 2: Nitrogen adsorption-desorption isotherms for saponite (a), Sap7 (b), and Sap10 (c).

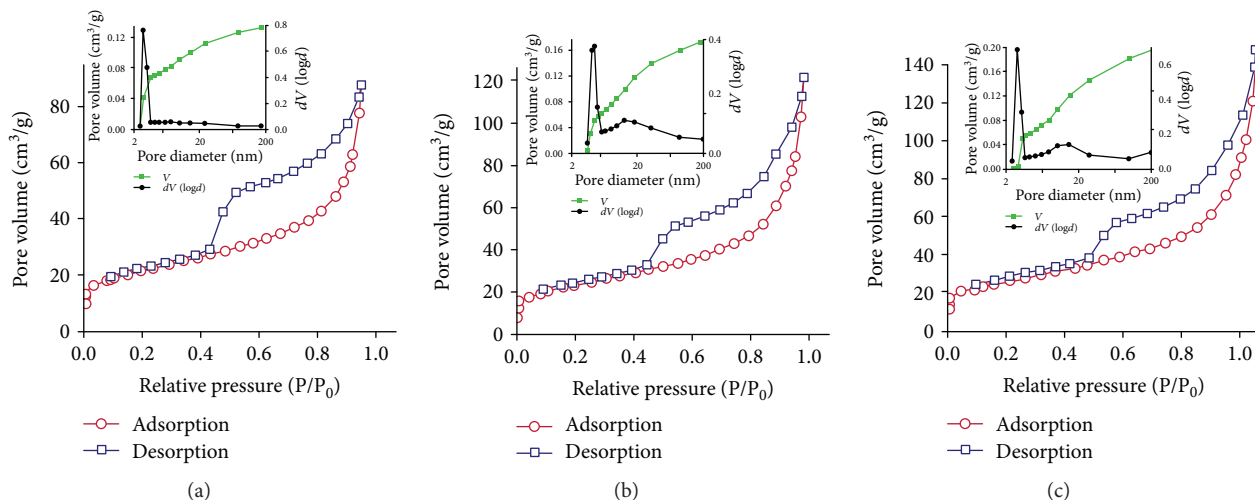


FIGURE 3: Nitrogen adsorption-desorption isotherms for palygorskite (a), Pal7 (b), and Pal10 (c).

magnetic nanocomposites. As it can be seen from the figures, all the presented isotherms refer to the IV type (according to IUPAC classification) that is typically of mesoporous

materials [27]. All investigated initial clays (Figures 2(a), 3(a), and 4(a)) are characterized by the average pore size in the range of 4 nm.

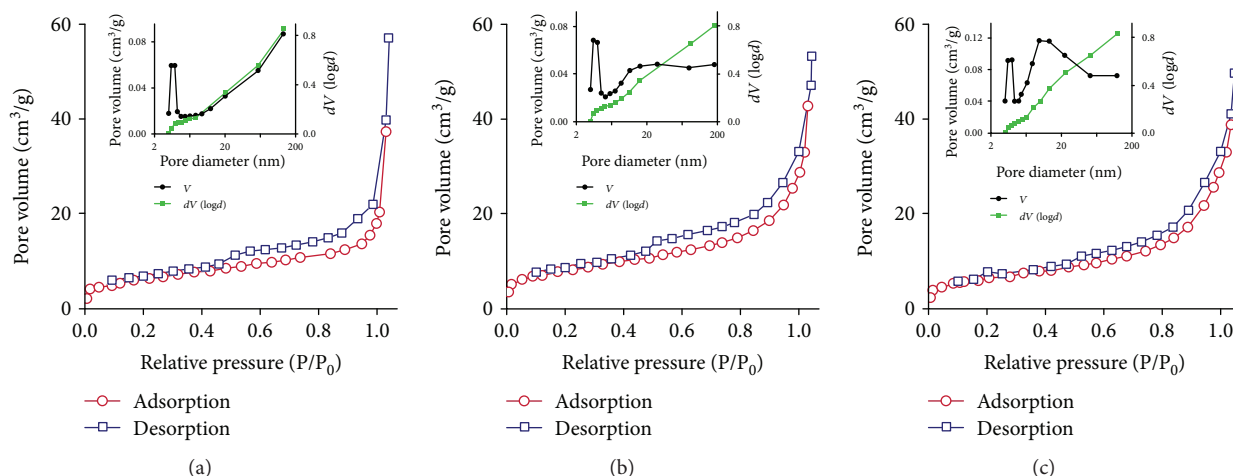


FIGURE 4: Nitrogen adsorption-desorption isotherms for spondyl slay (a), Spo7 (b), and Spo10 (c).

From the isotherms shown in Figure 2, it can be seen that the modification of saponite with magnetite has a significant effect on the adsorption and texture characteristics of composites. Thus, during the transition from the initial sample of saponite to the composites with a content of magnetite 7 wt.% and 10 wt.%, a change in the capillary-condensation hysteresis loop from H3 through the hybrid type H1 + H3 to H1 is observed. This indicates the predominant presence of cylindrical pores in the initial sample of saponite that are open on both sides, which are typical of the materials with a layered structure formed by parallel packed lamellar particles. The transition to a hybrid type of hysteresis loop for the composite with 7 wt.% was probably caused by the deposition and partial blocking of cylindrical pores by magnetite nanoparticles. This is confirmed by the shape of nitrogen adsorption-desorption isotherm of the Sap10 sample with 10 wt.% of magnetite, for which spontaneous filling of pores is observed in the range of high relative pressures,  $p/p_0$  0.9–1.0, which is typical of deadlock cylindrical pores. A similar effect was observed during adsorption of strontium ions on layered manganese oxide [28].

The increase in the BET specific surface area from  $35 \text{ m}^2/\text{g}$  to  $69 \text{ m}^2/\text{g}$  during the transition from the initial saponite to the Sap7 and Sap10 composites is caused by the presence of magnetite nanoparticles with a developed surface in their structure, which is confirmed by the transition of monomodal pore size distribution with a maximum of 4 nm for the initial clay to bimodal pore size distribution for composites with a second maximum for pores with size in the range of about 15–18 nm. At the same time, for a sample with a maximum magnetite content in Sap10, the maximum at 18 nm becomes predominant. Along with the growth of the specific surface area, the modification of saponite with nanoparticles of magnetite is accompanied by an increase in the pore volume from  $0.11 \text{ cm}^3/\text{g}$  to  $0.31 \text{ cm}^3/\text{g}$ , which is also caused by precipitation of magnetite with a developed porous structure. Thus, the modification of saponite clay with magnetite leads to the increase in the specific surface area and pore volume, as well as bimodal pore size

distribution due to the formation of a secondary porous structure on the surface of native clay.

Textural characteristics of palygorskite after modification with magnetite change less significantly. For all samples, H3 type of capillary-condensation hysteresis is observed that is typical of adsorbents with layered structure and open pores of cylindrical shape. At the same time, adsorption properties (specific surface area and pore volume) of palygorskite change in a similar way as the samples based on saponite clay. The addition of magnetite also increases the specific surface area from  $73 \text{ m}^2/\text{g}$  for palygorskite to  $82 \text{ m}^2/\text{g}$  and  $84 \text{ m}^2/\text{g}$  and pore volume from  $0.13 \text{ cm}^3/\text{g}$  to  $0.18 \text{ cm}^3/\text{g}$  and  $0.20 \text{ cm}^3/\text{g}$  for Pal 7 and Pal 10, respectively. On the pore size distribution curves, along with the maximum at 4 nm, an insignificant second peak appears with a maximum of about 18 nm. It is obvious that changes in adsorption characteristics are associated with the formation of the secondary porous magnetite structure, while preservation of textural characteristics is caused by the absence of pores blocking the initial palygorskite during the precipitation of magnetite for Pal 7 and Pal 10 samples.

Sorbent samples based on spondyl clay are characterized by similar H2 type of hysteresis loop that is typical of slit-like pores, regardless of the magnetite content. Although spondyl clay is characterized by a predominantly average mesopore size of 4 nm, macropores (see Figure 4(a)) are also present in its structure. With the increase in magnetite content, an insignificant increase in the adsorption characteristics is observed, namely, specific surface area increases from  $21 \text{ m}^2/\text{g}$  to  $31 \text{ m}^2/\text{g}$  and  $37 \text{ m}^2/\text{g}$  and pore volume from  $0.08 \text{ cm}^3/\text{g}$  to  $0.09 \text{ cm}^3/\text{g}$  and  $0.12 \text{ cm}^3/\text{g}$  for the initial spondyl clay and Spo7 and Spo10 composites, respectively. It should be noted that similar to the cases considered above, the modification with magnetite also leads to the formation of the secondary porous structure on the surface of spondyl clay macropores with an average mesopore diameter of 20 nm, the amount of which increases with the increase of the  $\text{Fe}_3\text{O}_4$  modifier.

Thus, different regularities of the adsorption and textural characteristics change of composites are observed that depend

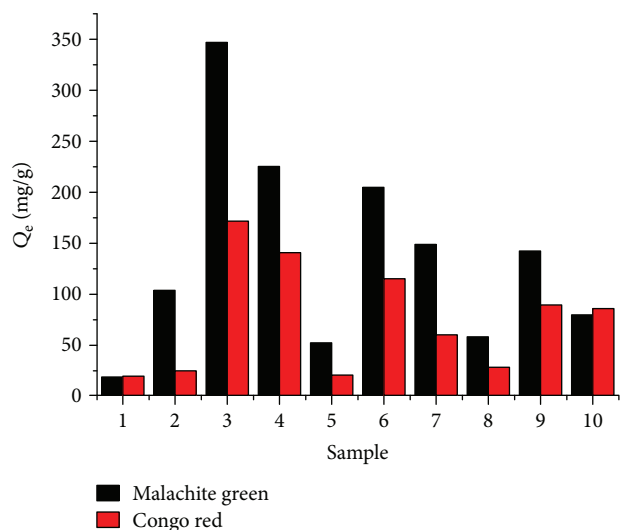


FIGURE 5: Sorption capacities of the sorbent samples regarding malachite green and Congo red: 1—magnetite, 2—saponite, 3—Sap7, 4—Sap10, 5—palygorskite, 6—Pal7, 7—Pal10, 8—spondyl clay, 9—Spo7, 10—Spo10.

on the type and porous structure of the initial clay. In all cases, the introduction of magnetite into the structure of clay minerals leads to the formation of the secondary porous structure and is accompanied by an increase in the specific surface area and pore volume of nanocomposite materials.

Sorption capacities of all native clays, as well as clay-based magnetic nanocomposites and magnetite with respect to malachite green and Congo red, are shown in Figure 5. According to the diagram shown in Figure 5, saponite-based sorbents demonstrate the best sorption properties in both dyes, which are characterized by larger surface areas than spondyl clay-based samples and smaller surface areas than palygorskite-based sorbents. In all cases, when clays are modified with magnetite, sorption properties are improved and the largest capacity is observed for magnetic sorbents with magnetite content of 7 wt.%. It should be noted that in spite of blocking the initial pores of the saponite, Sap10 is still quite active with regard to dyes of various natures.

An additional investigation of magnetite sorption properties has shown that it has the lowest sorption capacity with respect to both dyes. The highest sorption capacity (350 mg/g and 170 mg/g with respect to malachite green and Congo red, respectively) belongs to the magnetic nanocomposite sorbent based on saponite clay Sap7.

Thus, it is possible to establish a synergetic effect when nanomagnetite is introduced into a clay matrix in all cases.

**3.2. Magnetic Separation of the Spent Magnetic Sorbents.** Such important technological parameters as residual concentration of sorbent particles for a certain time period and humidity of precipitation were investigated after magnetic separation of spent sorbents.

The results of investigations of the spent sorbents separation using magnetic separation in the magnetic module are presented in Figure 6. The figure shows the residual

concentrations of suspended particles of clays and clay-based magnetic sorbents in the solution after 30-minute magnetic separation, and the moisture of the precipitates after their separation from the solution to be purified.

As it can be seen from Figure 6, in all cases, that the modified clays (positions 2 and 3) are separated from the solution 5 times faster than native clay materials. Moisture content of spent magnetic sorbent precipitates is at least 3.5 times lower than that of clay minerals.

The studies above indicate a significant perspective on the creation of magnetic nanocomposite sorbents based on natural clay matrices, which, as shown, are characterized by better textural characteristics and adsorption properties than natural clays. Also, their use will make it possible to get much faster separation of spent sorbents from the solution and obtain precipitates with lower moisture content.

So, based on the obtained results on textural characteristics, adsorption properties, and technological parameters for the investigation of additional modification with graphene-like particles of molybdenum disulphide, magnetic nanocomposite sorbent Sap7 was chosen.

**3.3. Effect of MoS<sub>2</sub> Modification on Sorption and Acid-Base Properties of Magnetic Nanocomposite Based on Sap7.** The change in the sorption activity of the magnetic sorbent Sap7 after its modification with molybdenum disulphide, as well as comparison with the initial saponite clay, is shown in Figure 7.

As it can be seen from Figure 7, an additional modification of the magnetic sorbent Sap7 with molybdenum disulphide results in a significant increase in the sorption capacity, namely, the sorption capacity of Sap7-MoS<sub>2</sub> with respect to malachite green is 1100 mg/g that is 11 times and 3.2 times higher than the same for saponite and Sap7, respectively. The sorption capacity of Sap7-MoS<sub>2</sub> with respect to Congo red is significantly higher and is at the level of 1830 mg/g that is 62 and 10.4 times more than the same for saponite and Sap7, accordingly.

The increase in the sorption capacity of Sap7-MoS<sub>2</sub> for both dyes cannot be explained only by changes in their textural characteristics. In our opinion, such sudden leap of the sorption capacity can be caused either by the appearance of additional surface active centers on the surface of the magnetic composite material or by the photocatalytic activity of the third-phase molybdenum disulphide in the composition of the magnetic nanocomposite Sap7-MoS<sub>2</sub>, which reveals in the visible light area [29]. In order to determine the first assumption, investigations were carried out concerning the total acidity of the surface and the distribution of surface centers along the acid-base properties of these three samples.

Figure 8 shows the pH changes of the sorbent suspension in double-distilled water over time for saponite, Sap7, and Sap7-MoS<sub>2</sub>. As it can be seen from the figure, in all cases, Lewis base centers predominate. After reaching the equilibrium, the value of the isoionic point for saponite, Sap7, and Sap7-MoS<sub>2</sub> was 9.3, 8.4, and 9.1, respectively. The steady-state pH values indicate the base state of the surface of all the investigated samples. Moreover, saponite is characterized by the highest basicity while Sap7 by the lowest.

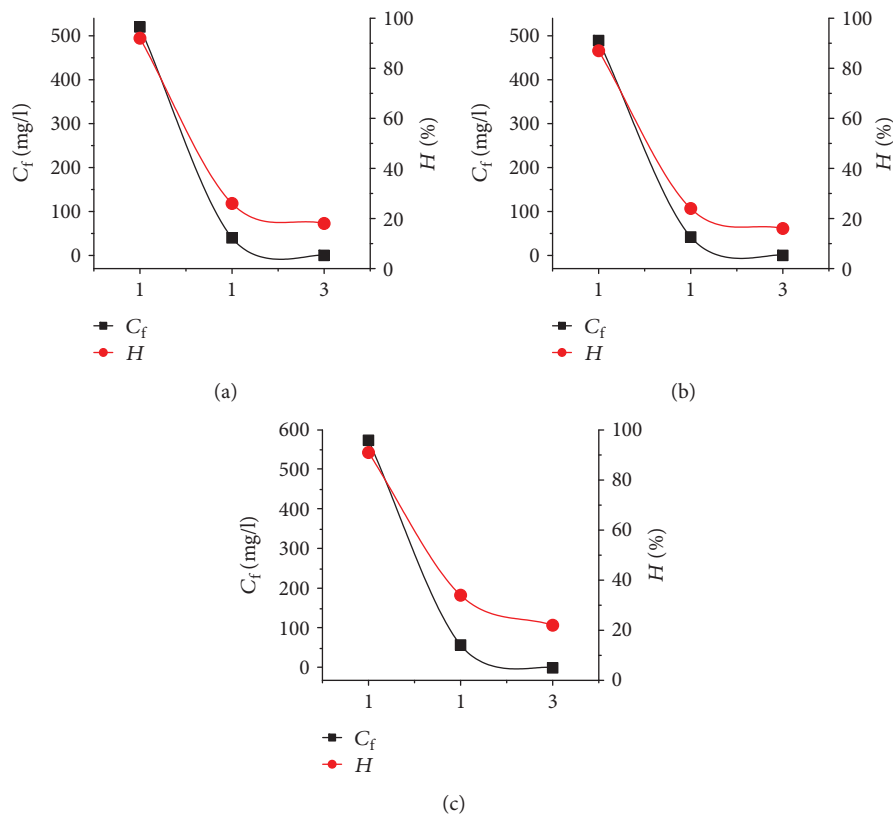


FIGURE 6: Residual concentration ( $C_f$ ) of spent sorbents particles and their moisture content ( $H$ ) after magnetic separation for 30 min: (a) for saponite and its magnetic composites, (b) for palygorskite and its magnetic composites, (c) for spondyl clay and its magnetic composites: 1—initial clays, 2—modified clays with 7 wt.% of magnetite, and 3—modified clays with 10 wt.% of magnetite.

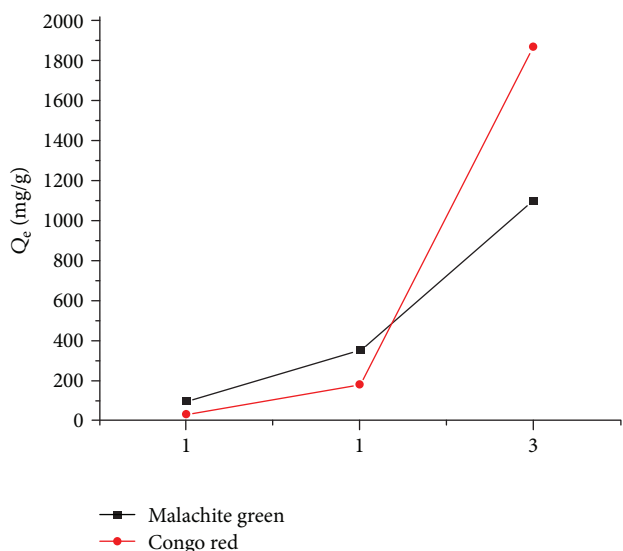


FIGURE 7: The change in the sorption activity: 1—saponite, 2—Sap7, and 3—Sap7-MoS<sub>2</sub>.

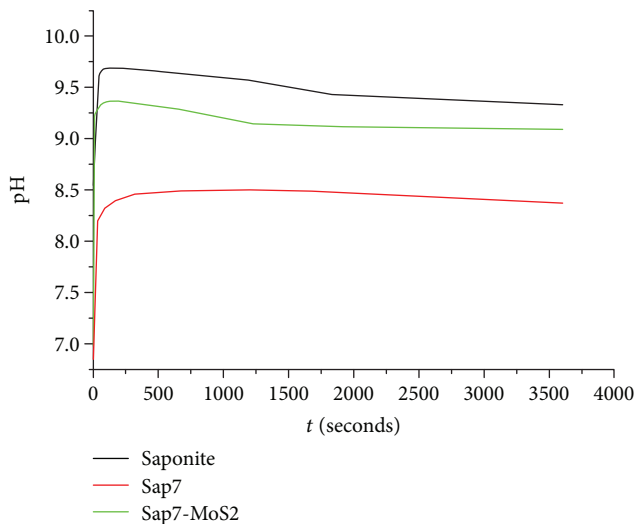


FIGURE 8: pH change of the aqueous suspensions over time for saponite, Sap7, and Sap7-MoS<sub>2</sub>.

The following Hammett indicators were selected for the investigations: o-nitroaniline ( $pK = -0.29$ ), fuchsine ( $pK = 2.1$ ), bromophenol blue ( $pK = 3.9$ ), methyl red ( $pK = 5.25$ ), bromothymol blue ( $pK = 6.8$ ), phenol red

( $pK = 7.6$ ), thymol blue ( $pK = 8.8$ ), and indigo carmine ( $pK = 12.8$ ). Figure 9 shows the distribution curves of the adsorption centers of Hammett indicators on the surface of saponite, Sap7, and Sap7-MoS<sub>2</sub> in the aqueous medium.

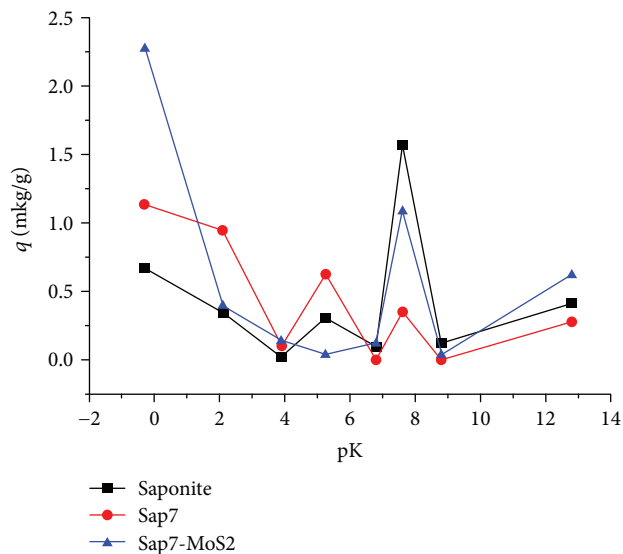


FIGURE 9: Distribution of the adsorption centers of indicators on the surface of sorbent samples.

Analysis of the obtained data on the distribution of the adsorption centers on the surface of saponite indicates the predominance of Brönsted base sites ( $pK = 7.6$ ,  $pK = 12.8$ ) and Lewis base sites ( $pK = -0.29$ ), as well as a small number of Brönsted acid sites ( $pK = 2.1$ ,  $pK = 5.25$ ).

Modification of the saponite surface with 7 wt.% of magnetite leads to the decrease in the number of Brönsted base sites ( $pK = 7.6$ ) and to the increase in the number of Brönsted acid sites ( $pK = 5.25$ ), which explains the decrease in  $pH_{iip}$  compared to saponite, as well as the higher adsorption affinity for anionic dye compared to saponite. The number of Lewis base sites ( $pK = -0.29$ ) increases compared with saponite in Sap7.

Additional modification of the magnetic sorbent Sap7 with molybdenum disulfide increases the number of the Brönsted base sites ( $pK = 7.6$ ,  $pK = 12.8$ ) on its surface in comparison with Sap7, but still there are less of them than in saponite. In addition, modification with graphene-like particles of  $MoS_2$  leads to an even more significant increase in the number of Lewis base sites ( $pK = -0.29$ ).

Thus, the increase in the Lewis base sites content from saponite to Sap7 and then to Sap7- $MoS_2$  leads to the increase in adsorption capacity towards malachite green, which is a cationic dye. The increase in sorption activity with respect to Congo red is caused by both the increase in the number of Brönsted acid sites (especially for Sap7) and, possibly, by the photocatalytic activity of molybdenum disulphide in Sap7- $MoS_2$ .

#### 4. Conclusions

The changes in the textural characteristics of clay matrices after their modification with nanomagnetite in the amount of 7 wt.% and 10 wt.% have been investigated and analyzed. It has been shown that in all cases the introduction of magnetite into the structure of clay minerals leads to the formation of the secondary porous structure and is accompanied by the

increase in the specific surface area and pore volume of nanocomposite materials.

As a result of magnetic separation of both magnetic nanocomposites and clay sorbents, it has been shown that magnetic sorbents are separated from the suspension at least 5 times faster than clays, and the moisture content of the precipitates decreases by 3.5–4.75 times. It has been established that the modification of clay matrices with nanomagnetite content that exceeds 7 wt.% is unreasonable due to the decrease in adsorption properties in all cases.

The additional modification of magnetic sorbents with graphene-like molybdenum disulphide (Sap7- $MoS_2$ ) significantly changes their adsorption and surface properties. The sorption capacity of the triple magnetic composite with respect to the cationic dye increases from 350 mg/g to 1100 mg/g and to the anionic dye from 176 mg/g to 1830 mg/g. The increase in the sorption capacity of Sap7- $MoS_2$  for both dyes is related, in our opinion, to the increase in the number of the Lewis base sites and increase in the number of Brönsted acid sites.

The obtained results demonstrate the considerable prospects for the creation of magnetic nanocomposite sorbents based on natural clay matrices, which, as shown, are characterized by better textural characteristics, adsorption properties, and technological parameters regarding separation after the sorption process than natural clays. In this case, additional modification with graphene-like molybdenum disulphide makes it possible to create absolutely new highly efficient magnetic nanocomposite sorbents of multifunctional purpose.

#### Data Availability

No data were used to support this study.

#### Conflicts of Interest

The authors declare that there is no conflict of interest regarding the publication of this paper.

#### Acknowledgments

The authors thank the staff of the Institute of Bioorganic Chemistry and Petrochemistry of the National Academy of Sciences for their help in conducting some studies. This research was supported by the Ministry Education and Science of Ukraine (grant number M/20-2018).

#### References

- [1] V. Singh, R. Madugundo, A. Annadi, B. Bhoi, K. D. Chandrasekhar, and M. Bohra, "Synthesis, properties and applications of multifunctional magnetic nanostructures," *Journal of Nanomaterials*, vol. 2017, Article ID 2638715, 2 pages, 2017.
- [2] G. Gangadhar, U. Maheshwari, and S. Gupta, "Application of nanomaterials for the removal of pollutants from effluent streams," *Nanoscience & Nanotechnology-Asia*, vol. 2, no. 2, pp. 140–150, 2012.

- [3] X. Qu, P. J. J. Alvarez, and Q. Li, "Applications of nanotechnology in water and wastewater treatment," *Water Research*, vol. 47, no. 12, pp. 3931–3946, 2013.
- [4] C. Santhosh, V. Velmurugan, G. Jacob, S. K. Jeong, A. N. Grace, and A. Bhatnagar, "Role of nanomaterials in water treatment applications: a review," *Chemical Engineering Journal*, vol. 306, pp. 1116–1137, 2016.
- [5] T. Kanjilal and C. Bhattacharjee, "Chapter 1: Green applications of magnetic sorbents for environmental remediation," *Materials Research Forum LLC Book "Organic Pollutants in Wastewater I"*, vol. 29, pp. 1–41, 2018.
- [6] J. Zhu, S. Wei, M. Chen et al., "Magnetic nanocomposites for environmental remediation," *Advanced Powder Technology*, vol. 24, no. 2, pp. 459–467, 2013.
- [7] A. E. Karatapanis, Y. Fiamegos, and C. D. Stalikas, "Silica-modified magnetic nanoparticles functionalized with cetylpyridinium bromide for the preconcentration of metals after complexation with 8-hydroxyquinoline," *Talanta*, vol. 84, no. 3, pp. 834–839, 2011.
- [8] K. Aguilar-Arteaga, J. A. Rodriguez, and E. Barrado, "Magnetic solids in analytical chemistry: a review," *Analytica Chimica Acta*, vol. 674, no. 2, pp. 157–165, 2010.
- [9] C. Li, L. Chen, and W. Li, "Magnetic titanium oxide nanoparticles for hemimicelle extraction and HPLC determination of organophosphorus pesticides in environmental water," *Microchimica Acta*, vol. 180, no. 11–12, pp. 1109–1116, 2013.
- [10] L. C. A. Oliveira, R. V. R. A. Rios, J. D. Fabris, V. Garg, K. Sapag, and R. M. Lago, "Activated carbon/iron oxide magnetic composites for the adsorption of contaminants in water," *Carbon*, vol. 40, no. 12, pp. 2177–2183, 2002.
- [11] Y. Zhang, B. Wu, H. Xu et al., "Nanomaterials-enabled water and wastewater treatment," *NanoImpact*, vol. 3–4, pp. 22–39, 2016.
- [12] A. V. Pastukhov, V. A. Davankov, V. V. Volkov, S. V. Amaratov, and K. I. Lubentsova, "Structure and sorption properties of hypercrosslinked polystyrenes and magnetic nanocomposite materials based on them," *Journal of Polymer Research*, vol. 21, no. 4, 2014.
- [13] S. De Gisi, G. Lofrano, M. Grassi, and M. Notarnicola, "Characteristics and adsorption capacities of low-cost sorbents for wastewater treatment: a review," *Sustainable Materials and Technologies*, vol. 9, pp. 10–40, 2016.
- [14] N. O. Mykhailenko, O. V. Makarchuk, T. A. Dontsova, S. Gorobets, and I. M. Astrelin, "Purification of aqueous media by magnetically operated saponite sorbents," *Eastern-European Journal of Enterprise Technologies*, vol. 4, no. 10, pp. 13–20, 2015.
- [15] J. Vereš and Z. Orolinová, "Study of the treated and magnetically modified bentonite as possible sorbents of heavy metals," *Acta Montanistica Slovaca*, vol. 14, no. 2, pp. 152–155, 2009.
- [16] F. S. Hashem, "Adsorption of methylene blue from aqueous solutions using Fe<sub>3</sub>O<sub>4</sub>/bentonite nanocomposite," *Scientific Reports*, vol. 549, pp. 1–5, 2012.
- [17] J. Chang, J. Ma, Q. Ma et al., "Adsorption of methylene blue onto Fe<sub>3</sub>O<sub>4</sub>/activated montmorillonite nanocomposite," *Applied Clay Science*, vol. 119, no. 1, pp. 132–140, 2016.
- [18] A. Magdy, Y. O. Fouad, M. H. Abdel-Aziz, and A. H. Konsowa, "Synthesis and characterization of Fe<sub>3</sub>O<sub>4</sub>/kaolin magnetic nanocomposite and its application in wastewater treatment," *Journal of Industrial and Engineering Chemistry*, vol. 56, pp. 299–311, 2017.
- [19] L. C. A. Oliveira, D. I. Petkowicz, A. Smaniotto, and S. B. C. Pergher, "Magnetic zeolites: a new adsorbent for removal of metallic contaminants from water," *Water Research*, vol. 38, no. 17, pp. 3699–3704, 2004.
- [20] L. C. A. Oliveira, R. V. R. A. Rios, J. D. Fabris, K. Sapag, V. K. Garg, and R. M. Lago, "Clay–iron oxide magnetic composites for the adsorption of contaminants in water," *Applied Clay Science*, vol. 22, no. 4, pp. 169–177, 2003.
- [21] T. Szabó, A. Bakandritsos, V. Tzitzios et al., "Magnetic iron oxide/clay composites: effect of the layer silicate support on the microstructure and phase formation of magnetic nanoparticles," *Nanotechnology*, vol. 18, no. 28, article 285602, 2007.
- [22] O. V. Makarchuk, T. A. Dontsova, and I. M. Astrelin, "Magnetic clay sorbent for the removal of dyes from aqueous solutions," *Research Bulletin of the National Technical University of Ukraine "Kyiv Polytechnic Institute"*, vol. 0, no. 6, pp. 109–114, 2015.
- [23] O. V. Makarchuk, T. A. Dontsova, and I. M. Astrelin, "Magnetic nanocomposites as efficient sorption materials for removing dyes from aqueous solutions," *Nanoscale Research Letters*, vol. 11, no. 1, pp. 161–167, 2016.
- [24] O. Makarchuk, T. Dontsova, A. Perekos, A. Skoblik, and Y. Svystunov, "Magnetic mineral nanocomposite sorbents for wastewater treatment," *Journal of Nanomaterials*, vol. 2017, Article ID 8579598, 7 pages, 2017.
- [25] O. V. Makarchuk, T. A. Dontsova, and A. E. Perekos, "Magnetic nanocomposite sorbents on mineral base," *Nanophysics, Nanomaterials, Interface Studies, and Applications*, vol. 195, pp. 705–719, 2017.
- [26] T. A. Dontsova, L. M. Kulikov, and I. M. Astrelin, "Adsorption photocatalytic properties of micron and graphene (2D) nanoparticles of molybdenum dichalcogenides," *Journal of Water Chemistry and Technology*, vol. 39, no. 3, pp. 132–137, 2017.
- [27] M. Thommes, K. Kaneko, A. V. Neimark et al., "Physisorption of gases, with special reference to the evaluation of surface area and pore size distribution (IUPAC technical report)," *Pure and Applied Chemistry*, vol. 87, no. 9–10, 2015.
- [28] A. I. Ivanets, V. G. Prozorovich, T. F. Kouznetsova et al., "Sorption behavior of strontium ions on manganese oxides with tunnel structure," *Journal of Radioanalytical and Nuclear Chemistry*, vol. 316, no. 2, pp. 673–683, 2018.
- [29] M. Wu, L. Li, N. Liu, D. J. Wang, Y. C. Xue, and L. Tang, "Molybdenum disulfide (MoS<sub>2</sub>) as a co-catalyst for photocatalytic degradation of organic contaminants: a review," *Process Safety and Environment Protection*, vol. 118, pp. 40–58, 2018.

## Research Article

# Magnetic Fe<sub>3</sub>O<sub>4</sub>@Chitosan Carbon Microbeads: Removal of Doxycycline from Aqueous Solutions through a Fixed Bed via Sequential Adsorption and Heterogeneous Fenton-Like Regeneration

Bo Bai <sup>1,2,3</sup>, Xiaohui Xu,<sup>2</sup> Changchuan Li,<sup>2</sup> Jianyu Xing,<sup>2</sup> Honglun Wang <sup>3</sup>, and Yourui Suo<sup>3</sup>

<sup>1</sup>Shaanxi Key Laboratory of Land Consolidation, Xi'an 710054, China

<sup>2</sup>Key Laboratory of Subsurface Hydrology and Ecological Effects in Arid Region, Ministry of Education, Chang'an University, Xi'an 710054, China

<sup>3</sup>State Key Laboratory of Plateau Ecology and Agriculture, Qinghai University, Xining 810016, China

Correspondence should be addressed to Bo Bai; [baibochina@163.com](mailto:baibochina@163.com)

Received 9 August 2018; Accepted 27 September 2018; Published 3 December 2018

Guest Editor: Murtaza Bohra

Copyright © 2018 Bo Bai et al. This is an open access article distributed under the Creative Commons Attribution License, which permits unrestricted use, distribution, and reproduction in any medium, provided the original work is properly cited.

The adsorptive removal of antibiotics from aqueous solutions is recognized as the most suitable approach due to its easy operation, low cost, nontoxic properties, and high efficiency. However, the conventional regeneration of saturated adsorbents is an expensive and time-consuming process in practical wastewater treatment. Herein, a scalable adsorbent of magnetic Fe<sub>3</sub>O<sub>4</sub>@chitosan carbon microbeads (MCM) was successfully prepared by embedding Fe<sub>3</sub>O<sub>4</sub> nanoparticles into chitosan hydrogel via an alkali gelation-thermal cracking process. The application of MCM composites for the adsorptive removal of doxycycline (DC) was evaluated using a fixed-bed column. The results showed that pH, initial concentration, flow rate, and bed depth are found to be important factors to control the adsorption capacity of DC. The Thomas and Yoon-Nelson models showed a good agreement with the experimental data and could be applied for the prediction of the fixed-bed column properties and breakthrough curves. More importantly, the saturated fixed bed can be easily recycled by H<sub>2</sub>O<sub>2</sub> which shows excellent reusability for the removal of doxycycline. Thus, the combination of the adsorption advantage of chitosan carbon with catalytic properties of magnetic Fe<sub>3</sub>O<sub>4</sub> nanoparticles might provide a new tool for addressing water treatment challenges.

## 1. Introduction

In the past years, doxycycline (DC) has gradually become one of the most widely used antibiotics in the world especially in human therapy and livestock industry because of its specific antimicrobial properties and minor adverse side effects [1–3]. Regrettably, the metabolism of humans or animals cannot decompose the DC antibiotic thoroughly, and only 20–50% of DC can be absorbed into the organism. Thus, the residues of antibiotics have been frequently detected in soil, surface water, groundwater, and other aquatic environment [4]. It has been verified that exposure to low-level and accumulative DC may lead to a variety of dangerous effects,

including destruction of aquatic photosynthetic organisms and indigenous microbial populations and dissemination into antibiotic-resistant genes among microorganisms [5, 6]. Hereby, DC wastewater has drawn great attention and is especially targeted in the field of wastewater treatment. Compared with the traditional chemical and biological strategies to purify the antibiotic wastewater, the adsorptive removal of antibiotic from aqueous solution is the most suitable approach for the treatment of toxic antibiotic wastewater because of its easy operation, low cost, nontoxic properties, and high efficiency [7, 8]. A series of adsorbents, such as activated carbon [9], clays [10], graphene oxide [11], and zeolites [12], have been exploited extensively and applied widely for

the removal of organic antibiotics. In particular, the utilization of costless, renewable, and environmentally friendly activated carbon (AC) as adsorbents has become popular owing to its abundant porous structure and stable chemical property [13–15]. However, the adsorption of toxic organic compounds with activated carbon only transfers the pollutants from the wastewater to the surface of adsorbents rather than decomposing them, which limited the recycling of the adsorbents. In order to deal with such conundrums, the periodical regeneration by traditional physicochemical approaches should be executed for the pollutant-loaded adsorbents, such as thermal regeneration [16], oxidative catalytic regeneration [17], ultrasound-assisted sorbent regeneration [18], electrochemical method [19], and microwave regeneration [20].

The Fenton oxidation is the most powerful method to decompose organic pollutants because the  $\cdot\text{OH}$  generated in the Fenton system ( $\cdot\text{OH}$ , oxidation potential: 2.8 V) is highly oxidative and nonselective, which can destruct many hazardous organic pollutants easily and effectively like azo dye [21], doxycycline [22], p-nitrophenol [23], sulfamethoxazole [24], and polyacrylamide [25]. In contrast, the heterogeneous Fenton oxidation, based on solid-liquid interface reactions, has more advantages than homogeneous Fenton reaction ( $\text{H}_2\text{O}_2 + \text{Fe}^{2+}/\text{Fe}^{3+}$ ) with regard to less sludge formation, expanded pH range, and generation of highly potent chemical oxidants. More importantly, the removal efficiency through heterogeneous Fenton can be increased significantly by an enrichment or preconcentration sorption process and subsequent oxidation of the contaminants [26]. Specifically, organic contaminants are first adsorbed by adsorbents from a large volume of effluent, then separated from the wastewater system and mineralized by advanced oxidation. At the same time, the pollutant-loaded adsorbents are regenerated. For example, in our previous study, raspberry-like  $\text{Fe}_3\text{O}_4$ @yeast shows excellent reusability for the removal of azo dyes because of the consecutive and synergistic effect of yeast biosorption and  $\text{Fe}_3\text{O}_4$  nanoparticles [27].

Herein, we synthesized magnetic  $\text{Fe}_3\text{O}_4$ @chitosan carbon microbeads (MCM) by a simple thermal cracking process under a nitrogen atmosphere at 350°C, aimed at combining the catalytic property of  $\text{Fe}_3\text{O}_4$  with the adsorption capacity of chitosan carbon microbeads. Based on the XRD, SEM, and FT-IR characterization results, a possible mechanism for the formation of MCM was proposed. A fixed-bed column was employed to investigate the removal efficiency of doxycycline. The effects of pH, initial concentration, flow rate, and bed depth were also analyzed. Afterward, the regeneration/recycling tests were carried out by triggering the Fenton oxidation in the presence of  $\text{H}_2\text{O}_2$  solution.

## 2. Materials and Methods

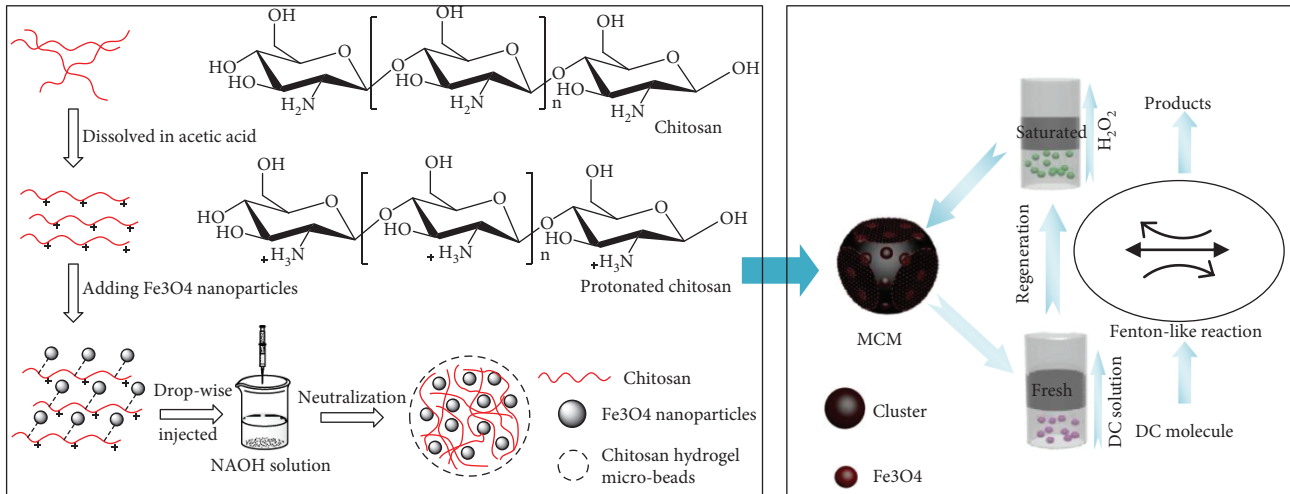
**2.1. Materials.** Chitosan,  $\text{Fe}_3\text{O}_4$  nanoparticles, glutaraldehyde (25% (v/v)) aqueous solution, and acetic acid (36% (v/v)) were provided by Xi'an Chemical Agent Corp. All chemicals used in this work were of analytical grade and used without further purification. Deionized water was used throughout this study.

**2.2. Preparation of Samples.** 0.3 gram of chitosan was dissolved in 10 mL of 1% aqueous acetic acid solution to prepare the chitosan solution. Then, 0.9 gram of  $\text{Fe}_3\text{O}_4$  nanoparticles was slowly added into the prepared chitosan solution. The homogenous solution was injected into a gently stirred sodium hydroxide solution using a syringe to form magnetic microspheres. After magnetic stirring for 4 h, the products were harvested by filtration, followed by washing with a copious amount of distilled water until the pH value was 7. Then, these magnetic microbeads were immersed in a cross-linking agent, 5% glutaraldehyde, for 8 h at room temperature. The cross-linked microbeads were filtered, washed, and dried at 60°C for 12 h. Finally, the resulting products were pyrolyzed in a tubular reactor at 350°C for 40 min under a nitrogen atmosphere. The synthesis of chitosan carbon microbeads (CSM) was also carried out in accordance with the above steps but without the adding of  $\text{Fe}_3\text{O}_4$ .

**2.3. Material Characterization of Samples.** The size and surface morphology of the samples were determined by a Philips XL 30 field emission scanning electron microscope (FE-SEM). The crystallographic structure of the samples was measured by X-ray diffraction (XRD) on a Rigaku D/MAX-3C diffractometer operated at a voltage of 40 kV and a current of 20 mA, at a 0.028 scan rate with  $\text{Cu K}\alpha$  radiation. Fourier transform infrared (FT-IR) spectra of samples were recorded on a Bio-Rad FTS135 spectrometer in the range 500–4000  $\text{cm}^{-1}$  using a KBr wafer technique, to study the functional groups of the samples. To obtain  $\text{N}_2$  adsorption/desorption curves (BET curves), adsorption-desorption experiments using liquid nitrogen were performed on a Micromeritics surface analyzer (WBL-8XX).

**2.4. Continuous Fixed-Bed Experiments.** The fixed-bed adsorption experiments were performed in up-flow columns with an internal diameter of 0.6 cm and a length of 15 cm. The influences of different initial concentrations of DC (20, 25, and 30 mg/L), flow rates (1.1, 2.1, and 3.1 mL/min), pH (2, 4, 7, 9, and 11), and bed depths (0.8, 1.2, and 1.6 cm) were studied. The pH of the DC solutions was adjusted by the addition of NaOH (0.1 mol/L) and HCl (0.1 mol/L). In order to exclude the trapped air and wet the porosity of activated carbon, water was pumped into the column at the flow rate of 8 mL/min for 10 min before starting the experiment. The column effluent samples were taken out at regular time intervals, and the concentration was analyzed by a Jenway 6405 UV-vis spectrophotometer at 351 nm.

The dynamic adsorption behavior of fixed-bed columns was investigated in terms of analyzing the shape of breakthrough curves. And the experimental breakthrough curves determined as the ratio of  $C_t/C_0$  vs.  $t$  (min) (where  $C_0$  is the inlet sample concentration,  $C_t$  is the outlet sample concentration, and  $t$  is the elapsed time) represent the loading of DC onto  $\text{Fe}_3\text{O}_4$ /chitosan carbon microspheres. From a practical point of view, operation of the column was stopped when the concentration in the effluent is higher than 90% of the influent concentration because of the establishment of the saturation time,  $t_s$ .



SCHEME 1: Schematic of the adsorption and in situ regeneration mechanism of MCM in the removal of DC.

The volume of the effluent,  $V_{\text{eff}}$  (mL), was defined as

$$V_{\text{eff}} = Q \cdot t_{\text{total}} \quad (1)$$

where  $t_{\text{total}}$  is the total flow time in min and  $Q$  is the flow rate which circulates through the column in mL/min.

The area above the breakthrough curve means the total mass of DC adsorbed, and  $q_{\text{total}}$ , in mg, was evaluated through the following equation:

$$q_{\text{total}} = \frac{Q}{1000} \int_{t=0}^{t=t_{\text{total}}} (C_0 - C_t) dt. \quad (2)$$

Equilibrium DC uptake per unit mass of adsorbent,  $q_e$  (mg/g), was calculated using the following equation when steady-state conditions were reached:

$$q_e = \frac{q_{\text{total}}}{m}, \quad (3)$$

where  $m$  (g) is the mass of adsorbent in the column.

The total amount of DC passed through the column  $m_{\text{total}}$  (mg) can be estimated from

$$m_{\text{total}} = \frac{C_0 \cdot Q \cdot t_{\text{total}}}{1000}. \quad (4)$$

**2.5. Heterogeneous Fenton Oxidation Regeneration.** After each adsorption cycle, the sorbent bed was washed by distilled water in the upward direction at a suitable flow rate (2.1 mL/min) to remove the residual DC. Then, the regeneration experiment was carried out by injecting various aqueous solutions through the column bed in an upward direction at a flow rate of 1.1 mL/min for 1.5 h. After the heterogeneous Fenton-like reaction, the column was rinsed again to remove the residual  $\text{H}_2\text{O}_2$ . Finally, the bed was reused for the next adsorption/regeneration cycle, up to three consecutive cycles.

### 3. Results and Discussion

**3.1. Formation Procedure of MCM and Characterization.** The formation of magnetic  $\text{Fe}_3\text{O}_4$ @chitosan carbon microbeads by alkali gelation-thermal cracking route was proposed in Scheme 1.

According to previous literatures, chitosan is insoluble in water but soluble in diluted acidic solution below its pKa (~6.3), in which the amine groups ( $-\text{NH}_2$ ) of chitosan can be facily converted into the soluble protonated form ( $-\text{NH}_3^+$ ) [28]. In the current study, the chitosan was dissolved in 1% acetic acid with vigorously stirring to obtain a homogeneous quaternized chitosan solution and then intertwined together to form a three-dimensional network linked by hydrogen bonding or Van der Waals forces. Owing to the fact that the amine groups ( $-\text{NH}_2$ ) of chitosan polymers were protonated easily, the chitosan network tends to expand due to the repulsive force among the protonation amine ions ( $-\text{NH}_3^+$ ). Such network expansion provides a great opportunity for  $\text{Fe}_3\text{O}_4$  nanoparticles to be fixed onto the linear scaffold of chitosan molecules. Thereafter, the mixture containing  $\text{Fe}_3\text{O}_4$  nanoparticles and chitosan was injected into NaOH solution drop by drop. Under alkaline condition,  $-\text{NH}_3^+$  groups were deprotonated and converted into insoluble forms ( $-\text{NH}_2$ ) [29], resulting in the disappearance of electrostatic repulsion between chitosan molecules. Consequently, the magnetic  $\text{Fe}_3\text{O}_4$ @chitosan hydrogel microbeads were formed through the sharing of the lone electron pairs from the nitrogen atom in amine with Fe irons [30, 31]. Then, the magnetic  $\text{Fe}_3\text{O}_4$ @chitosan hydrogel microbeads were pyrolyzed in a tubular reactor at  $350^\circ\text{C}$  for 40 min under a nitrogen atmosphere to obtain MCMs. The content of  $\text{Fe}_3\text{O}_4$  can be controlled precisely by tuning the dosage of reactants. Compared with the classical impregnation method, the present route by alkali gelation provides a better choice to synthesize functional composites containing  $\text{Fe}_3\text{O}_4$  nanoparticles and carbon-related materials with higher content of Fe irons.

From the above analysis, chitosan polymers play a significant trifunctional role in the formation of the  $\text{Fe}_3\text{O}_4$ @chitosan

composite. Firstly, the native entanglement or cross-linking property of chitosan chains helps  $\text{Fe}_3\text{O}_4$  nanoparticles reunite together tightly and become a stable three-dimensional network due to the strong hydrogen bonding or Van der Waals forces. Secondly, the water absorption capacity of the three-dimensional network is partly retained, which is beneficial to the formation of pores or channels in the MCM during the thermal cracking process. Thirdly, chitosan polymers can act as a carbon source, providing lots of active sites for the adsorption of pollutants. Similarly, the  $\text{Fe}_3\text{O}_4$  nanoparticles play two vital roles in the magnetic  $\text{Fe}_3\text{O}_4$ @chitosan carbon microbeads. On the one hand, the mechanical stability of MCM can be strengthened by embedding hard  $\text{Fe}_3\text{O}_4$  nanoparticles into chitosan. On the other hand, part of chitosan is replaced by  $\text{Fe}_3\text{O}_4$  nanoparticles, offering additional catalytic active sites on the MCM substance. From this point of view, the prepared MCMs are demonstrated to not only preserve the adsorption performance of chitosan carbon but also possess an in situ regeneration ability of  $\text{Fe}_3\text{O}_4$  nanoparticles.

The incorporation of  $\text{Fe}_3\text{O}_4$  nanoparticles into the CSM matrix can be observed straightforwardly from the microscopy photos. The optical microscopy photos of MCM and CSM are presented in Figures 1(a) and 1(b), respectively. It can be seen that the MCMs inherited the spherical shape after the addition of  $\text{Fe}_3\text{O}_4$  nanoparticles into the chitosan hydrogel microbeads. Correspondingly, the color of MCM substrates changed from white to black. Figures 1(a) and 1(b) show that the MCM outer surface was rough and interspersed with small bumps while the CSM outer surface was very smooth and flat. The loading of  $\text{Fe}_3\text{O}_4$  nanoparticles onto the MCM scaffold led to a rough topographical surface for the CSM substrate. Such unique regular surface morphology usually contributes to the relatively more catalytic active sites, which is expected to favor the adsorption of contaminants. The absence of scattering  $\text{Fe}_3\text{O}_4$  nanoparticles around the composite CSM implies a strong adhesion between the MCM scaffold and the  $\text{Fe}_3\text{O}_4$  nanoparticles.

The incorporation of  $\text{Fe}_3\text{O}_4$  nanoparticles into the CSM matrix can be further verified from the SEM images. SEM images of  $\text{Fe}_3\text{O}_4$  nanoparticles, CSM, and MCM are shown in Figures 1(c)–1(h). Figures 1(c) and 1(d) display the primitive  $\text{Fe}_3\text{O}_4$  nanoparticles, which exhibit irregular shape with the length of 0.2–0.3  $\mu\text{m}$ . The inset image in the bottom right corner of Figures 1(e) and 1(g) demonstrated that both MCM and CSM samples were spherical. The average diameter of MCM was around 1.5–2.0 mm, which was much bigger than that of CSM about 1.2–1.5 mm, implying that the successful decoration of chitosan carbon with  $\text{Fe}_3\text{O}_4$  nanoparticles enlarged the diameter size. On the other hand, the  $\text{Fe}_3\text{O}_4$  nanoparticles in MCM also provided a mechanical strength against shrinkage during drying and consequently make the MCM denser. In contrast, the drastic shrinkage phenomenon happened under absolute drying conditions on the surface of CSM which is smaller in diameter. Figure 1(e) presents a typical SEM micrograph of CSM. It can be observed that the surface of CSM is completely smooth and flat. Figure 1(f) shows that the internal morphology of CSM exhibits an ordered incompact structure probably caused by the thermal cracking process [25, 32]. However, with the introduction of magnetic

$\text{Fe}_3\text{O}_4$  nanoparticles, there are significant changes on the outer surface morphology of MCM. The SEM micrograph of MCM (Figure 1(g)) shows a rough topographical surface decorated with some small bumps, which increase the surface area of the MCMs and provide more active sites for the adsorption of pollutant molecules. Hereby, the MCM adsorbent should have a better adsorption performance compared with the CSM. At higher magnification (Figure 1(h)), some clusters resulted from the aggregation of  $\text{Fe}_3\text{O}_4$  nanoparticles distributed evenly in the MCM's core, suggesting that the  $\text{Fe}_3\text{O}_4$  nanoparticles were successfully embedded into the MCM substrate.

To explain chemical binding between  $\text{Fe}_3\text{O}_4$  and CSM, the Fourier transform infrared (FTIR) spectra of the pure  $\text{Fe}_3\text{O}_4$ , CSM, and MCM were recorded. In Figure 2, the IR spectrum of MCM was very similar to that of CSM, indicating that the introduction of magnetic particles did not destroy the function groups of chitosan. For CSM, the peak at  $3366\text{ cm}^{-1}$  resulted from axial stretching vibration of O-H superimposed on the N-H stretching band and intermolecular hydrogen bonds of the polysaccharide [33], and the adsorption peaks at  $2919$  and  $2874\text{ cm}^{-1}$  are assigned to the stretching vibration of C-H. The typical band of primary amine groups ( $-\text{NH}_2$ ) appears at  $1655\text{ cm}^{-1}$  [34]. The biosorption bands around  $1075$  and  $1027\text{ cm}^{-1}$  display the stretch vibration of the C-O bond. For magnetic  $\text{Fe}_3\text{O}_4$  nanoparticles, the peak at  $636\text{ cm}^{-1}$  relates to the Fe-O group [35]. The formation of a new peak at  $636\text{ cm}^{-1}$  in MCM is related to the blending of  $\text{Fe}_3\text{O}_4$  nanoparticles. The IR spectrum indicates that chitosan carbon and  $\text{Fe}_3\text{O}_4$  both existed in MCM, and the  $\text{Fe}_3\text{O}_4$  has been embedded into the MCM successfully. Notably, the N-H stretching vibration has a blue shift to  $1637\text{ cm}^{-1}$  due to the sharing of the lone electron pairs from the nitrogen atom in amine with Fe iron [30, 31].

Figure 3 shows the XRD patterns of chitosan carbon, pure  $\text{Fe}_3\text{O}_4$  nanoparticles, and the magnetic  $\text{Fe}_3\text{O}_4$ /chitosan composite microspheres (MCM). Diffraction peaks of pure  $\text{Fe}_3\text{O}_4$  nanoparticles at  $2\theta$  of  $18.4^\circ$ ,  $30.3^\circ$ ,  $35.6^\circ$ ,  $37.3^\circ$ ,  $43.2^\circ$ ,  $53.4^\circ$ ,  $57.2^\circ$ , and  $62.9^\circ$  corresponded to (110), (220), (311), (222), (400), (422), (511), and (440) in the face center-cubic phase of  $\text{Fe}_3\text{O}_4$ , which agree with the literature data [36]. In Figure 3, chitosan is seen to show only a typical peak at around  $2\theta = 18.3^\circ$ . This broad peak indicates the existence of amorphous structure [37]. As expected, the broad peak at  $2\theta = 18.3^\circ$  of MCM originates mainly from the amorphous structure of chitosan. Other diffraction peaks emerging in the XRD pattern of MCM are very close to the feature peak of  $\text{Fe}_3\text{O}_4$  nanoparticles, which indicates the existence of  $\text{Fe}_3\text{O}_4$  nanoparticles in the MCM, and no other diffractions are found, meaning the high purity of the samples.

The nitrogen adsorption isotherm of MCM is shown in Figure 4. Nitrogen adsorption isotherm is measured over a relative pressure ( $P/P_0$ ) range from approximately  $10^{-7}$  to 1. The BET surface area of MCM is estimated to be  $3.278\text{ m}^2/\text{g}$  by the Brunauer-Emmett-Teller (BET) equation. A sharp increase in the isotherm at a high relative pressure indicates capillary condensation in the mesopores. Nonlocal density functional theory (NLDFT) [38] was applied to calculate the pore size distribution of MCM (inset image). It

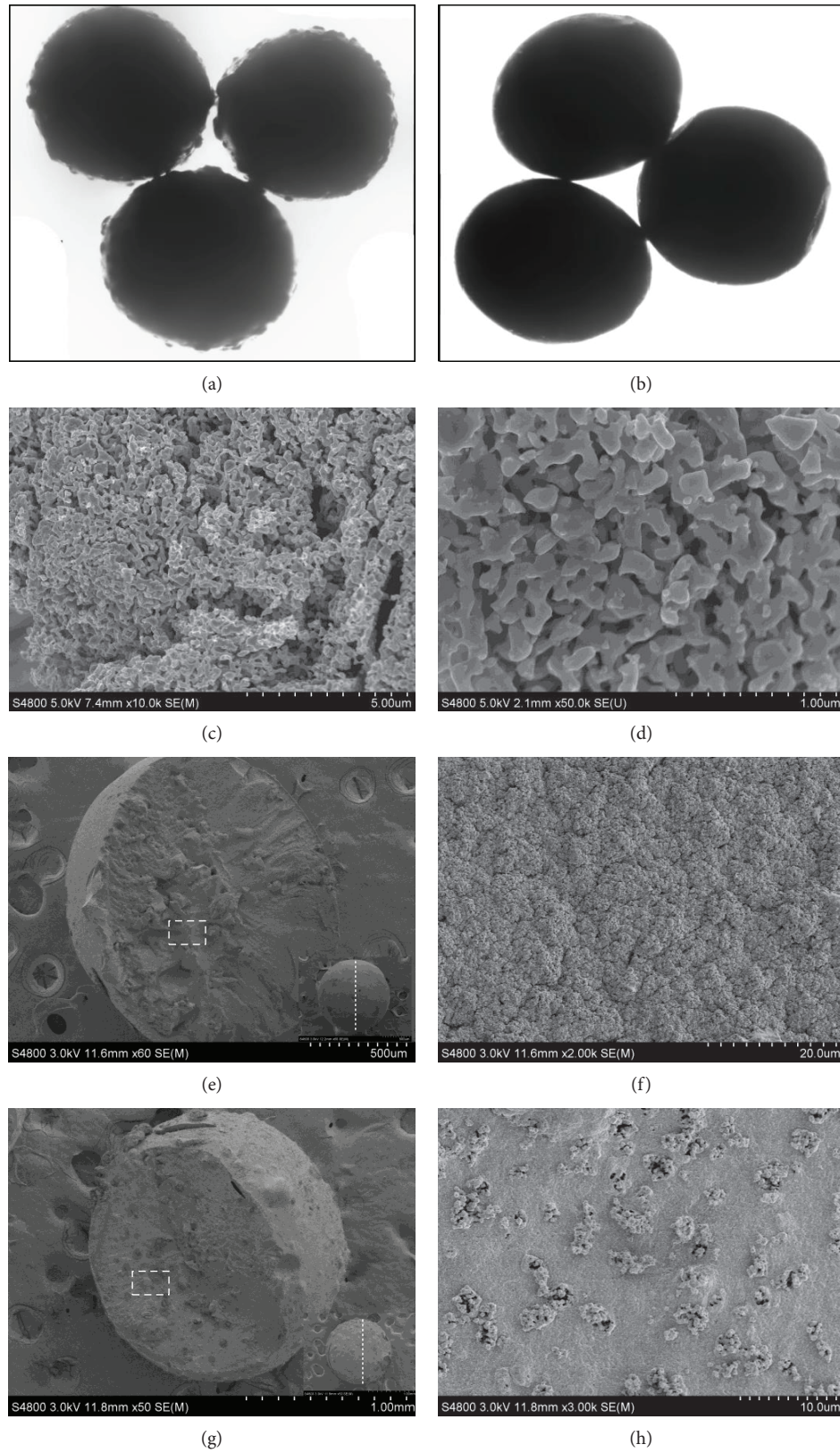


FIGURE 1: Optical microscopy photos (40 $\times$ ) of MCM (a) and CSM (b); FE-SEM images: (c, d)  $\text{Fe}_3\text{O}_4$  nanoparticles, (e) dissected CSM, (f) CSM under high magnification, (g) dissected MCM, and (h) MCM under high magnification.

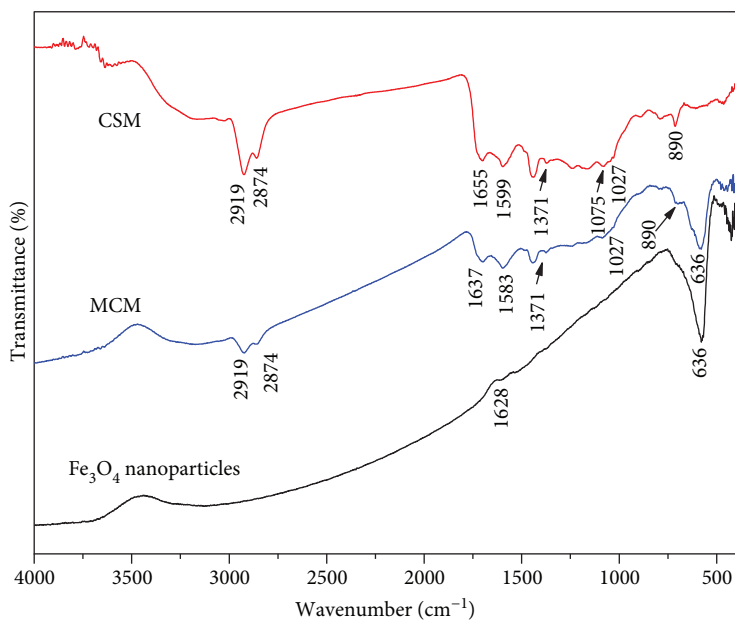


FIGURE 2: FT-IR spectra of  $\text{Fe}_3\text{O}_4$  nanoparticles, CSM, and MCM.

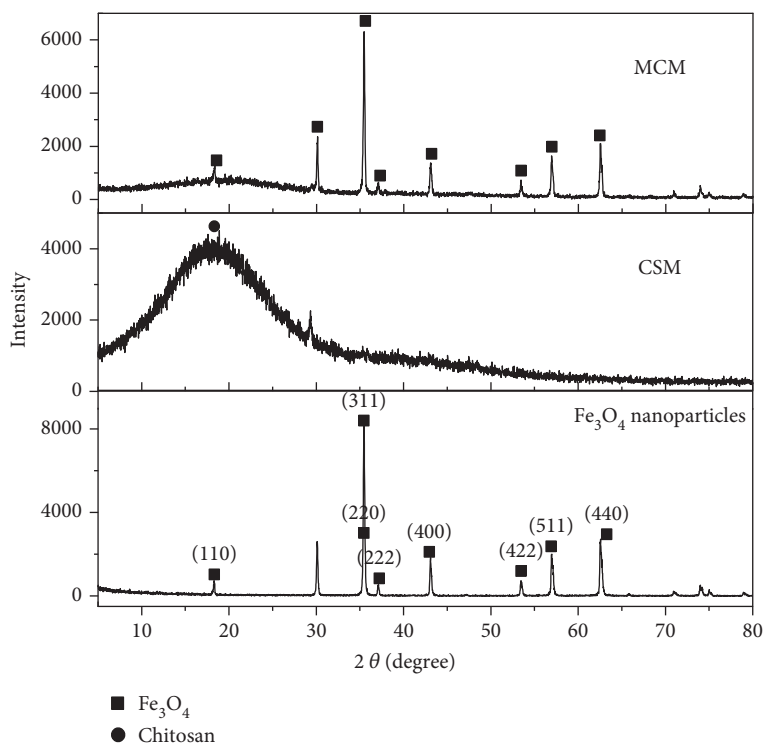


FIGURE 3: XRD spectra of  $\text{Fe}_3\text{O}_4$  nanoparticles, CSM, and MCM.

reveals that the MCM has a high proportion of microspore volume and a low average pore diameter, and the average microspore volume is evaluated to be 0.0083 cc/g.

**3.2. Removal of Doxycycline from Aqueous Solutions through a Fixed Bed via Adsorption.** The fixed-bed adsorption requires very few devices and low operational cost. The fixed-bed columns are essential towards the industrial scale

design and scale-up of the continuous system for required applications and performances [39]. Generally, the column process is continuous and the influent wastewater comes in touch with a certain amount of adsorbents, hereby affording room for a large volume of flowing polluted fluid [40]. To evaluate the effect of operating conditions on the adsorption of DC, a batch of adsorption experiments including the effect of pH, initial feed solution concentration ( $C_0$ ), bed depth ( $Z$ ),

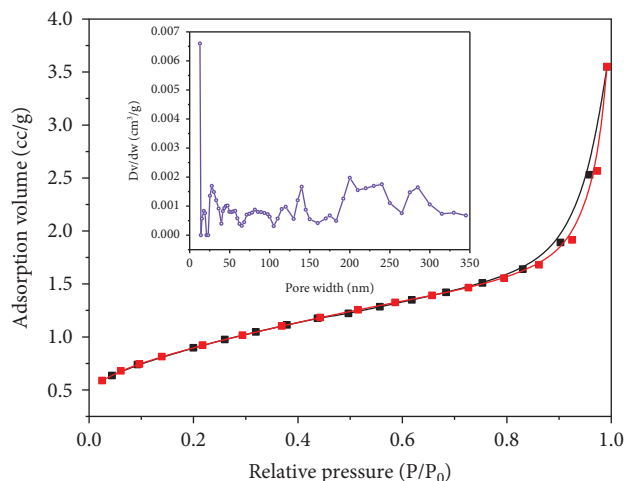


FIGURE 4: Nitrogen adsorption isotherm of the MCM.

and flow rate ( $Q$ ) has been conducted. The results are displayed in Table 1.

**3.2.1. pH Effect on the Adsorption Performance.** pH is one of the dominant factors that affect the removal efficiency of antibiotic, because pH can affect the speciation of a DC molecule in solution and the surface charge of the adsorbent. The pH affects the prevalent chemical mechanisms by controlling the electrostatic interaction between the adsorbent and organic molecules, consequently changing the removal rate of DC from the aqueous solution and the breakthrough curves [41]. Thus, the effect of pH was investigated by varying the pH of the aqueous DC solution from 2.0 to 11.0, while the DC concentration, flow rate, and bed height were kept constant at 25 mg/L, 1.1 mL/min, and 1.2 cm, respectively. Breakthrough curves for DC uptake at various pH values are presented in Figure 5(a). The results extracted from the breakthrough curves are listed in Table 1. As can be seen in Table 1, the adsorption capacity of DC shows a significant increase from 0.934 to 4.816 mg/g with the increase in pH values from 2.0 to 11.0. From Figure 5(a), much sharper breakthrough curves of DC adsorption onto the MCM at lower pH conditions are observed. It is clear that the breakthrough and exhaustion times increase with the increase in pH.

Two vital factors are likely responsible for the remarkable effect of pH on DC adsorption. Firstly, pH can change the surface charge of ionizable organic compounds in chemical speciation [42, 43], and DC is an amphoteric molecule with ionizable groups such as tricarbonyl amide, phenolic diketone, and dimethyl amine moieties, which has three pKa values (3.5, 7.7, and 9.5) [43, 44]. In addition, DC exists in various forms in aqueous solution and its predominant species forms are different, showing as cations, zwitterions, and anions under acid, neutral, and alkaline conditions, respectively. Below pH 3.5, the DC molecule exists as  $DC^+$  due to the protonation of the dimethyl ammonium group, while in the pH between 3.4 and 7.7,  $DC^0$  appears and becomes a predominant form. As pH increases, this form transforms to anion ( $DC^-$  and  $DC^{2-}$ , respectively, above pH 7.7 and 9.5), owing to the deprotonation of phenolic

diketone moiety and tricarbonyl system. Secondly, in acidic condition, the hydrogen atoms can protonate amine groups of chitosan [45] forming a positively charged surface on MCM. As a result, the electrostatic repulsion between the positive DC ions and MCM with the positively charged surface is against the sorption process, whereas the protonation reaction gets weak with increasing the pH value and the sorption capacity is enhanced. Finally, when the pH is above 9, a good adsorption performance is obtained. This is due to the excellent adsorption capacity of MCM with abundant absorptive sites and outstanding porosity. The relatively ample activated sites and the porous structure of adsorbent can supply more binding sites to remove more organic contaminants from aqueous solution.

**3.2.2. Effect of DC Concentration, Bed Depth, and the Feed Flow Rate.** As the DC concentration decreases, the adsorption capacity of MCM increases, reaching saturation in the fixed bed only when the DC concentration is 30 mg/L, while at other concentrations, especially at 20 mg/L, the saturated time has been prolonged to achieve adsorption equilibrium (Figure 5(b)). When  $C_0$  increased from 20 to 30 mg/L, the equilibrium adsorption capacity ( $q_e$ ) decreased from 3.128 to 2.045 mg/g (Table 1). This can be explained that at higher DC concentration, the bed exhaustion was reached more rapidly before the saturation of MCM caused by a relatively smaller depth of the mass transfer zone. Moreover, the adsorption process depends on the intraparticle diffusion of the DC. On the other hand, increasing influent concentration leads to the increment of the driving force for the mass transfer for a fixed adsorption zone length [46]. It should be noted that the highest experimental adsorption capacity (4.18 mg/g) was achieved at the lowest  $C_0$  (20 mg/L), which indicated that the adsorption process was favorable at lower solute concentration. The stronger driving force between the solute in the adsorbent and the solute in the solution makes the active sites of the adsorbent consume quickly, and finally an earlier breakthrough time and a sharper breakthrough curve were obtained [39]. The results obtained in the present study are in good agreement with the results obtained by Han et al. [47] where rice husk was used to adsorb methylene blue from the aqueous solution in a fixed-bed absorber at various inlet concentrations.

Figure 5(c) displays the results of the influence of the bed height on the breakthrough time. From Figure 5(c), it can be observed that with the increase in bed height, the breakthrough time increases and the slope of the breakthrough curve decreases, at a flow rate of 1.1 mL/min, a constant feed concentration of 25 mg/L, and a pH of 7. Under this situation, the highest DC adsorption capacity (2.787 mg/g) was obtained at the highest bed depth. The reason may be related to the situation that more effective adsorption on the surface of MCM had occurred with increasing bed depths. The BECT increases from 0.206 to 0.411 min as the bed depth increases, which suggests that more volume of DC solution could be treated and the enhanced contact time makes it possible to remove more contaminants. Furthermore, an increase in the bed depth results in a broadened mass transfer zone where the mass transfer zone formed can reach a deeper area,

TABLE 1: Parameters of Thomas and Yoon-Nelson models.

$C_0$ (mg/L)	$Z$ (cm)	$Q$ (mL/min)	pH	Thomas model			Yoon-Nelson model		
				$k_T \times 10^3$ (mL/(min·mg))	$q_0$ (mg/g)	$R^2$	$k_Y$ (min <sup>-1</sup> )	$\tau$	$R^2$
25	1.2	1.1	11	2.725	5.974	0.994	0.068	55.623	0.994
25	1.2	1.1	9	2.823	4.568	0.982	0.071	42.529	0.982
25	1.2	1.1	7	3.749	3.432	0.984	0.094	32.289	0.984
25	1.2	1.1	4	4.518	2.239	0.977	0.113	20.845	0.977
25	1.2	1.1	2	7.487	0.910	0.962	0.187	8.4716	0.962
20	1.2	1.1	7	4.107	4.168	0.983	0.082	48.139	0.983
25	1.2	1.1	7	3.749	3.432	0.984	0.094	32.289	0.984
30	1.2	1.1	7	2.834	2.168	0.985	0.095	16.806	0.985
25	0.8	1.1	7	4.647	2.487	0.998	0.116	15.286	0.998
25	1.2	1.1	7	3.749	3.432	0.984	0.094	32.289	0.984
25	1.6	1.1	7	2.817	3.538	0.982	0.070	45.545	0.982
25	1.2	1.1	7	3.749	3.432	0.984	0.094	32.289	0.984
25	1.2	2.1	7	4.108	2.959	0.996	0.103	14.429	0.996
25	1.2	3.1	7	5.518	0.840	0.929	0.138	2.775	0.929

and the diffusion phenomena are predominant compared with the axial dispersion phenomena in the mass transfer [48, 49]. In addition, an increase in the bed height leads to a larger specific surface of the adsorbent which provides more available binding sites. As expected, the adsorption capacity increases with an increase in the bed height, since the total surface area of the fixed-bed column increases [50, 51].

The effect of flow rate on DC biosorption by MCM was studied by varying it from 1.1 to 3.1 mL/min, keeping the bed height and initial solution concentration constant at 1.2 cm and 25 mg/L, respectively. A decrease in adsorption capacity from 2.448 to 2.282 mg/g by increasing the flow rate from 1.1 to 3.1 mL/min is shown in Table 1, from which it can be seen clearly that the flow rate has strong effects on the adsorption trend in a fixed-bed column. This behavior can be explained in terms of the fact that the high flow rate cannot provide the DC molecule enough time to migrate from the solution to the adsorbent surface and penetrate into the center of the adsorbent and then bind with the activated sites [52]. In other words, the contact time must be prolonged and the intraparticle diffusion is effective at a lower flow rate. Typical breakthrough curves are plotted in Figure 5(d) where a much sharper breakthrough curve with an increase in the flow rate was observed. An abatement removal efficiency and steeper breakthrough curve occurred, suggesting that the contaminant had inadequate time to react with the functional groups before the adsorption equilibrium is conducted [53]. This is because the adsorption process was affected by limited residence time of the adsorbate in the fixed bed. With increasing the flow rate, the residence time is longer as the DC molecule diffuses into the pore of the adsorbent. Additionally, an increase in the flow rate decreases the external diffusion mass transfer resistance at the surface of the adsorbents, finally leading to a fast saturation and an earlier breakthrough time.

**3.3. Breakthrough Model Analysis.** The design and scale-up of fixed-bed adsorption columns require the prediction of the

concentration-time profile or breakthrough curve for the effluent [54]. Many mathematical theory models with theoretical rigor are differential in nature and usually involve complex numerical methods. Because of this, in this study, we used the Thomas and Yoon-Nelson models to predict the dynamic performance of the column, which are empirical and semiempirical mathematical models. These semiempirical models are less rigorous than other theoretical models but easier to apply. All the model parameters are listed in Table 2.

**3.3.1. Thomas Model.** The Thomas model is one of the most popular and widely used to represent the behavior of the adsorption process. This model assumes that the main reason limiting the adsorption in a fixed-bed column is the mass transfer at the interface rather than the chemical reaction [55, 56]. The Thomas model is given in the following equation:

$$\ln \left( \frac{C_0}{C_t} - 1 \right) = \frac{k_T \cdot q_0 \cdot m}{Q} - k_t \cdot C_0 \cdot t, \quad (5)$$

where  $k_T$  (mL/(min·mg)) is the Thomas rate constant,  $q_0$  (mg/g) is the predicted adsorption capacity of the fixed-bed column,  $m$  (g) is the mass of adsorbent, and  $Q$  (mL/min) is the flow rate.  $C_0$  (mg/L) and  $C_t$  (mg/L) are the influent and the effluent concentrations of DC at interval time, respectively.

The adsorption capacity of the column  $q_0$  and the Thomas rate constant  $k_T$  are determined from the plot of  $\ln [(C_0/C_t) - 1]$  against  $t$ . The difference of the experimental and predicted adsorption capacity of DC in the fixed-bed columns is found to be not negligible. The fixed-bed columns did not reach their maximum capacity from the predicted results. But from the regression coefficient ( $R^2$ ) which ranged from 0.929 to 0.998, it can be concluded that the Thomas model fitted the experimental data very well. The value of constant  $k_T$  tends to increase as the initial influent DC concentrations decreased from 30 to 20 mg/L, which implies a lower mass transfer and an enhanced adsorption capacity at

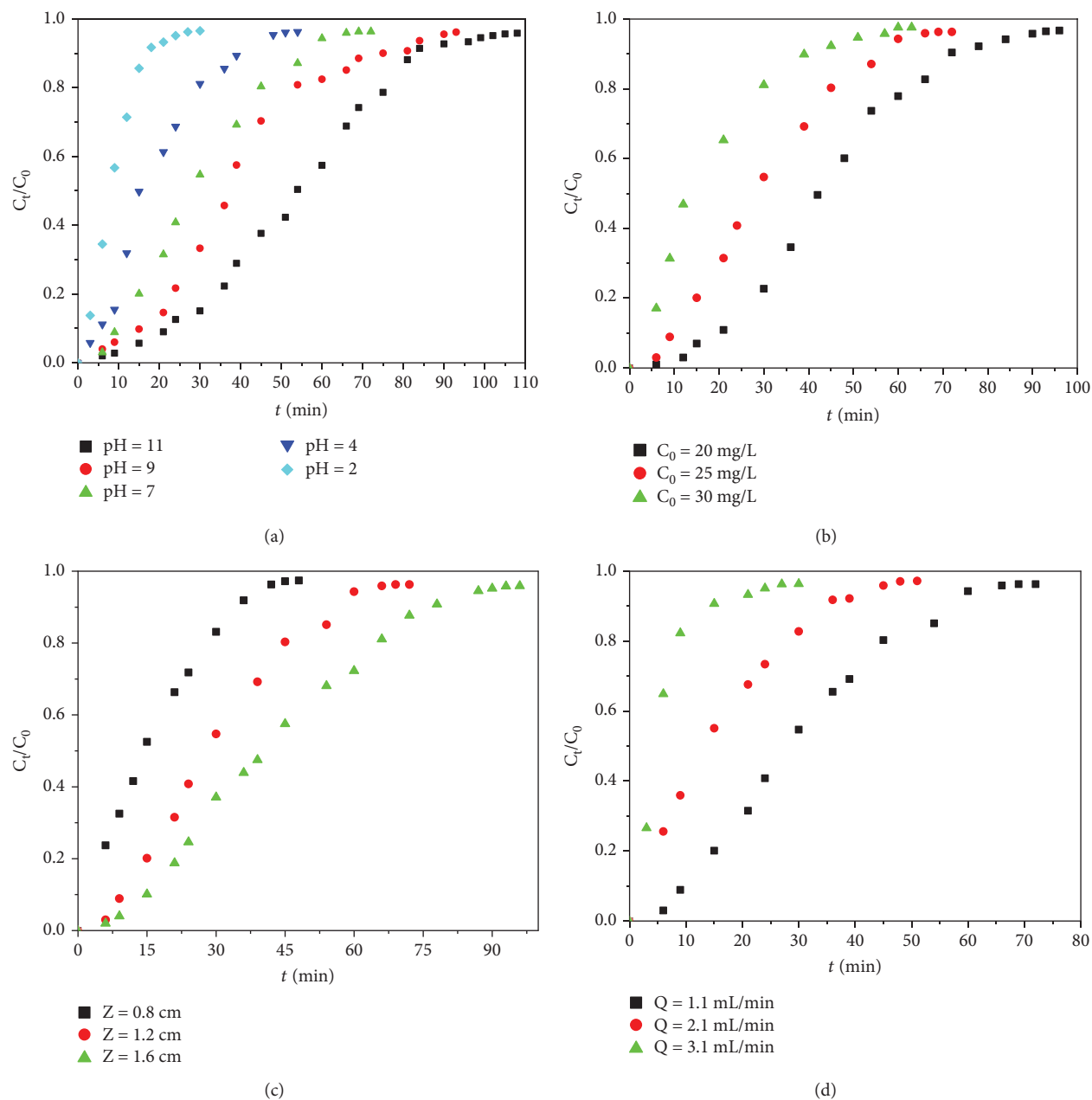


FIGURE 5: Breakthrough curve for adsorption of DC at different column conditions: (a) pH ( $Z = 1.2$  cm,  $Q = 1.1$  mL/min, and  $C_0 = 25$  mg/L); (b) initial concentration ( $Z = 1.2$  cm,  $Q = 1.1$  mL/min, and pH = 7); (c) bed depth ( $C_0 = 25$  mg/L,  $Q = 1.1$  mL/min, pH = 7); (d) flow rate ( $Z = 1.2$  cm,  $C_0 = 25$  mg/L, and pH = 7).

a lower concentration. Furthermore, this phenomenon is because of an increase in the influence of mass transfer on the adsorption process [41]. These results suggest that the driving force is mainly coming from the concentration difference between the DC molecule on the sorbent and the DC molecule in the solution. A similar trend has been obtained where the bed depth shows a decrease. As the bed depth decreases from 1.6 to 0.8 cm, the  $k_T$  value increases from 2.817 to 4.647 whereas the theory adsorption capacity showed a reverse trend. With the increase in the flow rate, the theory adsorption capacity  $q_0$  decreased but the  $k_T$  value increased. This phenomenon supposes that the contact time

is a predominant reason influencing adsorption capacity. The above results indicate that lower initial influent DC concentration, higher bed height, and lower flow rate are favorable for higher adsorption of DC onto MCM in a continuous column process.

3.3.2. *Yoon-Nelson Model.* The linearized Yoon-Nelson model is presented by the following equation [57–59]:

$$\ln \left( \frac{C_t}{C_0 - C_t} = k_Y \cdot t - \tau \cdot k_Y \right), \quad (6)$$

TABLE 2: Experimental parameters of adsorptive removal of DC in a fixed bed.

$C_0$ (mg/L)	$Z$ (cm)	$Q$ (mL/min)	pH	$t_{\text{total}}$ (min)	$m_{\text{total}}$ (mg)	$q_{\text{total}}$ (mg)	$q_e$ (mg/g)	$V_{\text{eff}}$ (mL)	EBCT (min)
25	1.2	1.1	11	108	2.970	1.233	4.816	118.8	0.308
25	1.2	1.1	9	93	2.558	0.839	3.281	102.3	0.308
25	1.2	1.1	7	72	1.980	0.627	2.448	79.2	0.308
25	1.2	1.1	4	54	1.485	0.426	1.666	59.4	0.308
25	1.2	1.1	2	30	0.825	0.239	0.934	33.0	0.308
20	1.2	1.1	7	96	2.112	0.801	3.128	105.6	0.308
25	1.2	1.1	7	72	1.980	0.627	2.448	79.2	0.308
30	1.2	1.1	7	63	2.079	0.523	2.045	69.3	0.308
25	0.8	1.1	7	48	1.320	0.396	2.333	52.8	0.206
25	1.2	1.1	7	72	1.980	0.627	2.448	79.2	0.308
25	1.6	1.1	7	96	2.640	0.989	2.787	105.6	0.411
25	1.2	1.1	7	72	1.980	0.627	2.448	79.2	0.308
25	1.2	2.1	7	51	2.678	0.598	2.334	107.1	0.162
25	1.2	3.1	7	30	2.325	0.585	2.282	93.0	0.109

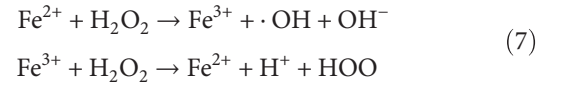
where  $k_Y$  is the adsorption rate constant ( $\text{min}^{-1}$ ),  $\tau$  is the time required to reach 50% adsorbate breakthrough (min), and  $t$  is the time (min). The parameters  $k_Y$  and  $\tau$  are obtained from the slope and intercept of the graph between  $\ln [C_t/(C_0 - C_t)]$  and time ( $t$ ).

Table 2 shows the results. The regression coefficient ( $R^2$ ) values are higher than 0.9. Consequently, the calculated  $\tau$  values are quite close to the time needed for 50% DC breakthrough from the experiments, which indicates that a good fitting has been obtained. The  $k_Y$  values increase with increasing DC concentration due to the increase in the force controlling the mass transfer between the liquid phase and solid phase [47]. In addition, the time necessary to reach 50% of the retention ( $\tau$ ) significantly increases with the decrease in DC concentration. This is because the bed exhaustion occurred more rapidly before the complete saturation of MCM at higher DC concentration. The  $k_Y$  values decrease but the 50% breakthrough time  $\tau$  shows a reverse trend when the bed depth increases. The  $k_Y$  values increase and the  $\tau$  decreases with an increasing flow rate.

**3.4. Regeneration of MCM via Heterogeneous Fenton Oxidation Reaction.** From an economic standpoint, the reusability of the adsorbents is one of the most important features to exemplify the potential of MCM for real applications. Moreover, both the magnetic and oxidation properties imparted by the mixing  $\text{Fe}_3\text{O}_4$  nanoparticles are important for practical application. In this study, the regeneration experiments were carried out by using  $\text{H}_2\text{O}_2$  solution to trigger the heterogeneous Fenton oxidation. According to the contrast experiments, the DC was hardly degraded in the absence of  $\text{H}_2\text{O}_2$  (or Fe ion).

During the adsorption/regeneration process, the DC molecules are first removed from polluted water by the adsorption process and pre-concentrated on the surface of MCM adsorbent. Then, the regeneration processes are carried out by triggering the heterogeneous Fenton oxidation. Namely, the decomposition of  $\text{H}_2\text{O}_2$  using  $\text{Fe}_3\text{O}_4$  nanoparticles as Fenton catalysts was able to generate principal

oxidizing species like  $\cdot\text{OH}$  radicals according to the following reactions:



In these ways, the saturated DC molecules on the surface of MCM adsorbent could be oxidized to degradation products.



To investigate the effect of  $\text{H}_2\text{O}_2$  doses on the regeneration efficiency of MCM, the regeneration process was conducted with different amounts of  $\text{H}_2\text{O}_2$ . And the performance of the continuous column was evaluated for three consecutive adsorption/regeneration cycles. The DC concentration, flow rate, bed depth, and pH were kept constant at 25 mg/L, 1.1 mL/min, 1.2 cm, and 7, respectively. The experimental results are shown in Figure 6.

In Figure 6, the regeneration efficiency is expressed as

$$\eta = \frac{t_r}{t_f} \cdot 100\%, \quad (9)$$

where  $\eta$  is the regeneration efficiency of the saturated MCM using  $\text{H}_2\text{O}_2$ ,  $t_r$  is the total flow time in the regeneration carbon, and  $t_f$  is the total flow time in the fresh carbon.

As shown in Figure 6, the regeneration efficiency can be easily controlled by adjusting the  $\text{H}_2\text{O}_2$  dosage, and the optimal  $\text{H}_2\text{O}_2$  concentration is 5% in this study. The regeneration efficiency is calculated as 78%, 93%, 72%, and 55% for  $\text{H}_2\text{O}_2$  dosage in feed of 2%, 5%, 8%, and 11%, respectively. The regeneration efficiency increased with ranging  $\text{H}_2\text{O}_2$  dosage from 2% to 5% and then decreased with ranging  $\text{H}_2\text{O}_2$  dosage 5%–11%. This phenomenon can be well explained from two aspects. On the one hand, the Fe ions play a significant role as a catalyst leading to the rapid

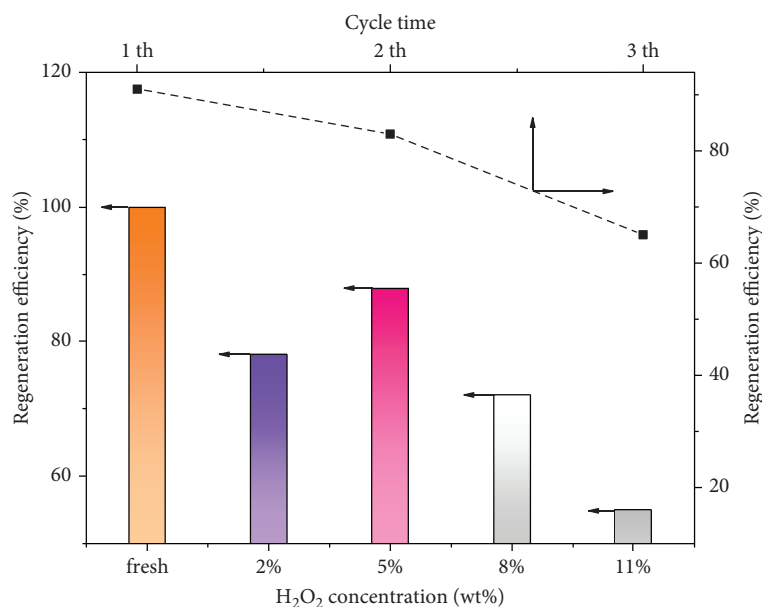


FIGURE 6: Regeneration efficiency of the saturated MCM at different H<sub>2</sub>O<sub>2</sub> concentrations and reusability of MCM with optimal H<sub>2</sub>O<sub>2</sub> concentration.

regeneration of reactive oxygen species, such as  $\cdot\text{OH}$  radicals which were mainly responsible for the degradation of organic contaminant [60]. Consequently, the heterogeneous Fenton oxidation process was carried out by degrading DC molecules easily in the presence of H<sub>2</sub>O<sub>2</sub> solution. On the other hand, the reduced catalytic rate with higher H<sub>2</sub>O<sub>2</sub> concentrations such as 8% and 11% was probably caused by the competition of the excessive H<sub>2</sub>O<sub>2</sub> and target DC molecule against the active sites of the catalyst. Additionally, if the original concentration of H<sub>2</sub>O<sub>2</sub> was higher, the H<sub>2</sub>O<sub>2</sub> might scavenge the  $\cdot\text{OH}$  radical seriously and hence the regeneration efficiency of the DC molecule decreased [61].

As seen in Figure 6, a saturated fixed bed can be easily restored by the Fe<sub>3</sub>O<sub>4</sub>/H<sub>2</sub>O<sub>2</sub> Fenton-like oxidation process following a relatively low concentration of aqueous H<sub>2</sub>O<sub>2</sub> (5%). And the good performance of a saturated fixed bed with 5% H<sub>2</sub>O<sub>2</sub> was calculated for three consecutive adsorption/regeneration cycles. The regeneration efficiency was generally above 80% in two previous cycles. The excellent reusability of MCM is because of its strong affinity on DC and high degradation ability during the first and second adsorption cycle, implying that the MCM integrating the adsorption feature of chitosan carbon and the catalytic property of Fe<sub>3</sub>O<sub>4</sub> may have a good application prospect on multiple adsorption cycles.

The embedding of Fe<sub>3</sub>O<sub>4</sub> nanoparticles into the CSM substrate is beneficial to the easy separation of catalysts from the aqueous system. In order to verify magnetic separation of MCM, an external magnet was used to separate the samples from mixture solution. Figure 7(a) shows that MCM was settled at the bottom of the test vessel by self-gravity without a magnetic field. When an external magnetic field was introduced, the MCMs can be completely attracted to the sidewall from the aqueous solution within about 5 seconds, as seen in Figure 7(b). Such excellent magnetic property

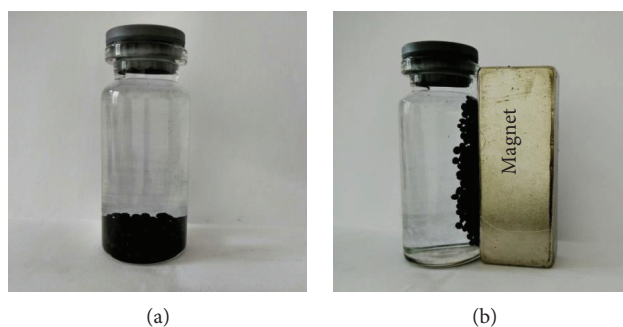


FIGURE 7: Photographs of separation of MCM by gravity (a) and magnetism (b).

means that MCM can be easily be separated and collected from the adsorption system by a simple magnetic process after adsorption.

#### 4. Conclusion

In summary, a low-cost magnetic chitosan@Fe<sub>3</sub>O<sub>4</sub> composite material, which integrates the adsorption features of chitosan with the magnetic and catalytic properties of Fe<sub>3</sub>O<sub>4</sub> nanoparticles, was synthesized via an alkali gelation-thermal cracking process. The mechanism for the formation of the product was discussed in detail. These composites exhibited excellent properties for the effective removal and oxidative destruction of DC from aqueous solution via a fixed-bed column method. The optimum conditions were observed at an initial DC concentration of 20 mg/L, a flow rate of 1.1 mL/min, and a bed depth of 1.6 cm. The Thomas and Yoon-Nelson models showed a good agreement with the experimental data and could be applied for the prediction of the fixed-bed column properties and breakthrough curves. The MCM possesses a ferromagnetic characteristic allowing them to be easily

separated from the aqueous system by an external magnet. The regeneration of the saturated adsorbent after the adsorption process can be realized using  $H_2O_2$  solution and could be controlled easily by adjusting the  $H_2O_2$  dosage. Considering the abundant and low-cost raw materials, the facile fabrication route, the easy recovery and separation process, and the excellent reusability, the magnetic  $Fe_3O_4$ @chitosan carbon microbeads may serve as a promising and scalable adsorbent for the removal and oxidation of organic compounds in practical applications.

### Data Availability

The data used to support the findings of this study are available from the corresponding author upon request.

### Conflicts of Interest

The authors declare that they have no conflicts of interest.

### Acknowledgments

This work was financially supported by the Fund Project of Shaanxi Key Laboratory of Land Consolidation and Fundamental Research Funds for the Central Universities (nos. 310829162014, 310829161015, 310829175001, and 310829165007).

### References

- [1] L. Ji, F. Liu, Z. Xu, S. Zheng, and D. Zhu, "Adsorption of pharmaceutical antibiotics on template-synthesized ordered micro- and mesoporous carbons," *Environmental Science & Technology*, vol. 44, no. 8, pp. 3116–3122, 2010.
- [2] M. Majewski, "A current opinion on the safety and efficacy of doxycycline including parenteral administration – a review," *Polish Annals of Medicine*, vol. 21, no. 1, pp. 57–62, 2014.
- [3] M. Ghaemi and G. Absalan, "Fast removal and determination of doxycycline in water samples and honey by  $Fe_3O_4$  magnetic nanoparticles," *Journal of the Iranian Chemical Society*, vol. 12, no. 1, pp. 1–7, 2015.
- [4] L.-J. Zhou, G.-G. Ying, S. Liu et al., "Occurrence and fate of eleven classes of antibiotics in two typical wastewater treatment plants in South China," *Science of the Total Environment*, vol. 452–453, no. 5, pp. 365–376, 2013.
- [5] Y. Zhao, F. Tong, X. Gu, C. Gu, X. Wang, and Y. Zhang, "Insights into tetracycline adsorption onto goethite: experiments and modeling," *Science of the Total Environment*, vol. 470–471, no. 2, pp. 19–25, 2014.
- [6] I. Braschi, S. Blasioli, L. Gigli, C. E. Gessa, A. Alberti, and A. Martucci, "Removal of sulfonamide antibiotics from water: evidence of adsorption into an organophilic zeolite Y by its structural modifications," *Journal of Hazardous Materials*, vol. 178, no. 1–3, pp. 218–225, 2010.
- [7] B. Pan and B. Xing, "Adsorption mechanisms of organic chemicals on carbon nanotubes," *Environmental Science & Technology*, vol. 42, no. 24, pp. 9005–9013, 2008.
- [8] Y. S. Ho and G. McKay, "The kinetics of sorption of divalent metal ions onto sphagnum moss peat," *Water Research*, vol. 34, no. 3, pp. 735–742, 2000.
- [9] C. Başar, "Applicability of the various adsorption models of three dyes adsorption onto activated carbon prepared waste apricot," *Journal of Hazardous Materials*, vol. 135, no. 1–3, pp. 232–241, 2006.
- [10] A. Baglieri, D. Borzi, C. Abbate, M. Nègre, and M. Gennari, "Removal of fenhexamid and pyrimethanil from aqueous solutions by clays and organoclays," *Journal of Environmental Science and Health, Part B*, vol. 44, no. 3, pp. 220–225, 2009.
- [11] Y. Gao, Y. Li, L. Zhang et al., "Adsorption and removal of tetracycline antibiotics from aqueous solution by graphene oxide," *Journal of Colloid and Interface Science*, vol. 368, no. 1, pp. 540–546, 2012.
- [12] P. Chutia, S. Kato, T. Kojima, and S. Satokawa, "Adsorption of As (V) on surfactant-modified natural zeolites," *Journal of Hazardous Materials*, vol. 162, no. 1, pp. 204–211, 2009.
- [13] I. D. Mall, V. C. Srivastava, N. K. Agarwal, and I. M. Mishra, "Adsorptive removal of malachite green dye from aqueous solution by bagasse fly ash and activated carbon-kinetic study and equilibrium isotherm analyses," *Colloids and Surfaces A: Physicochemical and Engineering Aspects*, vol. 264, no. 1–3, pp. 17–28, 2005.
- [14] B. Hameed, A. Din, and A. Ahmad, "Adsorption of methylene blue onto bamboo-based activated carbon: kinetics and equilibrium studies," *Journal of Hazardous Materials*, vol. 141, no. 3, pp. 819–825, 2007.
- [15] I. D. Mall, V. C. Srivastava, N. K. Agarwal, and I. M. Mishra, "Removal of Congo red from aqueous solution by bagasse fly ash and activated carbon: kinetic study and equilibrium isotherm analyses," *Chemosphere*, vol. 61, no. 4, pp. 492–501, 2005.
- [16] S. W. Nahm, W. G. Shim, Y.-K. Park, and S. C. Kim, "Thermal and chemical regeneration of spent activated carbon and its adsorption property for toluene," *Chemical Engineering Journal*, vol. 210, no. 6, pp. 500–509, 2012.
- [17] Y. I. Matatov-Meytal and M. Sheintuch, "Abatement of pollutants by adsorption and oxidative catalytic regeneration," *Industrial & Engineering Chemistry Research*, vol. 36, no. 10, pp. 4374–4380, 1997.
- [18] Y. Wang and R. T. Yang, "Desulfurization of liquid fuels by adsorption on carbon-based sorbents and ultrasound-assisted sorbent regeneration," *Langmuir*, vol. 23, no. 7, pp. 3825–3831, 2007.
- [19] S. N. Hussain, H. M. A. Asghar, H. Sattar, N. W. Brown, and E. P. L. Roberts, "Removal of tartrazine from water by adsorption with electrochemical regeneration," *Chemical Engineering Communications*, vol. 202, no. 10, pp. 1280–1288, 2015.
- [20] X. Liu, G. Yu, and W. Han, "Granular activated carbon adsorption and microwave regeneration for the treatment of 2, 4,5-trichlorobiphenyl in simulated soil-washing solution," *Journal of Hazardous Materials*, vol. 147, no. 3, pp. 746–751, 2007.
- [21] J. H. Ramirez, F. J. Maldonado-Hódar, A. F. Pérez-Cadenas, C. Moreno-Castilla, C. A. Costa, and L. M. Madeira, "Azodye Orange II degradation by heterogeneous Fenton-like reaction using carbon-Fe catalysts," *Applied Catalysis B Environmental*, vol. 75, no. 3–4, pp. 312–323, 2007.
- [22] X. Zhang, B. Bai, H. Wang, and Y. Suo, "Facile fabrication of sea buckthorn biocarbon (SB)@ $\alpha$ - $Fe_2O_3$  composite catalysts and their applications for adsorptive removal of doxycycline wastewater through a cohesive heterogeneous Fenton-like regeneration," *RSC Advances*, vol. 6, no. 44, pp. 38159–38168, 2016.

- [23] A. Zhang, N. Wang, J. Zhou, P. Jiang, and G. Liu, "Heterogeneous Fenton-like catalytic removal of p-nitrophenol in water using acid-activated fly ash," *Journal of Hazardous Materials*, vol. 201-202, no. 1, pp. 68-73, 2012.
- [24] C.-A. Chiu, K. Hristovski, S. Huling, and P. Westerhoff, "In-situ regeneration of saturated granular activated carbon by an iron oxide nanocatalyst," *Water Research*, vol. 47, no. 4, pp. 1596-1603, 2013.
- [25] T. Liu, H. You, and Q. Chen, "Heterogeneous photo-Fenton degradation of polyacrylamide in aqueous solution over Fe(III)-SiO<sub>2</sub> catalyst," *Journal of Hazardous Materials*, vol. 162, no. 2-3, pp. 860-865, 2009.
- [26] L. Gu, N. Zhu, H. Guo, S. Huang, Z. Lou, and H. Yuan, "Adsorption and Fenton-like degradation of naphthalene dye intermediate on sewage sludge derived porous carbon," *Journal of Hazardous Materials*, vol. 246-247, pp. 145-153, 2013.
- [27] R. Song, B. Bai, G. L. Puma, H. Wang, and Y. Suo, "Biosorption of azo dyes by raspberry-like Fe<sub>3</sub>O<sub>4</sub>@ yeast magnetic microspheres and their efficient regeneration using heterogeneous Fenton-like catalytic processes over an up-flow packed reactor," *Reaction Kinetics, Mechanisms and Catalysis*, vol. 115, no. 2, pp. 547-562, 2015.
- [28] D. Y. Pratt, L. D. Wilson, and J. A. Kozinski, "Preparation and sorption studies of glutaraldehyde cross-linked chitosan copolymers," *Journal of Colloid and Interface Science*, vol. 395, pp. 205-211, 2013.
- [29] Y. Li and F. S. Zhang, "Catalytic oxidation of methyl orange by an amorphous FeOOH catalyst developed from a high iron-containing fly ash," *Chemical Engineering Journal*, vol. 158, no. 2, pp. 148-153, 2010.
- [30] Y. Qiu, Z. Ma, and P. Hu, "Environmentally benign magnetic chitosan/Fe<sub>3</sub>O<sub>4</sub> composites as reductant and stabilizer for anchoring Au NPs and their catalytic reduction of 4-nitrophenol," *Journal of Materials Chemistry A*, vol. 2, no. 33, pp. 13471-13478, 2014.
- [31] D. Wei, Y. Ye, X. Jia, C. Yuan, and W. Qian, "Chitosan as an active support for assembly of metal nanoparticles and application of the resultant bioconjugates in catalysis," *Carbohydrate Research*, vol. 345, no. 1, pp. 74-81, 2010.
- [32] P. Zheng, Z. Tong, and B. Bai, "Facile synthesis of  $\alpha$ -Fe<sub>2</sub>O<sub>3</sub>@ porous hollow yeast-based carbonaceous microspheres for fluorescent whitening agent-VBL wastewater treatment," *Journal of Solid State Chemistry*, vol. 235, pp. 119-124, 2016.
- [33] D. Feng, B. Bai, H. Wang, and Y. Suo, "Enhanced mechanical stability and sensitive swelling performance of chitosan/yeast hybrid hydrogel beads," *New Journal of Chemistry*, vol. 40, no. 4, pp. 3350-3362, 2016.
- [34] J. Dean, *Lange's Handbook of Chemistry*, McGraw-Hill, 1999.
- [35] G.-Y. Li, Y.-R. Jiang, K.-L. Huang, P. Ding, and L.-L. Yao, "Kinetics of adsorption of Saccharomyces cerevisiae mandelated dehydrogenase on magnetic Fe<sub>3</sub>O<sub>4</sub>-chitosan nanoparticles," *Colloids and Surfaces A: Physicochemical and Engineering Aspects*, vol. 320, no. 1-3, pp. 11-18, 2008.
- [36] L. Zhou, Y. Wang, Z. Liu, and Q. Huang, "Characteristics of equilibrium, kinetics studies for adsorption of Hg(II), Cu(II), and Ni(II) ions by thiourea-modified magnetic chitosan microspheres," *Journal of Hazardous Materials*, vol. 161, no. 2-3, pp. 995-1002, 2009.
- [37] S.-F. Wang, L. Shen, W.-D. Zhang, and Y.-J. Tong, "Preparation and mechanical properties of chitosan/carbon nanotubes composites," *Biomacromolecules*, vol. 6, no. 6, pp. 3067-3072, 2005.
- [38] M. L. Occelli, J. P. Olivier, A. Petre, and A. Auroux, "Determination of pore size distribution, surface area, and acidity in fluid cracking catalysts (FCCs) from nonlocal density functional theoretical models of adsorption and from microcalorimetry methods," *The Journal of Physical Chemistry. B*, vol. 107, no. 17, pp. 4128-4136, 2003.
- [39] F. Kazemi, H. Younesi, A. A. Ghoreyshi, N. Bahramifar, and A. Heidari, "Thiol-incorporated activated carbon derived from fir wood sawdust as an efficient adsorbent for the removal of mercury ion: batch and fixed-bed column studies," *Process Safety and Environmental Protection*, vol. 100, no. 2-3, pp. 22-35, 2016.
- [40] S. K. Maji, Y. H. Kao, C. J. Wang, G. S. Lu, J. J. Wu, and C. W. Liu, "Fixed bed adsorption of As(III) on iron-oxide-coated natural rock (IOCNR) and application to real arsenic-bearing groundwater," *Chemical Engineering Journal*, vol. 203, no. 9, pp. 285-293, 2012.
- [41] Z. Aksu and F. Gönen, "Biosorption of phenol by immobilized activated sludge in a continuous packed bed: prediction of breakthrough curves," *Process Biochemistry*, vol. 39, no. 5, pp. 599-613, 2004.
- [42] Y. Chao, W. Zhu, X. Wu et al., "Application of graphene-like layered molybdenum disulfide and its excellent adsorption behavior for doxycycline antibiotic," *Chemical Engineering Journal*, vol. 243, no. 5, pp. 60-67, 2014.
- [43] G. D. Sheng, D. D. Shao, X. M. Ren et al., "Kinetics and thermodynamics of adsorption of ionizable aromatic compounds from aqueous solutions by as-prepared and oxidized multi-walled carbon nanotubes," *Journal of Hazardous Materials*, vol. 178, no. 1-3, pp. 505-516, 2010.
- [44] S. Hassan and F. G. Ali, "Equilibrium, thermodynamics and kinetics study of doxycycline adsorption from aqueous solution using spent black tea leaves and pomegranate peel wastes," *International Journal of Development Research*, no. 4, pp. 129-135, 2014.
- [45] N. Sakkayawong, P. Thiravetyan, and W. Nakbanpote, "Adsorption mechanism of synthetic reactive dye wastewater by chitosan," *Journal of Colloid and Interface Science*, vol. 286, no. 1, pp. 36-42, 2005.
- [46] S. Mondal, K. Aikat, and G. Halder, "Ranitidine hydrochloride sorption onto superheated steam activated biochar derived from mung bean husk in fixed bed column," *Journal of Environmental Chemical Engineering*, vol. 4, no. 1, pp. 488-497, 2016.
- [47] R. Han, Y. Wang, W. Yu, W. Zou, J. Shi, and H. Liu, "Biosorption of methylene blue from aqueous solution by rice husk in a fixed-bed column," *Journal of Hazardous Materials*, vol. 141, no. 3, pp. 713-718, 2007.
- [48] K. U. Ahamad and M. Jawed, "Breakthrough studies with mono- and binary-metal ion systems comprising of Fe(II) and As(III) using community prepared wooden charcoal packed columns," *Desalination*, vol. 285, pp. 345-351, 2012.
- [49] S. H. Hasan, P. Srivastava, and M. Talat, "Biosorption of lead using immobilized Aeromonas hydrophila, biomass in up flow column system: factorial design for process optimization," *Journal of Hazardous Materials*, vol. 177, no. 1-3, pp. 312-322, 2010.

- [50] P. D. Saha, S. Chakraborty, and S. Chowdhury, "Batch and continuous (fixed-bed column) biosorption of crystal violet by *Artocarpus heterophyllus* (jackfruit) leaf powder," *Colloids and Surfaces B: Biointerfaces*, vol. 92, no. 24, pp. 262–270, 2012.
- [51] J. Cruz-Olivares, C. Pérez-Alonso, C. Barrera-Díaz, F. Ureña-Núñez, M. C. Chaparro-Mercado, and B. Bilyeu, "Modeling of lead (II) biosorption by residue of allspice in a fixed-bed column," *Chemical Engineering Journal*, vol. 228, pp. 21–27, 2013.
- [52] S.-T. Song, Y.-F. Hau, N. Saman et al., "Process analysis of mercury adsorption onto chemically modified rice straw in a fixed-bed adsorber," *Journal of Environmental Chemical Engineering*, vol. 4, no. 2, pp. 1685–1697, 2016.
- [53] Y. Long, D. Lei, J. Ni, Z. Ren, C. Chen, and H. Xu, "Packed bed column studies on lead (II) removal from industrial wastewater by modified *Agaricus bisporus*," *Bioresource Technology*, vol. 152, no. 1, pp. 457–463, 2014.
- [54] M. T. Uddin, M. Rukanuzzaman, M. M. R. Khan, M. A. Islam, and M. Uddin, "Adsorption of methylene blue from aqueous solution by jackfruit (*Artocarpus heterophyllus*) leaf powder: a fixed-bed column study," *Journal of Environmental Management*, vol. 90, no. 11, pp. 3443–3450, 2009.
- [55] S. Sadaf and H. N. Bhatti, "Batch and fixed bed column studies for the removal of Indosol Yellow BG dye by peanut husk," *Journal of the Taiwan Institute of Chemical Engineers*, vol. 45, no. 2, pp. 541–553, 2014.
- [56] M. Riazi, A. R. Keshtkar, and M. A. Moosavian, "Batch and continuous fixed-bed column biosorption of thorium (IV) from aqueous solutions: equilibrium and dynamic modeling," *Journal of Radioanalytical and Nuclear Chemistry*, vol. 301, no. 2, pp. 493–503, 2014.
- [57] H. Muhamad, H. Doan, and A. Lohi, "Batch and continuous fixed-bed column biosorption of  $\text{Cd}^{2+}$  and  $\text{Cu}^{2+}$ ," *Chemical Engineering Journal*, vol. 158, no. 3, pp. 369–377, 2010.
- [58] M. Calero, F. Hernáinz, G. Blázquez, G. Tenorio, and M. A. Martín-Lara, "Study of Cr (III) biosorption in a fixed-bed column," *Journal of Hazardous Materials*, vol. 171, no. 1–3, pp. 886–893, 2009.
- [59] Y. H. Yoon and J. H. Nelson, "Application of gas adsorption kinetics. I. A theoretical model for respirator cartridge service life," *American Industrial Hygiene Association Journal*, vol. 45, no. 8, pp. 509–516, 2010.
- [60] H. Niu, D. Zhang, S. Zhang, X. Zhang, Z. Meng, and Y. Cai, "Humic acid coated  $\text{Fe}_3\text{O}_4$  magnetic nanoparticles as highly efficient Fenton-like catalyst for complete mineralization of sulfathiazole," *Journal of Hazardous Materials*, vol. 190, no. 1–3, pp. 559–565, 2011.
- [61] W. Wang, Y. Liu, T. Li, and M. Zhou, "Heterogeneous Fenton catalytic degradation of phenol based on controlled release of magnetic nanoparticles," *Chemical Engineering Journal*, vol. 242, no. 242, pp. 1–9, 2014.

## Research Article

# Appearance of Ferromagnetic Property for Si Nanopolycrystalline Body and Vanishing of Electrical Resistances at Local High Frequencies

Taku Saiki , Yukio Iida, and Mitsuru Inada

Faculty of Engineering Science, Kansai University, 3-3-35 Yamate, Suita, Osaka 564-8680, Japan

Correspondence should be addressed to Taku Saiki; [tsaiki@kansai-u.ac.jp](mailto:tsaiki@kansai-u.ac.jp)

Received 17 July 2018; Accepted 8 October 2018; Published 25 November 2018

Guest Editor: Vidyadhar Singh

Copyright © 2018 Taku Saiki et al. This is an open access article distributed under the Creative Commons Attribution License, which permits unrestricted use, distribution, and reproduction in any medium, provided the original work is properly cited.

Reduction in the skin effect for the sintered Si nanopolycrystalline body as an electricity conductor at a high frequency due to its nanostructure was studied. Singular disappearance of electrical resistances near a local high magnetic harmonic frequency of a few MHz was observed. This phenomenon has not been observed for conventional ferromagnetic metals. The measured electrical resistances changed to almost  $0\text{ m}\Omega$  at room temperature. At the same time, negative resistance of the sintered Si nanopolycrystalline body was observed. It will be applicable to electronic transmittance lines or semiconductors. Numerical calculation was also performed on the electrical resistance with frequency dependency while considering the electric field and magnetic field in the sintered Si nanopolycrystalline body. The experimental and calculated results are compared. The calculation could explain the variation of the relative permittivity of the Si nanopolycrystalline body and the phenomenon for the theoretical disappearance of the resistivity at the MHz frequency. Reduced Si nanoparticles from  $\text{SiO}_2$  powder were synthesized by laser ablation in liquid. A Si nanopolycrystalline body made of the reduced Si nanoparticles was fabricated. It was found by measuring the magnetization property of the body of the sintered Si nanopolycrystalline body which is ferromagnetic. Dangling bonds (unpaired electrons) have long been known to occur due to defects in Si crystals. Perfect Si without defective crystals has no dangling bonds. However, Si nanoparticles have many dangling bonds. High-density dangling bonds cause the sintered Si nanopolycrystalline body to have ferromagnetism. In this study, the density of the unpaired electrons in the sintered Si nanopolycrystalline body was observed using ESR. It has been clarified that the Si nanopowder and the sintered Si nanopolycrystalline body have numerous dangling bonds. Both densities of the dangling bonds were evaluated.

## 1. Introduction

Reduction of AC resistance owing to the skin effect at high frequency from MHz to GHz in electronic devices or transmittance lines has been attracting attention now due to its ability to realize low-power consumption. We can expect that low-loss electric power lines and low-power-consumption electronic devices with low heat generation can be achieved by developing metals and semiconductors that have the reduced skin effect [1–4]. Research has also been conducted on the reductions in the skin effect for electric power lines using litz wire [2] or the negative permittivity of magnetic materials [5, 6]. A multilayered material, which consists of different materials, such as metal and magnetic, is used for

reducing the skin effect when a high-frequency current is conducted. This makes the effective permittivity equal zero when magnetic resonance occurs in magnetic material, negative permittivity at the real part of the relative permeability appears, and magnetic flux is canceled in multilayered materials [6].

At the same time, a technology has been developed to make electrical circuits at low temperatures of below 470 K using paste or ink consisting of Au [7], Ag [8, 9], Cu [10], Fe [11, 12], Al [11, 12], and Mg [12] nanoparticles owing to the phenomena of melting point depression. The metal nanoparticle paste and ink have often been sintered by furnace or pulsed light-like Xe flash lamp [8, 9] or laser [12, 13] in a short time. A free-form electrical circuit

can be made in a short time and for low cost by using them. It is possible to make solids maintaining or improving the property of the nanoparticles through sintering.

Moreover, many methods to produce metal or nonmetal nanoparticles exist. Of all of them, the method for producing the metal nanoparticles using laser ablation in liquids with high speed and low cost has especially attracted attention [11–19]. Many kinds of magnetic nanoparticles [20–32] (such as Fe [20–24], iron oxide [26], Au [27], Ni [26], and Pd [27–29] nanoparticles) have already been researched. Ferromagnetism materials will be applicable to high-frequency core inductors [31, 32]. However, to realize our goal, only some materials meet the following conditions for the energy transfer or the semiconductor: (1) low resistivity, (2) low cost, and (3) abundance. Thus, we choose Si, which consists of a single atom and is used in standard semiconductors and solar panels. Some applications of Si are semiconductors and solar panels. Additionally, Si nanoparticles, which can emit visible light owing to the quantum size effects, can be used in color displays [15–19, 33, 34]. Also, researches on the spin wave propagation in Si nanoparticles [35, 36], optical switch for optical computing using carrier effect by controlling the transparency of the material [37–40], and application to air cells [13] are being conducted right now.

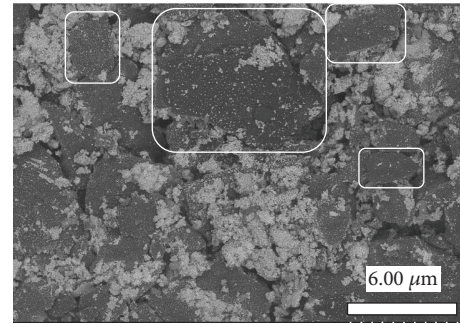
Unpaired electrons, i.e., dangling bonds, due to impurities in Si substrates have already been studied by many researchers.  $E'$  and Pb defects due to surface oxidation of Si have already been confirmed [41–51]. Also, a theoretical research reports that ferromagnetism of the Si material is generated by interaction between dangling bonds that become unpaired electrons [35]. However, the ferromagnetism of bulk Si has not been observed experimentally until now. High-density unpaired electrons are needed to generate ferromagnetism. Similar to Si material with crystal defects, the sintered Al polycrystalline bodies have been proven to be ferromagnetic even though common Al bulk is nonmagnetic [30]. Common nonmagnetic metals have been proposed to be able to change to being ferromagnetic when we make solids from nanoparticles.

The goal of our research is to develop low-power-consuming semiconductor devices by applying the prepared Si nanopolycrystalline with a reduced skin effect to semiconductors. We have recently fabricated nanostructured metals by the bottom-up process [11–13]. A sintered metal nanopolycrystalline body with low resistivity is a new material, and the resistivity has not been adequately investigated.

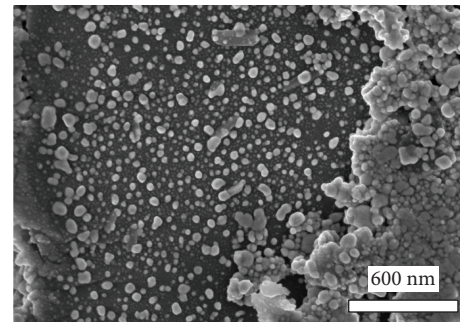
In this study, we investigated if sintered Si nanopaste is a ferromagnetic material. We also report on a significant reduction in the resistance at a specific frequency that was also observed.

## 2. Result

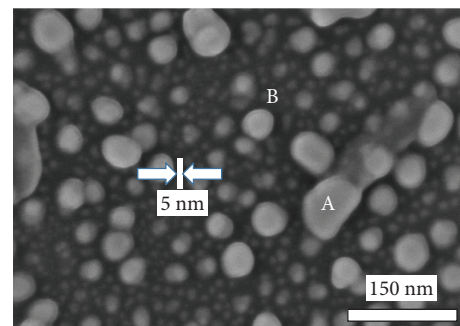
**2.1. Measurement by SEM.** We observed the structure of the sintered Si nanopolycrystalline body experimentally. A SEM image of a sintered Si nanopolycrystalline body is shown in Figure 1. It has been found by EDX analysis that the Si secondary particles consist of Si atoms. The mixed paste contains 6% of Ag atoms for all the atoms when we make



(a) Reflection electron image obtained by SEM (magnification: 5000 times)



(b) Secondary electron image obtained by SEM (magnification: 50000 times)



(c) Secondary electron image obtained by SEM (magnification: 200000 times)

FIGURE 1

Si nanopaste. After sintering, the amount will reduce to a few % because the Ag concentrated on the surface should be removed. It is hard to know the concentration. Numerous Si secondary particles below  $10\ \mu\text{m}$  were observed as shown in white lines of Figure 1(a). The part surrounded by the white line is a secondary Si particle. The magnified SEM image in Figure 1(b) shows that this secondary particle is clearly composed of many minute Si nanoparticles. The expanded SEM image in Figure 1(c) shows that the Si nanoparticles are around a few nm although there is some variation in size. Figure 2 shows the results of EDX analysis by specific X-rays. Figures 2(a) and 2(b) show results for part A in black and part B in white. Si, O, and Ag atoms on the nanoparticles were measured at part A by specific X-rays in Figure 2(a), and Si and O atoms on the nanoparticles were measured at part B by specific X-rays in Figure 2(b). Although oxygen appears strongly in the specific X-ray spectrum, it seems to be particularly attached to the surface of the Si nanoparticle and constitutes the interface of the secondary particle. Because the oxygen film is extremely thin,

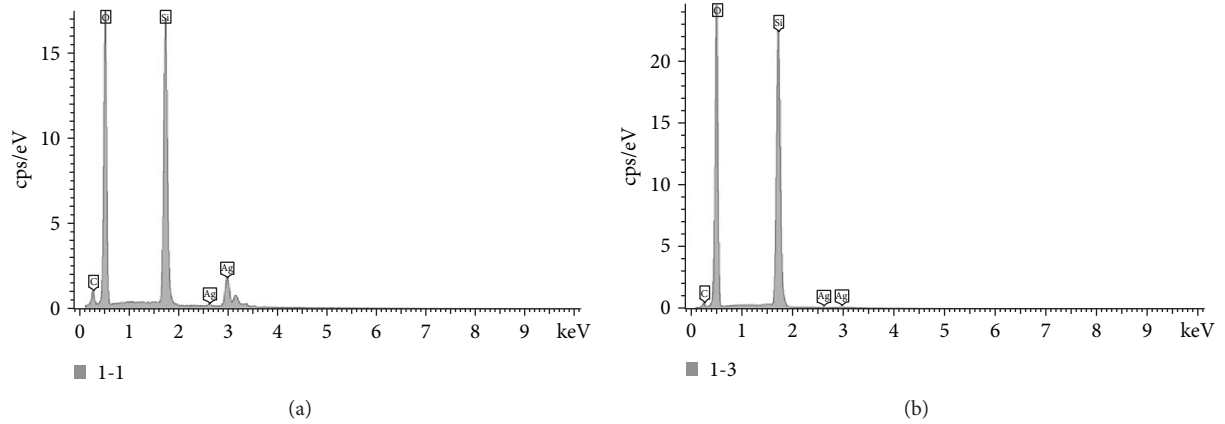


FIGURE 2: Results of EDX analysis by specific X-rays: (a) part A in Figure 1(c); (b) part B in Figure 1(c).

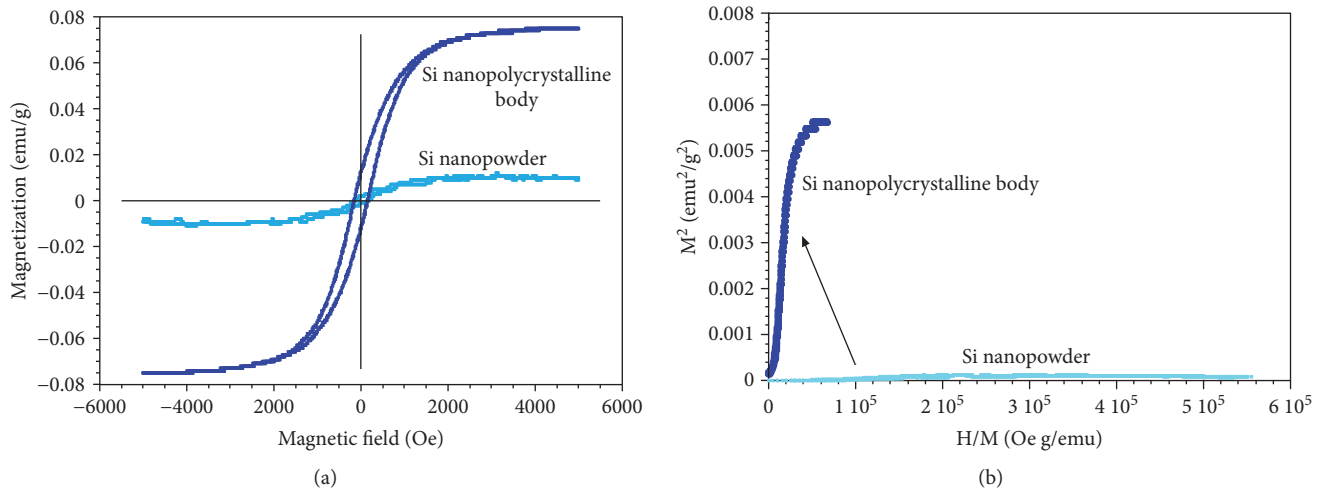


FIGURE 3: Magnetic property: (a) magnetization property; (b) Arrott plot.

the resistance does not increase. The diameter of the Si nanocrystals should not change during sintering. The oxygen film is thin and does not increase the resistance. It is clear from Figure 1(c) that secondary Si particles consist of numerous nanocrystals with a mean diameter of below 2 nm in three dimensions. The Si nanopolycrystalline body emits a photoluminescence with a peak wavelength of 550 nm excited by a violet light source due to the small size of the Si nanocrystals [33, 34].

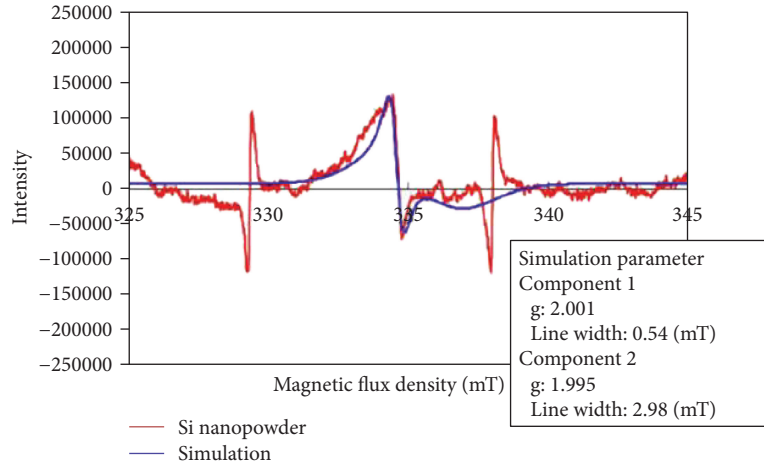
**2.2. Magnetization Property.** Normal Si has an antimagnetic property. The magnetization property of the reduced Si nanoparticles and the sintered Si nanopolycrystalline body was measured by VSM at a room temperature (293 K) to determine if the sintered Si nanopolycrystalline body has ferromagnetism. The measured magnetization of reduced Si nanopowder and sintered Si is shown as Figure 3(a). Also, their Arrott plot is shown in Figure 3(b). Their magnetic parameters are shown in Table 1.

The measured maximum magnetization of the reduced Si nanoparticles was 0.011 emu/g, and the measured maximum magnetization of the sintered Si nanopolycrystalline body

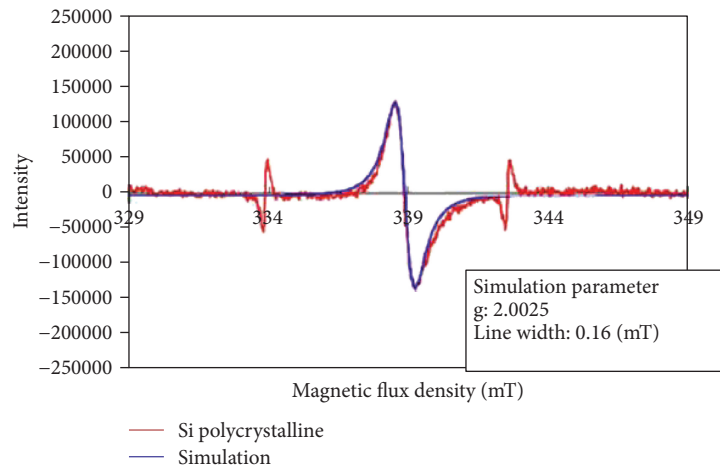
TABLE 1: Magnetic parameter.

	Saturated magnetization (emu/g)	Corrective force (Oe)
Si nanopowder	0.011	200
Si nanocrystalline	0.08	200
Fe powder [21]	210 (mean size: 150 nm)	280
Fe oxide [25]	74 (mean size: 30 nm)	700
Ni-doped ZnO [26]	4	90

was 0.075 emu/g. The magnetization of the sintered Si nanopolycrystalline body is 7 times larger than that of the reduced Si nanoparticles. The maximum magnetization of the conventional Fe bulk was 218 emu/g. The evaluated coercive force of the sintered Si nanopolycrystalline body was 200 Oe. From the measured magnetization property, the sintered Si nanopolycrystalline body includes a ferromagnetic phase because of the residual magnetization and coercive force as shown in Figures 3(a) and 3(b). Because the magnetization curve is saturated at 1000 Oe for the reduced



(a) Results of ESR analysis for Si nanopowder



(b) Results of ESR analysis for sintered Si nanopolycrystalline

FIGURE 4

Si nanoparticles, there was no evident spontaneous magnetization, but there were many defects of Si atoms with magnetic moment in the material, which react with the outer magnetic field.

**2.3. ESR Analysis.** Densities of the dangling bond in the Si nanopowder and the Si nanopolycrystalline were measured by electron spin resonance (ESR) and then compared. Results of ESR analysis for the Si nanopowder and the sintered Si nanopolycrystalline are shown in Figures 4(a) and 4(b). The measured densities of the dangling bonds for the Si nanopowder and the Si nanopolycrystalline are shown in Table 2. The  $g$  value for the Si nanopowder was 2.0000. It was considered from the  $g$  value that the Si nanopowder contains the dangling bonds of the Si oxides. Judging from the observed peak signal, the Si nanopowder contains more than two components. However, the structure of the Si nanoparticle is not recognized. It should be a kind of Si oxide. The  $g$  value for the Si nanopolycrystalline was 2.0025, which was between that for the Si crystals ( $g = 2.0050\sim 2.0060$ ) and that for the Si oxides ( $g = 2.0000$ ). It was found that intermediate dangling bonds between crystalline silicon and silicon oxide

TABLE 2: Result on evaluated density of dangling bond.

	$g$ value	Amount of dangling bond ( $\times 10^{13}$ spin/g)
Si nanopowder	2.0000	8.3
Si nanopolycrystalline	2.0025	16.0

exist in sintered Si nanopolycrystalline.  $E'$  centers and Pd centers in the reference [41–45] could not be separated in the electron spin resonance (ESR) spectrum. The amount of the dangling bonds calculated from the integrated value of the ESR spectrum and the area strength of the standard material (known amount of radical: DPPH) is estimated to be 1/2 that of the sintered Si nanopolycrystalline. Thus, it is concluded from this result that magnetization will be amplified up to seven times for one of the Si nanopowders because of the interaction between unpaired electrons called as exchange interactions in the sintered Si nanopolycrystalline.

**2.4. Measurement of Resistivity.** Measured resistance of the sintered Si as a function of frequency is shown in Figure 5.

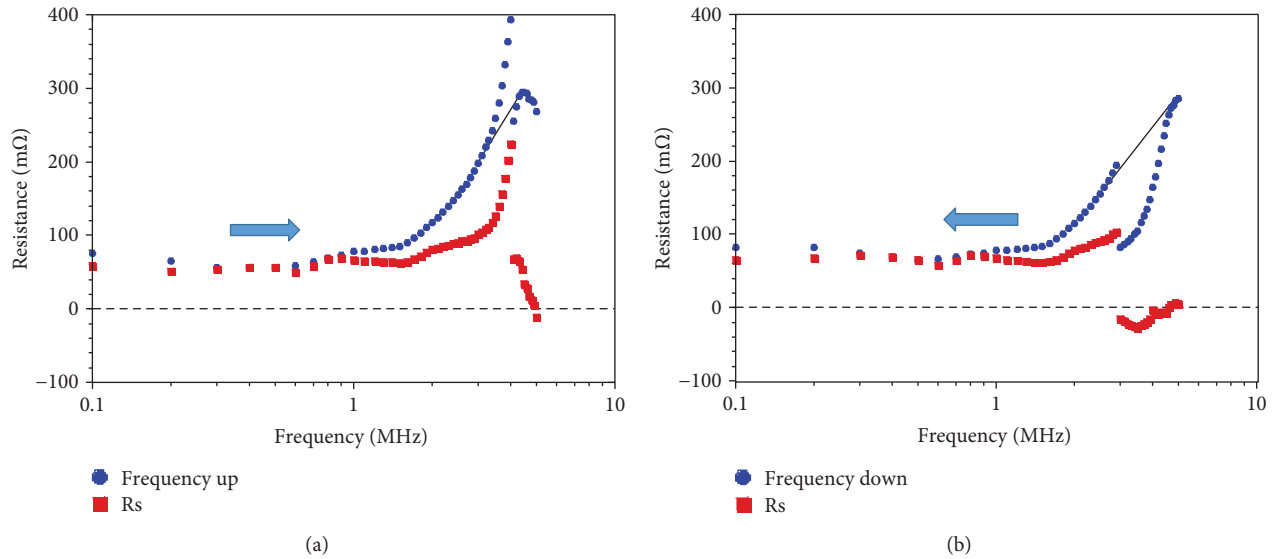


FIGURE 5: Measured resistivity as function of frequency when current at 5 MHz was 10 mA: (a) increasing frequency; (b) decreasing frequency.

The measured resistance with increasing frequency of the sine wave signal is shown in Figure 5(a), and that with decreasing frequency of the sine wave signal is shown in Figure 5(b). The blue line shows the resistance measured with copper lines. The red line shows the resistance without the resistance of the copper lines. We observed a clear difference between the two results. Discontinuities of the resistances as a function of frequency were observed.

The resistance of the sintered Si nanopolycrystalline body increased with increasing frequency, and the resistance returned to 60 mΩ at 4 MHz. After that, the resistance decreased continuously, as shown in Figure 5(a). The resistance of the sintered Si nanopolycrystalline body remained close to zero with decreasing frequency, and the resistance decreased around  $-20$  mΩ at 3 MHz. After that, the resistance decreased continuously from 100 mΩ as if the skin effect was weakened, as shown in Figure 5(b). The evaluated volume resistivity of the sintered Si nanopolycrystalline body was  $1.2 \times 10^{-6} \Omega \text{ m}$  at 100 Hz. A slight reduction in the resistance at 200 kHz was also observed.

The measured resistance of the sintered Si depending on the current is shown in Figure 6. The resistances were measured with decreasing frequency of the sine wave signal. The measured self-inductances of the sintered Si nanopolycrystalline body are shown in the inset figures of Figures 6(a)–6(c). Thus, from the current data, magnetic resonance occurs at these frequencies, and the relative permeability changes rapidly around these frequencies. The singular radical vanishing of the resistivity in the Si nanopolycrystalline body at high magnetic-resonance frequencies should occur because the sintered Si pastes are ferromagnetic and exhibit negative permittivity around these frequencies. The self-inductance increased at 2.8 MHz, as shown in the inset of Figure 6(a). The self-inductance changed discontinuously at 200 kHz, 2.8 MHz, and 5 MHz. The resistance of the sintered Si increased to 400 mΩ at 2.8 MHz, as shown in

Figure 6(a). At the same time, the current decreased to half that at 100 kHz.

The measured resistances of the Si nanopolycrystalline body depending on the current are shown in Figure 6(d). The resistance at 3 MHz was 190 mΩ when the current was 0.17 mA and changed to near  $-20$  mΩ when the current was changed from 2 to 8 mA. Finally, the resistance was 0 mΩ asymptotically when the current was changed from 10 to 18 mA. The resistance at 5 MHz was  $-120$  mΩ when the current was 0.17 mA and was 0 mΩ asymptotically when the current was changed from 3 to 8 mA.

The resistance at high frequency was calculated numerically while considering the permittivity of the Si nanopolycrystalline and the electric field and magnetic field. From the results, the resistance clearly varies in accordance with the relative permittivity of 1 as a function of the frequency as shown by the dashed lines in Figures 6(a)–6(c). This analysis result seems to be extraordinary because the sintered Si is metal. Thus, the relative permeability should degrade to below 1 as in the case of normal metal bulk. The lower relative permeability means an antimagnetic property such as that appearing in conventional Al bulk. However, it was found from numerical calculation that the relative permeability of the sintered Si nanopolycrystalline body degraded to close to 1.

Thus, the relative permittivity was changed so as to fit the measured resistance. The evaluated relative permittivities as function of frequency are shown in Figure 7. The resistance was recalculated using the relative permittivity as shown by the blue solid line in Figures 6(a)–6(c). The resistance increased to 400 mΩ when the frequency was 2.5 MHz as shown in Figure 6(a). This is because the generated magnetic field intensity is weak and the amplitude of the permittivity is maximized. It was thought that the phase of the permeability is inverted at 5 MHz, the real part of the relative permeability changed to be  $-1$ , and the

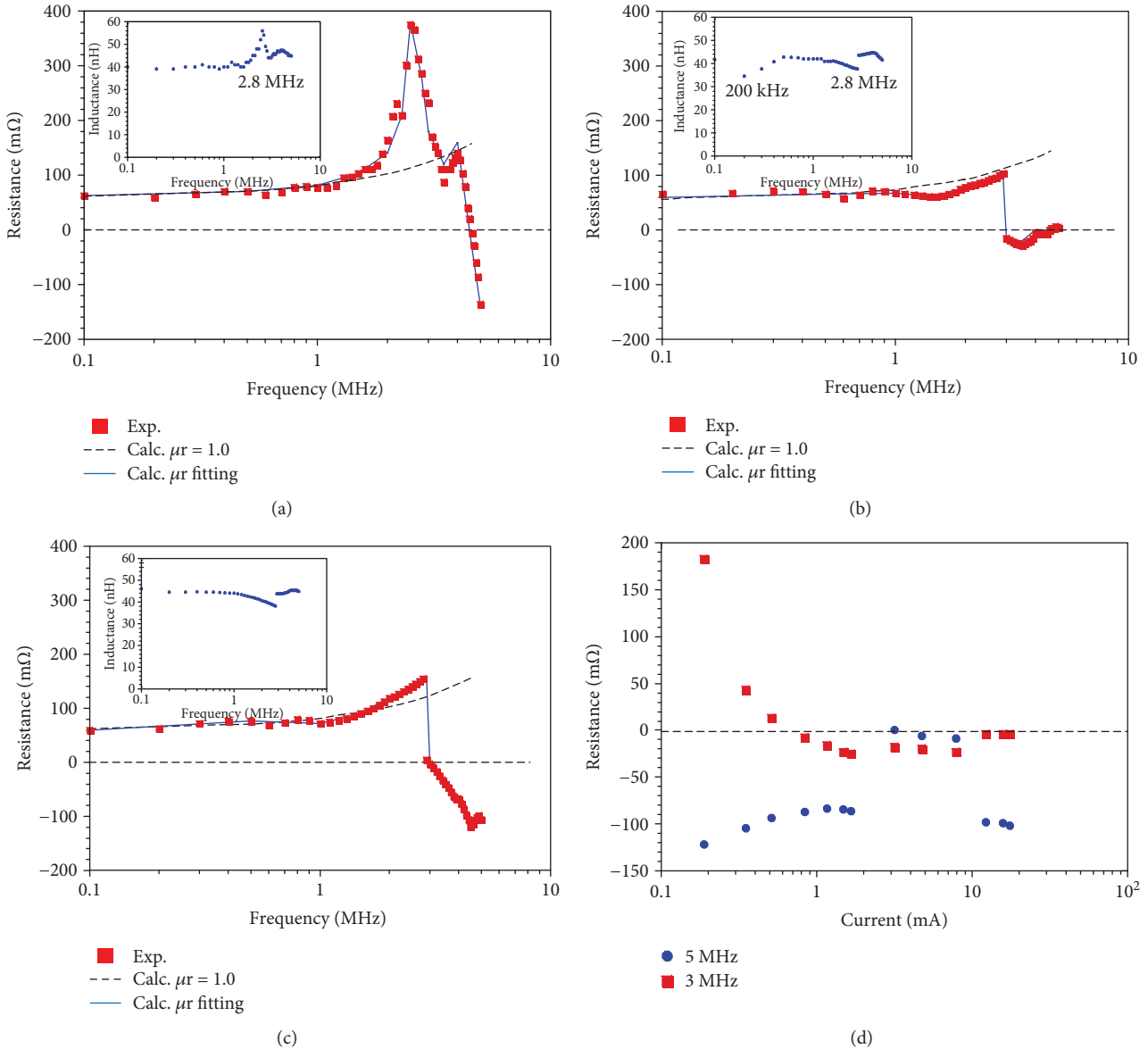


FIGURE 6: Results on measured resistance as function of frequency. Currents at 5 MHz were (a) 0.17, (b) 10, and (c) 20 mA. (d) Resistances with dependence on current.

direction of the electric field generated by the magnetic field is reversed.

For Figure 6(b), when the current increased, the intensity of the magnetic field increased by two orders of magnitude. The magnetic moment cannot keep up with the time change of the magnetic strength owing to the high frequency, and at 3 MHz, the real part of the relative permeability is a binary change of 1 or  $-1$ . It was also found that the phase of the permeability was inverted at 1.5 MHz.

For Figure 6(c), when the current increased, the magnetic field intensity became stronger. The magnetic moment cannot keep up with the temporal change of magnetic intensity owing to the high frequency, but at 3 MHz, the real part of the relative permeability is a binary change of 1.5 on the low-frequency side and  $-1$  on the high-frequency side.

In the case in Figure 6(a), the permeability was found to be consistent with that of the sintered Al having similar properties described in the reference [30], with the relative magnetic permeability at 2.5 MHz evaluated to be 7.

When the magnetic resonance occurred, the real part of the permeability changed to negative at 3 MHz, as shown in Figure 8. The calculated results show that the real part of the permeability inside the sintered Si should be changed to  $-\mu_0$ . The term  $E$  is the original electric field applied with the original sine wave signal, and  $E_B$  is the electric field generated by the current-induced magnetic field. These directions are the same because of the phase inversion of  $E_B$  when the real part of the relative permeability is negative. It was suggested that the electrons in the sintered Si nanopolycrystalline body were accelerated by the generated electric field.

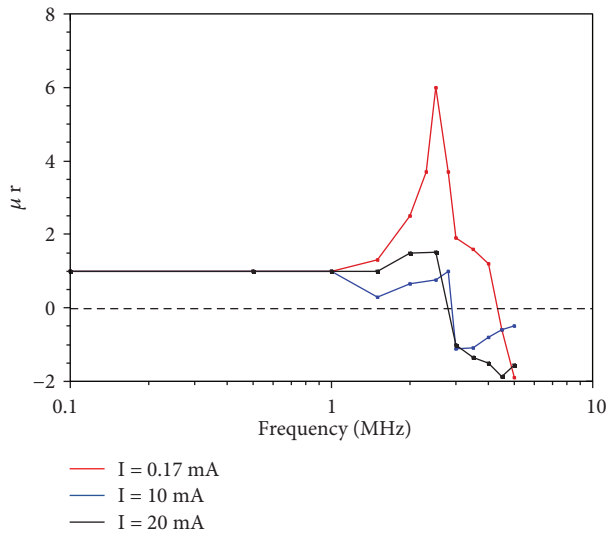


FIGURE 7: Evaluated relative permeability as a function of frequency. Currents at 5 MHz were 0.17, 10, and 20 mA.

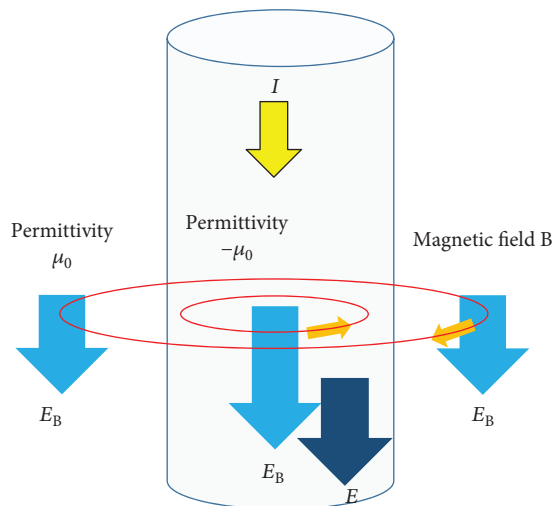


FIGURE 8: Spatial distribution of permeability when magnetic resonance occurred and real part of permeability changed to negative at 3 MHz.

However, at the same time, the sintered Si nanopolycrystalline body had a relative permeability of  $-1$ . The numerically calculated result shows that the current does not flow linearly in micro scale of the sintered Si and generation of the eddy current is prevented due to the structure.

The resistance of a sintered Ag nanopolycrystalline body with nonferromagnetism did not become zero at the magnetic-resonance frequencies of a few MHz. Thus, this phenomenon is thought to be intrinsic for a metal nanopolycrystalline body with ferromagnetism.

Common metal has effective permeability below 1, such as 0.5, at the MHz level, and resistance becomes low due to the generated  $E_B$ . Thus, because the  $E_B$  is weaker than that of metal in a ferromagnetic metal nanopolycrystalline body, the resistance does not degrade to zero.

It is considered that the resistances of almost all ferromagnetic metal nanopolycrystalline bodies change to zero at frequencies of a few MHz with no connection to the relative permeability.

However, resistance from 3 to 20 mA changed to close to zero by some cause. The resistance also changed to negative around 5 MHz when the current was 20 mA, as shown in Figure 6(d). The cause seems to be that the magnetic momentum of unpaired electrons at the surface of Si nanocrystals cannot follow the varying magnetic field at a high frequency of 5 MHz.

In these experiments, we did not observe the reduction of the skin effect by which the current distribution in the Si is close to uniform due to the nanostructure. We believe that sintered Si nanopaste with a Si nanopolycrystalline body will be applicable to magnetic materials.

**2.5. Calculated Magnetic Field Intensity and Electric Field Intensity.** Figure 9 shows the calculated results for the distribution of the magnetic field intensity at the profile of the Si nanopolycrystalline. The current is shown as the effective value. The thin direction of the material is the thickness direction, and the long 4 mm direction is the length direction. The magnetic field intensity at the center of both directions was calculated. It was found that a strong magnetic field is mainly generated near the surface in the direction perpendicular to the thickness direction. Also, a weak magnetic field of 1/10 was generated in the direction perpendicular to the length direction.

It was found that when the effective value of the current flowing in the Si nanopolycrystalline was 0.17, 10, and 20 mA, the calculated magnetic field intensity was 1, 80, and 160 A/m, respectively, in the direction perpendicular to the thickness direction.

Figure 10 shows the calculated distribution of the electric field, in which the direction of the electric field is the same as the direction of the current and the intensity is proportional to current. Here, the electrical field intensity in the longitudinal direction was normalized by the AC electrical field intensity added by a power source. When the normalized electric field is negative, it means that the current barely flows in the forward direction. When the normalized electric field is positive and larger than 1, this means that the flow of current is assisted by the electric field and the resistance is reduced.

For Figure 10(a), when the current is 0.17 mA, the electric field intensity at the center continues to decrease from 0.1 to 4 MHz and is lowest at 2.5 MHz. The real part of the permeability is changed to be negative by magnetic resonance. The distribution of the electric field intensity was dented downward, and the distribution reversed from 2.5 to 5 MHz. For Figure 10(b), when the current increased to 10 mA, the electric field intensity at the center continues to decrease from 0.1 to 2.9 MHz. The real part of the permeability is changed to be negative by magnetic resonance. The distribution of the electric field intensity was dented downward, and the distribution reversed from 3 to 5 MHz.

For Figure 10(c), when the current increased to 20 mA, the electric field intensity at the center continues to decrease

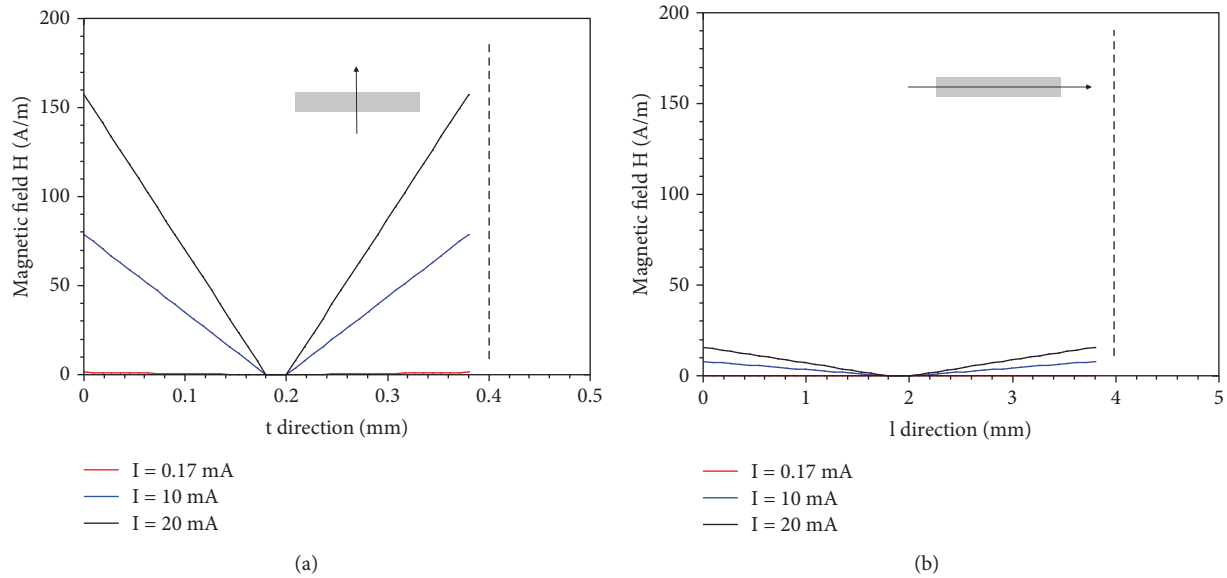


FIGURE 9: Calculated magnetic field intensity: (a) thickness direction; (b) length direction.

from 0.1 to 2.9 MHz and is lowest at 2.9 MHz. The phase of the permeability is inverted to be negative by magnetic resonance. The distribution of the electric field intensity was dented downward, and the distribution reversed from 3 to 5 MHz.

### 3. Conclusion

Reduction in the skin effect for the sintered Si nanopolycrystalline for semiconductor material at a high frequency due to its nanostructure has been studied. Singular disappearance of electrical resistances near a local high magnetic harmonic frequency of a few MHz has been observed in the experiments. Negative resistance of the sintered Si nanopolycrystalline has also been observed. Numerical calculation has also been performed on the electrical resistance with frequency dependency while considering the electric field and magnetic field in the sintered Si nanopolycrystalline. The experimental and calculated results are compared. The calculation could theoretically explain the phenomenon of vanishing resistivity at the MHz frequency. It was found by measuring the magnetization property that the sintered Si nanopolycrystalline has ferromagnetism. The density of the unpaired electrons in the sintered Si nanopolycrystalline was observed using ESR. It has been recognized that the sintered Si nanopolycrystalline has numerous dangling bonds.

### 4. Experimental Methods

**4.1. Production of Materials.** The laser ablation method in liquid is described in the paragraph below. When laser pulses are irradiated onto metal oxides in liquid, the metal oxides melt and resolve, and the melted oxides are set outside the metal nanoparticles [11]. The surrounding liquid cools the metal nanoparticles rapidly. The experimental setup for laser pulse ablation is shown here [11]. A microchip Nd:YAG laser was used in this experiment. The maximum output averaged

laser power was 250 mW, the laser wavelength was 1064 nm, the repetitive rate of the laser pulses was 18 kHz, and the pulse duration was 8 ns. A beam with a diameter of 6 mm ( $1/e^2$ ) was focused using a lens with a focal length of 50 mm. Thus, the diameter of the focused beam was  $20 \mu\text{m}$  at the front of each glass bottle. Glass bottles with a size of  $38 \text{ ml} \times 20 \text{ mm}$  were used in the experiment. Reduced Si nanoparticles were produced by laser ablation in liquid. The liquid we used was pure water. The  $\text{SiO}_2$  powder (mean diameter of  $5 \mu\text{m}$ , purity 99.9%, Koujyund Chemical, Japan) was used to produce reduced Si nanoparticles. The  $\text{SiO}_2$  powder was mixed with the water in each glass bottle for the experiment. The glass bottle was set after the focused laser beam. The weight of the  $\text{SiO}_2$  powder was measured using an electronic force balance. The measured weight was 1.0 g. 12 mL of pure water was placed in each glass bottle. Laser pulses were irradiated to the water with the metal oxide in the glass bottle for 10 minutes. Here, we neglect the oxidation at the surface of metal nanoparticles. A magnetic stirrer was used to mix the liquid. The color after laser irradiation changed to gray, which is close to the color of the reduced Si powder. The powder after irradiating laser pulses in the water was dried so as not to change chemically.

A sintered Si nanopaste (Si nanopolycrystalline body) was made using the reduced Si nanoparticles. The dried Si nanopowders were mixed with 5 mg of Ag nanopastes (NAG-10 Daiken Chemical); the viscosity of the paste was high. The size of the sintered Si nanopolycrystalline body was determined to be  $4 \times 10 \times 0.3 \text{ mm}$ . The current was conducted in the longitudinal dimension, and the resistivity at a high frequency was measured. The Si paste was sintered using an electrical hot plate (CHP-170AN, ASONE) at 473 K (1 min) and 533 K (4 min), enabling us to obtain sintered Si pastes.

**4.2. Analysis of Material and Measurement Method.** The magnetization properties of the reduced Si nanoparticles

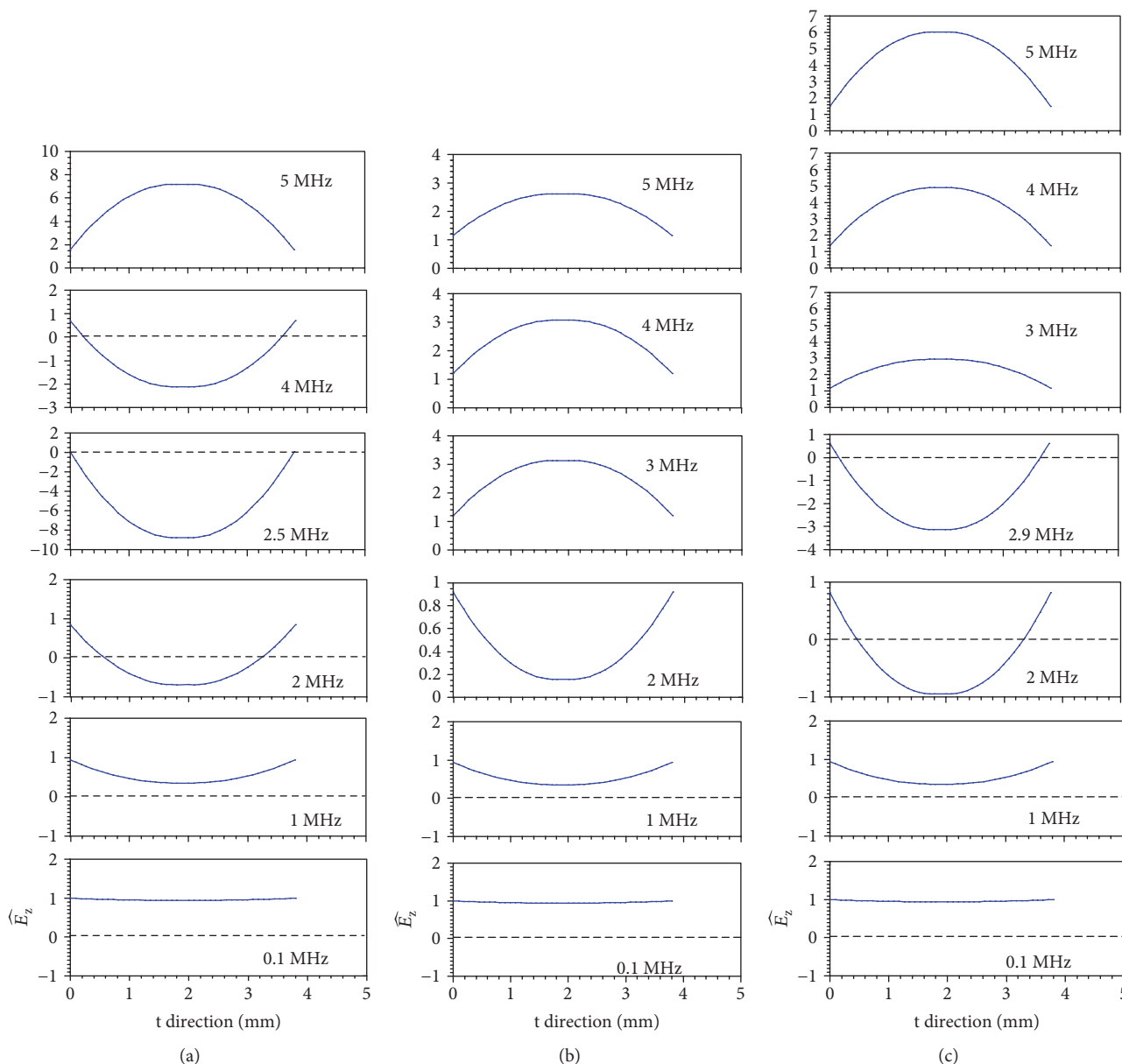


FIGURE 10: Calculated electric field: (a) 0.17 mA, normalized by  $E_{AC} = 0.0022$  V/m; (b) 10 mA, normalized by  $E_{AC} = 0.013$  V/m; (c) 20 mA, normalized by  $E_{AC} = 0.026$  V/m.

and the sintered Si nanopolycrystalline body were measured using a vibrating sample magnetometer (VSM) (BHV-30T, Riken Denshi, Japan) at room temperature (20°C). The sintered Si was observed by a scanning electron microscope (SEM) (S-4700 with low resolution and SU8240 with high resolution, Hitachi High-Technologies, Japan), and the existence of Ag, Si, and O atoms was analyzed by energy-dispersive X-ray spectrometry (EDX) (EMAX7000, Horiba, Japan).

We show the measurement condition for ESR analysis in Table 3.

FT-IR, S-FA200 type, JEOL was used for ESR analysis. The weight of the used sintered Si nanopolycrystalline body is 170 mg. The size was 20 mm × 2.5 mm × 1 mm.

The resistance and inductance of the sintered Si pastes were measured using an LCR meter (3532-50 LCR, high tester, Hioki, Japan). The inductance and resistance from 42 Hz to 5 MHz were measured. The inductors and electric power transmitters were assumed to have components of inductance and resistance. The phase angles of cascaded resistances and inductors in the stick-type sintered Si pastes were also measured.

**4.3. Calculation for Skin Effect.** We resolved the integration Maxwell-Faraday equation numerically and calculated the electric field generated by the current-generated magnetic field inside the metal. We observed spatial distribution of the electric field in the thickness and longitudinal directions.

TABLE 3: Measurement condition.

Microwave frequency	9.3–9.4 GHz
Intensity of microwave	12 mW
Range of maneuvering magnetic field	20 mT
Modulated magnetic field frequency	100 kHz
Modulated magnetic field amplitude	1.0mT
Sampling time	81.92 ms
Accumulation count	3 times
Measurement temperature	10 K (liquid He cooling)
Standard substance	1-Diphenyl-2-picrylhydrazyl (DPPH)
Index	Mn marker (Mn <sup>2+</sup> )

The electric field was added to the original electric field applied from the sine wave signal source. The resistance was calculated with the recalculated electric field. We considered only the real part of the relative permeability. The special mesh was set to be 40 in both length and thickness directions. It was assumed that the permeability is uniform in the profile.

The current-generated magnetic field intensities in the directions of the length and thickness are given as

$$\begin{aligned} H_l(r) &= \frac{Ir}{2Lt}, \\ H_t(r) &= \frac{IrL}{2t^3}, \end{aligned} \quad (1)$$

where  $I$  is the AC current and the  $l$  and  $t$  are the length and the thickness, respectively, in the profile of the Si nanopoly-crystalline body. The effective resistance at a high frequency is given as

$$R_{\text{hef}} = R_{\text{DC}} \left( 1 + \frac{E_{\text{Bav}}}{E_{\text{AC}}} \right), \quad (2)$$

where  $R_{\text{DC}}$  is the DC resistance, the  $E_0$  is the original AC electric field intensity, and  $E_{\text{Bav}}$  is the averaged electrical field intensity generated by the current-generated magnetic field intensity. The resistance was calculated using the ratio of the electric field generated by the current-generated magnetic field to the original AC electric field.  $R_{\text{DC}}$  was set to be 60 mΩ.

## Data Availability

No data were used to support this study.

## Conflicts of Interest

The authors declare that they have no competing interests.

## Authors' Contributions

T. S., Y. I., and M. I. contributed to the experimental design, data analyses and interpretation of the findings, and preparation of the manuscript. All authors approved the final version of the manuscript.

## References

- [1] D. G. Fink and H. W. Beatty, *Standard Handbook for Electrical Engineers*, McGraw Hill, 11 edition, 1978.
- [2] C. R. Sullivan, "Optimal choice for number of strands in a litz-wire transformer winding," *IEEE Transactions on Power Electronics*, vol. 14, no. 2, pp. 283–291, 1999.
- [3] H. Lamb, "On electrical motions in a spherical conductor," *Philosophical Transactions of the Royal Society of London*, vol. 174, pp. 519–549, 1883.
- [4] W. H. Hayt, *Engineering Electromagnetics*, McGraw-Hill, 5th edition, 1989.
- [5] Function Investigation Committee of Nanoscale Magnetic Material, *Nanostructured Magnetic Materials -Physics, Function, Design-*, Kyoritsu Publishing, Tokyo, Japan, 2010, Chapter 1 and 2.
- [6] K. Yamada, K. Kim, and M. Yamaguchi, "Slit design consideration on the ferromagnetic RF integrated inductor," *IEEE Transactions on Magnetics*, vol. 42, no. 10, pp. 3341–3343, 2006.
- [7] P. Buffat and J. P. Borel, "Size effect on the melting temperature of gold particles," *Physical Review A*, vol. 13, no. 6, pp. 2287–2298, 1976.
- [8] W. H. Chung, H. J. Hwang, S. H. Lee, and H. S. Kim, "In situ monitoring of a flashlight sintering process using silver nano-ink for producing flexible electronics," *Nanotechnology*, vol. 24, no. 3, article 035202, 2013.
- [9] W. M. Neill, C. Choi, C. Chang, and R. Malhotra, "On the self-damping nature of densification in photonic sintering of nanoparticles," *Scientific Reports*, vol. 5, no. 1, article 14845, 2015.
- [10] S.-H. Park, W.-H. Chung, and H.-S. Kim, "Temperature changes of copper nanoparticle ink during flash light sintering," *Journal of Materials Processing Technology*, vol. 214, no. 11, pp. 2730–2738, 2014.
- [11] T. Saiki, T. Okada, K. Nakamura, T. Karita, Y. Nishikawa, and Y. Iida, "Air cells using negative metal electrodes fabricated by sintering pastes with base metal nanoparticles for efficient utilization of solar energy," *International Journal of Energy Science*, vol. 2, no. 6, pp. 228–234, 2012.
- [12] T. Saiki, Y. Iida, K. Ri, M. Yoshida, and Y. Koga, "Electrical property of laser-sintered nanopastes with reduced metal nanoparticles prepared by laser ablation in liquids," *Advances in Materials*, vol. 3, no. 6, pp. 75–88, 2014.
- [13] T. Saiki, K. Nakamura, J. Tokumoto, K. Nakamura, and T. Uematsu, "Fabrication of metal air cells using sintered Si nanopaste with reduced Si nanoparticles," *The Review of Laser Engineering*, vol. 45, no. 6, pp. 364–370, 2017.
- [14] A. Henglein, "Physicochemical properties of small metal particles in solution: "microelectrode" reactions, chemisorption, composite metal particles, and the atom-to-metal transition," *The Journal of Physical Chemistry*, vol. 97, no. 21, pp. 5457–5471, 1993.
- [15] L. T. Canham, "Silicon quantum wire array fabrication by electrochemical and chemical dissolution of wafers," *Applied Physics Letters*, vol. 57, no. 10, pp. 1046–1048, 1990.
- [16] V. Švrček, T. Sasaki, Y. Shimizu, and N. Koshizaki, "Blue luminescent silicon nanocrystals prepared by ns pulsed laser ablation in water," *Applied Physics Letters*, vol. 89, no. 21, article 213113, 2006.
- [17] K. Saitow and T. Yamamura, "Effective cooling generates efficient emission: blue, green, and red light-emitting Si

- nanocrystals," *Journal of Physical Chemistry C*, vol. 113, no. 19, pp. 8465–8470, 2009.
- [18] I. Umez, A. Sugimura, M. Inada, T. Makino, K. Matsumoto, and M. Takata, "Formation of nanoscale fine-structured silicon by pulsed laser ablation in hydrogen background gas," *Physical Review B*, vol. 76, no. 4, article 045328, 2007.
- [19] L. Brus, "Electronic wave functions in semiconductor clusters: experiment and theory," *The Journal of Physical Chemistry*, vol. 90, no. 12, pp. 2555–2560, 1986.
- [20] T. Ogawa, Y. Ogata, R. Gallage et al., "Challenge to the synthesis of  $\alpha''$ - $\text{Fe}_{16}\text{N}_2$  compound nanoparticle with high saturation magnetization for rare earth free new permanent magnetic material," *Applied Physics Express*, vol. 6, no. 7, article 073007, 2013.
- [21] R. J. Joseyphusa, K. Shinodac, D. Kodamab, and B. Jayadevanb, "Size controlled Fe nanoparticles through polyol process and their magnetic properties," *Materials Chemistry and Physics*, vol. 123, no. 2-3, pp. 487–493, 2010.
- [22] M. Kamata, H. Kura, M. Takahashi, T. Ogawa, and T. Tanaka, "Direct synthesis of single crystalline-Fe nanoparticles with high saturation magnetization by mixed surfactant," *IEEE Transactions on Magnetics*, vol. 48, no. 11, pp. 3944–3946, 2012.
- [23] H. Kura, M. Takahashi, and T. Ogawa, "Synthesis of monodisperse iron nanoparticles with a high saturation magnetization using an  $\text{Fe}(\text{CO})_x$ -oleylamine reacted precursor," *Journal of Physical Chemistry C*, vol. 114, no. 13, pp. 5835–5838, 2010.
- [24] S. Peng, C. Wang, J. Xie, and S. Sun, "Synthesis and stabilization of monodisperse Fe nanoparticles," *Journal of the American Chemical Society*, vol. 128, no. 33, pp. 10676–10677, 2006.
- [25] D. Cao, H. Li, L. Pan et al., "High saturation magnetization of  $\gamma$ - $\text{Fe}_2\text{O}_3$  nano-particles by a facile one-step synthesis approach," *Scientific Reports*, vol. 6, no. 1, pp. 1–9, 2016.
- [26] X. He, W. Zhong, C.-T. Au, and Y. Du, "Size dependence of the magnetic properties of Ni nanoparticles prepared by thermal decomposition method," *Nanoscale Research Letters*, vol. 8, no. 1, p. 446, 2013.
- [27] H. Hori, T. Teranishi, Y. Nakae, Y. Seino, M. Miyake, and S. Yamada, "Anomalous magnetic polarization effect of Pd and Au nano-particles," *Physics Letters*, vol. 263, no. 4–6, pp. 406–410, 1999.
- [28] F. Aguilera-Granja, J. M. Montejano-Carrizales, and A. Vega, "Twining effects in the magnetism of small Pd clusters," *Solid State Communications*, vol. 133, no. 9, pp. 573–578, 2005.
- [29] Y. T. Jeon and G. H. Lee, "Magnetism of the fcc Rh and Pd nanoparticles," *Journal of Applied Physics*, vol. 103, no. 9, article 094313, 2008.
- [30] S. Masuda, T. Saiki, Y. Iida, and M. Inada, "High frequency core inductor using sintered aluminum nano-paste with aluminum nano-polycrystalline structure," in *Conference on the Lasers and Electro-Optics (CLEO)*, San Jose, CA, USA, May 2017, paper STh1J.3.
- [31] V. Korenivski, "GHz magnetic film inductors," *Journal of Magnetism and Magnetic Materials*, vol. 215–216, pp. 800–806, 2000.
- [32] P. Marín, D. Cortina, and A. Hernando, "Electromagnetic wave absorbing material based on magnetic microwires," *IEEE Transactions on Magnetics*, vol. 44, no. 11, pp. 3934–3937, 2008.
- [33] N. Hill and K. Whaley, "Size dependence of excitations in silicon nanocrystals," *Physical Review Letters*, vol. 75, no. 6, pp. 1130–1133, 1995.
- [34] T. Saiki and Y. Iida, "Fabrication of sintered Si nanopolycrystalline with reduced Si nanoparticles and property of photoluminescence in visible regime for sintered Si nanopolycrystalline by violet light excitation," *American Journal of Nano Research and Applications*, vol. 3, no. 5, pp. 82–88, 2015.
- [35] S. Okada, K. Shiraishi, and A. Oshiyama, "Magnetic ordering of dangling bond networks on hydrogen-deposited Si(111) surfaces," *Physical Review Letters*, vol. 90, no. 2, 2003.
- [36] P. N. Hai, S. Ohya, and M. Tanaka, "Long spin-relaxation time in a single metal nanoparticle," *Nature Nanotechnology*, vol. 5, no. 8, pp. 593–596, 2010.
- [37] H. Kobayashi, Y. Iida, and Y. Omura, "Single-mode silicon optical switch with T-shaped  $\text{SiO}_2$  optical waveguide as a control gate," *Japanese Journal of Applied Physics*, vol. 41, 4B, Part 1, pp. 2563–2565, 2002.
- [38] D. K. Schroder, R. N. Thomas, and J. C. Swartz, "Free carrier absorption in silicon," *IEEE Journal of Solid-state Circuits*, vol. SC-13, pp. 180–187, 1978.
- [39] R. A. Soref and B. R. Bennet, "Electrooptical effects in silicon," *IEEE Journal of Quantum Electronics*, vol. 23, no. 1, pp. 123–129, 1987.
- [40] R. Terawaki, Y. Takahashi, M. Chihara, Y. Inui, and S. Noda, "Ultrahigh-Q photonic crystal nanocavities in wide optical telecommunication bands," *Optics Express*, vol. 20, no. 20, pp. 22743–22752, 2012.
- [41] R. A. Weeks, "The many varieties of  $E'$  centers: a review," *Journal of Non-Crystalline Solids*, vol. 179, pp. 1–9, 1994.
- [42] D. L. Griscom, "Defect structure of glasses: some outstanding questions in regard to vitreous silica," *Journal of Non-Crystalline Solids*, vol. 73, no. 1-3, pp. 51–77, 1985.
- [43] H. Imai, K. Arai, H. Hosono, Y. Abe, T. Arai, and H. Imagawa, "Dependence of defects induced by excimer laser on intrinsic structural defects in synthetic silica glasses," *Physical Review B*, vol. 44, no. 10, pp. 4812–4818, 1991.
- [44] K. Awazu, H. Kawazoe, K. Harada, K. Kido, and S. Inoue, "Precursor to paramagnetic centers induced in gamma-irradiated doped silica glasses," *Journal of Applied Physics*, vol. 73, no. 4, pp. 1644–1649, 1993.
- [45] Y. Nishi, "Study of silicon-silicon dioxide structure by electron spin resonance I," *Japanese Journal of Applied Physics*, vol. 10, no. 1, pp. 52–62, 1971.
- [46] E. H. Poindexter, G. J. Gerardi, M.-E. Rueckel, P. J. Caplan, N. M. Johnson, and D. K. Biegelsen, "Electronic traps and  $\text{P}_b$  centers at the Si/ $\text{SiO}_2$  interface: band-gap energy distribution," *Journal of Applied Physics*, vol. 56, no. 10, pp. 2844–2849, 1984.
- [47] E. Holzenkämpfer, F. W. Richter, J. Stuke, and U. Voget-Grote, "Electron spin resonance and hopping conductivity of a- $\text{SiO}_x$ ," *Journal of Non-Crystalline Solids*, vol. 32, no. 1-3, pp. 327–338, 1979.
- [48] Y. Shiraishi, K. Takano, J. Matsubara et al., "Growth of silicon crystal with a diameter of 400 mm and weight of 400 kg," *Journal of Crystal Growth*, vol. 229, no. 1–4, pp. 17–21, 2001.
- [49] J. Ryuta, E. Morita, T. Tanaka, and Y. Shimanuki, "Crystal-originated singularities on Si wafer surface after SC1 cleaning," *Japanese Journal of Applied Physics*, vol. 29, no. 11, Part 2, pp. L1947–L1949, 1990.

- [50] A. Ikari, K. Nakai, Y. Tachikawa et al., "Defect control in nitrogen doped Czochralski silicon crystals," *Solid State Phenomena*, vol. 69-70, pp. 161–166, 1999.
- [51] K. Wada, H. Nakanishi, H. Takaoka, and N. Inoue, "Nucleation temperature of large oxide precipitates in as-grown Czochralski silicon crystal," *Journal of Crystal Growth*, vol. 57, no. 3, pp. 535–540, 1982.

## Research Article

# Surface Profile Measurement and Error Compensation of Triangular Microstructures Employing a Stylus Scanning System

Qin Yin,<sup>1</sup> Bin Xu ,<sup>1</sup> Guofu Yin,<sup>1</sup> Peng Gui,<sup>2</sup> Wei Xu,<sup>2</sup> and Bin Tang<sup>2</sup>

<sup>1</sup>School of Manufacturing Science and Engineering, Sichuan University, Chengdu 610065, China

<sup>2</sup>Institute of Electronic Engineering, China Academy of Engineering Physics, Mianyang 621999, China

Correspondence should be addressed to Bin Xu; [bin\\_xu@outlook.com](mailto:bin_xu@outlook.com)

Received 13 June 2018; Revised 29 August 2018; Accepted 17 September 2018; Published 22 November 2018

Guest Editor: Vidyadhar Singh

Copyright © 2018 Qin Yin et al. This is an open access article distributed under the Creative Commons Attribution License, which permits unrestricted use, distribution, and reproduction in any medium, provided the original work is properly cited.

Microstructure-based function components are widely used in precision engineering. Surface profile measurement is an essential tool to verify the manufacturing quality of microstructures and to enhance the working performance of the device employing microstructures as function components. However, highly accurate surface profile measurements are difficult to perform for microstructures owing to their complex surface topographies. In this paper, a measurement system is proposed for the surface profile measurement of microstructures. The main components of the measurement system are a precision displacement stage to move the workpiece, a homemade probing system with a diamond microstylus to sense the surface profile variation of the microstructures on the workpiece, and a vibration isolation table to reduce the disturbance of the measurement environment. In addition, the stability of the measurement was experimentally investigated. Microstructures with shape of equilateral right triangle were employed as the measurement specimen, and the surface profile of triangular microstructures was measured by employing two methods to correct errors caused by the specimen inclination and the radius of the stylus tip. The shape, depth, and period of the measured microstructures were also detected based on the results of the surface profile measurement. Experimental results demonstrate the feasibility of the proposed surface profile measurement for microstructures with complex surface topographies.

## 1. Introduction

Microstructures are key components that have attracted much attention for wide applications in the field of optical communication, optical storage, and flat panel displays [1–4]. Usually, microstructure-based components/systems have special designed functions, which result from the geometrical characteristics of the employed microstructures [5]. For instance, the backlight module in liquid crystal display panels uses triangular microstructures as the key component to enhance the working performance based on optical properties [4, 6, 7]. Therefore, it is important to precisely measure the surface profiles of microstructures. Typical microstructures have triangular, pyramidal, spherical, and aspherical surfaces with critical dimensions from several microns to several hundred microns, and their maximum local slope is up to 45–90° [8–10]. Because of the surface geometric features, accurate surface profile

measurement is difficult to perform using conventional surface profile measurement instruments [4, 11–14].

Commercially available surface profile measurement instruments, such as scanning electron microscopes (SEMs), optical profilers, and atomic force microscopes (AFMs), encounter unsolvable difficulties in the surface profile measurement of microstructures [15–21]. For instance, SEMs can carry out fast measurements with a high horizontal resolution of up to nanometers [17, 18, 22]. However, the result obtained by SEM has limited gray scales to characterize the surface variation in the vertical direction, that is, the vertical measuring scale has a lower resolution and cannot be quantified. An optical microscope is usually used to measure flat-type surfaces [18, 22–24]. During the measurement of microstructures with a slope of 45–90°, the measurement result has large errors in the area with a sharp surface slope because of the effect of light reflection. On the other hand, AFMs have extremely high spatial resolutions both in the

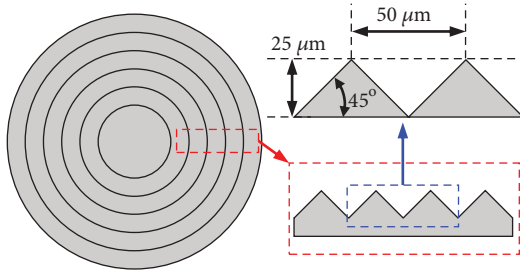


FIGURE 1: Schematic of the microstructures.

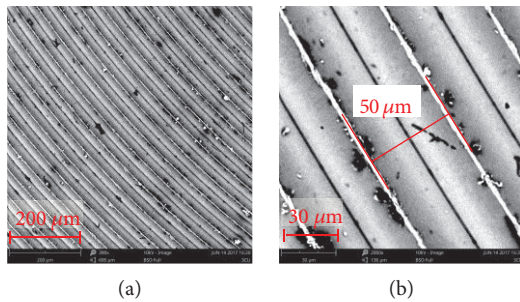


FIGURE 2: SEM images of the microstructures on the surface of the measured workpiece: (a) SEM image (scale:  $200\ \mu\text{m}$ ) and (b) details of microstructures (scale:  $30\ \mu\text{m}$ ).

horizontal and vertical directions and are usually employed for imaging nanoscale surfaces [19–21, 25]. However, its measurement ranges in the horizontal and vertical directions are limited to several microns, and therefore, it cannot effectively measure the surface profiles of microstructures with sizes ranging from several microns to several hundred microns. A stylus profiler, such as the Alpha-Step IQ Surface Profiler of KLA-Tencor, is another kind of powerful instrument that combines a high measurement precision (as low as  $0.1\ \text{nm}$ ) with a large measurement range (up to  $2\ \text{mm}$ ). Commercial stylus profilers employ a design of the leverage structure that leads to nonlinear errors while measuring in the horizontal direction [26]. Commercial stylus profilers are also called step profilers because they are usually used for high measurement precision of the step height of a workpiece.

Surface profile measurement of triangular microstructures not only requires a large measurement range and high measurement resolution but also a high measurement accuracy in both vertical and horizontal directions. Over the years, numerous works have been conducted to resolve this issue. Tian et al. developed a multifunction stylus profiling system employing a special sensing probe [2, 27, 28]. The sensing probe has an electromagnetic force actuator and three precision capacitive sensors, which lead to a slower measurement speed and limited measurement range in the vertical direction (only  $10\ \mu\text{m}$ ). Fang et al., Claverley and Leach, and Pawlus and Śmieszek studied methods to reduce dynamic errors, which are larger on steeper surfaces [6, 29, 30]. Fang et al., Chen et al., and Ju et al. proposed the sample tilting method for profile measurement of microstructured surfaces using a stylus-based profiler

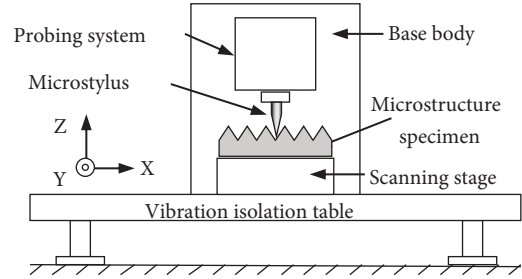


FIGURE 3: Schematic of the constructed measurement system.

[7, 31, 32]. Schuler et al. and Beutler also proposed a profile measurement method by tilting the sensor heads [14, 15]. The above approaches focused on employing a high-precision hardware, which is expensive and technologically unviable. Therefore, a simple and cost-effective method for surface profile measurement of microstructures is desired in precision engineering.

This paper describes a measurement system specifically designed and constructed for surface profile measurement of triangular microstructures generated on the surface of flat workpieces. Microstructures with shape of equilateral right triangle were employed as the measurement specimen. The surface profile measurement of triangular microstructures was carried out by employing two methods to correct errors caused by the specimen inclination and the radius of the stylus tip. The shape, depth, and period of the measured microstructures were also detected based on the results of surface profile measurement. In addition, the stability of the measurement was experimentally investigated. Experimental results demonstrate the feasibility of the proposed surface profile measurement for microstructures with complex surface topographies.

## 2. Measurement System for Triangular Microstructures

Figure 1 shows a schematic of the employed workpiece, which is flat and round, with several triangular microstructures fabricated on its surface along the radial direction using a homemade ultraprecision diamond cutting machine tool. The diameter of the workpiece is  $20\ \text{mm}$ . The nominal height of the microstructure is  $25\ \mu\text{m}$ , the period is  $50\ \mu\text{m}$ , and the shape is equilateral right triangle.

Figure 2(a) shows the SEM images obtained using an SEM (Phenom<sup>TM</sup>). As can be seen, the workpiece has inerratic periodic microstructures on its surface. Figure 2(b) shows the high-resolution image of the microstructures. The horizontal period of the microstructures was approximately  $50\ \mu\text{m}$ . Although the SEM is a powerful tool with a high resolution for imaging subtle features of a workpiece, the vertical features could not be detected, and the shape and height of the microstructures remained unknown even after SEM analysis.

To achieve highly accurate profile measurements of the triangular microstructures, a measurement system has been proposed, as shown in Figure 3. The system mainly consists of a precision scanning stage, a probing system, a microstylus, and a vibration isolation table. In the setup, the workpiece

TABLE 1: Key parameters of the proposed measurement system.

Probing system	Measurement range	30 mm
	Resolution (linear encoder)	2.5 nm
	Sampling frequency	Up to 20 MHz
	Stability (RMS)	1.6 nm
Microstylus	Tip material	Diamond
	Tip radius	2 $\mu\text{m}$
	Tip angle	20°
Linear scanning stage	Scanning range	5 mm
	Resolution	7 nm
	Min. incremental motion	50 nm
	Velocity	1 mm/s (max.)

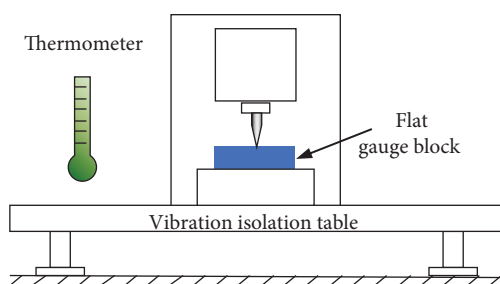


FIGURE 4: Schematic of the experimental setup for the stability test.

with triangular microstructures was mounted on the surface of the scanning stage, which was horizontally mounted on the vibration isolation table. The probing system was vertically set up and its sensing axis was perpendicular to the surface of the scanning stage. The microstylus, which had a small included angle and a spherical tip, was mounted on the shaft end of the probing system. During measurement, the scanning stage moved the workpiece, and the probing system with a microstylus sensed the vertical variation in the surface profile of the workpiece. The data from the scanning stage and the probing system was employed to reconstruct the surface profile of the measured microstructures.

The probing system has a measurement range of 30 mm, resolution of 2.5 nm, and sampling frequency of up to 20 MHz. The stability of the probing system is 1.6 nm. Since the included angle of the stylus tip is 20°, it can be used to measure a steep surface with a slope of up to 80°. The tip radius of the stylus is 2  $\mu\text{m}$ . The linear stage has a scanning range of 5 mm with a resolution of 7 nm. Its minimum incremental motion is 50 nm and its maximum moving velocity is up to 1 mm/s. The parameters of the proposed measurement system are shown in Table 1.

### 3. Experiments

**3.1. Stability Test.** Figure 4 shows a schematic of the experimental setup for the stability test of the constructed measurement system. The microstylus of the probing system was made to contact with the surface of a flat gauge block, which

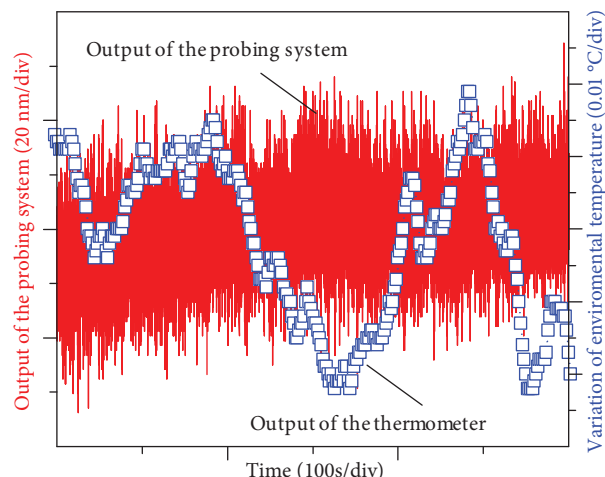


FIGURE 5: Stability of the constructed measurement system.

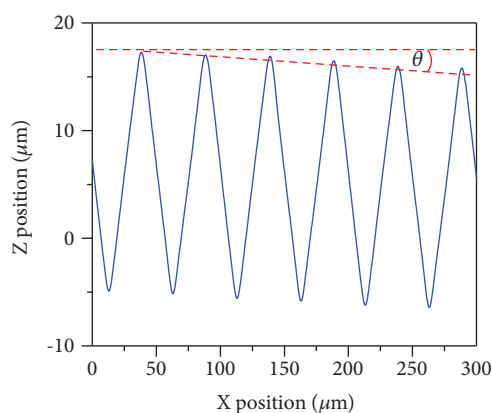


FIGURE 6: Surface profile measurement results of the microstructures.

was rigidly fixed on the scanning stage surface by screws. A highly accurate thermometer with a resolution of 0.001°C was employed to measure the variation in ambient temperature. The time intervals of data sampling for the probing system and the thermometer were set as 0.1 s and 0.50 s, respectively. The test duration was 300 s.

The acquired results are summarized in Figure 5. The variation in the probing system was  $\pm 30$  nm, and the temperature variation of the measurement environment is  $\pm 0.03^\circ\text{C}$ .

**3.2. Surface Profile Measurement.** The surface profiles of the triangular microstructures on the surface of the workpiece, whose schematic is shown in Figure 1, were measured by the constructed measurement system. The workpiece was scanned by the linear stage with a speed of 0.3 mm/min. During scanning, the surface profile variation in the vertical direction was traced by the diamond microstylus and detected by a linear encoder inside the probing system. The microstructures were measured in the range of 300  $\mu\text{m}$  and the measurement time was 1 min.

The raw data of the measured profile is plotted in Figure 6, wherein data related to the lower horizontal axis

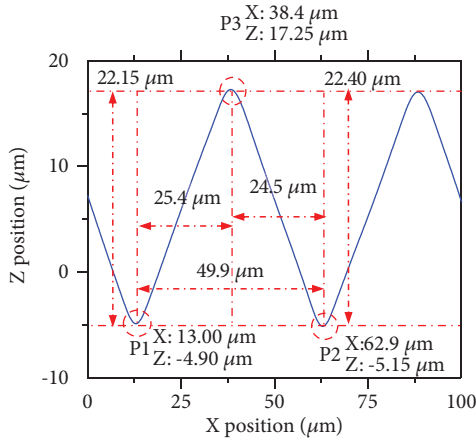


FIGURE 7: Details of the measured surface profile.

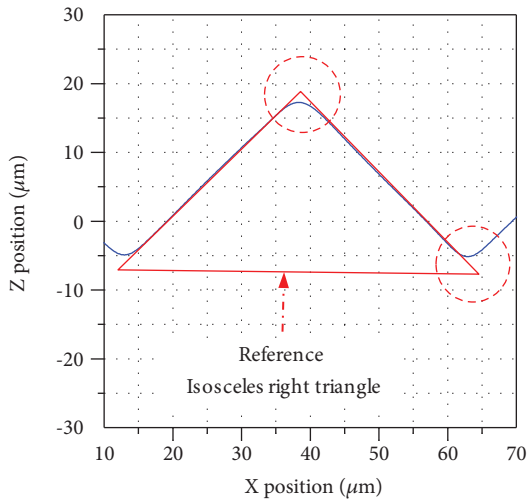


FIGURE 8: Shape comparison of the measured microstructures.

was obtained from the output of the scanning stage, and that related to the vertical axis was obtained from the output of the probing system. The measured microstructures were found to have been fabricated with a highly uniform period. However, the top surface of each period of the microstructures decreased regularly in the vertical direction. This was caused by the mounting process, and the inclination angle is denoted by  $\theta$ . The error caused by the inclination should be corrected for highly accurate measurements.

To obtain more information from the measurement results, the details of the surface profile were replotted, as shown in Figure 7, and the  $x$ -axis range was changed to  $100 \mu\text{m}$ . In this figure, three feature points—P1 and P2 at the surface bottom and P3 at the surface top—were extracted to measure the height and period of the microstructures. As shown in Figure 7, the first period of the measured microstructures was about  $49.9 \mu\text{m}$ , and the heights of the first microstructures in the left and right sides were  $22.15 \mu\text{m}$  and  $22.40 \mu\text{m}$ , respectively.

The surface profile of the first measured microstructure was replotted, as shown in Figure 8, by employing the same

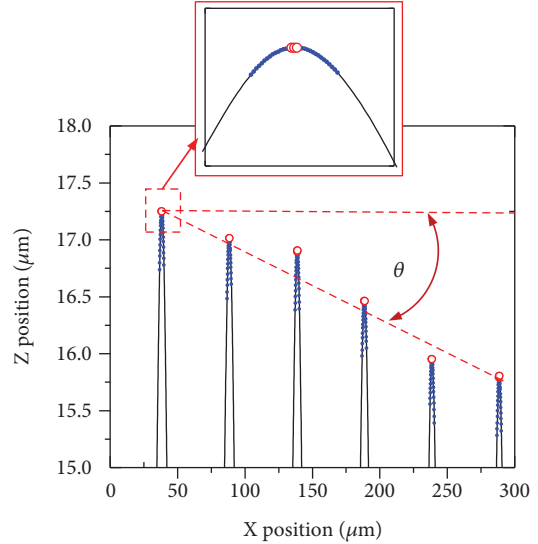


FIGURE 9: Compensation of inclination error.

vertical and horizontal plotting scales. An equilateral right triangle as a reference was used to verify the shape of the measured microstructure. It shows that the shape of the measured microstructure was equilateral right triangle. However, the shapes at the top and bottom were smoother compared to the endpoints of a triangle, which are indicated by two red circles in Figure 8. This error was caused by the stylus tip radius.

## 4. Error Compensations

**4.1. Inclination Error Compensation.** In the inclination error compensation, the top surface of the microstructures was used as a reference surface. The compensation process is illustrated in Figure 9. First, the top surface of each microstructure was extracted (blue dots). The top three points of each period (red circles) were fitted to a straight line. Then, the measured surface profile was rotated around the first point of the top three points of the first period. The rotated angle was the inclination angle of the fitted straight line, but the direction was opposite. In this measurement, the inclination angle is  $-0.36^\circ$ . Therefore, the measured surface profile was rotated  $0.36^\circ$  along the anti-clockwise direction. The results for inclination error compensation are shown in Figure 10.

**4.2. Stylus Tip Radius Correction.** Although the influence of the inclination error was compensated, the measured data still cannot provide the correct surface profile for the measured microstructures. The raw data of measurement results are a trace of the stylus tip center, which deviate from the real profile of the measured microstructures. Figure 11 schematizes the influence of the stylus tip radius in the surface profile measurement.

As shown in Figure 11, the nature of the surface profile measurement employing a contact-type stylus can be modeled as a tangential contact between a sphere and a surface.

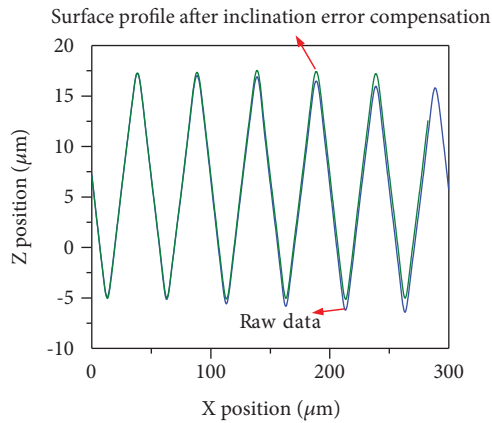


FIGURE 10: Results for inclination error compensation.

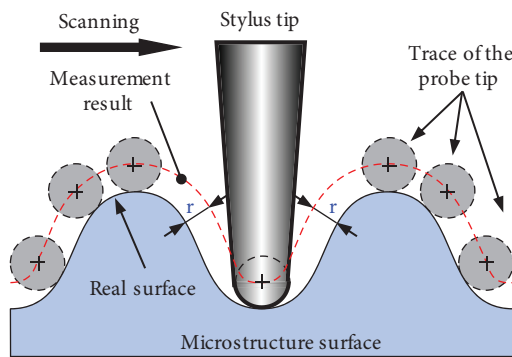
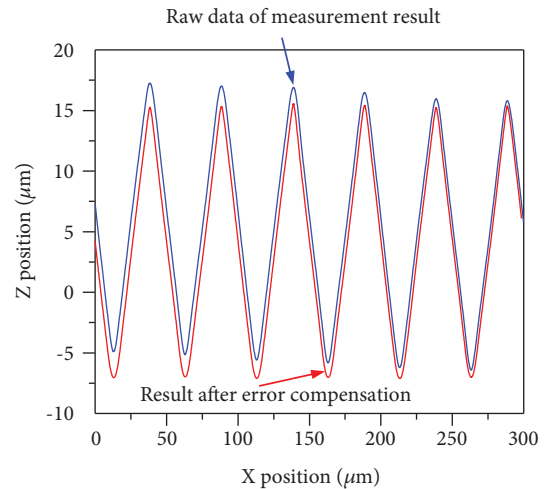


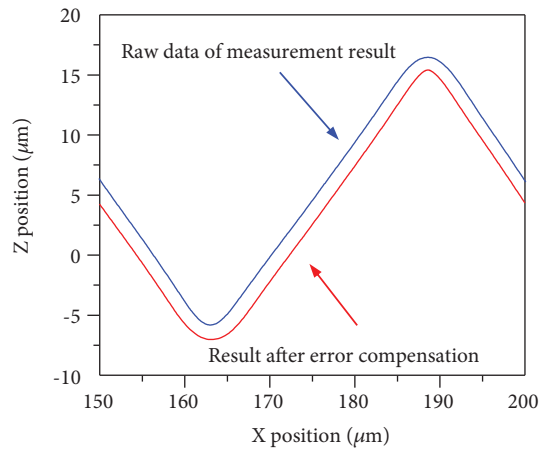
FIGURE 11: Influence of the stylus tip radius on the measurement result.

Therefore, the measurement result (outputs of the probing system and scanning stage) was an envelope curve of the real surface profile of the measured microstructures. One point of the measurement results one contacting point on the real surface. Both points have the same normal vector, and the distance between the two points along the direction of the normal vector is equal to the stylus tip radius. Therefore, the primary task when correcting the probe tip radius is to estimate the normal vector for the points of the measurement result. First-order linear fitting was employed to estimate the normal vector. Each point of the measurement results was first-order linear fitted with two points before and after. The normal vectors of the fitting results and the stylus tip radius were used to calculate the position of the contacting point. The obtained positions of the contacting points were used to reconstruct the surface profile for the measured microstructure. This reconstructed profile was considered the real profile of the measured microstructure with the stylus tip radius error compensated [33].

The surface profile after stylus tip radius compensation is shown in Figure 12(a). Note that the errors of both, inclination and stylus tip radius, were compensated for the final measurement results. More detail of the compensation result is shown in Figure 12(b).



(a)



(b)

FIGURE 12: Compensation of the measured surface profile before and after error compensation. (a) Comparison of the raw data and result after error compensation. (b) Details of the surface profile after error compensation.

## 5. Depth and Period Measurements

The depth and period, which are two most important features of manufacturing, were evaluated based on the well-measured surface profile of the measured microstructures. As shown in Figure 13, the period of the microstructures was evaluated by the peak-to-peak difference in the  $x$ -direction. The depth of the microstructures was evaluated by the peak-to-valley difference along the  $z$ -direction.

Figure 14 shows the evaluation result of the period of the measured microstructures. The mean value of each period was  $50.065 \mu\text{m}$ , and the maximum variation was from  $-0.360 \mu\text{m}$  to  $0.425 \mu\text{m}$ . The standard deviation of periods was  $0.291 \mu\text{m}$ .

Figure 15 shows the evaluation result of the depth of the measured microstructures. The mean depth for each case was  $22.408 \mu\text{m}$ , and the maximum variation was from  $-0.093 \mu\text{m}$  to  $0.240 \mu\text{m}$ . The standard deviation of periods was  $0.126 \mu\text{m}$ .

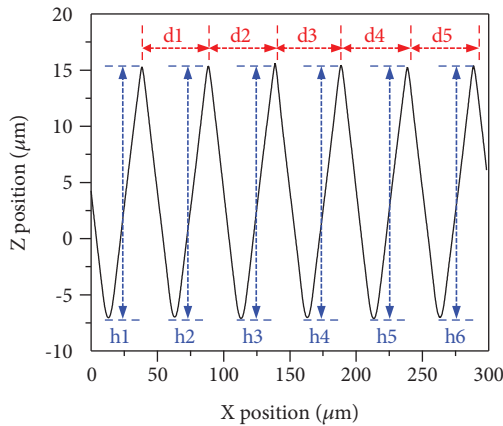


FIGURE 13: Evaluation of the period and depth.

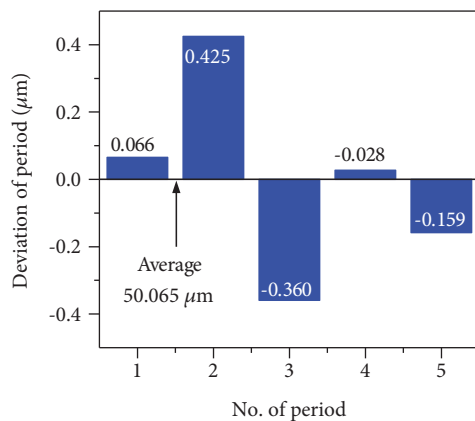


FIGURE 14: Evaluation result of the period of microstructures.

## 6. Conclusions

A measurement system, which employs a probing system with a microstylus and a linear scanning precision stage, is proposed in this paper. Surface profile measurement of the triangular microstructures was carried out to verify the performance of the developed system. Two methods were employed to correct the measurement errors caused by the specimen inclination and the radius of the stylus tip. The shape, depth, and period of the measured microstructures were also detected based on the results of surface profile measurement. The variation of the probing system was  $\pm 30$  nm. The shape of the measured microstructures was an equilateral right triangle. The period of the measured microstructures was  $50.065 \mu\text{m}$ , with a standard deviation of  $0.291 \mu\text{m}$ . The depth of the measured microstructures was  $22.408 \mu\text{m}$  with a standard deviation of  $0.126 \mu\text{m}$ . Experimental results demonstrate the feasibility of the proposed surface profile measurement for microstructures with complex surface topography.

The proposed method can potentially measure the surface of more types of microstructures, and the measurement uncertainty can be evaluated by standard samples of the

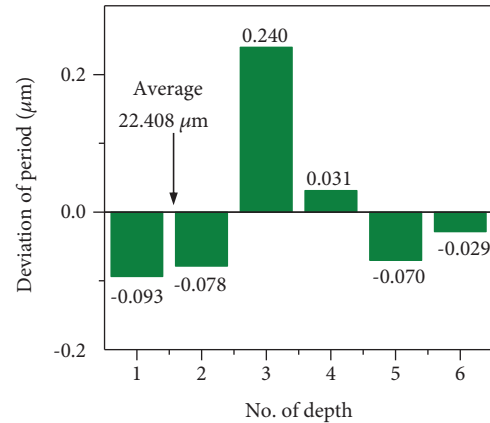


FIGURE 15: Evaluation result of the depth of microstructures.

microstructure with highly geometrical accuracy; these can constitute future work.

## Data Availability

1. The (SEM image) data used to support the findings of this study are included within the article. 2. The (measurement result obtained by the proposed system) data used to support the findings of this study are available from the corresponding author upon request.

## Conflicts of Interest

The authors declare that they have no competing interests.

## Acknowledgments

This research is sponsored by the National Major Projects of High-End CNC Machine Tools and Basic Manufacturing Equipment (no. 2017ZX04020001-005).

## References

- [1] X. Li, K. Ni, Q. Zhou, P. Yan, J. Pang, and X. Wang, "Improved master-replica separation process for fabrication of a blazed concave grating by using a combination-type convex grating," *Applied Optics*, vol. 56, no. 2, pp. 298–302, 2017.
- [2] J. Tian, Y. Tian, Z. Guo, F. Wang, D. Zhang, and X. Liu, "Structure design and experimental investigation of a multi-function stylus profiling system for characterization of engineering surfaces at micro/nano scales," *Microsystem Technologies*, vol. 24, no. 5, pp. 2177–2187, 2018.
- [3] Y. Cai, Y.-L. Chen, M. Xu et al., "An ultra-precision tool nano-indentation instrument for replication of single point diamond tool cutting edges," *Measurement Science and Technology*, vol. 29, no. 5, article 54004, 2018.
- [4] Z. Guo, Y. Tian, X. Liu, F. Wang, C. Zhou, and D. Zhang, "Modeling and simulation of the probe tip based nanochannel scratching," *Precision Engineering*, vol. 49, pp. 136–145, 2017.
- [5] X. Li, H. Wang, K. Ni et al., "Two-probe optical encoder for absolute positioning of precision stages by using an improved scale grating," *Optics Express*, vol. 24, no. 19, pp. 21378–21391, 2016.

- [6] H. Fang, B. Xu, D. Yin, and S. Zhao, "A method to control dynamic errors of the stylus-based probing system for the surface form measurement of microstructures," *Journal of Nanomaterials*, vol. 2016, Article ID 3727514, 8 pages, 2016.
- [7] H. Fang, B. Xu, W. Chen, H. Tang, and S. Zhao, "A slope-adapted sample-tilting method for profile measurement of microstructures with steep surfaces," *Journal of Nanomaterials*, vol. 2015, Article ID 253062, 8 pages, 2015.
- [8] M. Yamamoto, H. Takeuchi, and S. Aoki, "Dimensional measurement of high aspect ratio micro structures with a resonating micro cantilever probe," *Microsystem Technologies*, vol. 6, no. 5, pp. 179–183, 2000.
- [9] Y. Takaya, M. Michihata, T. Hayashi, and T. Washitani, "Dimensional measurement of microform with high aspect ratio using an optically controlled particle with standing wave scale sensing," *CIRP Annals*, vol. 61, no. 1, pp. 479–482, 2012.
- [10] B. F. Ju, Y. L. Chen, W. Zhang, and F. Z. Fang, "Rapid measurement of a high step microstructure with 90° steep sidewall," *Review of Scientific Instruments*, vol. 83, no. 1, article 13706, 2012.
- [11] P. Thomsen-Schmidt, "Characterization of a traceable profiler instrument for areal roughness measurement," *Measurement Science & Technology*, vol. 22, no. 9, article 94019, 2011.
- [12] Y. Shi, C. Sun, P. Wang, Z. Wang, and H. Duan, "High-speed measurement algorithm for the position of holes in a large plane," *Optics and Lasers in Engineering*, vol. 50, no. 12, pp. 1828–1835, 2012.
- [13] R. Henselmans, L. A. Cacace, G. F. Y. Kramer, P. C. J. N. Rosielle, and M. Steinbuch, "The NANOMEFOS non-contact measurement machine for freeform optics," *Precision Engineering*, vol. 35, no. 4, pp. 607–624, 2011.
- [14] A. Schuler, A. Weckenmann, and T. Hausotte, "Setup and evaluation of a sensor tilting system for dimensional micro- and nanometrology," *Measurement Science and Technology*, vol. 25, no. 6, article 64010, 2014.
- [15] A. Beutler, "Flexible, non-contact and high-precision measurements of optical components," *Surface Topography-Metrology and Properties*, vol. 4, no. 2, 2016.
- [16] S. H. JANG, Y. SHIMIZU, S. ITO, and W. GAO, "Development of an optical probe for evaluation of tool edge geometry," *Journal of Advanced Mechanical Design, Systems, and Manufacturing*, vol. 8, no. 4, 2014.
- [17] M. B. Bauza, S. C. Woody, B. A. Woody, and S. T. Smith, "Surface profilometry of high aspect ratio features," *Wear*, vol. 271, no. 3–4, pp. 519–522, 2011.
- [18] H. N. Hansen, K. Carneiro, H. Haitjema, and L. De Chiffre, "Dimensional micro and nano metrology," *CIRP Annals*, vol. 55, no. 2, pp. 721–743, 2006.
- [19] A. Ahmad, A. Schuh, and I. W. Rangelow, "Adaptive AFM scan speed control for high aspect ratio fast structure tracking," *Review of Scientific Instruments*, vol. 85, no. 10, article 103706, 2014.
- [20] W. Yang, X. Liu, W. Lu, and X. Guo, "Influence of probe dynamic characteristics on the scanning speed for white light interference based AFM," *Precision Engineering*, vol. 51, pp. 348–352, 2018.
- [21] W. Yang, X. Liu, W. Lu, C. Hu, and X. Guo, "Towards a traceable probe calibration method for white light interference based AFM," *Precision Engineering*, vol. 51, pp. 40–47, 2018.
- [22] B. Xu, Z. Jia, X. H. Li et al., "Surface form metrology of micro-optics," in *International Conference on Optics in Precision Engineering and Nanotechnology (icOPEN2013)*, vol. 876902, pp. 1–15, Singapore, June 2013.
- [23] S. C. H. Thian, W. Feng, Y. S. Wong et al., "Dimensional measurement of 3D microstructure based on white light interferometer," *Journal of Physics: Conference Series*, vol. 48, pp. 1435–1446, 2006.
- [24] R. J. Hocken, N. Chakraborty, and C. Brown, "Optical metrology of surfaces," *CIRP Annals*, vol. 54, no. 2, pp. 169–183, 2005.
- [25] A. Elkaseer and E. B. Brousseau, "Modelling the surface generation process during AFM probe-based machining: simulation and experimental validation," *Surface Topography: Metrology and Properties*, vol. 2, no. 2, 2014.
- [26] C. Li, S. Yang, Y. Wang, C. Wang, W. Ren, and Z. Jiang, "Measurement and characterization of a nano-scale multiple-step height sample using a stylus profiler," *Applied Surface Science*, vol. 387, pp. 732–735, 2016.
- [27] Z. Guo, Y. Tian, J. Tian et al., "Probe system design for three dimensional micro/nano scratching machine," *Microsystem Technologies-Micro- and Nanosystems-Information Storage and Processing Systems*, vol. 23, no. 6, pp. 2285–2295, 2017.
- [28] J. Tian, Y. Tian, Z. Guo et al., "Development of a novel 3-DOF suspension mechanism for multi-function stylus profiling systems," *International Journal of Precision Engineering and Manufacturing*, vol. 17, no. 11, pp. 1415–1423, 2016.
- [29] J. D. Claverley and R. K. Leach, "A vibrating micro-scale CMM probe for measuring high aspect ratio structures," *Microsystem Technologies-Micro- and Nanosystems-Information Storage and Processing Systems*, vol. 16, no. 8–9, pp. 1507–1512, 2010.
- [30] P. Pawlus and M. Śmieszek, "The influence of stylus flight on change of surface topography parameters," *Precision Engineering*, vol. 29, no. 3, pp. 272–280, 2005.
- [31] Y.-L. Chen, W.-L. Zhu, S. Yang, B.-F. Ju, and Y. Ge, "Large-area profile measurement of sinusoidal freeform surfaces using a new prototype scanning tunneling microscopy," *Precision Engineering*, vol. 38, no. 2, pp. 414–420, 2014.
- [32] B.-F. Ju, Y.-L. Chen, W. Zhang, W. Zhu, C. Jin, and F. Z. Fang, "Note: long range and accurate measurement of deep trench microstructures by a specialized scanning tunneling microscope," *Review of Scientific Instruments*, vol. 83, no. 5, article 56106, 2012.
- [33] B. Xu, Y. Shimizu, S. Ito, and W. Gao, "Surface profile measurement of internal micro-structures," *International Journal of Precision Engineering and Manufacturing*, vol. 14, no. 9, pp. 1535–1541, 2013.

## Research Article

# Preparation and Evaluation of Smart Nanocarrier Systems for Drug Delivery Using Magnetic Nanoparticle and Avidin-Iminobiotin System

Shuguo Sun <sup>1,2</sup>, Beiping Li,<sup>1</sup> Tao Yang <sup>1</sup>, Meihu Ma <sup>2</sup>, Qinlu Lin <sup>1</sup>, Juanhong Zhao,<sup>1</sup> and Feijun Luo<sup>1,3</sup>

<sup>1</sup>National Engineering Laboratory for Rice and Byproduct Processing, Central South University of Forestry and Technology, Changsha, Hunan 410004, China

<sup>2</sup>National R&D Center for Egg Processing, Huazhong Agricultural University, Wuhan, Hubei 430070, China

<sup>3</sup>Department of Pathology, Addenbrooke's Hospital, University of Cambridge, Cambridge, UK

Correspondence should be addressed to Tao Yang; [yangtao807@163.com](mailto:yangtao807@163.com) and Meihu Ma; [mameihuhn@163.com](mailto:mameihuhn@163.com)

Received 30 March 2018; Accepted 27 May 2018; Published 28 August 2018

Academic Editor: Vidyadhar Singh

Copyright © 2018 Shuguo Sun et al. This is an open access article distributed under the Creative Commons Attribution License, which permits unrestricted use, distribution, and reproduction in any medium, provided the original work is properly cited.

Therapeutic efficacy and the regulation of drug release can be improved by using selective targeting drug delivery systems. In this paper, we have demonstrated avidin-immobilized magnetic nanoparticles (AMNPs) as a novel targeted drug delivery system to deliver iminobiotinylated daunomycin (IDAU). TEM, XRD, VSM, and FTIR were employed for the physicochemical characterization of the drug-loaded MNPs. The binding of IDAU had little effect on sizes of AMNPs (~35 nm), but the stability and dispersibility of the nanoparticles were improved. The study also found that the loading capacity and efficiency of nanoparticles were mainly dependent on affinity interaction between IDAU and AMNPs. The optimal loading capacity and efficiency of MNPs for IDAU were  $0.408 \pm 0.012$  mg/g and  $94.18 \pm 2.64\%$  according to the reversed-phase high-performance liquid chromatography (RP-HPLC) data, respectively. Under the conditions of pH 6.8 and 1 mmol/L of biotin, the drug-loaded MNPs released rapidly at beginning and then maintained at a certain controllable release level. The effect of IDAU on DLKP proliferation was tested, and the results showed that IC<sub>50</sub> was  $(1.60 \pm 0.05) \times 10^{-3}$  mg/mL. Our findings indicated that AMNPs hold tremendous potential as an effective drug delivery system.

## 1. Introduction

Preventing the spread of malignant cells in the human body is a matter of serious concern. Presently, surgical resection, radiation, and chemotherapy are generally used to treat the cancer cells, but the selection of the treatment option depends on the location of the tumor and whether the tumor is at an early or advanced stage. Meanwhile, new types of anticancer drugs are being developed unceasingly [1–3], and some drug delivery devices/systems have received considerable attention, such as macromolecular carrier system [4], microcapsule drug delivery system [5], and magnetic drug delivery system [6–8].

The biggest challenge in drug delivery is the transportation of drug agents to the targeted site at the appropriate time

[9]. The release rate of conventional administered antitumor drugs or injections is uncontrolled, which may lead to harmful side effects and toxicity due to quick drug release. For an excellent drug delivery system, it must be controllable and then the therapeutic levels can extend over long periods of time, which can eliminate the abovementioned side effects and toxicity. In the controlled delivery, the drug delivery may commence with first-order kinetics to an optimum and effective drug concentration to the targeted site, followed by zero-order kinetics, which may be one of the best ways to release the drug. There are two controlled-release mechanisms for selected drug delivery systems. One mechanism is physical adsorption, and the drug may be automatically released at the appropriate time. Biodegradable polymers, for example, adsorb the drugs due to hydrogen bond and/

or dipole-charge interactions with the polymer chains. The main disadvantage of this system is that it cannot effectively control the rate of drug release. The other mechanism is that the drugs are attached to a carrier through a covalent bond or via an affinity interaction, the most common affinity tag of this type being the avidin-biotin system [10, 11]. This drug delivery system has an advantage that it is influenced by the ambient factors timely. However, the drugs are difficult to release from the carrier in the condition of pH 6.8. The iminobiotin coupled with anticancer drugs shows a high affinity to avidin (and avidin-immobilized magnetic nanoparticles (AMNPs)) at elevated pH (9.5–10.8) but releases the drugs easily at lower pH (~4) or under the presence of a certain concentration of biotin at pH 6.8 according to the manufacturer's instructions. In this system, the drug release can be controlled under mild conditions. Therefore, the application of avidin-iminobiotin technology in drug delivery systems creates an opportunity for the development of new smart drug delivery systems because of its controllable, easy release of the drug under the condition of pH 6.8.

There is currently a great concern about magnetic field-induced, targeted drug delivery [12–15], in spite of extensive applications of MNPs in biomedical and diagnostic fields and nanoreactor systems, including *in vitro* cell separation, *in vivo* antimycotic agent, contrast agent for magnetic resonance imaging, magnetic particle imaging, hyperthermia, tumor therapy, or cardiovascular disease [16–24]. The conjugation of a drug to magnetic nanoparticle (MNP) entrapped polymer or antibody is an effective method for controlled delivery of the drug to the targeted site. Under such medication, the drug can be released at the desired location and act locally until the therapy is completed. Therefore, the dosage of medication can be reduced, and the harmful side effects and toxicity of drugs kept to a minimum [25, 26]. It is worth noting that the MNPs used for the drug delivery system always require adequate magnetic strength, biocompatibility, and functional active groups on the surface [27]. Nanoparticles used in the drug-loaded system will generally be administered by intravenous injection and then transported in the blood. Therefore, the dispersibility and biocompatibility in blood and interaction between plasma proteins and MNPs should be fully considered [28, 29].

The conjugation of a drug to MNPs functionalized with polymer or bioactive macromolecules is a viable method for controlled delivery of a drug to the desired site. In the present study, an iminobiotinylated drug, iminobiotinylated daunomycin (IDAU), was connected to avidin-immobilized magnetic nanoparticles (AMNPs) based on the avidin-iminobiotin binding system. The drug loading capacity and release behavior were then determined through adsorption/dissociation kinetics experiments, and the inhibitory effects of IDAU on liver tumor cell DLKP growth was also evaluated.

## 2. Experiment

**2.1. Materials.** Unless stated, all chemicals were commercially available and of analytical grade. EZ-Link® NHS-iminobiotin and DLKP cell medium were purchased from Invitrogen (Life Technologies, Carlsbad, CA, USA). DAU hydrochloride

standard preparation was purchased from Sigma. Fetal bovine serum (FBS) was purchased from Hangzhou Sijiqing Company (Hangzhou, China). Other chemicals were of laboratory grade purity and used as obtained.

### 2.2. Preparation of Functionalized MNPs

**2.2.1. Preparation and Glutaraldehyde Activation of PEI-Coated MNPs.** MNPs were prepared via a facile solvothermal synthesis method, in which polyethyleneimine (PEI) was used as the protective agent to prevent the particles from aggregation [30]. The typical synthetic procedure was as follows.  $\text{FeCl}_3 \cdot 6\text{H}_2\text{O}$  (0.135 g), PEI (0.5 g), and sodium acetate (1.8 g) were added to ethylene glycol (20.0 mL) to form colloid mixture under vigorous stirring at room temperature for 45 min. Then, 18.0 mL of the mixture was sealed in Teflon-lined stainless steel autoclave of 20 mL capacity. Finally, the autoclave was heated and maintained at 200°C for 12 h and allowed to cool down to room temperature naturally. The back products were washed twice with absolute ethanol and twice with Milli-Q water. MNPs were then dispersed in Milli-Q water and stored in sealed cell (50 mL) at room temperature.

To activate PEI-coated MNPs with glutaraldehyde, the nanoparticles were dispersed in 20 mL PBS buffer (0.1 mol/L, pH 8.0) containing 2% glutaraldehyde. The suspension was mechanically stirred at room temperature in the dark for 4 h. The glutaraldehyde-activated MNPs were separated from unconjugated glutaraldehyde by magnetically driven separation at room temperature for 5 min and then washed three times with PBS buffer (0.1 mol/L, pH 8.0). The final glutaraldehyde-activated MNPs were dispersed in 20 mL PBS buffer (0.1 mol/L, pH 8.0) and kept in the dark at 4°C until use.

**2.2.2. Immobilization of Avidin onto MNPs.** To immobilize avidin, 15 mg of glutaraldehyde activated MNPs was dispersed in 20 mL PBS buffer (0.1 mol/L, pH 8.0) and sonicated for 5 s at 20 W by a Ti probe (Branson 450 sonifier). 5 mL of avidin (100  $\mu\text{g}/\text{mL}$ ) was introduced to the PBS buffer solution, and the suspension was mechanically stirred at 4°C in the dark for 4 h. AMNPs were separated from unconjugated avidin by magnetically driven separation at 4°C for 5 min and then washed three times with PBS buffer (0.1 mol/L, pH 8.0). The final AMNPs were dispersed in 20 mL PBS buffer (0.1 mol/L, pH 8.0) and kept in the dark at 4°C until use.

### 2.3. Conjugation of Drug to AMNPs

**2.3.1. Preparation of IDAU.** IDAU was prepared by reaction between 1.5 mg DAU and 1.0 mg NHS-iminobiotin at 4°C for 24 h in 20 mL of PBS buffer (0.1 mol/L, pH 10.8), and then the buffer was adjusted to pH 8.0 with 1 mol/L phosphoric acid. The product need not be separated from the excessive DAU and kept in the dark at 4°C until use.

**2.3.2. Conjugation of IDAU to MNPs.** AMNPs were dispersed in 20 mL of PBS buffer (0.1 mol/L, pH 8.0) containing 0.1 mg/mL of IDAU, followed by incubation for 4 h at 4°C with gentle stirring. The DAU-loaded MNPs were separated

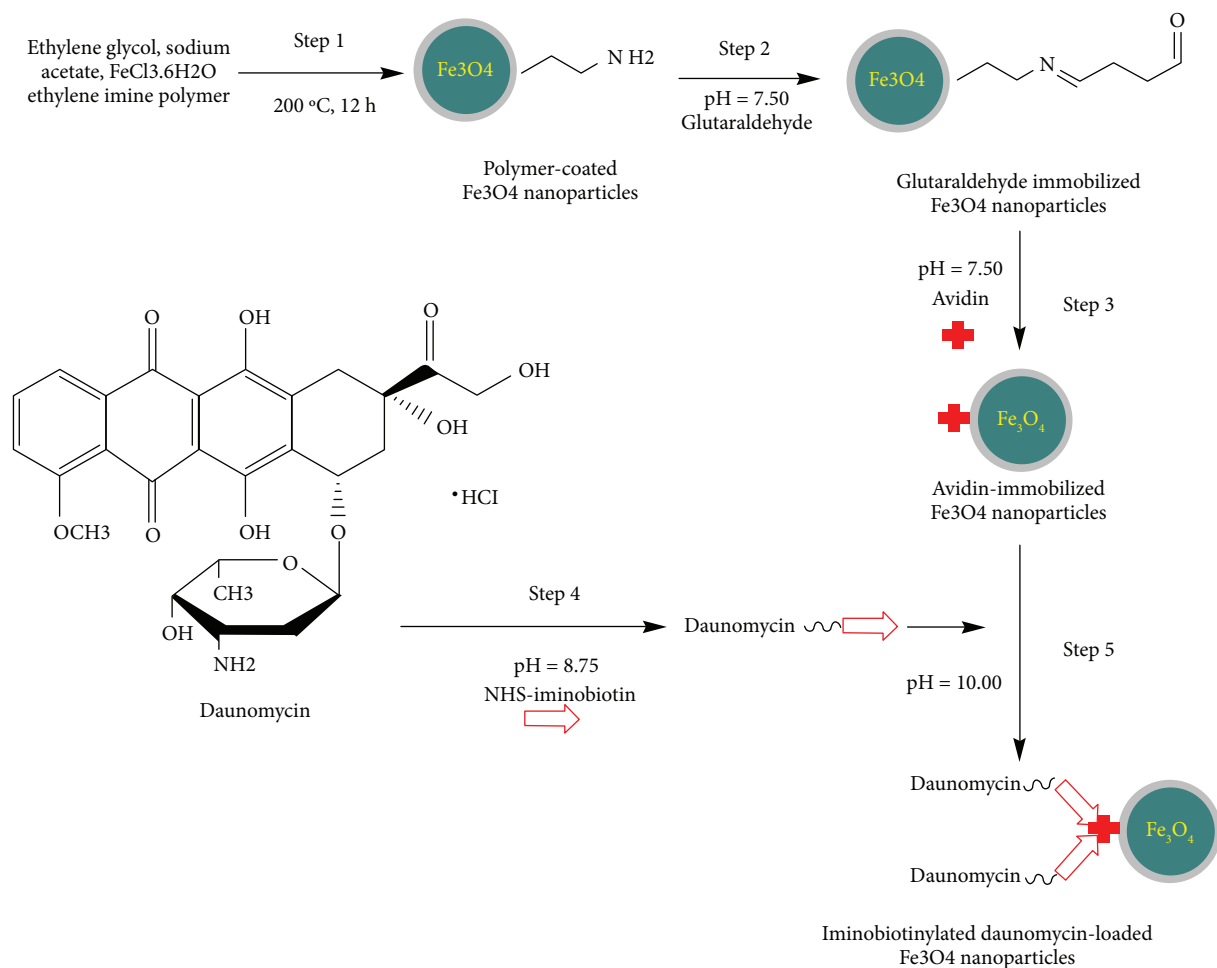


FIGURE 1: Schematic of the different steps in the preparation of iminobiotinylated daunomycin-loaded  $\text{Fe}_3\text{O}_4$  nanoparticles.

from the solution with the aid of a magnet and then washed three times with PBS buffer (0.1 mol/L,  $\text{pH} 8.0$ ). The final IDAU-loaded MNPs (IDAU-MNPs) were dispersed in 20 mL PBS buffer (0.1 mol/L,  $\text{pH} 7.0$ ) and kept in the dark at  $4\text{ }^\circ\text{C}$  until use. A schematic of the different steps in the preparation of iminobiotinylated daunomycin-loaded  $\text{Fe}_3\text{O}_4$  nanoparticles (IDAU-MNPs) is summarized in Figure 1.

## 2.4. Physicochemical Characterization of MNPs

**2.4.1. Particle Shape Analysis and Size Analysis.** The size and morphology of AMNPs and DAU-immobilized MNPs were examined under a transmission electron microscope (TEM) operated at 100 KV (model JEM 2010, JeM Inc., Japan). The nanoparticles were first diluted in deionized water to an appropriate concentration ( $7.5\text{ }\mu\text{g}/\text{mL}$ ) and then ultrasonicated for 10 s. A copper grid (200 mesh and cover with formvar/carbon) was coated with the thin layer of diluted particle suspension and allowed to stand for 2 min. The excess liquid was drained off by filter paper and the samples were then examined by TEM.

**2.4.2. X-Ray Diffraction (XRD).** XRD experiments of the crystalline phase of a powder sample of MNPs, AMNPs, and

IDAU-MNPs were performed using an X-ray diffractometer (Rigaku D/max- $\gamma$ , Japan) and  $\text{Cu-K}\alpha$  ( $\lambda = 0.154056\text{ nm}$ ) radiation. The parameters of the measurements were: 40 kV and 20 mA, angular variation ranging from  $20$  to  $80^\circ$  in steps of  $10.0^\circ$  for each 1 min (geometry  $\theta$ - $2\theta$ ).

**2.4.3. Vibrating-Sample Magnetometry (VSM).** MNPs, AMNPs, and IDAU-MNPs were checked for magnetic susceptibility using vibrating-sample magnetometer (PARC, 155, USA) which provided magnetization ( $\text{emu g}^{-1}$ ) of magnetic particles in response to an external magnetic field (Oe).

**2.4.4. Fourier-Transform Infrared Spectroscopy (FTIR).** Avidin and DAU anchoring onto the surface of MNPs were monitored by FTIR. Data were collected on a Nicolet Avatar-330 Spectrometer (Thermo Nicolet, USA) with  $4\text{ cm}^{-1}$  resolution using the KBr pellet technique.

**2.5. Drug Loading Determination (Indirect Estimation).** The degree of IDAU incorporation into AMNPs was analyzed by RP-HPLC and monitored using a UV-VIS detector. IDAU-MNPs were separated from unconjugated DAU and IDAU by magnetically driven separation at  $4\text{ }^\circ\text{C}$  for 5 min and then rinsed with PBS buffer (0.1 mol/L,  $\text{pH} 8.0$ ) until

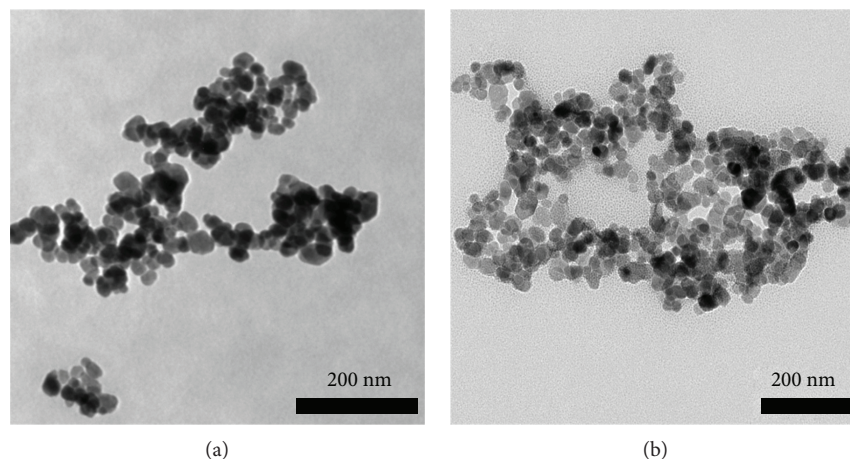


FIGURE 2: TEM images of AMNPs (a) and IDAU-MNPs (b).

no DAU was detected in washings. The IDAU loading capacity (LC, mg/g) was determined as

$$LC(\text{mg/g}) = 100 \times \frac{C_d}{C_n} = 100 \times \frac{(C_0 - C_1)}{C_n}, \quad (1)$$

where  $C_d$ ,  $C_n$ ,  $C_0$ , and  $C_1$  are the concentrations of IDAU incorporated in nanoparticles (mg/mL), MNPs offered for DAU incorporation (g/mL), initial additions of IDAU (mg/mL), and IDAU remained in PBS buffer after the DAU-loaded MNPs were separated from the solution (mg/mL), respectively.

## 2.6. In Vitro Evaluation of the Anticancer Drug

**2.6.1. Kinetics of Drug Release.** Two methods for drug release were investigated in our experiments. On the one hand, appropriate amounts of IDAU-MNPs samples were dispersed in 20 mL of incubation medium (PBS buffer containing 1 mM of biotin, pH 6.8) and maintained under constant mild agitation in a water bath (37°C). On the other hand, the same amounts of drug-loaded MNPs samples were dispersed in 20 mL of 0.1 mol/L ammonium acetate buffer at pH 4.0 (the buffer containing 0.5 mol/L NaCl and 1.0 mmol/L EDTA) and maintained under constant mild agitation in a water bath (37°C). The final concentration of IDAU was chosen to ensure sink conditions for the in vitro study. Aliquots (15  $\mu\text{L}$ ) were taken in predetermined time intervals from 2 to 540 min. Each aliquot was analyzed with RP-HPLC for IDAU content as described above.

**2.6.2. In Vitro Cytotoxicity.** A proliferation method was used to measure the cytotoxicity of IDAU-MNP samples towards the DLKP cell line [30–33], with slight modifications. Cytotoxicity of drugs was measured as previously described. Briefly, cells were seeded at  $1 \times 10^3$  cells/well in a 96-well plate and left to attach overnight in a 5%  $\text{CO}_2$  incubator at 37°C. The appropriate concentrations of IDAU-MNPs were prepared freshly at twice their final concentration and added to the plate on the following day. The assay was terminated after further 7-day incubation. The effect of treatment was examined by comparing the growth of cells in the treated rows to

the growth of cells in the control rows and expressed as percentage. All assays were performed at least in triplicate.

## 3. Results and Discussion

### 3.1. Physicochemical Characterization of MNPs

**3.1.1. Transmission Electron Microscope and X-Ray Diffraction.** Typical TEM micrographs for AMNPs and IDAU-MNPs were shown in Figures 2(a) and 2(b), respectively, which indicated that the diameter of these particles was approximately 35 nm. The shape of MNPs was spherical and its particles were well-distributed. After the IDAU was connected to AMNPs, no significant difference in sizes of AMNPs and IDAU-MNPs were observed, but the IDAU-MNPs had more uniform size distribution. Because of these features of MNPs described above, MNPs had good stability, better dispersibility, huge surface area, and greater loadspace. It was also observed in our study that the dispersity and stability of MNP-loaded IDAU increased compared to AMNPs, indicating that the hydrophilic groups on the MNP surface increased and the biocompatibility of MNPs enhanced when IDAU was loaded onto the nanoparticles.

Crystallinity and crystal size are important properties to be considered for the present study as they affect the magnetic susceptibility. X-ray diffraction is a useful technique for characterizing the crystalline samples. XRD patterns (Figure 3(a)) of MNPs, AMNPs, and IDAU-MNPs were used for determining the crystallographic identity and phase purity and for calculating the average crystallite diameter based on the full width at half maximum (FWHM) in the XRD profile. There were 6 peaks at 30.14, 35.47, 43.14, 53.45, 57.08, and 62.63 ( $2\theta$ ) in the XRD profile, which was characteristic of  $\text{Fe}_3\text{O}_4$ . It was confirmed by ICDD database (reference code 01076-0955) and showed 100% purity. The average crystallite size of MNPs was calculated by the X-ray line broadening method by the use of Debye–Scherrer's equation taking FWHM of peak at 35.47 ( $2\theta$ ) as this peak showed least interferences, giving the average particle size of about 30.02, 35.46, and 35.61 nm for MNPs, AMNPs,

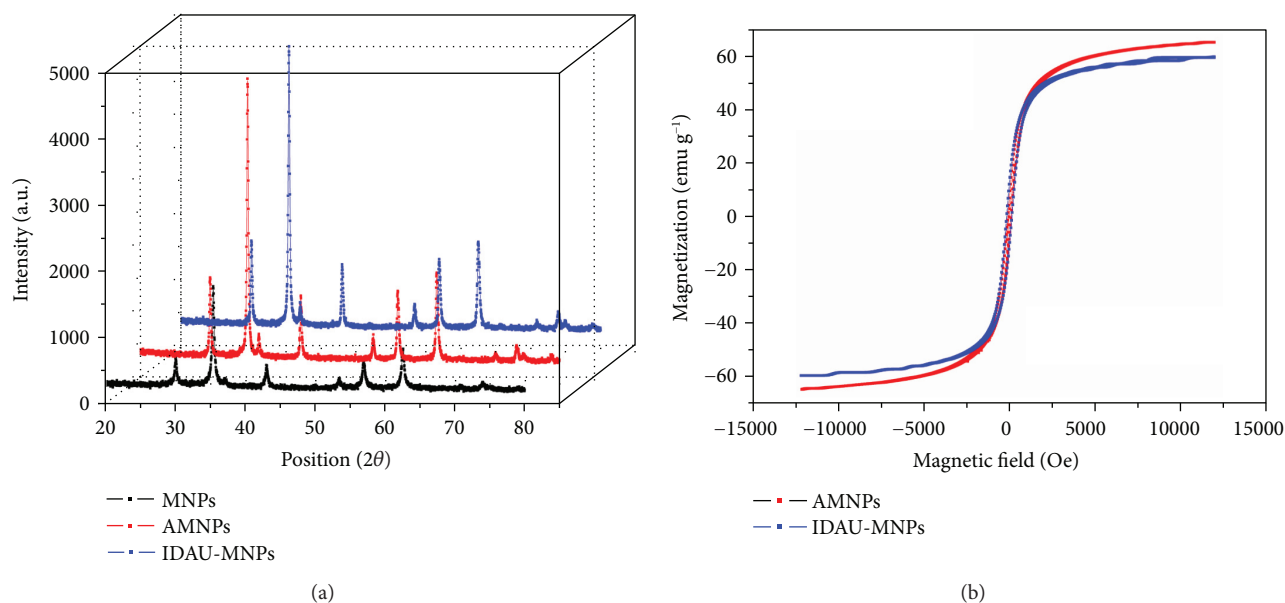


FIGURE 3: XRD diffractogram of MNPs (black), AMNPs (red), and IDAU-MNPs (blue) (a) and the magnetic hysteresis loops for AMNPs (red) and IDAU-MNPs (blue) (b).

and IDAU-MNPs, respectively. These sizes are in agreement with the sizes measured by TEM.

It is very important that the prepared MNPs possess sufficient magnetic and superparamagnetism property for practical application. Figure 3(b) displayed the VSM magnetization curves of AMNPs and IDAU-MNPs at room temperature; the results indicated the saturation magnetization of AMNPs and IDAU-MNPs were  $64.92$  and  $59.63 \text{ emu g}^{-1}$ , respectively. All of the magnetic nanoparticles showed quasi-superparamagnetic behavior and had little remanence and coercivity. Drug loading into MNPs in significant amounts resulted in the slight decrease in magnetic strength of the composite because of the weight contribution from the nonmagnetic portion. The saturation magnetization of IDAU-MNPs was sufficient for the magnetically driven transport of drugs with a conventional magnet.

**3.1.2. Fourier-Transform Infrared Spectroscopy (FTIR).** FTIR spectroscopy is an appropriate technique to confirm drug insertion into the nanoparticles. In the FTIR spectrum of AMNPs (Figure 4(a)), three strong bands were observed at  $568.0$ ,  $1637.1$ , and  $1655.4 \text{ cm}^{-1}$ . The first was due to the Fe-O stretching mode of the  $\text{Fe}_3\text{O}_4$  MNPs, and the second and third were associated with the  $\alpha$ -helical and  $\beta$ -folded types of secondary structure of avidin, respectively [34, 35]. The presence of two bands at  $1637.1$  and  $1655.4 \text{ cm}^{-1}$  confirmed that avidin was immobilized successfully on  $\text{Fe}_3\text{O}_4$  MNPs.

In the FTIR spectrum of IDAU (Figure 4(b)), the characteristic C=O (hydrogen-bonded quinone carbonyl group), C=C, and C-OH stretching modes of IDAU were observed at  $1618.0$ ,  $1578.1$ , and  $1115.9 \text{ cm}^{-1}$ , respectively [36], and there was a large difference in intensity between the two strong bands at  $1618.0$  and  $1578.1 \text{ cm}^{-1}$ . However, in the FTIR spectrum of DAU, two strong bands of similar intensity were found at  $1617.0$  and  $1580.0 \text{ cm}^{-1}$  [37]. The

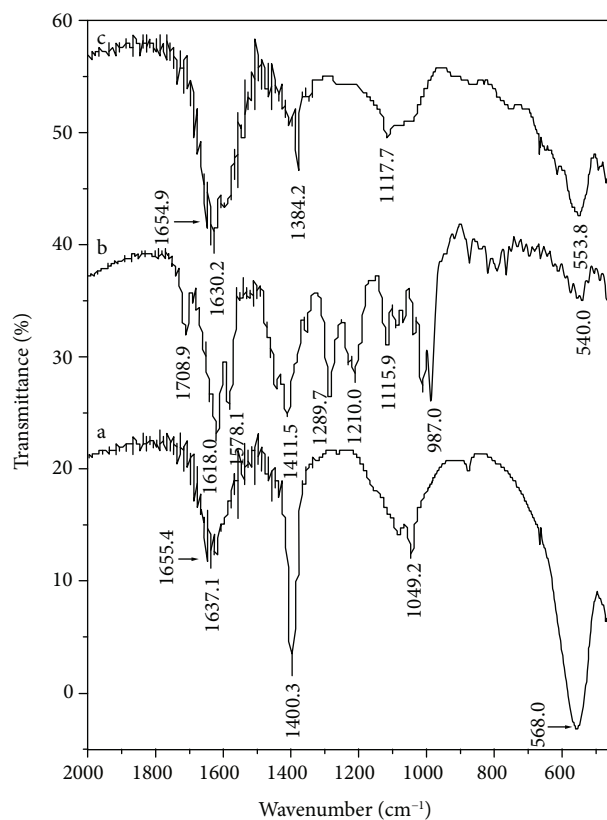


FIGURE 4: FTIR spectra of avidin-immobilized magnetic nanoparticles (a), daunomycin (b), and iminobiotinylated daunomycin-loaded magnetic nanoparticles (c).

intensity changes in the infrared spectra showed that the molecular structure of DAU was changed after it was 2-iminobiotinylated. Furthermore, the characteristic C-O and

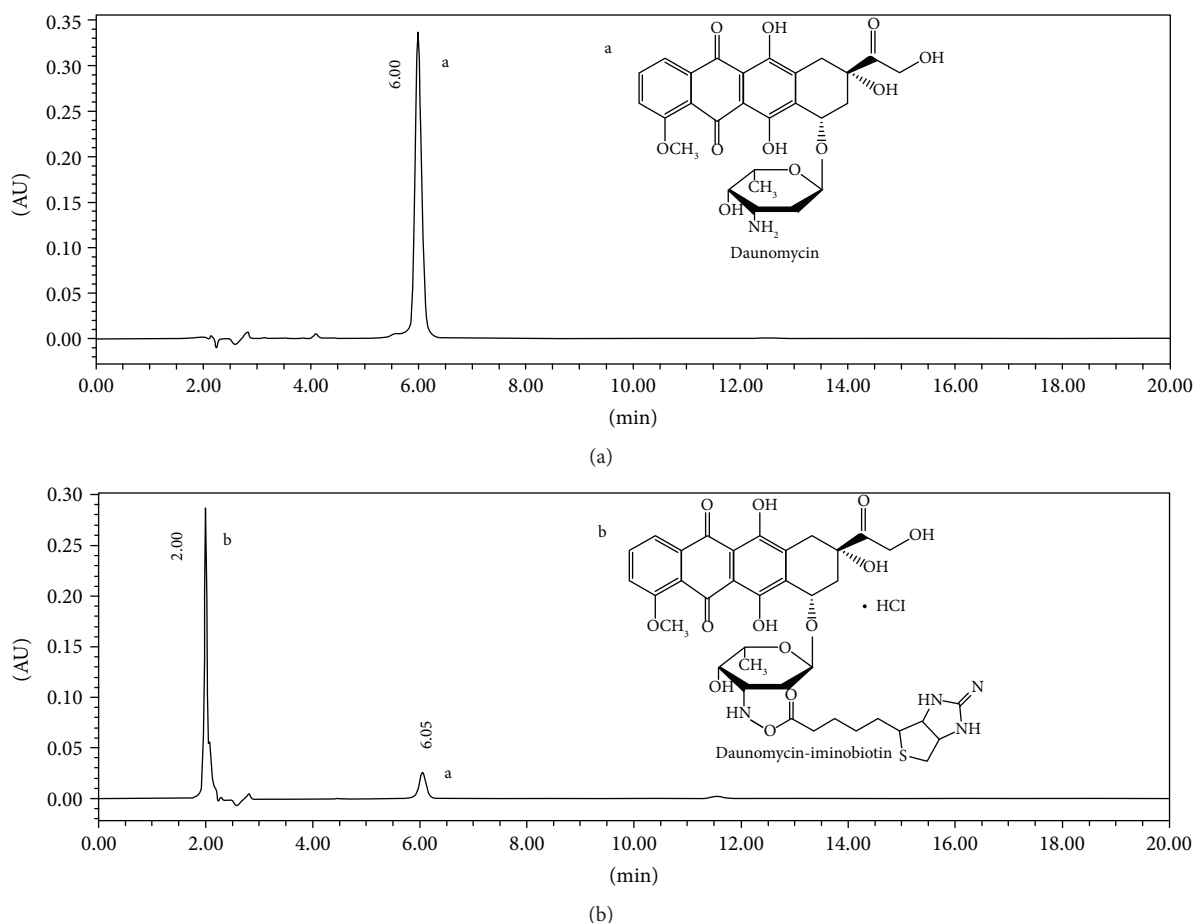


FIGURE 5: HPLC analysis of the mixtures containing only daunomycin (a), iminobiotinylated daunomycin, and daunomycin (b).

N-H stretching modes of IDAU were also observed at  $1210.0$  and  $1289.7\text{ cm}^{-1}$ , respectively [38], but they were not found in DAU, which indicated IDAU was successfully prepared by reaction between DAU and NHS-iminobiotin.

In the FTIR spectrum of IDAU-MNPs (Figure 4(c)), the characteristic absorption of Fe-O bond of drug-loaded MNPs was discovered at  $553.8\text{ cm}^{-1}$ , which shifted from  $568.0$  to  $553.8\text{ cm}^{-1}$  (Figure 4(a)). The characteristic C-OH stretching mode of drug-loaded MNPs was observed at  $1117.7\text{ cm}^{-1}$ . There was strong evidence for the presence of drug molecules in MNPs. However, the characteristic bands (such as at  $1618.0$  and  $1578.1\text{ cm}^{-1}$ ) of IDAU could not be found after it was connected to MNPs, with the exception of the band assigned to C-OH, which shifted from  $1115.9$  to  $1117.7\text{ cm}^{-1}$  (Figure 4(b)). The absence of the two characteristic bands confirmed a strong interaction between IDAU and AMNPs.

### 3.2. Drug Loading Determination

**3.2.1. Determination of DAU and IDAU.** RP-HPLC adopted to determine DAU has the advantages of high sensitivity and good reproducibility. The chromatogram of RP-HPLC determining DAU was shown in Figure 5(a). According to the result, the retention time of DAU was at 6.00 min, and the intralaboratory reproducibility was very

good, with 90% of the replicates analyzed in the same laboratory differing by  $\leq 2.8\%$ . The regression equation for determining DAU was established through several experiments ( $y = 31139161.20x - 54373.54$ , where  $y$  was the peak area and  $x$  was the concentration of DAU,  $R^2 = 0.9995$ ). IDAU was generated by reaction of DAU with NHS-iminobiotin in alkaline condition. The best rate of DAU acylation determined by the above formula was  $78.90 \pm 2.13\%$ . After the reaction between excessive DAU and NHS-iminobiotin, RP-HPLC was used to analyze IDAU. The chromatogram of the DAU and IDAU mixture was shown in Figure 5(b). The results showed that the separation effect of liquid chromatography about these two substances was very good, and the retention time of DAU exceeded was at 6.05 min, while the retention time of IDAU was at 2.00 min. Here, we created a standard curve and used linear regression analysis (called a trendline in excel) to determine the concentration of IDAU ( $y = 31139161.20x - 54373.54$ , where  $y$  was the peak area and  $x$  was the concentration of IDAU,  $R^2 = 0.9991$ ).

**3.2.2. Adsorption Dynamics of IDAU on AMNPs.** The drug loading efficiency of MNPs and their loading capacity are two important indicators for the drug delivery system. For this reason, the IDAU loading efficiency of MNPs and their

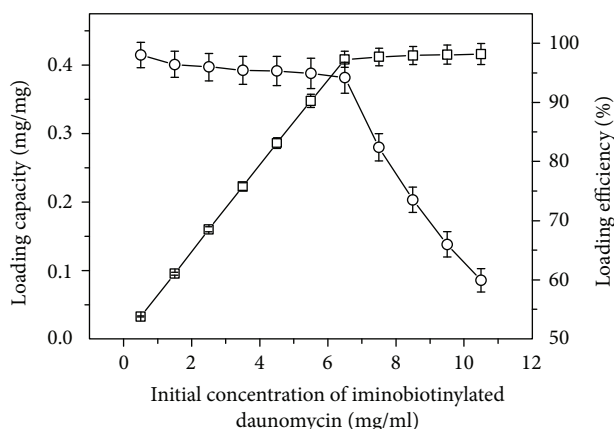


FIGURE 6: Dependence of the loading capacity (□) and loading efficiency (○) on initial concentration of iminobiotinylated daunomycin used during the preparation. Each result is the average calculated in 95% confidence interval of five parallel studies.

loading capacity were studied using indirect RP-HPLC analysis. The results were presented in Figure 6. When the initial concentration of IDAU was less than 7 mg/mL, the loading efficiency of more than 90% was observed. However, upon increasing the initial drug concentration, the loading efficiency decreased rapidly, but the drug adsorption capacity was unchanged. This strongly suggested that the drug adsorption behaviors were mainly dependent on affinity interaction between IDAU and AMNPs, and the nonspecific adsorption of the drug was extremely low. The same phenomenon could also be observed in the other molecular adsorption processes using the avidin-biotin binding system [39–41]. The increase of the initial concentration of IDAU needs more iminobiotin binding sites of AMNPs. When the iminobiotin binding sites of AMNPs were not sufficiently high (saturation) with increasing IDAU concentration, the amount of specific adsorption capability for IDAU was unchanged. Therefore, the optimum initial concentration of IDAU was 7 mg/mL, and the loading capacity and loading efficiency of MNPs were  $0.408 \pm 0.012$  mg/g and  $94.18 \pm 2.64\%$ , respectively. Compared with the drug loaded into MNPs through physical encapsulation or adsorption, the drug connected to AMNPs based on the avidin-iminobiotin system would not be easily released during transportation of the drug due to the effects of environmental parameters such as temperature, pH, ionic strength, and sodium nitrate. The drugs could be delivered to the targeted site at the appropriate time successfully. The controllable drug delivery system could maximize its bioefficacy, reduce the side effects, and facilitate clinical applicability [42].

### 3.3. Performance Evaluation of Drug-Nanoparticle Formulations

**3.3.1. In Vitro Drug Release.** The in vitro drug release from IDAU-MNPs was monitored as a function of time in PBS buffer at pH 6.8 or in ammonium acetate buffer at pH 4.0 as shown in Figures 7(a) and 7(b), respectively. For method 1, IDAU could be completely released from MNPs for 30 min

at pH 4.0, but the drug did not readily dissociate at pH 6.8. The reason was that the drug release behavior from nanoparticles was mainly dependent on the interaction between IDAU and AMNPs at different pH values [43–45]. Practical applications of method 1 in the clinical laboratory were limited because of the rapid and transient release of the drug and its strict dissociation conditions. For method 2, IDAU was released by adding a certain concentration of biotin at pH 6.8, because under that specific condition, the strength of affinity interaction between biotin and AMNPs was more than that of iminobiotin and AMNPs, and IDAU was replaced by biotin. Fortunately, the conditions were relatively mild. The amount of IDAU released to the outer medium was measured using RP-HPLC, and the drug release data were presented in Figure 7(c). A low concentration of biotin (1 mmol/L) was used in our research. The results showed that the initial stage was characterized by a fast release of a limited quantity of IDAU, and the second stage was described by a slow, steady, and controlled release of the drug. The maximum concentration of IDAU released to the outer medium was strongly correlated with the concentration of IDAU loading on MNPs, but the maximum concentration of IDAU loading on MNPs did not release the maximum concentration of IDAU at the same concentration of biotin. The release profiles exhibited strong dependence on the concentration of IDAU connected to MNPs. When the concentration was 0.015 mg/mL, 38.9% of the loaded drug could be released within 150 min, and the concentration of the drug released was  $5.84 \mu\text{g/mL}$ . When the concentration of IDAU connected to MNPs was 0.055 mg/mL, only 10.5% of the loaded drug could be released within the same time, and the concentration of the drug released was  $5.78 \mu\text{g/mL}$ . However, when the concentration of the drug connected to MNPs was 0.035 mg/mL, the concentration of the drug released could reach  $6.49 \mu\text{g/mL}$ . According to these results, it could be concluded that the optimum concentration of IDAU connected to MNPs was 0.035 mg/mL. The different concentrations of the drug released might be attributed to the interaction between biotin and drug-loaded MNPs, and the interaction was a complex, dynamic process. The first process was the dissociation of IDAU from AMNPs at pH 6.8. At the same time, a high concentration of biotin and strong affinity interaction between biotin and avidin at pH 6.8 promoted the interaction between biotin and AMNPs, and the loaded IDAU would be rapidly released. When the dissociation reactions between IDAU and AMNPs reached equilibrium, a slow, steady, and controlled release of the drug would be obtained. However, the majority of drugs would overcome some resistance to diffuse across avidin and PEI to the surface of MNPs and finally into aqueous medium. A high concentration of IDAU connected to MNPs might need more proteins and polymers and create conversely more resistance to hold back the effective drug release. Therefore, a low concentration of released IDAU present in the aqueous medium would be obtained.

**3.3.2. Toxicity in Cell Culture.** The potential of AMNPs to be used as a carrier for IDAU was evaluated in vitro by comparing the cytotoxicity of four formulations: free

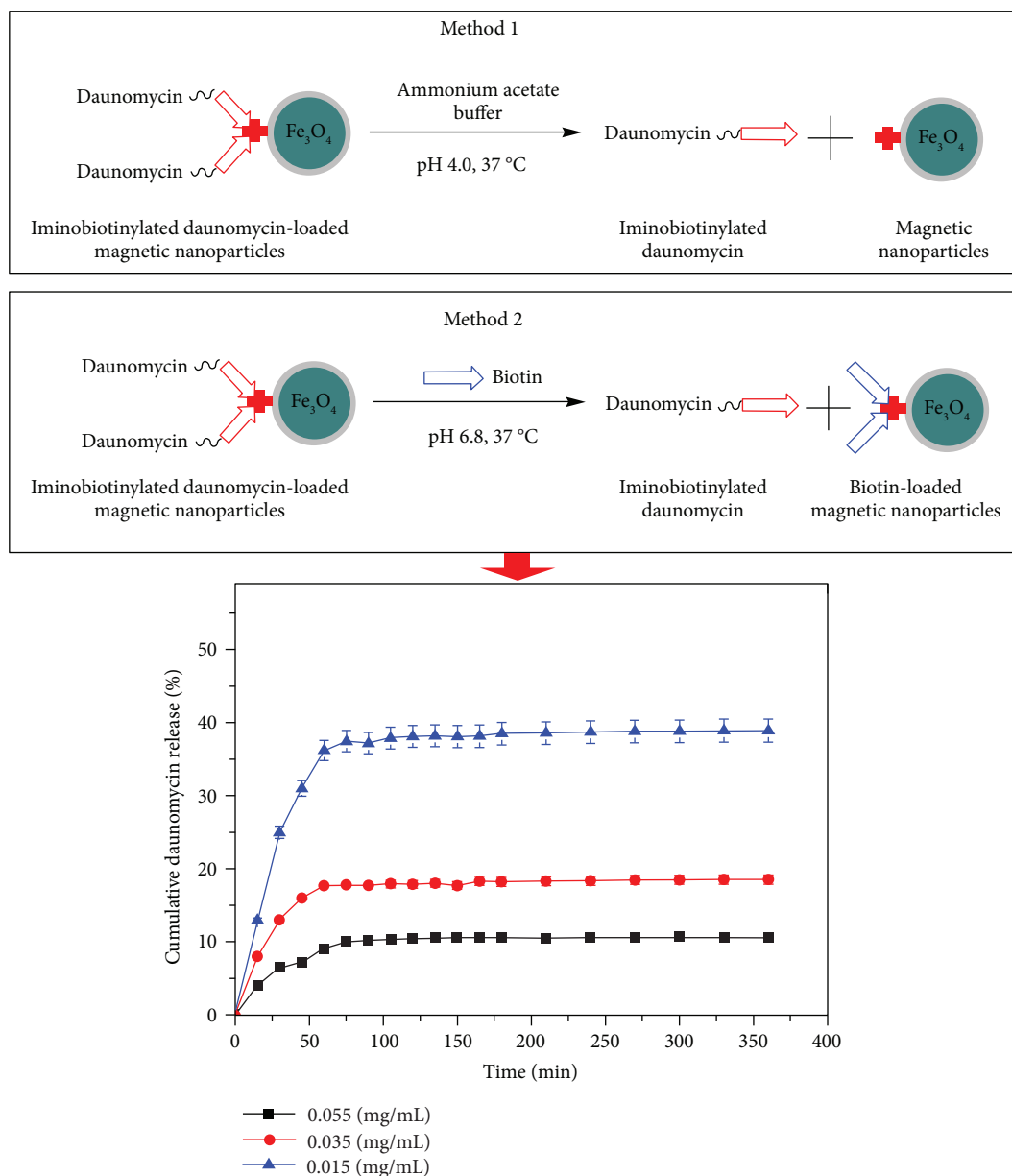


FIGURE 7: Two methods for releasing of iminobiotinylated daunomycin from nanoparticles and drug release behavior as a function of loaded iminobiotinylated daunomycin concentration (0.015 mg/mL (blue triangle), 0.035 mg/mL (red circle), and 0.055 mg/mL (black square)). Each result is the average calculated in 95% confidence interval of five parallel studies.

DAU (Sample 1), 0.04 mg/mL; IDAU (sample 2), 0.06 mg/mL; IDAU-MNPs (the concentration of IDAU on the surface was 0.06 mg/mL, sample 3); and unloaded MNPs (AMNPs, sample 4), 0.15 mg/mL. The in vitro models chosen for investigating the potential of these materials were the DLKP cell line, and 50% inhibitory concentrations (IC<sub>50</sub>) of the four samples were determined. As depicted in Figure 8, the results indicated that the IC<sub>50</sub> of IDAU was  $(1.60 \pm 0.05) \times 10^{-3}$  mg/mL, and it retained significant activity against DLKP cells ( $P < 0.05$ ), although its antitumor activity was lower than that of free DAU. The IC<sub>50</sub> of IDAU-MNPs was  $0.02 \pm 0.007$  mg/mL and was much lower than that of free DAU or IDAU, but the presence of low activity against DLKP cells confirmed that a small

quantity of IDAU on the surface of MNPs stretched in aqueous medium and interacted with tumor cells. Another reason that IDAU-MNPs had anticancer activity in vitro was a pumping mechanism that enabled diffusion of the drug out of avidin on the surface of nanoparticles [46–48].

The above experimental data clearly demonstrated that IDAU could not only be adsorbed, transported, and released controllably on the surface of MNPs but also exhibited high inhibitory activity against DLKP cells. However, since the delivery of the drug from MNPs carriers in vivo was a complex process, the effectiveness of the present method needs to be further verified. Furthermore, the in vivo tumor inhibition experiments in the external magnetic field are in progress in our research group, and IDAU-MNPs are supposed

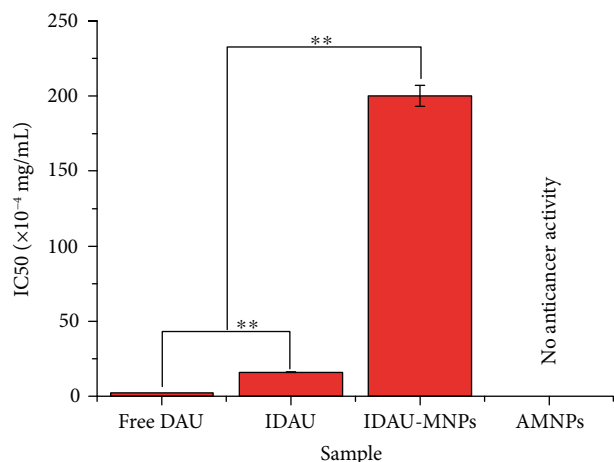


FIGURE 8: Fifty percent inhibitory concentrations (IC<sub>50</sub>) of free DAU (sample 1), IDAU (sample 2), IDAU-MNPs (sample 3), and unloaded MNPs (AMNPs, sample 4). Each result is the average calculated in 95% confidence interval of five parallel studies \*\* $P < 0.01$ .

to achieve the magnetic drug targeting and improve the therapeutic efficacy.

#### 4. Conclusion

We described here a novel experimental approach to the design and preparation of IDAU-MNPs through the affinity interaction between IDAU and AMNPs. DAU was first 2-iminobiotinylated, which was then attached to AMNPs using the avidin-iminobiotin system. The results obtained using RP-HPLC studies indicated that the optimal acylation rate of IDAU was  $78.90 \pm 2.13\%$ . The results obtained using FTIR studies strongly suggested that IDAU could be firmly affixed to AMNPs using the avidin-iminobiotin system. The study also found that the loading capacity and efficiency of nanoparticles were mainly dependent on affinity interaction between IDAU and AMNPs, which was impacted obviously by the initial concentration of IDAU. Under the conditions of pH 6.8 and 1 mmol/L of biotin, the drug release was characterized by an initial rapid drug release followed by a slow, steady and controlled release of the drug. The effect of IDAU on DLKP proliferation was tested, the results showed that IC<sub>50</sub> was  $(1.60 \pm 0.05) \times 10^{-3}$  mg/mL. It could come to a conclusion that the drug had good inhibitory effect on tumor cell growth.

#### Data Availability

The data used to support the findings of this study are available from the corresponding author upon request.

#### Conflicts of Interest

The authors declare that there are no conflicts of interest regarding the publication of the paper.

#### Acknowledgments

The work was supported by the Key Technology R&D Program of Hunan Province of China (Grant no. 2016NK2146), key scientific research projects of Tibet Autonomous Region of China (Project code no. ZD20170014), and National Natural Science Foundation of China (Grant nos. 31360367 and 31571911).

#### References

- [1] N. P. E. Barry and P. J. Sadler, "Exploration of the medical periodic table: towards new targets," *Chemical Communications*, vol. 49, no. 45, pp. 5106–5131, 2013.
- [2] E. M. Greer, C. V. Cosgriff, and O. Lavinda, "Towards the development of new anticancer drugs: the Bergman cyclization of an 11-membered ring-constrained enediynes," in *Abstracts of Papers of the American Chemical Society*, vol. 244, American Chemical Society, 1155 16th St, NW, Washington, DC 20036 USA, 2012.
- [3] X. Jiang, Y. Sun, J. Yao et al., "Core scaffold-inspired concise synthesis of chiral spirooxindole-pyranopyrimidines with broad-spectrum anticancer potency," *Advanced Synthesis & Catalysis*, vol. 354, no. 5, pp. 917–925, 2012.
- [4] C. Dufes, M. Al Robaian, and S. Somani, "Transferrin and the transferrin receptor for the targeted delivery of therapeutic agents to the brain and cancer cells," *Therapeutic Delivery*, vol. 4, no. 5, pp. 629–640, 2013.
- [5] W. Li, Y. Cai, Q. Zhong, Y. Yang, S. C. Kundu, and J. Yao, "Silk sericin microcapsules with hydroxyapatite shells: protection and modification of organic microcapsules by biomimetic mineralization," *Journal of Materials Chemistry B*, vol. 4, no. 2, pp. 340–347, 2016.
- [6] F. Dilnawaz and S. K. Sahoo, "Enhanced accumulation of curcumin and temozolomide loaded magnetic nanoparticles executes profound cytotoxic effect in glioblastoma spheroid model," *European Journal of Pharmaceutics and Biopharmaceutics*, vol. 85, no. 3, pp. 452–462, 2013.
- [7] F. Dilnawaz, A. Singh, S. Mewar, U. Sharma, N. R. Jagannathan, and S. K. Sahoo, "The transport of non-surfactant based paclitaxel loaded magnetic nanoparticles across the blood brain barrier in a rat model," *Biomaterials*, vol. 33, no. 10, pp. 2936–2951, 2012.
- [8] Q. Zhang, J. Tong, H. Chen et al., "A novel magnetic nanoparticle hyperthermia combined with ACMF-dependant drug release by DAMMs injection in VX-2 liver tumors," *Journal of Nanoscience and Nanotechnology*, vol. 12, no. 1, pp. 127–131, 2012.
- [9] K. K. Jain, "Current status and future prospects of drug delivery systems," *Methods in Molecular Biology*, vol. 1141, pp. 1–56, 2014.
- [10] D. Shetty, J. K. Khedkar, K. M. Park, and K. Kim, "Can we beat the biotin-avidin pair?: cucurbit[7]uril-based ultrahigh affinity host-guest complexes and their applications," *Chemical Society Reviews*, vol. 44, no. 23, pp. 8747–8761, 2015.
- [11] D. Torrecilla, M. V. Lozano, E. Lallana et al., "Anti-tumor efficacy of chitosan-g-poly(ethylene glycol) nanocapsules containing docetaxel: anti-TMEFF-2 functionalized nanocapsules vs. non-functionalized nanocapsules," *European Journal of Pharmaceutics and Biopharmaceutics*, vol. 83, no. 3, pp. 330–337, 2013.

- [12] Z. Fan, M. Shelton, A. K. Singh, D. Senapati, S. A. Khan, and P. C. Ray, "Multifunctional plasmonic shell-magnetic core nanoparticles for targeted diagnostics, isolation, and photothermal destruction of tumor cells," *ACS Nano*, vol. 6, no. 2, pp. 1065–1073, 2012.
- [13] J. Gautier, E. Munnier, A. Paillard et al., "A pharmaceutical study of doxorubicin-loaded PEGylated nanoparticles for magnetic drug targeting," *International Journal of Pharmaceutics*, vol. 423, no. 1, pp. 16–25, 2012.
- [14] M. G. Krukemeyer, V. Krenn, M. Jakobs, and W. Wagner, "Magnetic drug targeting in a rhabdomyosarcoma rat model using magnetite-dextran composite nanoparticle-bound mitoxantrone and 0.6 tesla extracorporeal magnets – sarcoma treatment in progress," *Journal of Drug Targeting*, vol. 20, no. 2, pp. 185–193, 2012.
- [15] S. K. Sahu, S. Maiti, A. Pramanik, S. K. Ghosh, and P. Pramanik, "Controlling the thickness of polymeric shell on magnetic nanoparticles loaded with doxorubicin for targeted delivery and MRI contrast agent," *Carbohydrate Polymers*, vol. 87, no. 4, pp. 2593–2604, 2012.
- [16] R. Bayford, T. Rademacher, I. Roitt, and S. X. Wang, "Emerging applications of nanotechnology for diagnosis and therapy of disease: a review," *Physiological Measurement*, vol. 38, no. 8, pp. R183–R203, 2017.
- [17] M. David-Pur, L. Bareket-Keren, G. Beit-Yaakov, D. Raz-Prag, and Y. Hanein, "All-carbon-nanotube flexible multi-electrode array for neuronal recording and stimulation," *Biomedical Microdevices*, vol. 16, no. 1, pp. 43–53, 2014.
- [18] X. L. Liu, E. S. G. Choo, A. S. Ahmed et al., "Magnetic nanoparticle-loaded polymer nanospheres as magnetic hyperthermia agents," *Journal of Materials Chemistry B*, vol. 2, no. 1, pp. 120–128, 2014.
- [19] Q. Pankhurst, S. Jones, and J. Dobson, "Applications of magnetic nanoparticles in biomedicine: the story so far," *Journal of Physics D: Applied Physics*, vol. 49, no. 50, article 501002, 2016.
- [20] S. Sharma, K. Sethi, and I. Roy, "Magnetic nanoscale metal-organic frameworks for magnetically aided drug delivery and photodynamic therapy," *New Journal of Chemistry*, vol. 41, no. 20, pp. 11860–11866, 2017.
- [21] E. Tombácz, R. Turcu, V. Socoliuc, and L. Vékás, "Magnetic iron oxide nanoparticles: recent trends in design and synthesis of magnetoresponsive nanosystems," *Biochemical and Biophysical Research Communications*, vol. 468, no. 3, pp. 442–453, 2015.
- [22] P. Sharma, A. Sharma, M. Sharma et al., "Nanomaterial fungicides: in vitro and in vivo antimycotic activity of cobalt and nickel nanoferrites on phytopathogenic fungi," *Global Challenges*, vol. 1, no. 9, article 1700041, 2017.
- [23] S. F. Bakshi, N. Guz, A. Zakharchenko et al., "Nanoreactors based on DNzyme-functionalized magnetic nanoparticles activated by magnetic field," *Nanoscale*, vol. 10, no. 3, pp. 1356–1365, 2018.
- [24] R. Orendorff, A. J. Peck, B. Zheng et al., "First in vivo traumatic brain injury imaging via magnetic particle imaging," *Physics in Medicine & Biology*, vol. 62, no. 9, pp. 3501–3509, 2017.
- [25] M. Stimac, T. Dolinsek, U. Lamprecht, M. Cemazar, and G. Sersa, "Gene electrotransfer of plasmid with tissue specific promoter encoding shRNA against endoglin exerts antitumor efficacy against murine TS/A tumors by vascular targeted effects," *PLoS One*, vol. 10, no. 4, article e0124913, 2015.
- [26] E. E. Weinberger, A. Isakovic, S. Scheibelhofer et al., "The influence of antigen targeting to sub-cellular compartments on the anti-allergic potential of a DNA vaccine," *Vaccine*, vol. 31, no. 51, pp. 6113–6121, 2013.
- [27] N. Depalo, R. M. Iacobazzi, G. Valente et al., "Sorafenib delivery nanoplatform based on superparamagnetic iron oxide nanoparticles magnetically targets hepatocellular carcinoma," *Nano Research*, vol. 10, no. 7, pp. 2431–2448, 2017.
- [28] F. Dilnawaz, S. Acharya, and S. K. Sahoo, "Recent trends of nanomedicinal approaches in clinics," *International Journal of Pharmaceutics*, vol. 538, no. 1-2, pp. 263–278, 2018.
- [29] J. R. Heath, "Nanotechnologies for biomedical science and translational medicine," *Proceedings of the National Academy of Sciences of the United States of America*, vol. 112, no. 47, pp. 14436–14443, 2015.
- [30] S. Sun, M. Ma, N. Qiu et al., "Affinity adsorption and separation behaviors of avidin on biofunctional magnetic nanoparticles binding to iminobiotin," *Colloids and Surfaces B: Biointerfaces*, vol. 88, no. 1, pp. 246–253, 2011.
- [31] Y. Dai, J. DeSano, W. Tang et al., "Natural proteasome inhibitor celastrol suppresses androgen-independent prostate cancer progression by modulating apoptotic proteins and NF-kappaB," *PLoS One*, vol. 5, no. 12, article e14153, 2010.
- [32] Y. Meng, W. Tang, Y. Dai et al., "Natural BH3 mimetic (-)-gossypol chemosensitizes human prostate cancer via Bcl-xL inhibition accompanied by increase of Puma and Noxa," *Molecular Cancer Therapeutics*, vol. 7, no. 7, pp. 2192–2202, 2008.
- [33] X. Wu, M. Li, Y. Qu et al., "Design and synthesis of novel gefitinib analogues with improved anti-tumor activity," *Bioorganic & Medicinal Chemistry*, vol. 18, no. 11, pp. 3812–3822, 2010.
- [34] G. D. Nardo, M. Breitner, S. J. Sadeghi, S. Castrignanò, and G. Gilardi, "FTIR spectroscopy applied to study dynamics and flexibility of human aromatase: SW02.S8–39," *The FEBS Journal*, vol. 280, p. 163, 2013.
- [35] S. A. Tatulian, "Structural characterization of membrane proteins and peptides by FTIR and ATR-FTIR spectroscopy," *Methods in Molecular Biology*, vol. 974, pp. 177–218, 2013.
- [36] P. Ghosh, G. P. Devi, R. Priya et al., "Spectroscopic and in silico evaluation of interaction of DNA with six anthraquinone derivatives," *Applied Biochemistry and Biotechnology*, vol. 170, no. 5, pp. 1127–1137, 2013.
- [37] V. Staneva, G. Ivanova, and M. Simeonova, "Surface modified poly (butyl cyanoacrylate) nanoparticles loaded with indomethacin: preparation and physicochemical characterization," *Bulgarian Chemical Communications*, vol. 47, pp. 93–99, 2015.
- [38] O. V. Zemtsova and K. N. Zheleznov, "Synthesis and specific features of mesomorphic behavior of new polysubstituted triphenylenes," *Russian Chemical Bulletin*, vol. 53, no. 8, pp. 1743–1748, 2004.
- [39] L. Bai, Y. Chai, R. Yuan, Y. Yuan, S. Xie, and L. Jiang, "Amperometric aptasensor for thrombin detection using enzyme-mediated direct electrochemistry and DNA-based signal amplification strategy," *Biosensors and Bioelectronics*, vol. 50, pp. 325–330, 2013.
- [40] C. Liu, S. Wang, C. Fu, H. Li, S. Xu, and W. Xu, "Preparation of surface-enhanced Raman scattering(SERS)-active optical fiber sensor by laser-induced ag deposition and its application in

- bioidentification of biotin/avidin,” *Chemical Research in Chinese Universities*, vol. 31, no. 1, pp. 25–30, 2015.
- [41] Y. Liu, L. Feng, T. Liu et al., “Multifunctional pH-sensitive polymeric nanoparticles for theranostics evaluated experimentally in cancer,” *Nanoscale*, vol. 6, no. 6, pp. 3231–3242, 2014.
- [42] J. Zhang, J. Li, Y. Ju, Y. Fu, T. Gong, and Z. Zhang, “Mechanism of enhanced oral absorption of morin by phospholipid complex based self-nanoemulsifying drug delivery system,” *Molecular Pharmaceutics*, vol. 12, no. 2, pp. 504–513, 2015.
- [43] H. R. Jia, H. Y. Wang, Z. W. Yu, Z. Chen, and F. G. Wu, “Long-time plasma membrane imaging based on a two-step synergistic cell surface modification strategy,” *Bioconjugate Chemistry*, vol. 27, no. 3, pp. 782–789, 2016.
- [44] S. L. Kuan, D. Y. W. Ng, Y. Wu et al., “pH responsive Janus-like supramolecular fusion proteins for functional protein delivery,” *Journal of the American Chemical Society*, vol. 135, no. 46, pp. 17254–17257, 2013.
- [45] H. Y. Wang, X. W. Hua, H. R. Jia et al., “Enhanced cell membrane enrichment and subsequent cellular internalization of quantum dots via cell surface engineering: illuminating plasma membranes with quantum dots,” *Journal of Materials Chemistry B*, vol. 4, no. 5, pp. 834–843, 2016.
- [46] K. S. Bielawski and N. J. Sniadecki, “A magnetic post approach for measuring the viscoelasticity of biomaterials,” *Journal of Microelectromechanical Systems*, vol. 25, no. 1, pp. 153–159, 2016.
- [47] M. C. Chen, H. A. Chan, M. H. Ling, and L. C. Su, “Implantable polymeric microneedles with phototriggerable properties as a patient-controlled transdermal analgesia system,” *Journal of Materials Chemistry B*, vol. 5, no. 3, pp. 496–503, 2017.
- [48] C. G. Madsen, A. Skov, S. Baldursdottir, T. Rades, L. Jorgensen, and N. J. Medlicott, “Simple measurements for prediction of drug release from polymer matrices-solubility parameters and intrinsic viscosity,” *European Journal of Pharmaceutics and Biopharmaceutics*, vol. 92, pp. 1–7, 2015.

## Research Article

# Structural, Morphological, Optical, and Room Temperature Magnetic Characterization on Pure and Sm-Doped ZnO Nanoparticles

Khalil Badreddine <sup>1</sup>, I. Kazah <sup>1</sup>, M. Rekaby <sup>2</sup> and R. Awad<sup>1</sup>

<sup>1</sup>Physics Department, Faculty of Science, Beirut Arab University, Beirut, Lebanon

<sup>2</sup>Physics Department, Faculty of Science, Alexandria University, Alexandria, Egypt

Correspondence should be addressed to Khalil Badreddine; [khalil1978july@hotmail.com](mailto:khalil1978july@hotmail.com)

Received 22 March 2018; Accepted 29 May 2018; Published 3 July 2018

Academic Editor: Murtaza Bohra

Copyright © 2018 Khalil Badreddine et al. This is an open access article distributed under the Creative Commons Attribution License, which permits unrestricted use, distribution, and reproduction in any medium, provided the original work is properly cited.

Nano crystalline  $Zn_{1-x}Sm_xO$ , ( $0.00 \leq x \leq 0.10$ ), were prepared by wet chemical coprecipitation method. The effect of samarium doping on the structural, morphological, optical, and magnetic properties of ZnO nanoparticles was examined by X-ray powder diffraction (XRD), Transmission electron microscopy (TEM), Fourier-transform infrared spectroscopy (FTIR), Ultraviolet-visible spectroscopy (UV) and M-H magnetic hysteresis. XRD analysis showed the hexagonal wurtzite structure of ZnO. The absence of  $Sm_2O_3$  as separate phase may be attributed to the complete dissolving of samarium in ZnO lattice. The lattice parameters ( $a$  and  $c$ ) of  $Zn_{1-x}Sm_xO$  were calculated and they fluctuated with the increase of Sm doping which indicated that the structure of ZnO was perturbed by the doping of Sm. The crystallite size was computed for all the samples using Debye-Scherrer's method. The crystallite size decreased with the increase of Sm doping. TEM micrographs revealed that the size and the shape of the ZnO nanocomposites were changed by modifying the doping level of samarium. FTIR analysis spectrum confirmed the formation of ZnO phase and revealed a peak shift between pure and Sm-doped ZnO. The band gap energy and Urbach energy were calculated for  $Zn_{1-x}Sm_xO$ , ( $0.00 \leq x \leq 0.10$ ). The band energy gaps of pure and Sm doped ZnO samples are in the range 2.6–2.98 eV. M-H hysteresis inspection, at room temperature, showed that the pure ZnO exhibited a ferromagnetic behavior incorporated with diamagnetic and paramagnetic contributions. Ferromagnetic behavior was reduced for the doped samples with  $x = 0.01$  and  $x = 0.04$ . The samples with  $x = 0.02$  and  $0.06 \leq x \leq 0.10$  tend to be superparamagnetic. The saturation magnetization ( $M_s$ ), the coercivity ( $H_c$ ), and the retentivity ( $M_r$ ) were recorded for  $Zn_{1-x}Sm_xO$ , ( $0.00 \leq x \leq 0.10$ ).

## 1. Introduction

The unusual physical properties and broad range of applications of semiconductor nanoparticles or quantum dots (QDs) [1, 2], basically II-VI materials, have attracted great attention recently. The phenomenon called “quantum confinement” occurs when the size of the nanocrystals becomes smaller than the corresponding Bohr radius of the exciton. Consequently, the band gap increases and discrete energy levels exist at the edges of the valence and conduction bands [3, 4]. Among the II-VI semiconductors, zinc oxide (ZnO) is very promising due to its essential uses in many research domains. ZnO semiconductor exhibits electronic properties as large exciton binding energy of 60 meV with direct band

gap of 3.37 eV [5, 6]. It is nontoxic, cheap, biosafe, and biocompatible [7]. Zinc oxide is a transparent electro conductive material, ultraviolet absorber, and antibacterial agent. Owing to their electrical, optical, mechanical, and magnetic properties resulting from quantum confinement effects, nanoparticles of ZnO are candidates of applications in piezoelectric transducers, transparent field-effect transistors, gas sensors, optical waveguides, transparent conductive films, ultraviolet nanolasers, varistors, photodetectors, solar cells, blue and ultraviolet (UV) optical devices, and bulk acoustic wave devices [8–13]. The modification of metal oxide nanoparticles by doping with special metal and nonmetal elements makes it possible to enhance the electrical and optical properties of materials by changing the surface properties. Doping

semiconductor nanocrystals with transition metals (TMs) forms diluted magnetic semiconductors (DMSs) [14–18]. A vital characteristic of ZnO is the presence of intrinsic defects. The optical, electronic, and magnetic characteristics of ZnO can be modified by doping or the formed intrinsic lattice defects. Recently, room temperature ferromagnetism in ZnO doped with TMs has been studied both theoretically and experimentally [19–21]. ZnO-based DMSs attracted more attention in spintronic applications and optoelectronic devices [22–24]. Doping ZnO nanocrystals with rare earth (RE) ions [25, 26] is identified as candidates for luminescence centers via their optical advantages and in improving the magnetic properties of ZnO. Among the rare earth elements, samarium has allured recognition because of its prospective in different applications. We will briefly introduce some previous studies regarding rare earth and transition element-doped ZnO. Liu et al. [27] integrated  $\text{Nd}^{3+}$  ions into hexagonal ZnO nanocrystals. Karthikeyan et al. [28] studied the optical properties of ZnO nanoparticles doped by  $\text{Dy}^{3+}$ . Oprea et al. [29] reported the influence of  $\text{Gd}^{3+}$  doping on the photoluminescence, magnetic properties, and photocatalytic activity of ZnO nanoparticles synthesized by simple sol-gel method. The optical and magnetic properties in the  $\text{Eu}^{3+}$ -doped ZnO nanocrystals were reported by Yoon et al. [30]. Using coprecipitation method, Lotey et al. [31] investigated the room temperature ferromagnetism in ZnO nanoparticles when doped by  $\text{Tb}^{3+}$ . Sekhar et al. [32] researched the effect of  $\text{Sm}^{3+}$  doping on the structural, optical, and magnetic properties of ZnO nanopowders using the chemical refluxing technique. Farhat et al. [33] reported the influence of  $\text{Er}^{3+}$  doping on ZnO nanoparticles prepared by wet chemical coprecipitation method. By coprecipitation technique, Sharrouf et al. [34] investigated the result of  $\text{Mn}^{2+}$  doping on ZnO nanoparticles.

Out of the various techniques that were used for the synthesis of undoped and doped ZnO nanoparticles, coprecipitation is one of the most important techniques in preparing metal-oxide nanoparticles that are highly reactive at low temperature sintering. Within the coprecipitation synthesis technique, the particle size can be controlled by adjusting the pH value using inorganic base, the temperature of the reaction, the annealing temperature, and time [35]. The present work reports the effect of Sm doping with different concentrations up to 10% on the structural, morphological, optical, and magnetic properties of the ZnO nanoparticles. The aim of this work is to reach better results regarding optical and magnetic properties for their importance in luminescence centers and spintronic devices, respectively. The ZnO/Sm nanoparticles were prepared by coprecipitation technique that provides nanopowders with good quality despite of the low cost and simplicity of this method.

## 2. Materials and Methods

**2.1. Preparation of ZnO Nanoparticles.** The  $\text{Zn}_{1-x}\text{Sm}_x\text{O}$  nanopowders ( $x = 0.00, 0.01, 0.02, 0.04, 0.06, 0.08, \text{ and } 0.10$ ) were synthesized by coprecipitation technique using zinc chloride as the source of zinc and samarium (III) chloride hexahydrate as the source of dopants. Pure ZnO nanoparticles were

prepared by considering 0.2 M zinc chloride ( $\text{ZnCl}_2$ ) and an alkali solution of 4.0 M sodium hydroxide (NaOH of pH = 13.8). The solution was prepared by adding 20 g of zinc chloride and 3.72 g of Edta disodium dehydrate into 146.735 ml of purified water. 16 g of NaOH was added to 100 ml of distilled water then added dropwise to the above solution under magnetic stirring for 2 hours at 60°C. The final pH of the solution is  $\approx 12$ , because a highly basic condition is convenient for the direct preparation of wurtzite-type ZnO crystals to reduce the respective zinc salt and vigorous synthetic environment [36]. The precipitate was separated from the mixture by filtration where it was washed with purified water until pH  $\approx 7$  and then dried at 100°C for 18 hours. The dried ingots were calcined using the muffle furnace (Gallenkamp FSL-340) at 500°C for 5 hours. Doped Sm-ZnO nanoparticles were synthesized by a similar process except that the used amount of samarium (III) chloride hexahydrate was dependent on the needed concentration of Sm relative to Zn.

**2.2. Characterization Methods.** The synthesized  $\text{Zn}_{1-x}\text{Sm}_x\text{O}$  nanoparticles were characterized by X-ray powder diffraction at room temperature using Bruker D8 advance powder diffractometer with  $\text{Cu-K}_\alpha$  radiation ( $\lambda = 1.54056 \text{ \AA}$ ) in the range  $10^\circ \leq 2\theta \leq 80^\circ$ . TEM micrographs were obtained by using JEOL transmission electron microscope JEM-100CX operated at 80 kV. The FTIR spectra of the powder samples were displayed using FTIR Nicolet iS5-Thermoscientific where about 5 mg of the  $\text{Zn}_{1-x}\text{Sm}_x\text{O}$  powder were mixed with 100 mg of KBr and then pressed to form a disk of 0.6 mm thickness and 1.3 cm diameter. UV-visible measurements were recorded, at room temperature, using the ultraviolet-visible-near infrared (NIR) spectrophotometer V-670 that registered the absorption spectra at a range of wavelengths of 190–2500 nm where 5 mg of  $\text{Zn}_{1-x}\text{Sm}_x\text{O}$  powder was dissolved in 50 ml of ethanol. Magnetic measurements were performed at room temperature using a vibrating sample magnetometer (Lake Shore 7410) having temperature range capability from 4.2 K to 1273 K.

## 3. Results and Discussion

**3.1. Structure and Morphology.** Figure 1 shows the XRD patterns of  $\text{Zn}_{1-x}\text{Sm}_x\text{O}$  for  $0.00 \leq x \leq 0.10$ . The diffraction peaks belong to the planes (100), (002), (101), (102), (110), (103), (200), (112), (201), and (202). All of the observed peaks harmonized with those of wurtzite hexagonal structure ZnO (JCPDS card number 36-1451,  $a = b = 3.249 \text{ \AA}$ ,  $c = 5.206 \text{ \AA}$ ) with the preferred orientation of (101) planes and no additional peaks appeared for secondary phases that may originate from Sm doping, revealing the good synthesis of ZnO:Sm nanoparticles. The nonexistence of  $\text{Sm}_2\text{O}_3$  as separate phase may be attributed to the complete dissolving of samarium in ZnO lattice [37]. The diffraction peaks are sharp and narrow, showing the high crystallinity and purity of the synthesized nanoparticles as reported by Ramimoghdam et al. [38] for ZnO nanoparticles prepared using palm olein as biotemplate.

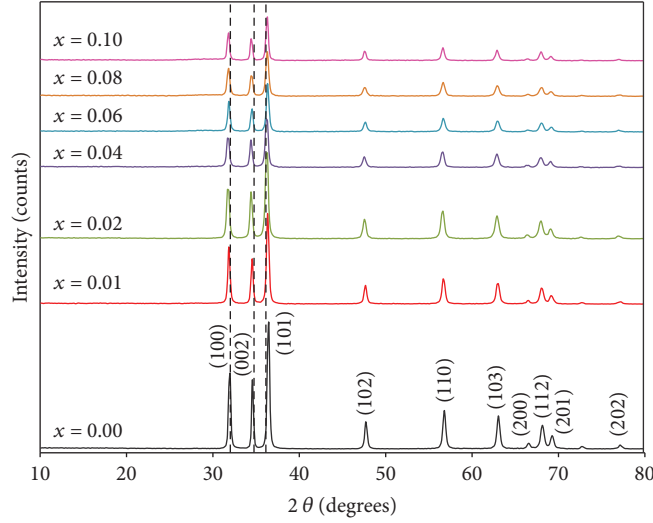


FIGURE 1: XRD patterns of  $Zn_{1-x}Sm_xO$  for  $0.01 \leq x \leq 0.10$ .

In Sm-doped ZnO, the diffraction angle ( $2\theta$ ) for the first three peaks showed a slight shift towards lower angles corresponding to pure ZnO sample, and this result was reported by Sekhar et al. [32]. This phenomenon can be interpreted to the difference in the ionic radius of  $Sm^{3+}$  (0.95 Å) and  $Zn^{2+}$  (0.74 Å). The result of shifted position peaks ensures that the  $Sm^{3+}$  ions substituted  $Zn^{2+}$  ions in the ZnO matrix and consequently a change in the average of crystal size.

The lattice parameters ( $a$  and  $c$ ) and the unit cell volume ( $V$ ) of  $Zn_{1-x}Sm_xO$  nanoparticles, ( $0.00 \leq x \leq 0.10$ ), were calculated using the following equations:

$$\frac{1}{d^2} = \frac{4}{3} \left( \frac{h^2 + hk + k^2}{a^2} \right) + \frac{l^2}{c^2}, \quad (1)$$

$$V = \frac{\sqrt{3}}{2} a^2 c, \quad (2)$$

where  $d$  is the interplanar distance and ( $h$ ,  $k$ , and  $l$ ) are the Miller indices.

The average crystallite sizes of the synthesized samples were calculated from XRD spectra using Debye-Scherrer's equation:

$$D = \frac{0.9\lambda}{\beta \cos \theta}, \quad (3)$$

where  $D$  is the average crystallite size of the particle,  $\lambda$  is the incident X-ray wavelength,  $\beta$  is the angular peak width at half maximum in radians, and  $\theta$  is the Bragg's diffraction angle. The calculated lattice parameters, the ratio  $c/a$ , the unit cell volume ( $V$ ), and the average crystallite size ( $D$ ) of the synthesized samples are listed in Table 1. The crystallite size calculated from XRD was found to decrease with the increase of Sm doping which can be attributed to the intervention of  $Sm^{3+}$  in the ZnO crystal growth. The influence of this intrusion can be related with the distortion of the crystal lattice as

TABLE 1: Values of the lattice parameters ( $a$  and  $c$ ), the ratio ( $c/a$ ), the unit cell volume ( $V$ ), and the crystallite size ( $D$ ) of  $Zn_{1-x}Sm_xO$ .

$x$	$a$ (Å)	$c$ (Å)	$c/a$	$V$ (Å <sup>3</sup> )	$D_{(XRD)}$ (nm)	$D_{(TEM)}$ (nm)
0.00	3.2422	5.1936	1.601	47.27	54.0	49.0
0.01	3.2363	5.1643	1.595	46.84	43.0	38.0
0.02	3.2438	5.1946	1.601	47.33	36.0	33.0
0.04	3.2444	5.1974	1.601	47.38	35.0	31.0
0.06	3.2348	5.1827	1.602	46.96	35.0	30.0
0.08	3.2396	5.1888	1.601	47.16	35.0	29.0
0.10	3.3564	5.3920	1.606	52.60	33.0	27.0

a result of substitution with larger ionic radii of  $Sm^{3+}$  ions (0.95 Å) compared to  $Zn^{2+}$  ions with ionic radii (0.74 Å) [39]. Arora et al. [40] reported Sm-doped ZnO samples with average crystallite sizes ranging from 41 to 37 nm. Wang et al. [41] found that the average crystallite sizes of Sm-doped ZnO samples ranges from 10.5 to 7.5 nm. From Table 1, it is clear that the average crystallite size for the prepared samples ranges from 54 to 33 nm which is much closer to Arora et al.'s [40] findings.

The lattice parameters fluctuated with the increase of Sm doping, which indicates that the structure of ZnO was perturbed by the doping of Sm. The results in Table 1 show that the lattice constants  $a$  and  $c$  of samarium-doped ZnO nanoparticles were larger than those of pure ZnO for  $x = 0.02$ , 0.04, and 0.10. On the other hand, the lattice parameters decreased for  $x = 0.01$ , 0.06, and 0.08 relative to pure ZnO. Decrease in lattice parameters is expected when Sm substitutes Zn while the lattice parameter will increase when Sm occupies interstitial sites [42]. The ratio ( $c/a$ ) is approximately 1.60 for all samples which is compatible with the ideal value for hexagonal cell ( $c/a = 1.633$ ) [43].

Figures 2(a)–2(d) show the TEM micrographs of  $Zn_{1-x}Sm_xO$  nanoparticles for  $x = 0.00$ ,  $x = 0.01$ ,  $x = 0.06$ , and  $x = 0.10$ , respectively. The size of the particles was

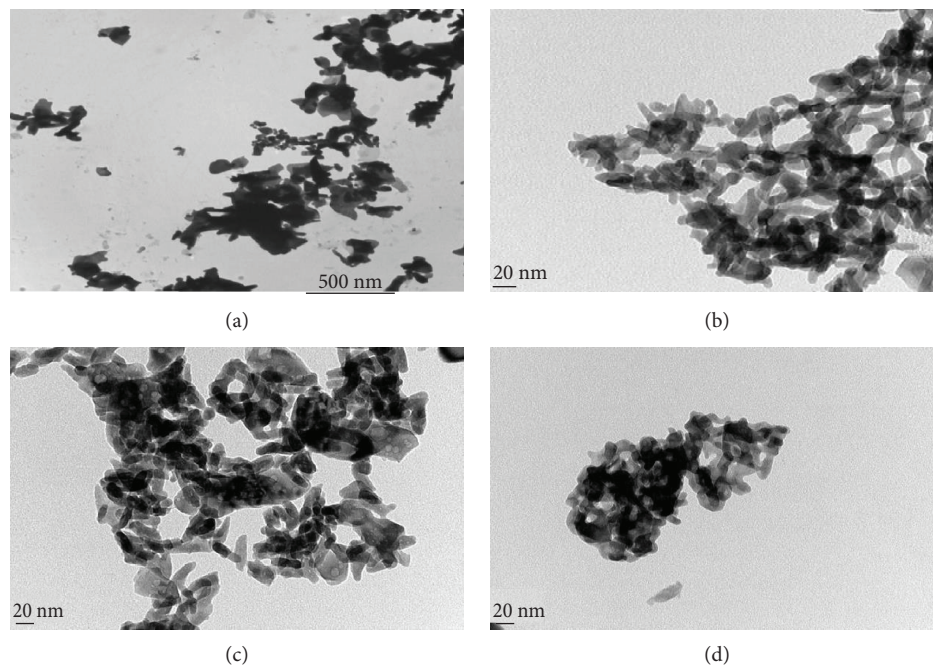


FIGURE 2: TEM micrographs for  $\text{Zn}_{1-x}\text{Sm}_x\text{O}$  with (a)  $x = 0.00$ , (b)  $x = 0.01$ , (c)  $x = 0.06$ , and (d)  $x = 0.10$ .

measured and showed a similar decreasing trend as the crystallite size obtained by XRD measurements with the increase in Sm content. The results are given in Table 1. The particles did not exhibit definite shape for the investigated samples with  $x = 0.00$  and  $x = 0.10$  which was interpreted by Vaseem et al. [44] that when the reaction is accomplished in dry air, the synthesized ZnO nanoparticles have absence of defined shape or size. The high temperature heating process [45] explains the lack of definite shape, which indicates that destruction in recrystallization of ZnO lattice happened. The particle's shape was modified to nanolike rods for samples with  $0.01 \leq x \leq 0.08$  due to the doping level of samarium that results in the alter of the nanoparticle's form [34]. Figure 2(d) shows an agglomeration of the synthesized nanoparticles when the doping level of samarium reaches a concentration of  $x = 0.10$ .

**3.2. Atomic Bonding Vibration Mode Analysis.** The composition and quality of the prepared samples were investigated by the FTIR spectroscopy. Figure 3 shows the FTIR spectra of pure and samarium-doped ZnO nanoparticles with  $x = 0.00, 0.04, 0.06$ , and  $0.10$ . Magnified positions of the first absorption band of  $\text{Zn}_{1-x}\text{Sm}_x\text{O}$  samples for  $x = 0.00, 0.04, 0.06$ , and  $0.10$  are revealed in the inset of Figure 3. The peaks communicating to the vibrational characteristics of ZnO are viewed for the samples in the range  $[397-431] \text{ cm}^{-1}$  which is ascribed to the Zn-O stretching band [46]. The shift of the peak's position in the doped samples relative to the pure one reflects that the Zn-O structure was perturbed by the presence of Sm in its environment. The slight shift in the Zn-O stretching peak might be due to the change in the parameters and the bond properties of Zn perturbed by Sm doping [34]. This result is similar to that obtained in

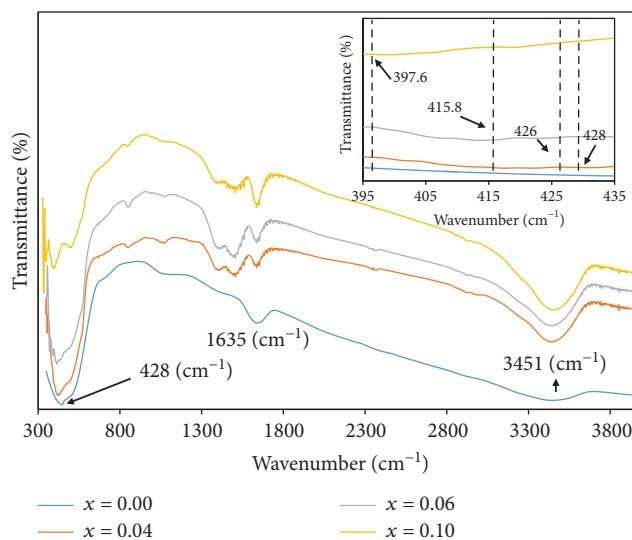
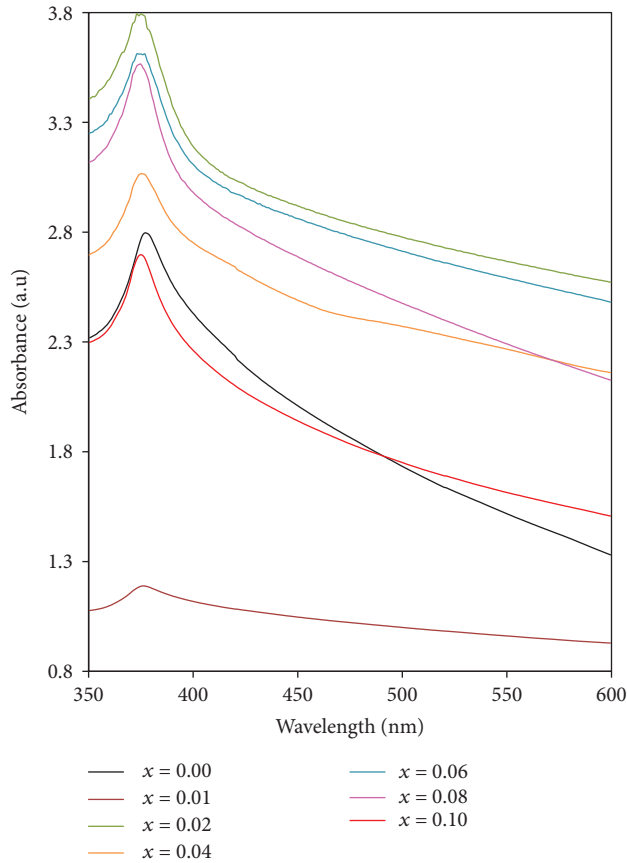


FIGURE 3: FTIR spectra of  $\text{Zn}_{1-x}\text{Sm}_x\text{O}$  nanoparticles with  $x = 0.00, x = 0.04, x = 0.06$ , and  $x = 0.10$ . The inset shows the absorption peaks of  $\text{Zn}_{1-x}\text{Sm}_x\text{O}$  with  $x = 0.00, x = 0.04, x = 0.06$ , and  $x = 0.10$  at Zn-O stretching vibration.

Fe-doped ZnO films by Srivastava et al. [47], and it is also explained by Armelao et al. [48] reporting that the stretching modes of ZnO are modified due to the different ionic radii of  $\text{Zn}^{2+}$  and  $\text{Mn}^{2+}$ . The values of the absorption peak of Zn-O for  $0.00 \leq x \leq 0.10$  are listed in Table 2. The peak present at  $1635 \text{ cm}^{-1}$  is assigned to the OH bending of water, and the broad peak at  $3451 \text{ cm}^{-1}$  is ascribed to the O-H stretching mode [49]. Presence of O-H group indicates the presence of water molecules on the surface of ZnO nanoparticles even after drying condition in the preparation technique. The

TABLE 2: Wavelength of Zn-O stretching vibrations.

$x$	0.00	0.01	0.02	0.04	0.06	0.08	0.10
Wavenumber ( $\text{cm}^{-1}$ )	428.9	431.6	430.4	426.1	415.8	413.6	397.6

FIGURE 4: The UV-visible spectroscopy of  $\text{Zn}_{1-x}\text{Sm}_x\text{O}$  for  $0.01 \leq x \leq 0.10$ .

noticeable bands between  $750\text{ cm}^{-1}$  and  $1090\text{ cm}^{-1}$  in the synthesized samples may correlate with the bending and twisting modes of vibration of ZnOH. In the range of  $1100\text{--}1600\text{ cm}^{-1}$ , the absorption peaks could be ascribed to the bending mode of Zn-OH, plane bending of C-OH, and C-OH out-of-plane bending [50].

**3.3. Spectrophotometric Measurements of ZnO:Sm Nanoparticles.** Figure 4 shows the optical absorption of ZnO:Sm nanoparticles ( $0.00 \leq x \leq 0.10$ ) which was measured by using the UV-visible optical spectroscopy in a scanning range of wavelength from 350 to 600 nm at room temperature, with scan interval of 1 nm. By the optical absorption result, it is possible to determine each of optical energy band gaps of direct transition occurring in band gap and Urbach energy.

The absorption band edge of undoped ZnO was spotted at 377 nm and it got shifted slightly for the Sm-doped samples which might be attributed to surface effects,

modification in the crystallite size, morphology or evidence that the electronic structure of pure ZnO is changed by the doping of samarium [51]. This transposition designates that the Sm ions have incorporated well in the ZnO matrix.

**3.3.1. Determination of Optical Energy Band Gap of Direct Transition of ZnO:Sm Nanoparticles.** The deviation of the absorption edge, due to doping, explains the change in the energy gap of the prepared samples. The optical band gap of the nanopowders was determined by applying the Tauc relationship as given below [52]:

$$\alpha h\nu = C(h\nu - E_g)^n, \quad (4)$$

where  $\alpha$  is the absorption coefficient ( $\alpha = 2.303A/L$ , here A is the absorbance and L is the thickness of the cuvette), C is the constant,  $h$  is Planck's constant,  $\nu$  is the photon frequency, and  $E_g$  is the optical band gap. The value of  $n = 1/2, 3/2, 2,$  or 3 depends on the nature of electronic transition responsible for absorption. Wurtzite ZnO has a direct band gap and  $n = 1/2$  in this case.

Figures 5(a) and 5(b) show the graph of  $(\alpha h\nu)^2$  versus photon energy  $h\nu$  for ZnO:Sm nanoparticles with  $x = 0.00$  and  $x = 0.08$ . The linear dependences of  $(\alpha h\nu)^2$  on  $h\nu$  of ZnO:Sm at higher photon energies reveal that these nanoparticles are essentially direct-transition-type semiconductors. The respective values of  $E_g$  for pure and Sm-doped ZnO nanoparticles were obtained by extrapolating to  $(\alpha h\nu)^2 = 0$ . The values of energy band gap are recorded in Table 3 and it was found that the band energy gaps of pure and Sm-doped ZnO samples are in the range 2.6-2.98 eV. The results show that the band gap energy of Sm-doped ZnO nanoparticles with  $x = 0.01$  decreased relative to pure ZnO; then, it increased to 2.98 eV for  $x = 0.02$ . The value of  $E_g$  decreased again for  $x = 0.04$  then it rose for  $0.08 \leq x \leq 0.10$ . Based on the second order perturbation theory, the lowering in  $E_g$  may be attributed to  $sp-d$  interchange interactions and ascribed to  $p-d$  and  $s-d$  interactions leading to band gap bowing [51]. Identical results were investigated by Mote et al. [53], Mondal et al. [54], and Singh et al. [55] where the shift in  $E_g$  between undoped ZnO and Mn-doped ZnO was found to be 3.26-2.96 eV, 3.22-3.06 eV, and 3.24-3.14 eV, respectively. Recently, Sekhar et al. [32] noticed a decrease in band gap energy of Sm-doped ZnO which was ascribed to the increase in the particle size with increasing Sm concentration. Similar results were recorded by Arora et al. [40] where the decrease in  $E_g$  of Sm-doped ZnO was attributed to an increase in the number of defects. Hosseini et al. [56] reported a decrease in  $E_g$  of Ag-doped ZnO which was related to the presence of p-type conductivity in the silver-doped ZnO nanoparticles where this reduction in energy gap led to increase the efficiency in the use of these

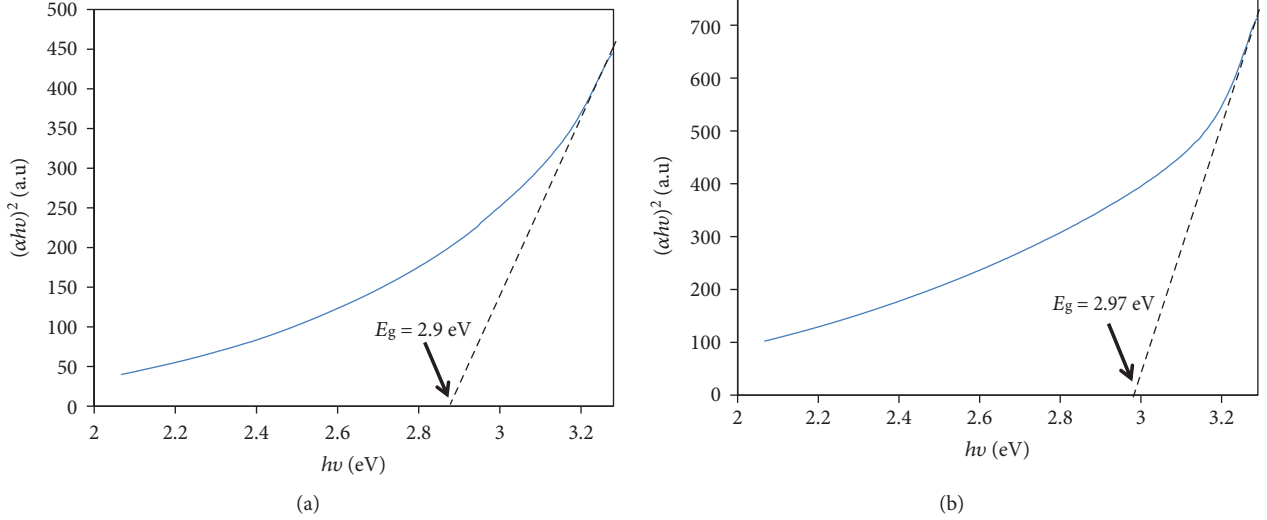


FIGURE 5:  $(\alpha hv)^2$  versus photon energy ( $hv$ ) of  $Zn_{1-x}Sm_xO$  for (a)  $x = 0.00$  and (b)  $x = 0.08$ .

TABLE 3: Values of energy band gap and Urbach energy for  $Zn_{1-x}Sm_xO$ .

$x$	$E_g$ (eV)	$E_u$ (eV)
0.00	2.90	2.03
0.01	2.60	6.43
0.02	2.98	4.09
0.04	2.60	4.60
0.06	2.80	4.24
0.08	2.97	3.08
0.10	2.97	2.62

materials in optoelectronic devices. Jayachandriah et al. [57] interpreted the decrease in  $E_g$  to the electron localized states of rare earth activator ion that develop and insert new electronic states nearer to conduction band. Increasing the band gap energy, as a result of quantum confinement effect, is attributed to the reduction in the particle size along with enlarging the doping concentration [39]. Farhat et al. [33] reported that the variation of  $E_g$  relies on the particle size and lattice parameters. According to Bras' effective mass model,  $E_g$  of nanoparticles can be expressed as a function of particle size as follows:

$$E_g = E_{\text{bulk}} + \frac{\hbar^2 \pi^2}{2R^2} \left[ \frac{1}{m_e} + \frac{1}{m_h} \right] - \frac{1.8 e^2}{\epsilon R}, \quad (5)$$

where  $E_{\text{bulk}}$  is the band gap of the bulk semiconductor,  $\hbar$  is the second Plank's constant,  $R$  is the radius of the nanoparticle,  $m_e$  is the effective mass of the electron,  $m_h$  is the effective mass of the hole,  $e$  is the charge of electron, and  $\epsilon$  is the electric permittivity of the material.

**3.3.2. Determination of Urbach Energy of ZnO:Sm Nanoparticles.** In the absorption edge, the size of the exponential tail is identified by the Urbach energy which relies

on thermal vibrations in the lattice, temperature, average photon energies, static disorder, induced disorder, and on strong ionic bonds. In the low photon energy scale, the spectral dependence of the absorption edge is given by the empirical Urbach rule [58].

$$\alpha = \beta e^{hv/E_u} \quad (6)$$

where  $\beta$  is constant,  $E_u$  is the Urbach energy and ( $\nu$ ) is the frequency of the radiation.

The graphs of the logarithm of the absorption coefficient  $\ln(\alpha)$  as a function of the photon energy for ZnO:Sm nanoparticles with  $x = 0.00$  and  $x = 0.08$  are shown in Figures 6(a) and 6(b), respectively. The Urbach energy was determined, in the lower photon energy of these plots, by calculating the reciprocals of the slope of the linear part. The values of  $E_u$  are listed in Table 3.

**3.4. Magnetic Study.** Magnetic behavior of  $Zn_{1-x}Sm_xO$  nanoparticles was investigated by tracing, at room temperature, the variation of the magnetization ( $M$ ) in emu/g as a function of an applied magnetic field ( $H$ ) as shown in Figures 7(a)–7(d) for the samples with  $x = 0.00, 0.01, 0.08,$  and  $0.10,$  respectively. The pure ZnO reveals a ferromagnetic behavior. In general, the three possible reasons for ferromagnetism can be summarized as the following: (i) defect related mechanism that is often announced for DMSs [59], (ii) presence of secondary phases of impurities, and (iii) appearance of micro Sm clusters. However, in the present work, the XRD of Sm-doped ZnO nanoparticles did not show indication of secondary phases. Moreover, signs of Sm clusters were not noticed, which display that the samarium atoms successfully replaced the regular Zn sites. In conclusion, the existence of ferromagnetism at room temperature (RTFM) is interpreted by defect-related mechanism. In our samples, the exchange interactions connecting unpaired electron spins emerging from oxygen vacancies along the surface of nanoparticles may be the origin of ferromagnetism. Generally, magnetic semiconducting systems can be

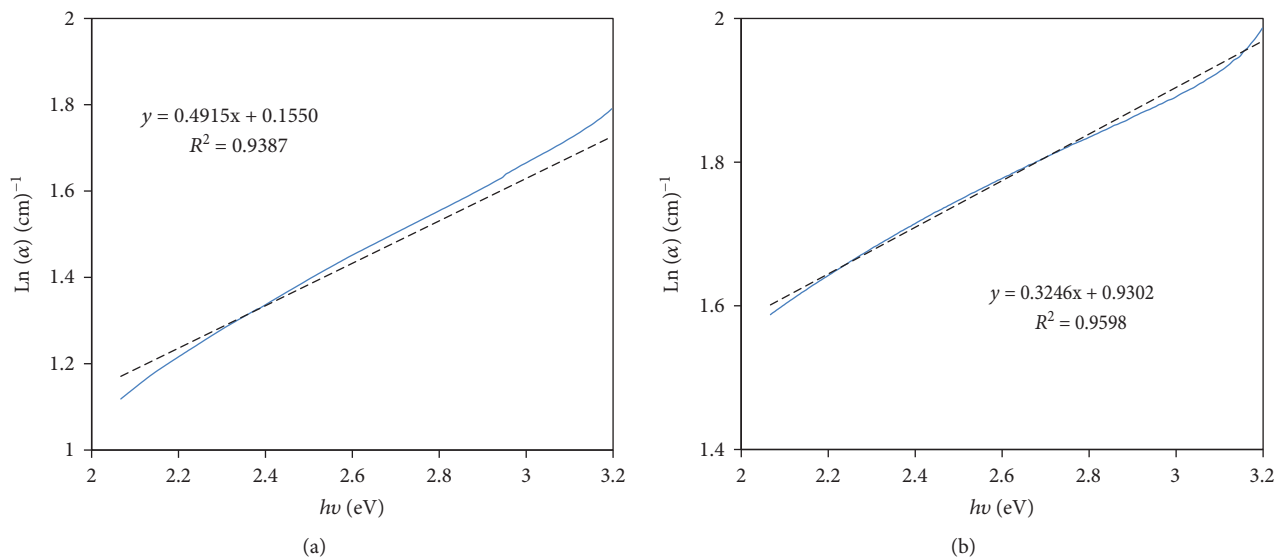


FIGURE 6:  $\ln(\alpha)$  versus photon energy ( $h\nu$ ) is shown in the inset for (a)  $x = 0.00$  and (b)  $x = 0.08$ .

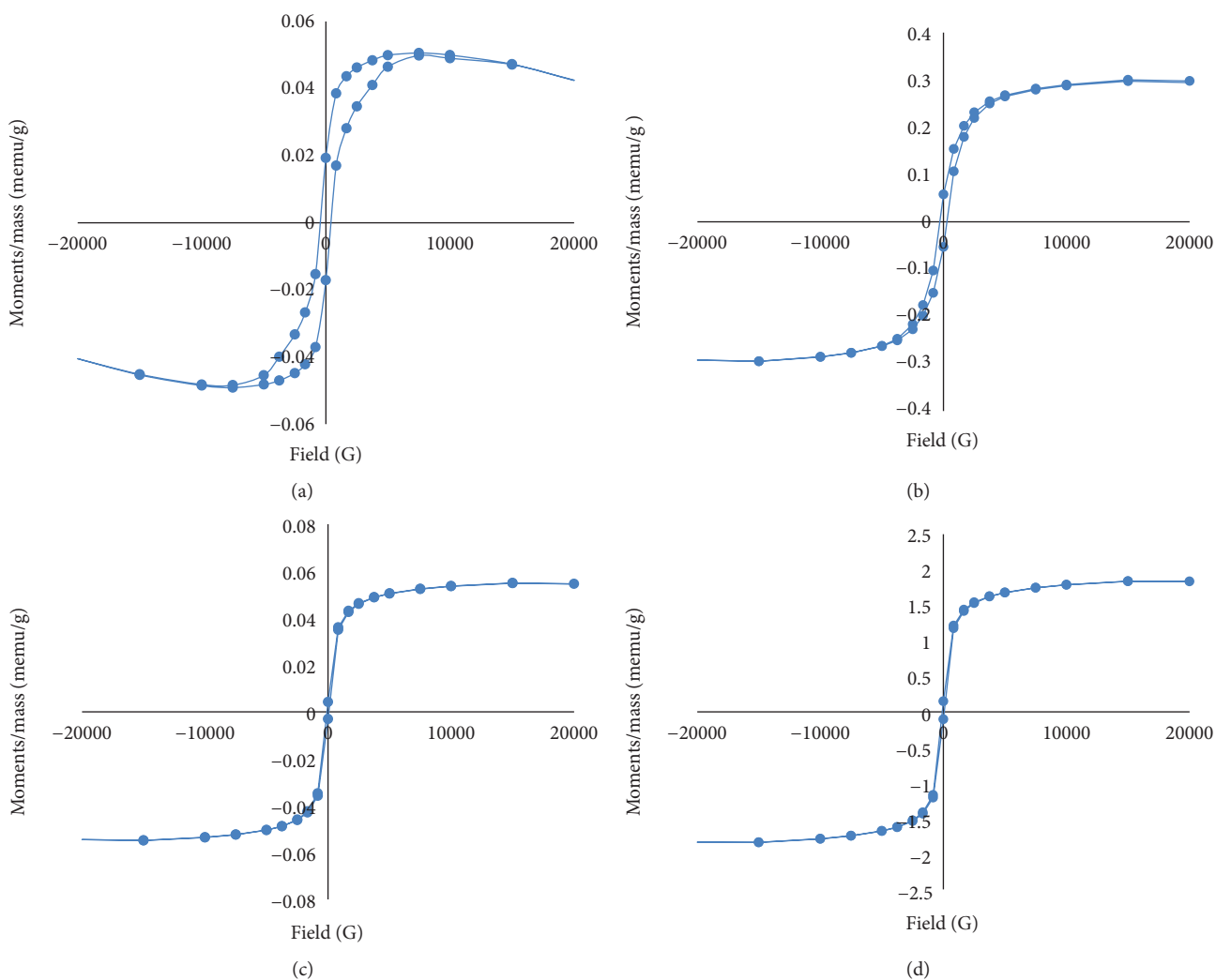


FIGURE 7: (M-H) hysteresis loop of  $Zn_{1-x}Sm_xO$  nanoparticles for (a)  $x = 0.00$ , (b)  $x = 0.01$ , (c)  $x = 0.08$ , and (d)  $x = 0.10$ .

TABLE 4: The variation of  $M_s$ ,  $M_r$ ,  $H_c$ , and  $S$  as a function of  $x$ .

$x$	$M_s$ (emu/g)	$M_r$ (emu/g)	$H_c$ (G)	$S = M_r/M_s$
0.00	0.0498	0.0182	441.30	0.36546
0.01	0.2970	0.0554	288.36	0.18653
0.02	1.2602	0.0631	61.28	0.05014
0.04	0.3243	0.0050	227.49	0.01541
0.06	1.3665	0.0691	61.54	0.05058
0.08	0.0540	0.0036	78.56	0.06722
0.10	1.8370	0.0001	81.14	0.00006

identified by delocalized band electrons. Magnetic ions are specified by localized 3d or 4f shells. The magnetic properties are determined by the localized magnetic moments accompanied with the magnetic ions and their interaction with the host semiconductor. The interaction accountable for the magnetic behavior is s, p-f in rare earth magnetic ions. Consequently, samarium-doped ZnO shows dilute magnetic semiconducting behavior. The hysteresis loop of undoped ZnO sample also displayed diamagnetic and paramagnetic participations since the magnetization  $M$  decreased with the increase of applied magnetic field  $H$  after 0.05 G. Phadnis et al. [60] reported similar observations regarding ZnO nanocrystals covered with polyvinyl pyrrolidone (PVP) and prepared by the wet chemical route technique at room temperature.

As the concentration of Sm increased, a serious modification in the magnetic hysteresis loops existed. The RTFM was also observed for the doped samples with concentrations  $x = 0.01$  and  $x = 0.04$  which may be ascribed to the substitutional inclusion of Sm in Zn-sites. The ferromagnetic nature decreased for these concentrations which may be ascribed to the fact that some Sm atoms approach each other leading to superexchange interactions between them. Thus, RTFM is lowered relative to pure ZnO, and the antiferromagnetic coupling grows in nature.

The hysteresis loops for  $x = 0.02$ ,  $x = 0.06$ ,  $x = 0.08$ , and  $x = 0.10$  are very narrow in comparison with the other samples. Kittel [61] established theoretical predictions regarding energetic stability of a single magnetic domain, determining a critical dimension of a particle (typically nanometers for normal ferromagnets). In smaller particles, existence of a single ferromagnetic zone is favored. Thermal fluctuations acting upon small particles cannot confirm stable bulk magnetization; consequently, the system displays superparamagnetism (SPM) [62]. In accordance with the TEM technique, all synthesized samples have unlike domains of nanoparticle sizes and those for  $x = 0.02$  and  $0.06 \leq x \leq 0.10$ , possess number of particles with sizes smaller than 35 nm that might explain the emergence of superparamagnetism and accordingly smaller contribution to ferromagnetism.

The values of saturation magnetization ( $M_s$ ), retentivity ( $M_r$ ), coercivity ( $H_c$ ) and squareness ratio  $S = (M_r/M_s)$  are presented in Table 4.

It can be noticed that the values of  $M_s$  and  $M_r$  have the same variation trends for  $0.00 \leq x \leq 0.08$ . The highest value of the saturation magnetization and the lowest value of the

retentivity are revealed for  $x = 0.10$ . The  $H_c$  values vary with increasing the doping values. For the samples that showed ferromagnetic behavior with  $x = 0.00$ ,  $x = 0.01$  and  $x = 0.04$ , the values of  $H_c$  decreased while the values of  $M_s$  increased. Variations in the coercive field were produced by dissimilarity in defect states and anisotropy contribution due to the clusters of crystallites [63]. Jung et al. [64] reported that remanence to saturation ratio ( $S = M_r/M_s$ ) characterizes the squareness of the hysteresis loops, where  $S \ll 0.01$  is a typical value for SPM particles. The data of  $S$  in our samples are lower than 0.5, denoting that the particles communicate by magnetostatic interaction and the anisotropy decreases in crystal lattice [65, 66]. The squareness ratio ( $S$ ) of the sample with  $x = 0.10$  is 0.00006 which indicates a superparamagnetic behavior.

## 4. Conclusions

Pure and samarium-doped ZnO nanoparticles ( $Zn_{1-x}Sm_xO$ ), ( $0.00 \leq x \leq 0.10$ ), were prepared by chemical coprecipitation method. XRD investigation revealed the existence of hexagonal wurtzite structure of ZnO with the absence of  $Sm_2O_3$  as separate phase. TEM micrographs revealed that the synthesized particles have no definite shape for  $x = 0.00$  and  $x = 0.10$  and the form of the particles was modified to nanolike rods for  $0.01 \leq x \leq 0.08$ . FTIR analysis for pure and doped ZnO samples admitted the existence of O-H and Zn-O stretching modes around  $3451 \text{ cm}^{-1}$  and  $428 \text{ cm}^{-1}$ , respectively, with a peak shift regarding Zn-O stretching mode attributed to modifications in parameters and bond properties of ZnO lattice when perturbed by samarium doping. The band gap energies ( $E_g$ ) and Urbach energies ( $E_u$ ) were computed from the UV-VIS spectra. The calculated values of  $E_g$  were in the range 2.6-2.98 eV. Hysteresis curves from vibrating sample magnetometer study, at room temperature, revealed that undoped ZnO nanoparticles exhibited a ferromagnetic signal merged with diamagnetic and paramagnetic behavior. The ferromagnetism behavior was diminished for the synthesized samples with  $x = 0.01$  and  $x = 0.04$ . A superparamagnetic behavior appeared for samples with  $x = 0.02$  and  $0.06 \leq x \leq 0.10$  revealing the potential applications in different industries triggering further research. Other parameters such as saturation magnetization, coercive field, and remanent magnetism from VSM analysis were calculated.

## Data Availability

The data used to support the findings of this study are included within the article. Any more specific details in the data will be delivered by the corresponding author upon request.

## Conflicts of Interest

The authors declare that they do not have conflicts of interest.

## Acknowledgments

This work has been performed in the Materials Science Lab, Physics Department, Faculty of Science, Beirut Arab University, Debbieh, in cooperation with the Faculty of Science, Alexandria University, Alexandria, Egypt.

## References

- [1] V. L. Colvin, M. C. Schlamp, and A. P. Alivisatos, "Light-emitting diodes made from cadmium selenide nanocrystals and a semiconducting polymer," *Nature*, vol. 370, no. 6488, pp. 354–357, 1994.
- [2] A. P. Alivisatos, "Perspectives on the physical chemistry of semiconductor nanocrystals," *The Journal of Physical Chemistry*, vol. 100, no. 31, pp. 13226–13239, 1996.
- [3] A. A. Bol, R. van Beek, and A. Meijerink, "On the incorporation of trivalent rare earth ions in II–VI semiconductor nanocrystals," *Chemistry of Materials*, vol. 14, no. 3, pp. 1121–1126, 2002.
- [4] F. Dejene, A. Ali, H. Swart et al., "Optical properties of ZnO nanoparticles synthesized by varying the sodium hydroxide to zinc acetate molar ratios using a Sol-Gel process," *Open Physics*, vol. 9, no. 5, 2011.
- [5] Y. Li, X. Liu, and J. Li, "Preparation and characterization of CeO<sub>2</sub> doped ZnO nano-tubes fluorescent composite," *Journal of Rare Earths*, vol. 28, no. 4, pp. 571–575, 2010.
- [6] Y. I. Jung, B. Y. Noh, Y. S. Lee, S. H. Baek, J. H. Kim, and I. K. Park, "Visible emission from Ce-doped ZnO nanorods grown by hydrothermal method without a post thermal annealing process," *Nanoscale Research Letters*, vol. 7, no. 1, p. 43, 2012.
- [7] J. Zhou, N. S. Xu, and Z. L. Wang, "Dissolving behavior and stability of ZnO wires in biofluids: a study on biodegradability and biocompatibility of ZnO nanostructures," *Advanced Materials*, vol. 18, no. 18, pp. 2432–2435, 2006.
- [8] S. B. Rana, P. Singh, A. K. Sharma, A. W. Carbonari, and R. Dogra, "Synthesis and characterization of pure and doped ZnO nanoparticles," *Journal of Optoelectronics and Advanced Materials*, vol. 12, no. 2, p. 257, 2010.
- [9] M. de la L. Olvera and R. Asomoza, "SnO<sub>2</sub> and SnO<sub>2</sub>:Pt thin films used as gas sensors," *Sensors and Actuators B: Chemical*, vol. 45, no. 1, pp. 49–53, 1997.
- [10] C. R. Gorla, N. W. Emanetoglu, S. Liang et al., "Structural, optical, and surface acoustic wave properties of epitaxial ZnO films grown on (0112) sapphire by metalorganic chemical vapor deposition," *Journal of Applied Physics*, vol. 85, no. 5, pp. 2595–2602, 1999.
- [11] K. Nomura, H. Ohta, K. Ueda, T. Kamiya, M. Hirano, and H. Hosono, "Thin-film transistor fabricated in single-crystalline transparent oxide semiconductor," *Science*, vol. 300, no. 5623, pp. 1269–1272, 2003.
- [12] M. H. Huang, S. Mao, H. Feick et al., "Room-temperature ultraviolet nanowire nanolasers," *Science*, vol. 292, no. 5523, pp. 1897–1899, 2001.
- [13] C. T. Lee, Y. K. Su, and H. M. Wang, "Effect of r.f. sputtering parameters on ZnO films deposited onto GaAs substrates," *Thin Solid Films*, vol. 150, no. 2–3, pp. 283–289, 1987.
- [14] J. K. Furdyna, "Diluted magnetic semiconductors," *Journal of Applied Physics*, vol. 64, no. 4, pp. R29–R64, 1988.
- [15] J. M. D. Coey, "Dilute magnetic oxides," *Current Opinion in Solid State and Materials Science*, vol. 10, no. 2, pp. 83–92, 2006.
- [16] I. Žutić, J. Fabian, and S. Das Sarma, "Spintronics: fundamentals and applications," *Reviews of Modern Physics*, vol. 76, no. 2, pp. 323–410, 2004.
- [17] H. Ohno, "Making nonmagnetic semiconductors ferromagnetic," *Science*, vol. 281, no. 5379, pp. 951–956, 1998.
- [18] S. A. Wolf, D. D. Awschalom, R. A. Buhrman et al., "Spintronics: a spin-based electronics vision for the future," *Science*, vol. 294, no. 5546, pp. 1488–1495, 2001.
- [19] R. G. Hernández, W. L. Pérez, and M. Jairo Arbey Rodríguez, "Electronic structure and magnetism in Ni<sub>0.0625</sub>Zn<sub>0.9375</sub>O: an ab initio study," *Journal of Magnetism and Magnetic Materials*, vol. 321, no. 17, pp. 2547–2549, 2009.
- [20] S. J. Pearton, D. P. Norton, Y. W. Heo et al., "ZnO spintronics and nanowire devices," *Journal of Electronic Materials*, vol. 35, no. 5, pp. 862–868, 2006.
- [21] B. Pandey, S. Ghosh, P. Srivastava, D. K. Avasthi, D. Kabiraj, and J. C. Pivin, "Synthesis and characterization of Ni-doped ZnO: a transparent magnetic semiconductor," *Journal of Magnetism and Magnetic Materials*, vol. 320, no. 24, pp. 3347–3351, 2008.
- [22] M. Subramanian, P. Thakur, M. Tanemura et al., "Intrinsic ferromagnetism and magnetic anisotropy in Gd-doped ZnO thin films synthesized by pulsed spray pyrolysis method," *Journal of Applied Physics*, vol. 108, no. 5, article 053904, 2010.
- [23] M. H. N. Assadi, Y. B. Zhang, P. Photongkam, and S. Li, "Intrinsic ambient ferromagnetism in ZnO:Co induced by Eu codoping," *Journal of Applied Physics*, vol. 109, no. 1, article 013909, 2011.
- [24] G. R. Li, X. H. Lu, C. Y. Su, and Y. X. Tong, "Facile synthesis of hierarchical ZnO:Tb<sup>3+</sup> nanorod bundles and their optical and magnetic properties," *The Journal of Physical Chemistry C*, vol. 112, no. 8, pp. 2927–2933, 2008.
- [25] L. Armelao, F. Heigl, A. Jürgensen et al., "X-ray excited optical luminescence studies of ZnO and Eu-doped ZnO nanostructures," *The Journal of Physical Chemistry C*, vol. 111, no. 28, pp. 10194–10200, 2007.
- [26] F. J. Duarte, *Tunable Laser Applications*, CRC, New York, NY, USA, 2nd edition, 2009.
- [27] Y. Liu, W. Luo, R. Li, and X. Chen, "Optical properties of Nd<sup>3+</sup> ion-doped ZnO nanocrystals," *Journal of Nanoscience and Nanotechnology*, vol. 10, no. 3, pp. 1871–1876, 2010.
- [28] B. Karthikeyan, C. S. Suchand Sandeep, T. Pandiyarajan, P. Venkatesan, and R. Philip, "Spectrally broadened excitonic absorption and enhanced optical nonlinearities in Dy<sup>3+</sup>-doped ZnO nanoparticles," *Applied Physics A*, vol. 102, no. 1, pp. 115–120, 2011.
- [29] O. Oprea, O. R. Vasile, G. Voicu, L. Craciun, and E. Andronescu, "Photoluminescence, magnetic properties and photocatalytic activity of Gd<sup>3+</sup> doped ZnO nanoparticles," *Digest Journal of Nanomaterials & Biostructures*, vol. 7, no. 4, pp. 1757–1766, 2012.
- [30] H. Yoon, J. Hua Wu, J. Hyun Min, J. Sung Lee, J. S. Ju, and Y. Keun Kim, "Magnetic and optical properties of monosized Eu-doped ZnO nanocrystals from nanoemulsion," *Journal of Applied Physics*, vol. 111, no. 7, article 07B523, 2012.
- [31] G. S. Lotey, J. Singh, and N. K. Verma, "Room temperature ferromagnetism in Tb-doped ZnO dilute magnetic

- semiconducting nanoparticles,” *Journal of Materials Science: Materials in Electronics*, vol. 24, no. 9, pp. 3611–3616, 2013.
- [32] M. C. Sekhar, U. Chalaphthi, V. K. Madhu Smitha, P. T. Poojitha, S. Uthanna, and B. Poornaprakash, “Influence of Sm doping on the structural, optical, and magnetic properties of ZnO nanopowders,” *Journal of Superconductivity and Novel Magnetism*, vol. 30, no. 7, pp. 1937–1941, 2017.
- [33] S. Farhat, M. Rekaby, and R. Awad, “Synthesis and characterization of Er-doped nano ZnO samples,” *Journal of Superconductivity and Novel Magnetism*, pp. 1–11, 2018.
- [34] M. Sharrouf, R. Awad, S. Marhaba, and D. El-Said Bakeer, “Structural, optical and room temperature magnetic study of Mn-doped ZnO nanoparticles,” *Nano*, vol. 11, no. 4, article 1650042, 2016.
- [35] P. Tartaj, M. del Puerto Morales, S. Veintemillas-Verdaguer, T. González-Carreño, and C. J. Serna, “The preparation of magnetic nanoparticles for applications in biomedicine,” *Journal of Physics D: Applied Physics*, vol. 36, no. 13, pp. R182–R197, 2003.
- [36] A. Naveed Ul Haq, A. Nadhman, I. Ullah, G. Mustafa, M. Yasinzai, and I. Khan, “Synthesis approaches of zinc oxide nanoparticles: the dilemma of ecotoxicity,” *Journal of Nanomaterials*, vol. 2017, Article ID 8510342, 14 pages, 2017.
- [37] N. R. E. Radwan, “Modification of surface and catalytic properties of Fe<sub>2</sub>O<sub>3</sub> due to doping with rare-earth oxides Sm<sub>2</sub>O<sub>3</sub> and Y<sub>2</sub>O<sub>3</sub>,” *Applied Catalysis A: General*, vol. 273, no. 1-2, pp. 21–33, 2004.
- [38] D. Ramimoghadam, M. Z. B. Hussein, and Y. H. Taufiq-Yap, “Synthesis and characterization of ZnO nanostructures using palm olein as biotemplate,” *Chemistry Central Journal*, vol. 7, no. 1, p. 71, 2013.
- [39] H. Y. He, J. Fei, and J. Lu, “Sm-doping effect on optical and electrical properties of ZnO films,” *Journal of Nanostructure in Chemistry*, vol. 5, no. 2, pp. 169–175, 2015.
- [40] D. Arora, K. Asokan, A. Mahajan, H. Kaur, and D. P. Singh, “Structural, optical and magnetic properties of Sm doped ZnO at dilute concentrations,” *RSC Advances*, vol. 6, no. 81, pp. 78122–78131, 2016.
- [41] Y. Wang, J. Piao, Y. Lu, S. Li, and J. Yi, “Intrinsic ferromagnetism in Sm doped ZnO,” *Materials Research Bulletin*, vol. 83, pp. 408–413, 2016.
- [42] S. U. Awan, S. K. Hasanain, G. Hassnain Jaffari, D. H. Anjum, and U. S. Qurashi, “Defects induced luminescence and tuning of bandgap energy narrowing in ZnO nanoparticles doped with Li ions,” *Journal of Applied Physics*, vol. 116, no. 8, article 083510, 2014.
- [43] H. Kim, A. R. M. Yusoff, H. Lee et al., “Effect of ZnO:Cs<sub>2</sub>CO<sub>3</sub> on the performance of organic photovoltaics,” *Nanoscale Research Letters*, vol. 9, no. 1, p. 323, 2014.
- [44] M. Vaseem, A. Umar, and Y. B. Hahn, “ZnO nanoparticles: growth, properties, and applications,” in *Metal Oxide Nanostructures and their Applications*, vol. 5, pp. 1–36, American Scientific Publishers, New York, NY, USA, 2010.
- [45] N. K. Divya and P. P. Pradyumnan, “Solid state synthesis of erbium doped ZnO with excellent photocatalytic activity and enhanced visible light emission,” *Materials Science in Semiconductor Processing*, vol. 41, pp. 428–435, 2016.
- [46] R. F. Silva and M. E. D. Zaniquelli, “Morphology of nanometric size particulate aluminium-doped zinc oxide films,” *Colloids and Surfaces A: Physicochemical and Engineering Aspects*, vol. 198–200, pp. 551–558, 2002.
- [47] A. Srivastava, N. Kumar, and S. Khare, “Enhancement in UV emission and band gap by Fe doping in ZnO thin films,” *Opto-Electronics Review*, vol. 22, no. 1, p. 68, 2014.
- [48] L. Armelao, M. Fabrizio, S. Gialanella, and F. Zordan, “Sol-gel synthesis and characterisation of ZnO-based nanosystems,” *Thin Solid Films*, vol. 394, no. 1-2, pp. 89–95, 2001.
- [49] Y. M. Hao, S. Y. Lou, S. M. Zhou, R. J. Yuan, G. Y. Zhu, and N. Li, “Structural, optical, and magnetic studies of manganese-doped zinc oxide hierarchical microspheres by self-assembly of nanoparticles,” *Nanoscale Research Letters*, vol. 7, no. 1, p. 100, 2012.
- [50] J. Das, I. R. Evans, and D. Khushalani, “Zinc glycolate: a precursor to ZnO,” *Inorganic Chemistry*, vol. 48, no. 8, pp. 3508–3510, 2009.
- [51] A. Azam, A. S. Ahmed, S. S. Habib, and A. H. Naqvi, “Effect of Mn doping on the structural and optical properties of SnO<sub>2</sub> nanoparticles,” *Journal of Alloys and Compounds*, vol. 523, pp. 83–87, 2012.
- [52] R. Dogra, A. P. Byrne, and M. C. Ridgway, “PAC investigations of radiation damage annealing in <sup>111</sup>In implanted ZnO,” *Optical Materials*, vol. 31, no. 10, pp. 1443–1447, 2009.
- [53] V. D. Mote, J. S. Dargad, and B. N. Dole, “Effect of Mn doping concentration on structural, morphological and optical studies of ZnO nano-particles,” *Nanoscience and Nanoengineering*, vol. 1, no. 2, pp. 116–122, 2013.
- [54] S. Mondal, S. R. Bhattacharyya, and P. Mitra, “Preparation of manganese-doped ZnO thin films and their characterization,” *Bulletin of Materials Science*, vol. 36, no. 2, pp. 223–229, 2013.
- [55] P. Singh, A. Kaushal, and D. Kaur, “Mn-doped ZnO nanocrystalline thin films prepared by ultrasonic spray pyrolysis,” *Journal of Alloys and Compounds*, vol. 471, no. 1-2, pp. 11–15, 2009.
- [56] S. M. Hosseini, I. A. Sarsari, P. Kameli, and H. Salamati, “Effect of Ag doping on structural, optical, and photocatalytic properties of ZnO nanoparticles,” *Journal of Alloys and Compounds*, vol. 640, pp. 408–415, 2015.
- [57] C. Jayachandriah and G. Krishnaiah, “Erbium induced raman studies and dielectric properties of Er-doped ZnO nanoparticles,” *Advanced Materials Letters*, vol. 6, no. 8, pp. 743–748, 2015.
- [58] M. A. Hassan and C. A. Hogarth, “A study of the structural, electrical and optical properties of copper tellurium oxide glasses,” *Journal of Materials Science*, vol. 23, no. 7, pp. 2500–2504, 1988.
- [59] B. Panigrahy, M. Aslam, and D. Bahadur, “Effect of Fe doping concentration on optical and magnetic properties of ZnO nanorods,” *Nanotechnology*, vol. 23, no. 11, article 115601, 2012.
- [60] C. Phadnis, D. Y. Inamdar, I. Dubenko, A. Pathak, N. Ali, and S. Mahamuni, “Ferromagnetic ZnO nanocrystals and Al-induced defects,” *Journal of Applied Physics*, vol. 110, no. 11, article 114316, 2011.
- [61] C. Kittel, “Domain theory and the dependence of the coercive force of fine ferromagnetic powders on particle size,” *Physical Review*, vol. 73, no. 7, pp. 810–811, 1948.
- [62] W. Wernsdorfer, R. Clérac, C. Coulon, L. Lecren, and H. Miyasaka, “Quantum nucleation in a single-chain magnet,” *Physical Review Letters*, vol. 95, no. 23, article 237203, 2005.
- [63] N. Doğan, A. Bingölbali, and L. Arda, “Preparation, structure and magnetic characterization of Ni doped ZnO nano-

- particles,” *Journal of Magnetism and Magnetic Materials*, vol. 373, pp. 226–230, 2015.
- [64] J. S. Jung, L. Malkinski, J. H. Lim et al., “Fabrication and magnetic properties of Co nanostructures in AAO membranes,” *Bulletin of the Korean Chemical Society*, vol. 29, no. 4, pp. 758–760, 2008.
- [65] S. Xavier, S. Thankachan, B. P. Jacob, and E. M. Mohammed, “Effect of samarium substitution on the structural and magnetic properties of nanocrystalline cobalt ferrite,” *Journal of Nanoscience*, vol. 2013, Article ID 524380, 7 pages, 2013.
- [66] E. C. Stoner and E. P. Wohlfarth, “A mechanism of magnetic hysteresis in heterogeneous alloys,” *Philosophical Transactions of the Royal Society A: Mathematical, Physical and Engineering Sciences*, vol. 240, no. 826, pp. 599–642, 1948.